DISSERTATION

KINETIC AND MECHANISTIC STUDIES OF SUPPORTED-NANOPARTICLE HETEROGENEOUS CATALYST FORMATION IN CONTACT WITH SOLUTION

Submitted by

Joseph E. Mondloch

Department of Chemistry

In partial fulfillment of the requirements

For the Degree of Doctor of Philosophy

Colorado State University

Fort Collins, Colorado

Summer 2011

Doctoral Committee:

Advisor: Richard G. Finke

Travis S. Bailey
Eric M. Ferreira
Amy L. Prieto
Matthew P. Shores

ABSTRACT

KINETIC AND MECHANISTIC STUDIES OF SUPPORTED-NANOPARTICLE HETEROGENEOUS CATALYST FORMATION IN CONTACT WITH SOLUTION

This dissertation begins with a comprehensive and critical review of the literature addressing the kinetics and mechanism(s) of supported-nanoparticle heterogeneous catalyst formation. The review chapter that follows makes apparent that routine kinetic monitoring methods, as well as well-defined supported-nanoparticle formation systems, are needed in order to gain fundamental insights into the mechanisms of supported-nanoparticle heterogeneous catalyst formation—a somewhat surprising finding given the long history as well as commercial importance of heterogeneous catalysis. Hence, the research presented within this dissertation is focused on (i) developing a kinetic monitoring method (i.e., in what follows, the cyclohexene reporter reaction method) capable of measuring supported-nanoparticle formation in contact with solution, and (ii) developing a well-defined supported-nanoparticle formation system, also in contact with solution, that is amenable to rigorous mechanistic studies.

Development of the cyclohexene reporter reaction has allowed for the rapid and quantitative monitoring of the kinetics of $Pt(0)_n/Al_2O_3$ and $Pt(0)_n/TiO_2$ supported-nanoparticle heterogeneous catalyst formation in contact with solution from

H_2PtCl_6/Al_2O_3 and H_2PtCl_6/TiO_2 respectively. Importantly, those kinetic studies revealed conditions where the most desirable, chemical-reaction-based, supported-nanoparticle formation conditions are present rather than diffusional-limited kinetic regimes. The largest drawback when utilizing the H_2PtCl_6 as a supported-precatalyst is its speciation—that is, other solvated Pt-based species form when in contact with solution. Such non-uniform speciation leads to a large variation in the supported-nanoparticle formation kinetics, observations that were obtained through the use of the cyclohexene reporter reaction kinetic monitoring method.

Due to the large variability in the formation kinetics associated with the H_2PtCl_6 precatalyst speciation, synthesized next as a part of this dissertation work was the well-defined, fully characterized, speciation-controlled supported-organometallic precatalyst, Ir(1,5-COD)Cl/γ-Al_2O_3. When in contact with acetone, cyclohexene and H_2 this supported-precatalyst was found to evolve into a highly active and long-lived $Ir(0)_{\sim 900}$/γ-Al_2O_3 supported-nanoparticle catalyst. The kinetics of $Ir(0)_{\sim 900}$/γ-Al_2O_3 formation were successfully followed by the cyclohexene reporter reaction method and found to be well-fit by a two-step mechanism consisting of nucleation (A → B, rate constant k_1) followed by autocatalytic surface growth (A + B → 2B, rate constant k_2) previously elucidated by Finke and Watzky. More specifically, nucleation was found to occur in solution from Ir(1,5-COD)Cl(solvent), while nanoparticle growth occurs on the γ-Al_2O_3 support, but in a reaction that involves the Ir(1,5-COD)Cl(solvent) species in solution.

Most importantly, the fits to the two-step mechanism suggest that the nine synthetic and mechanistic insights, of nanoparticle formation in solution, should now be applicable to the formation of supported-nanoparticle heterogeneous catalysts in contact with

solution. That is, it seems reasonable to expect that these studies will allow a more direct avenue for transferring both the mechanistic and synthetic insights that have resulted from the modern revolution in nanoparticle science to the synthesis of size, shape and compositionally controlled supported-nanoparticle catalysts under the nontraditional, mild and flexible conditions where supported organometallics and other precursors are in contact with solution.

ACKNOWLEDGEMENTS

This dissertation and the work contained within would not have been possible without the help of many people. To start, my beautiful wife Shannon Riha, who consistently motivated, supported and challenged me for the past four years. I am thankful to my wonderful family and many friends who for the most part, “do not quite understand what I do”, but regardless, offer continuous support. Finally, I would like to thank my advisor Professor Richard G. Finke as well as the Finke group members that have been at Colorado State University over the course of the past five years, without them the science would not have been possible.

TABLE OF CONTENTS

CHAPTER 1

INTRODUCTION

The theme of this dissertation is to understand the kinetics and associated mechanisms that govern the formation of supported-nanoparticle heterogeneous catalysts at the gas-liquid-solid interface. This dissertation is written in the "journals-format" style, the details of which are provided in Appendix A of this dissertation for the interested reader. This dissertation is based on four separate publications, the first of which is a literature review (Chapter II) submitted for publication (and hence has been formatted for that submission) to the *Journal of Molecular Catalysis A: Chemical (Elsevier)*. The three subsequent chapters (Chapters III–V) have already been published in the *Journal of the American Chemical Society* and are, therefore, written in the format set forth by the American Chemical Society. Continuity of this dissertation (as a single document) is achieved through the use of (i) this introduction, (ii) bridging sections between each individual chapter and (iii) a summary chapter. Presented below is a concise overview of each of the chapters II–V within this dissertation.

Chapter II is a critical review of the literature regarding the kinetics and mechanisms of formation of supported-nanoparticle heterogeneous catalysts. The review is broken down into two sections: (i) supported-nanoparticle formation at the gas-solid interface, and (ii) supported-nanoparticle formation at the gas-liquid-solid interface. Also presented are sections discussing supported-nanoparticle heterogeneous

catalyst preparation and the physical methods capable of monitoring the kinetics of formation of such heterogeneous catalysts. The primary literature is given in the form of relevant case studies that highlight the current state of knowledge regarding measuring the kinetics, and then deducing the most probable mechanisms of formation, of supported-nanoparticle heterogeneous catalysts via both the gas-solid, and gas-liquid-solid, interfaces. Finally a conclusions section is provided that summarizes the pertinent literature and suggests needed future studies. Of central importance to the present dissertation is that the comprehensive review of the literature makes apparent the need for more routine kinetic monitoring methods, as well as the need for well-defined supported-nanoparticle formation systems amenable to such kinetic and mechanistic studies, all while the gas-liquid-solid interface is present.

Chapter III is a second publication (Mondloch, J. E.; Yan, X.; Finke, R. G *J. Am. Chem. Soc.* **2009,** *131,* 6389–6396) that describes the development of a kinetic monitoring method for following the kinetics of supported-nanoparticle formation in contact with solution. More specifically, the kinetics of the classic H_2PtCl_6/Al_2O_3 to $Pt(0)_n/Al_2O_3$ system, and also H_2PtCl_6/TiO_2 to $Pt(0)_n/TiO_2$, were followed by the cyclohexene reporter reaction method. Key mechanistic insights from that work include: (i) the $Pt(0)_n/Al_2O_3$ supported-nanoparticle formation kinetics are well-fit to the Finke-Watzky two-step mechanism consisting of nucleation (A $\rightarrow$ B, rate constant k_1) and autocatalytic surface growth (A + B $\rightarrow$ 2B, rate constant k_2); (ii) the speciation of that H_2PtCl_6/Al_2O_3 precatalyst in contact with EtOH and cyclohexene yields irreproducible kinetics unless a pre-equilibration period is present; and (iii) that the $Pt(0)_n/TiO_2$ supported-nanoparticle formation kinetics are dominated by H_2 gas-to-solution mass transfer limitations, which is consistent with an earlier literature report of $Pt(0)_n/TiO_2$ supported-nanoparticle formation at the gas-solid interface from Chupas and co-workers.

Chapter IV is a third publication (Mondloch, J. E.; Wang, Q.; Frenkel, A. I.; Finke, R. G. *J. Am. Chem. Soc.* **2010,** *132,* 9701–9714), that develops a prototype Ir(1,5-COD)Cl/γ-Al_2O_3 to $Ir(0)_{\sim 900}$/γ-Al_2O_3 supported-nanoparticle formation system in contact with acetone and cyclohexene solution plus the reductant, H_2. Extensive state-of-the-art efforts were made to thoroughly characterize the Ir(1,5-COD)Cl/γ-Al_2O_3 precatalyst (via ICP, CO adsorption, IR and XAFS spectroscopies), the $Ir(0)_{\sim 900}$/γ-Al_2O_3 supported-nanoparticle catalyst (via TEM, XAFS spectroscopy and catalytic activity and lifetime measurements) and also the reaction stoichiometry (via cyclooctane evolution and H_2 uptake measurements). The kinetics of the $Ir(0)_{\sim 900}$/γ-Al_2O_3 supported-nanoparticle formation were also followed via the cyclohexene reporter reaction method. Key mechanistic insights from Chapter IV include: (i) that the $Ir(0)_{\sim 900}$/γ-Al_2O_3 supported-nanoparticle formation kinetics are well-fit to the two-step mechanism consisting of nucleation (A → B, rate constant k_1) and autocatalytic surface growth (A + B → 2B, rate constant k_2) and (ii) that speciation is not present when starting from the well-defined supported-precatalyst, Ir(1,5-COD)Cl/γ-Al_2O_3.

Chapter V is a final publication (Mondloch, J. E.; Finke, R. G. *J. Am. Chem. Soc.* **2011,** *133,* 7744–7756.) that probes the more intricate mechanistic details of the Ir(1,5-COD)Cl/γ-Al_2O_3 to $Ir(0)_{\sim 900}$/γ-Al_2O_3 supported-nanoparticle formation system while in contact with solution (acetone, cyclohexene and dissolved H_2). Emphasis is placed on determining where (in solution, on the support, or in both phases) the supported-nanoparticle catalyst formation steps are occurring. Key mechanistic insights from Chapter V include: (i) that nucleation occurs in solution from Ir(1,5-COD)Cl(solvent) that dissociated from the γ-Al_2O_3 support; (ii) that small $Ir(0)_n$ nanoparticles are then captured by the γ-Al_2O_3 support; (iii) that the autocatalytic surface growth step occurs between $Ir(0)_n$/γ-Al_2O_3 and Ir(1,5-COD)Cl(solvent) and (iv) that the dissociative equilibrium nucleation step is analogous to the kinetically and mechanistically well-studied, Ir(1,5-

COD)•$P_2W_{15}Nb_3O_{62}^{8-}$ to $Ir(0)_{\sim 300}$•$(P_2W_{15}Nb_3O_{62}^{8-})_n^{-8n}$ solution-based, polyoxoanion-stabilized nanoparticle formation and stabilization system.

Chapter VI is a summary section that concisely details the material presented within, and the main scientific findings from, this dissertation.

CHAPTER II

A REVIEW OF THE KINETICS AND MECHANISM(S) OF FORMATION OF SUPPORTED-NANOPARTICLE HETEROGENEOUS CATALYSTS

This dissertation chapter consists of a review article, which has been submitted for publication to the *Journal of Molecular Catalysis A: Chemical*. This chapter is a critical review of the extant literature regarding supported-nanoparticle heterogeneous catalyst formation at the gas–solid and gas–liquid–solid interfaces. Despite the commercial importance of supported-nanoparticle heterogeneous catalysts, this review is the first-of-its-kind.

The primary literature regarding supported-nanoparticle heterogeneous catalyst formation was gathered and complied by Joseph E. Mondloch. Ercan Bayram helped construct the first initial draft of the manuscript after the primary literature had been gathered and analyzed. Specifically, Ercan Bayram constructed first drafts of the sections now titled “X-ray Absorbance Fine Structure (XAFS) Spectroscopy”, as well as a section no longer contained within the submitted manuscript (titled “Model-UHV Catalyst Systems”). The remaining portions (see the Table of Contents Pg V) of the manuscript were written by Joseph E. Mondloch and edited by Professor Richard G. Finke.

The page numbers listed in the table of contents of this literature review (Chapter II) have been altered to reflect the final page numbers of this independently formatted dissertation.

A REVIEW OF THE KINETICS AND MECHANISMS OF FORMATION OF SUPPORTED-NANOPARTICLE HETEROGENEOUS CATALYSTS

Joseph E. Mondloch, Ercan Bayram and Richard G. Finke

Overview

Nanoparticles supported on high surface area supports are commonly used in many industrially relevant catalytic reactions. This review examines the existing literature of the mechanisms of formation of practical, non-ultra high vacuum, supported-nanoparticle heterogeneous catalysts. Specifically, this review includes: (i) a brief review of the synthesis of supported-nanoparticles, (ii) an overview of the physical methods for following the kinetics of formation of supported-nanoparticles, and then (iii) a summary of the kinetic and mechanistic studies of the formation of supported-nanoparticle catalysts, performed under the traditional synthetic conditions of the gas-solid interface. This review then also discusses (iv) the synthesis, (v) physical methods, and (vi) the extant kinetic and mechanistic studies under the less traditional, less examined conditions of the gas-*liquid*-solid interface. A summary of the main insights from each section of the review is also given. We will see that surprisingly little is known about the mechanism(s) of formation of the desired size, shape and compositionally controlled supported-nanoparticle catalysts.

1. Introduction

1.1. The Importance of Mechanistic Studies of Heterogeneous Catalyst Formation

Heterogeneous catalysts are used in many important and industrially relevant catalytic reactions such as hydrogenations, catalytic cracking, or naptha reforming; heterogeneous catalysts are also employed in the water-gas shift reaction, the synthesis of ammonia and for ethylene oxidation, to name a few additional reactions [1,2,3,4]. Often these heterogeneous catalysts take the form of nanoparticles supported on high-surface-area supports [3,5]. Key properties inherent to these supported-nanoparticle catalysts are known to affect greatly the resultant catalytic performance [6,7]. For example, the size [8,9,10], structure [11,12,13] and the lesser-investigated, but crucial, surface composition [14,15,16,17] of the supported-nanoparticles can influence the catalytic selectivity [6,13,18,19], activity [8,20] and lifetime [21]. Hence, in order to exploit these key catalytic properties for catalysis, uniform catalysts of the appropriate size, structure and composition are needed [22,23].

Unfortunately, as Schlögl has recently noted [7], "catalysts are currently prepared rather than synthesized" so that rationally guided syntheses of the desired size, structure and compositionally controlled supported-nanoparticle catalysts are generally lacking. One main reason for this gap is the *relatively poor understanding of the mechanism(s) that govern the formation of these supported-nanoparticle heterogeneous catalysts*. In particular, kinetic studies are often lacking, kinetics being one of the general tools crucial in elucidating reliable reaction mechanisms [24,25,26,27,28].[1]

[1] Complete mechanistic studies require more than just kinetic studies; for example, mechanistic studies of homogeneous organic [24], organometallic [25,26], or inorganic [27,28] reactions typically employ the following types of measurements: (i) first and foremost, determination of the balanced, complete reaction stoichiometry including identification of all trace products; (ii) thermochemical data; (iii) early and direct detection of intermediates—so that multistep reactions can be broken into elementary steps; (iv) kinetic studies, which typically elucidate the composition of the transition-state of the rate-determining step; (v) stereochemistry; (vi) indirect detection or other evidence for (e.g., trapping of) intermediates; (vii) independent syntheses and study of those key intermediates; and (viii) other specialized measurements such as crossover experiments, isotopic labeling or isotope effect studies, to name a few.

1.2. Organization and Scope of the Kinetic and Mechanistic Studies at the Gas-Solid and Gas-Liquid-Solid Interfaces

Herein we focus on reactions that assemble supported-nanoparticles starting from molecular precursors. What follows is organized into two main sections: studies of supported-nanoparticle formation and the *gas-solid* interface (Section 2), and then studies of supported-nanoparticle formation at the gas-*liquid*-solid interface (Section 3). Sections 2 and 3 each contain: (i) a fundamental background information section which details the synthesis of supported-nanoparticles as well as the physical methods that have been utilized to measure their kinetics of formation; (ii) case studies regarding the kinetics and mechanisms of supported-nanoparticle formation; and (iii) a conclusions section that summarizes the key results in each section. A summary section (Section 4) is also provided listing the broader key insights obtained from this first-of-its kind review.

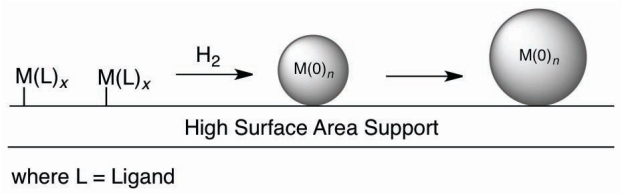

Scheme 1. A pictorial representation of supported-nanoparticle heterogeneous catalyst formation at the gas-solid interface.

To start, in Section 2 we focus on systems involving the *gas-solid* interface as depicted in Scheme 1. We were only able to find thirty-nine papers [29,30,31,32,33,34,35,36,37,38,39,40,41,42,43,44,45,46,47,48,49,50,51,52,53,54,55,56,57,58,59,60,61,62,63,64,65,66,67] (which are given in Table S1, a condensed version of which is shown in Table 2) that address the kinetics and mechanism(s) of practical, non-ultra-high vacuum, supported-nanoparticle heterogeneous catalyst formation at the gas–solid interface, under traditional preparation conditions [22]. Then, in Section 3 we

review systems occurring at the less-commonly studied, but potentially quite valuable, gas-*liquid*-solid interface. We found an additional eight kinetic and mechanistic studies [68,69,70,71,72,73,74,75], listed in Table 3, performed at the less-studied, gas-liquid-solid interface. The presence of a solvent means that the supported-nanoparticle formation steps can occur in solution, on the support, or possibly in both phases as depicted in Scheme 2.

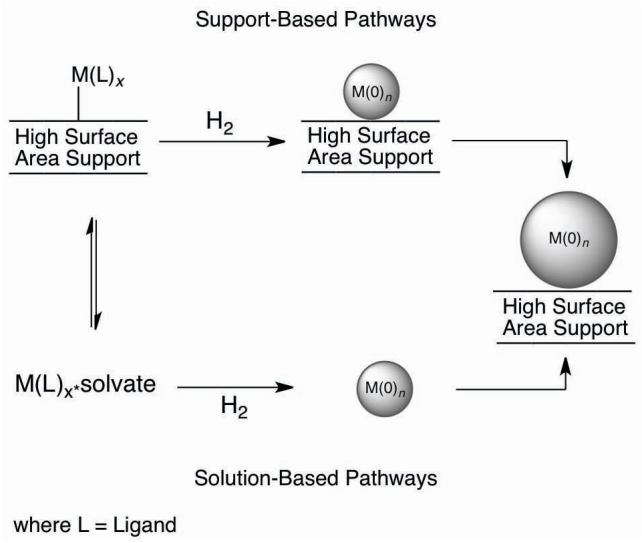

Scheme 2. A pictorial representation of the a priori plausible pathways for supported-nanoparticle formation at the gas-liquid-solid interface. The supported-nanoparticle formation can in principle occur on the support (top), in solution (bottom) or via some combination of these pathways. Section 3.2.2.4, vide infra, will examine the possible pathways in more detail.

Note that the gas-solid and gas-liquid-solid synthetic conditions stand in stark contrast to the cleaner, better studied (and thoroughly reviewed [76,77,78,79]), but model catalysts made under ultra high vacuum (UHV) conditions. The difference between those high-vacuum, ultra-clean, often single-crystal/single facet vapor-deposited metal(0) atom model studies vs. the studies emphasized herein (on "practical, dirty" catalysts) are the so-called "pressure", "temperature" and "materials" gaps [80,81,82,83,84]. The uncertainty at present of how to bridge these gaps means that we

will not cover, but will supply lead references when necessary to the: (i) kinetics and mechanisms of model UHV studies [79,80]; (ii) to reactions that are occurring non-deliberately during catalyst preparation such as "autoreduction";[2] and also references to (iii) to so-called "dynamic adsorbate induced phase changes" [85] of supported metal nanoparticles (such as are present in the reduction of CuO/ZnO to Cu(0)/ZnO [113,86] or the reduction of Rh_2O_3/Al_2O_3 to $Rh(0)/Al_2O_3$ [87], as well as in their single crystalline counterparts [11,88]). In addition, due to space limitations and the desire to focus this review as much as possible we will not cover (iv) the reduction of bulk metal oxides to their metallic counterparts, for example the reduction of $(CuO)_n$ [89] to $Cu(0)_n$. There are some reports of supported-nanoparticle formation at the gas-liquid-solid phase that occur under photo-deposition [90] or γ-irradiation [91] conditions, but those, too, have been deemed beyond the scope of this review.

2. Studies of Supported-Nanoparticles at the Gas-Solid Interface

To begin, it is important to describe the synthetic methods available at present for preparing supported-nanoparticles at the gas-solid interface. Right after that a summary

[2] The phenomenon of "autoreduction" can be described as the formation of supported $M(0)_n$ clusters or nanoparticles under conditions where a typical reductant, such as H_2, is not deliberately introduced into the system. Hence, a reduction reaction can occur under what would otherwise be oxidative (e.g., under O_2 calcination conditions) or inert (e.g., He) conditions. Generally speaking, the primary possible sources of the required reducing equivalents appear at present to be either a ligand or the support [98,151,175]. For example, when starting with $M(NH_3)_4^{2+}$/zeolite (M = Pt, Pd) supported precatalysts, Sachtler has noted that "the formation of metal clusters and zeolite protons in the reducing atmosphere of (decomposing) amine ligands" occurs [98]. An excellent account of "autoreduction" due to ligand-induced reduction, when starting with those $M(NH_3)_4^{2+}$ complexes, is given in the introduction of a paper by van Santen and co-workers [151]. Alternatively, an example where the support appears to supply the reducing equivalent is given by Jacobs and co-workers [175]; they propose that a zeolite support can generate reducing equivalents during thermal dehydration via the following reaction: $2(Ag^+ZO^-) \rightarrow \frac{1}{2}O_2 + Ag_2{}^0 + ZO^- + Z^+$ (where Z indicates the zeolite lattice). Note that high temperature, a relatively weak Ag^+–$^-$OZ bond energy, and a basic/somewhat reducing, anionic site appear to be factors in the driving force of this particular "autoreduction" reaction.

of the physical methods capable of following the kinetics of supported-nanoparticle formation at the gas-solid interface will be given.

2.1. Fundamental Background Information Regarding Supported-Nanoparticle Heterogeneous Catalyst Formation at the Gas-Solid Interface

2.1.1. Preparation Methods for the Synthesis of Supported-Nanoparticle Heterogeneous Catalysts at the Gas-Solid Interface

Many synthetic methods exist for preparing supported-nanoparticle heterogeneous catalysts; hence, several books [3,92,93,94] and reviews [8,95] thoroughly describe such preparation. Therefore, for the purpose of this review it will suffice to briefly outline the most common heterogeneous catalyst preparation techniques. The interested reader is referred to that literature [3,8,92-95] for more detailed discussions of these well-established heterogeneous catalyst preparation methods.

In a simplified view, supported-nanoparticle heterogeneous catalyst preparation consists of three steps: (i) contact of a metal precursor with the support material; (ii) oxidation/calcination of the resultant precatalyst precursor/support material, and then (iii) formation of the active catalyst species via reduction (e.g., often under H_2)—it is this reduction step during which the supported-nanoparticles are typically formed [8].

Introduction of metal precursors onto a suitable support can be accomplished by several, established methods. Common methods include: (i) impregnation [96], which involves deposition of a metal precursor onto a support, typically from an aqueous solution (e.g. the well-studied system of H_2PtCl_6 impregnation onto γ-Al_2O_3, vide infra); (ii) deposition-precipitation (also known as coprecipitation) [97], in which the support and metal precursor are simultaneously precipitated from solution, and (iii) ion-exchange, as commonly used for the preparation of zeolite supported catalysts, for example, where metal salts such as $Pt(NH_3)_4^{2+}$ in aqueous solution are exchanged with 2 K^+ cations from a zeolite support [98]. One can also (iv) employ preformed metal clusters, such as metal

carbonyls, $M(CO)_x$ or $M_y(CO)_z$ [99,100,101], or (v) deposit preformed colloids [8] (and, more recently, preformed/ligated nanoparticles [102,103,104,105],[3] vide infra). Each method has advantages and disadvantages, as discussed in detail elsewhere [8,106], some of which will be brought out in what follows. A relevant point that is often ignored (vide infra) is that of the *metal precatalyst speciation* [72,74]—that is, the specific composition and number of chemical species present post the precatalyst/support contact step, species—are often multiple species, ones that can lead to complex supported-nanoparticle formation reactions and kinetics. Hence, *it is of the utmost importance to synthesize speciation-controlled supported-metal precatalysts in order to achieve the best supported-nanoparticle formation reactions as well as the requisite kinetic and mechanistic studies of those (improved) synthetic reactions.*

The next step in catalyst preparation is often calcination. Che and coworkers have correctly noted that "calcination may have a pronounced effect on the reducibility, dispersion, and distribution of the metal in the final catalyst" [8]. Calcination, typically in air is carried out to oxidatively remove unwanted ligands inherent to the metal precursor

[3] It has been pointed out [102] that modern transition-metal nanoparticles can be distinguished from classical colloids via: (i) their typically smaller size and narrower size distributions; (ii) their isolability; (iii) their better compositional definition, and (iv) their reproducible preparation and subsequent reproducible catalysis [102]. Another relevant distinction here, as discussed previously [104], is that between nano*particles,* nano*clusters* and *clusters*. Schmid and co-workers noted in 2010 [105] that there "is still no clear discrimination between the terms "cluster" and "nanoparticle". Historically, clusters have not been specified in size, but have been considered to be discrete, atomically precise species containing metal–metal bonds "exactly defined in (their) chemical composition and structure" [105]. A plethora of "clusters" are known in the literature; metal carbonyl clusters $M_y(CO)_z$ being among the most well-studied [102,105]. In contrast, the terms nanoparticles and nanoclusters imply a size between 1–100 nm (which are used interchangeably within the extant literature), but "usually mean particles of less precise characterization" [105], often particles with a range of sizes and chemical composition. Hence, the use of the terms nanoparticles, nanoclusters or clusters are used almost interchangeably at present in the literature. To achieve a much more precise vocabulary, we suggest the use of the following terms: (i) *nanoparticle*, when the precise structure of the particle is not known and a range of particle sizes between 1–100 nm are present; (ii) *nanocluster*, when the precise structure of the particle is known and is ≥1 nm in size, and (iii) *cluster*, when the precise composition and structure of the compound are known and the cluster is <1 nm in size.

complex and to attempt to remove, completely, unwanted carbonaceous (overlayer) species that may be present. An important point relevant to the present review, noted by Schwarz and co-workers [106], is that "*calcination can change the metal precatalyst complex, typically forming metal-oxide species that are often ill-defined*"—and, we would add, that are, therefore, typically *not speciation controlled*. Clearly, strongly-ligated precatalysts that yield poorly defined, speciation uncontrolled, secondary precatalysts are non-ideal for both synthetic, as well as kinetic and mechanistic, studies. Beginning with a single, precisely compositionally and structurally defined molecular precursor will be one of the more important, fundamental points apparent throughout this review, vide infra.

The final step in supported-nanoparticle heterogeneous catalyst preparation is the transformation of the precatalyst—or, really and typically, the range of precatalyst species present post the contact and calcination steps, vide infra—to the $M(0)_n$ supported-nanoparticle catalyst(s), typically by reduction under H_2. Again the experimental conditions, such as the temperature or H_2, pressure can change the observed catalyst product so that the reduction step needs to be optimized for each individual supported-metal precatalyst [3]. Importantly, the reduction of non-speciation controlled supported-metal precatalysts often leads to a wide distribution of supported-nanoparticle products (vide supra and vide infra), so that precise, careful control of the precatalyst speciation is essential for preparing the next generation of size-, shape- and composition-controlled supported-nanoparticle catalysts. Overall and ultimately, it will become apparent throughout this review that *each of the catalyst preparation steps (i.e., precursor/support contact, calcination and reduction) can dramatically affect the mechanism(s) by which supported-nanoparticles are formed* (vide infra).

2.1.2 Characterization Methods for Following the Kinetics of Supported-Nanoparticle Heterogeneous Catalyst Formation at the Gas-Solid Interface

Nuzzo and co-workers correctly [45] noted that “methods available to characterize the phase dynamics of nanoscale systems are limited”. This sentiment was echoed by Chupas and co-workers who remarked in 2007 that “the kinetics and mechanisms of nanoparticle formation…have been largely overlooked [56], due to a lack of adequate experimental methodology”.

Table 1 highlights the nine physical methods that have been identified by this review for following the kinetics of supported-nanoparticle heterogeneous catalyst formation in real time and at the gas-solid interface. In addition, Table 1 identifies how many times each physical method has been utilized (see Table S1 of the Supporting Information for a full list of papers identified by this review, from which Table 1 was constructed). Table 1 also lists whether each physical method is direct or indirect in its ability to monitor M–M bond formation or net $M(0)_n$ nanoparticle formation,[4] and indicates whether that physical method is typically used in situ or ex situ. Notably, only five direct methods have been utilized for following supported-nanoparticle heterogeneous catalyst formation, data that reaffirm the aforementioned statements of Nuzzo and co-workers [45] as well as Chupas and co-workers [56].

[4] Herein we have defined a direct measurement as one that can detect M–M bond formation *or* net $M(0)_n$ nanoparticle formation, while an indirect measurement is one that does not routinely detect M–M bond formation (nor net $M(0)_n$ nanoparticle formation). In addition, a direct physical method as defined herein should be able to measure those M–M bonds or $M(0)_n$ over the concentration range of interest.

Table 1. Physical methods used in the literature for measuring the kinetics of supported-nanoparticle heterogeneous catalyst formation at the gas-solid interface.

Method	Times Utilized in Table 2	Direct/ Indirect [a]	In Situ or Ex Situ (as Used to Date)
Extended X-ray Absorbance Fine Structure	18	Direct	In Situ
X-ray Absorbance Near Edge Structure	15	Indirect to Direct [b]	In Situ
H_2 Uptake	8	Indirect	In Situ
Infrared Spectroscopy	5	Indirect	In Situ
Electron Spin Resonance	2	Direct	Ex Situ
H_2 Chemisorption	1	Indirect	Ex Situ
Total High Energy X-ray Scattering Plus Pair-Distribution-Function Analysis	2	Direct	In Situ
UV-Visible Spectroscopy	1	Indirect to Direct [c]	In Situ
X-ray Diffraction	1	Direct	In Situ

[a] Direct vs. indirect indicates whether the physical method can directly monitor M–M or net $M(0)_n$ nanoparticle formation. [b] XANES could in principle be used to follow $M(0)_n$ formation if one has the independent XANES spectrum for both the reactants and products. For the studies identified within this review, the XANES edge has typically been used to follow the loss of the starting material qualitatively. [c] UV-Visible spectroscopy can be direct if the metal of interest contains a plasmon resonance band in the visible region (e.g., Au, Ag and Cu).

Ideally, the use of multiple, complimentary, direct and in situ—or better yet operando[5] [107,108,109,110,111]—physical methods should be used to monitor all of

[5] In principle, all supported-nanoparticle heterogeneous catalyst formation kinetics would be monitored under operando (i.e., working) conditions [107]. The term "operando" implies the "simultaneous evaluation of both catalyst active site structure and catalytic activity/selectivity" [111]. Note here that while "catalyst preparation" does not typically occur under operando conditions, *ideally it should*, so that at least in some cases the M^{x+} to $M(0)_n$ catalyst formation steps would occur, and be monitored, under the actual

the catalyst preparation steps and, then, the evolution kinetics of the supported-nanoparticle catalyst.[5] Below, key physical methods for following the kinetics of supported-nanoparticle heterogeneous catalyst formation are discussed (i.e., and based on the literature results from Table 1); key advantages and disadvantages of each physical method are also highlighted. In addition, recent advances in TEM instrumentation and imaging, ideally of in situ samples [112,113,114,115], promise to prove useful in understanding the mechanisms of supported-nanoparticle heterogeneous catalyst formation.

2.1.2.1. X-ray Absorbance Fine Structure (XAFS) Spectroscopy: X-ray Absorbance Near Edge Spectroscopy (XANES) and Extended X-ray Absorbance Fine-Structure Spectroscopy (EXAFS)

XAFS spectroscopy is a local, average, but generally powerful method for following the kinetics of supported-nanoparticle heterogeneous catalyst formation that can yield (average) structural information for metal-metal and metal-ligand interactions, Table 1. Of the thirty-nine mechanistic studies regarding supported-nanoparticle heterogeneous catalyst formation listed in Table S1 of the Supporting Information, *18 utilize XAFS to obtain their kinetic data*. XAFS is particularly attractive as it can in principle be used at both the gas-solid and gas-liquid-solid interfaces, as well as for all metals and supports of interest. However, one important pitfall to be aware of is that the high energy X-rays can cause beam damage to the sample so that controls, for example varying the beam exposure time, should be performed [52].

Another important experimental consideration is the required data acquisition time—is it slow or relatively fast? Early XAFS data were collected by slow monochromator

---

catalytic reaction conditions of interest. Such studies would, therefore, also be intimately related to so-called dynamic adsorbate induced restructuring [85]. Hence, and at least in principle, complete operando *synthesis* and *monitoring* of all catalyst preparation steps should become the norm en route to the next generation of size-, shape- and composition-controlled supported-nanoparticle catalysts.

scanning, over the course of minutes, the entire X-ray range point-by-point in energy space, making impossible time-resolved experiments on sub-minute time scales [116]. Recently however, quick XAFS (QXAFS, which employs faster scanning) yields data acquisition time scales on the order of seconds. Moreover, energy-dispersive XAFS (DXAFS, which utilizes a bent monochromator to produce the range of required X-rays, so that scanning is not necessary) yields millisecond data-acquisition time scales [116]. Herein, we will refer to all forms of the experiment, including QXAFS and DXAFS, simply as XAFS, but with it being understood that both QXAFS and DXAFS should be employed as required.

Further details regarding the experimental and theoretical details of the XAFS experiment have been extensively covered in a book edited by Koningsberger and Prins [117]. Hence, in what follows we focus on the data that can be obtained via XAFS spectroscopy along with the specific strengths and weaknesses of both the XANES and EXAFS components of XAFS for following the kinetics and mechanism(s) of formation of supported-nanoparticle heterogeneous catalysts.

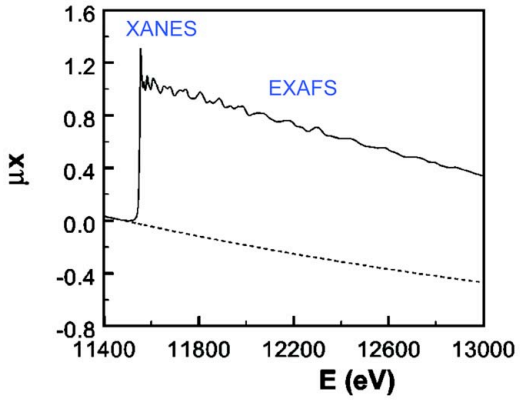

Figure 1. XAFS spectrum for a Pt foil [118]: μX (measured absorption coefficient) vs. E (eV, energy of the incident X-ray) with the XANES and EXAFS regions identified as shown. Reprinted with permission from [118]. Copyright (2000) Springer.

An example XAFS spectrum, shown in Figure 1, is composed of two distinct regimes, the XANES and EXAFS regimes. XANES is both metal and ligand dependent, and starts with the lowest energy photoinonization process leading to the XANES edge (i.e., the so-called "jump" [117]) and continues up to ~40 eV beyond the initial edge [119], Figure 1. XANES provides information on the electronic and geometric properties of the metal of interest, including the relative oxidation state and, in favorable cases, the symmetry environment of the adsorbing atom site [117]. Hence XANES is poised to probe changes in the formal metal oxidation state and the ligand environment [118,120], as well as any changes that occur during the supported-nanoparticle heterogeneous catalyst formation reaction. Shown in Figure 2 is an example, from Gates and co-workers [61], which utilizes XANES to monitor the change over time in the Rh K-edge of $Rh(C_2H_4)_2$ supported on dealuminated zeolite–Y (under H_2 and at 298 K).

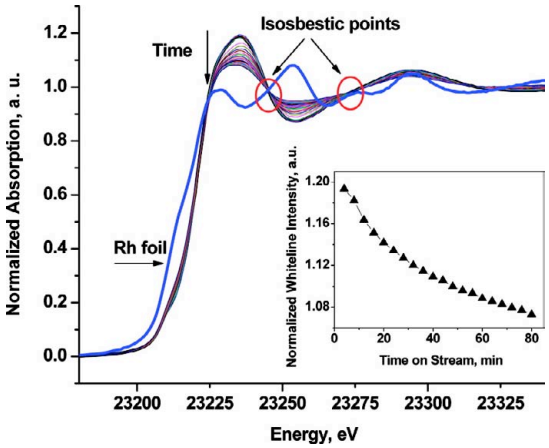

Figure 2. An excellent example of the changes in a series of raw XANES spectra and the white line intensity (insert) during the reduction of $Rh(C_2H_4)_2$/zeolite–DAY under H_2 (at 298 K) [61]. Reprinted with permission from [61]. Copyright (2008) American Chemical Society.

Unfortunately, XANES is often qualitative, so that precise identification of the formal oxidation state and ligand environment is only obtained in reference to known, structurally well-characterized, model complexes [130]. Advances in XANES fitting

theory (e.g., improvements in algorithms and calculation speed) are progressing and should help in ab initio XANES modeling; however, at present XANES is often considered semi-quantitative in many cases [121].

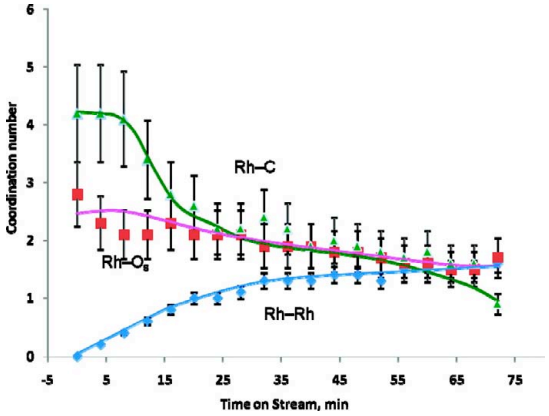

Figure 3. An example of the changes in Rh–C, Rh–$O_{Support}$ and Rh–Rh coordination numbers obtained from EXAFS spectra of $Rh(C_2H_4)_2$ supported on dealuminated zeolite–Y at 298 K under H_2 and vs. time [61]. Reprinted with permission from [61]. Copyright (2008) American Chemical Society.

The remaining portion of the XAFS spectrum is the EXAFS region, Figure 1, which arises from the backscattering of excited low kinetic energy (10-40 eV) photoelectrons by neighboring atom(s) at distances up to 4-5 Å, typically with an accuracy of ± 0.2 Å [117,122]. Overall, EXAFS yields average, local structural information concerning the relative positions of neighboring atom(s), as well as their relative distances and coordination numbers to the adsorbing atom of interest [123]. Hence, EXAFS can follow directly M–M bond formation (when appropriate models are used) and, therefore, can follow directly the formation of $M(0)_n$ supported-nanoparticle heterogeneous catalysts. Shown in Figure 3 is an example of the changes in the Rh–C, Rh–$O_{Support}$ and Rh–Rh coordination numbers over time (under H_2 and at 298 K), extracted from the EXAFS portion of the spectra for the aforementioned $Rh(C_2H_4)_2$ complex supported on dealuminated zeolite–Y system by Gates and co-workers. Noteworthy is that each Rh

first nearest neighbor (i.e., each of Rh–C, Rh–$O_{Support}$ and Rh–Rh) can be followed in real time, yielding information regarding both the loss of the precursor (i.e., -d[$Rh(C_2H_4)_2$]/dt) and formation of the Rh_n clusters (i.e., +d[Rh_n]/dt).

EXAFS is able to follow directly dilute molecular species (e.g., 0.4-wt% Pd on zeolite H-USY has been analyzed [50]) [130]. In addition, EXAFS is now commonly used to analyze supported-nanoparticles [123], making it a valuable method for following the kinetics of those supported-nanoparticle formation reactions. Unfortunately, however, EXAFS yields only relative scattering distances and not absolute bond distances; the latter require the use of known model structures and their measured EXAFS or other simulations from known structural data (e.g., from single crystal X-ray structures). Hence, quantitative EXAFS-based structural data are typically obtained only when a good fit is observed between a known model structure and the experimental data. However, even in the most favorable cases the fitting procedure (containing up to five fitting parameters per scattering path [117]) can often "lead to more than one statistically valid and physically possible structural model", as Gates and co workers have emphasized [124]. Therefore, *EXAFS is often best used only as a complimentary role with several other physical methods*. In addition, EXAFS requires the use of synchrotron sources to provide the intense (10^{10} flux vs. 10^3 flux with an X-ray tube) continuum (3-30 keV) of required X-ray radiation [117,125], so it is not yet what one would term a "routine method" available to each and every laboratory.

2.1.2.2. Total High-Energy X-Ray Scattering and Pair-Distribution-Function (PDF) Analysis

A relatively new[6] and potentially powerful technique for following the kinetics of supported-nanoparticle heterogeneous catalyst formation is total high-energy X-ray

[6] While the PDF analysis method is not new, its recent coupling with the total high-energy X-ray scattering data has allowed the combined technique of total high-energy X-

scattering coupled with PDF analysis. To date, only two studies (Table 1) have utilized total high-energy X-ray scattering coupled with PDF analysis to follow the formation of supported-nanoparticles [56,66]. Billinge has discussed the experimental and theoretical details of total high-energy X-ray scattering plus PDF analysis extensively [126,127]; hence, only a very brief overview is given below, one largely focused on PDF analysis. The focus herein is, instead, on the data that can be obtained along with our perception of the strengths and weaknesses at present of the total high-energy X-ray scattering plus PDF analysis technique.

Total high-energy X-ray scattering utilizes all of the "structure-relevant" diffraction data from a powder sample, including the Bragg and diffuse scattering components (vs. for example just the Bragg scattering components in conventional powder X-ray diffraction analysis) [128]; high-energy X-rays are required for adequate real-space resolution from the sample [129]. The experimentally measured scattering function (i.e., background subtracted and normalized), termed the total scattering function *S(Q)*, is given by equation 1:

$$S(Q) = \frac{I^{coh}(Q) - \sum c_i \left| f_i(Q) \right|^2}{\left| \sum c_i f_i(Q) \right|^2} \qquad (1)$$

In equation 1, c_i is the atomic concentration, f_i the X-ray atomic form factor, $I^{coh}(Q)$ is the measured scattering intensity from a powder sample, and $Q = 4\pi \sin(\lambda)/\theta$ [126,127]. Billinge has noted that "it is worth remembering that *S(Q)* is nothing other than the powder diffraction pattern that has been corrected for experimental artifacts and suitably normalized" [127].

ray scattering coupled with PDF analysis to become increasingly valuable for the analysis of complex materials [130].

The total scattering function, *S(Q)* (equation 1), is transformed into the atomic PDF (*G(r)*, equation 2), through a Fourier transform over a measured range, *Q*, of the total structure function, equation 1 [126,127].

$$G(r) = 4\pi r[\rho(r) - \rho_0] \quad (2)$$

In equation 2, $\rho(r)$ is the local atomic number density, ρ_0 is the average atomic number density and *r* the radial distance. Hence, *G(r)* is a representation of the coherent scattering of the total diffracted intensity of the material and, physically contains information regarding the distances between pairs of atoms [129]. The atomic PDF (*G(r)*) data are then modeled to obtain quantitative structural information [128].

Figure 4 (left) shows an illustrative example, reported by Chupas and co-workers [56], of raw and differential (i.e., support-subtracted) atomic PDF data vs. time for the formation of $Pt(0)_n/TiO_2$ under H_2 (at 200 °C). From the differential atomic PDF data, *local* Pt–Cl (at 2.5 Å) and Pt–Pt (at 2.77 Å), atomic pair correlations can be extracted, Figure 4 (right). While not shown, it is also possible to obtain further, atomically resolved, structural information such as nanoparticle size or number of atoms per particle via the Pt–Pt atomic pair correlations without the need of infinite periodicity (see, for example, the Supporting Information of Chupas and co-workers paper [56]). Hence, the *total high-energy X-ray scattering plus PDF method is complimentary to EXAFS (with its local ~0.5–1 nm scale) and XRD (with its long range bulk analysis, >10 nm), in that the X-ray scattering plus PDF method can yield atomic resolution information at length scales up to 10 nm (i.e., at the nanoscale) for either crystalline or noncrystalline materials* [129,130].

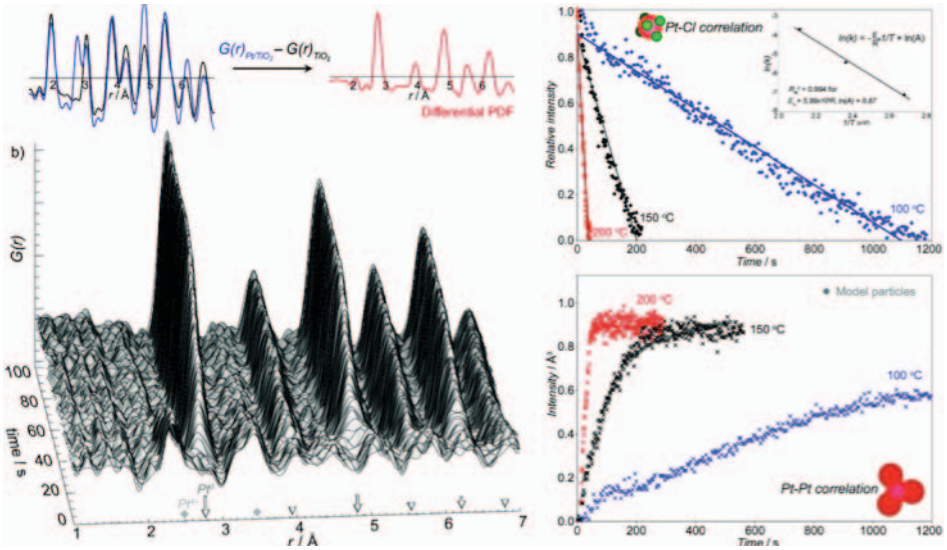

Figure 4. Kinetic data obtained by the high energy X-ray scattering plus PDF method, from the work of Chupas and co-workers [56]. Shown to the left is the raw differential (supported-subtracted) PDF for the formation of $Pt(0)_n/TiO_2$ under H_2 over time. Shown to the right are the extracted Pt–Cl (top right) and Pt–Pt contributions (bottom right) over time for the formation of $Pt(0)_n/TiO_2$. Reprinted with permission from [56]. Copyright (2007) American Chemical Society.

The total high-energy X-ray scattering plus PDF analysis method clearly has several advantages, including: (i) the ability to follow directly both the loss of a metal precursor complex and the formation of $M(0)_n$ nanoparticles; (ii) the atomically resolved, absolute bond distances, which result and which *are not model dependent*; and (iii) the fact that this method can be used under in situ (and, in principle, under operando) conditions. Despite these advantages, as with any technique, disadvantages exist, including: (i) the need for synchrotron sources; (ii) the challenge of quantitative analysis of the data (such analysis can take a significant amount of time, presently up to even 1–2 yrs in the case that we are aware of, as discussed in footnote 16 of reference [72]); and (iii) "…the limitation brought by inadequate data analysis software" [128]. More specific to the heterogeneous catalysis community there is also the limitation (iv) that loadings below 5-wt% have proven difficult to analyze, at least to date [66]. Despite this, total high-energy X-ray scattering plus PDF analysis is a powerful, evolving method that holds

considerable promise for monitoring supported-nanoparticle heterogeneous catalyst formation. Hence, its enhanced use, especially as a complement to other direct physical methods such as XAFS and XRD and even indirect methods (such as IR spectroscopy, H_2 uptake or others, vide infra), is urged and can be anticipated.

2.1.2.3. IR Spectroscopy

IR spectroscopy relies on the absorption of infrared light by vibrational levels within a molecule of interest. The theoretical details of IR spectroscopy can be found in many textbooks [3,131,132]. The experimental details regarding measuring IR spectra of supported-metal complexes and supported-nanoparticles have been recently and expertly discussed by Gates and co-workers [133].

Five studies in Table S1 have utilized IR spectroscopy to follow the kinetics of the loss of a supported-precatalyst [29,51,60,61,64]. An example is that of $Ir(C_2H_4)_2$ on zeolite–Y from Gates and co-workers [60], Figure 5. The peaks at 2964, 2936, 2876 and 2854 cm^{-1} show the formation of ethyl ligands on the Ir/zeolite–Y (from the $Ir(C_2H_4)_2$/zeolite–Y precatalyst) and subsequent loss of those ethyl ligands over 1 h under H_2 (and with a temperature ramp).

Importantly, IR spectroscopy often yields information regarding the ligand shell of a supported-metal precatalyst and, therefore, is highly complementary to the methods that are capable of following M–M bond or net $M(0)_n$ nanoparticle formation directly. IR spectroscopy is particularly useful when supported-organometallics are present that contain CO or hydrocarbon ligands [133]. Additional advantages of IR spectroscopy include its ease of use and broad availability. Unfortunately, IR spectroscopy is typically indirect in terms of nanoparticle formation in that it has not been used to follow the formation of M–M bonds; absorption from support vibrations often overlap with the M–M bond vibrations of interest. However, IR spectroscopy is still very useful for routine, first-

screenings of the kinetics of the loss of supported-organometallic or other precatalyst complexes.

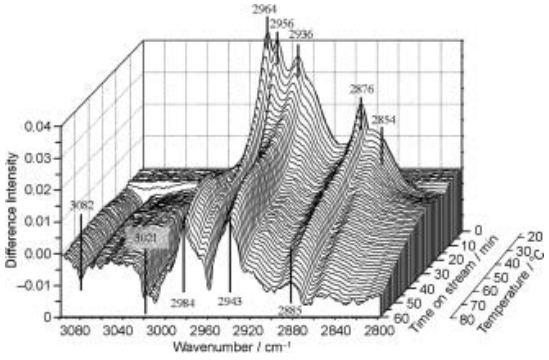

Figure 5. An example of IR spectra data obtained for the formation and loss of ethyl ligands (shown at 2964, 2936, 2876 and 2854 cm^{-1}) from $Ir(C_2H_4)_2$/zeolite–Y under H_2 and a temperature ramp. Reproduced with permission from [60]. Copyright (2008) Wiley-VCH.

2.1.2.4. H_2 Uptake Kinetics: A Chemical Based Method

Early literature studies trying to understand supported-nanoparticle heterogeneous catalyst formation kinetics, as well as the associated M^{x+} reduction reaction, relied on H_2 uptake monitoring. More specifically, eight studies in Table S1 [30-33,34,35,37,52] utilized H_2 uptake measurements to obtain kinetic data. The H_2 uptake experiment is in principle simple: the material of interest is placed in a closed vessel, exposed to H_2 and either a change in pressure, or H_2 uptake in an apparatus that maintains constant pressure, is measured quantitatively. Under the appropriate conditions, H_2 uptake kinetic data (for example when coupled to a reporter reaction, vide infra) can reveal information about supported-nanoparticle heterogeneous catalyst formation [72,74,75]. Shown in Figure 6 is an example of H_2 uptake kinetic measurements (coupled to a cyclohexene reporter reaction, vide infra) for following $Pt(0)_n/\gamma\text{-}Al_2O_3$ supported-nanoparticle formation, as reported by Mondloch, Finke and co-workers [72].

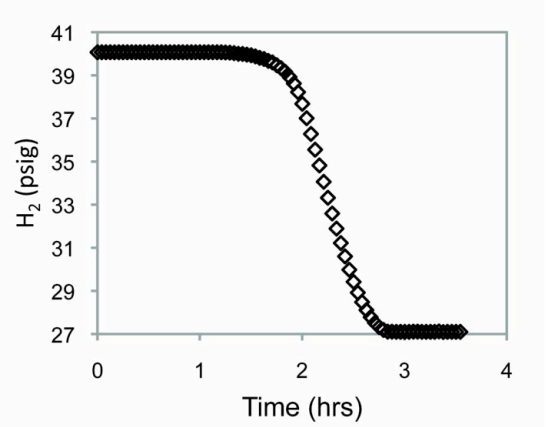

Figure 6. An example of H_2 uptake kinetics for following the formation of $Pt(0)_n/g\text{-}Al_2O_3$ [72]. The sigmoidal kinetics [72] will be discussed in Section 3.2.2.3. Adapted with permission from [72]. Copyright (2009) American Chemical Society.

The largest advantage of using H_2 uptake as a kinetic monitoring method is *its ease of use, ready availability, and sample compatibility* typically (e.g., both solids and liquids are readily analyzed). Another advantage is that H_2-uptake measurements of just the precatalyst can yield information regarding the crucial stoichiometry of the supported-nanoparticle formation reaction. These advantages so noted, the two greatest *disadvantages* of the H_2-uptake method are its indirect nature and the thermodynamic constraints of using H_2 as a reductant. An example of the latter constraint arises when cheaper, earth-abundant first-row metal catalysts made from Co (- 0.28 V vs. NHE) and Ni (-0.257 V vs. NHE) are present; these metals are not reducible thermodynamically to the M(0) state by H_2, at least under mild, room temperature and standard pressure conditions.

2.1.2.5. Electron Microscopy

Transmission electron microscopy (TEM) is one of the most commonly used imaging methods for analyzing supported-nanoparticle heterogeneous catalysts or, for that matter, nanoparticle catalysts made in solution and then deposited for ex situ analysis on a TEM grid [134]. In general, TEM provides largely direct and powerful, albeit historically

ex situ, images of the presumed catalyst (or perhaps often the O_2-exposed, oxidized form of the previously $M(0)_n$ nanoparticle). Concerns with this method include (i) the possibility of electron beam induced damage as "in the end you can damage virtually anything you put into the TEM" [135], (ii) the ex situ nature of a typical TEM experiment (which has made it largely ineffective for following the kinetics of the formation of supported-nanoparticles), and (iii) the "non-canonical ensemble" nature of TEM measurements (i.e., the ability to see even single nanoparticles that may be grossly unrepresentative of the bulk sample). Hence, such potential disadvantages necessitate the use of the appropriate control experiments.

Worth noting is that recent advances[7] in the design of environmental TEM cells have allowed in situ TEM measurements under non-high-vacuum conditions [112,136]. For example, Creemer and co-workers recently studied the reduction of the well-known CuO/ZnO methanol synthesis precatalyst [3] in situ, under 1.2 bar H_2 (i.e., approximately atmospheric pressure), at temperatures up to 500 ℃ and at a resolution of 0.18 nm. The reduction of CuO to Cu(0) on the ZnO surface [113] could be directly imaged; the migration of 5-10 nm $Cu(0)_n$ nanoparticles on the ZnO support was also observed.

In another recent study, Alivisatos and co-workers employed an in situ, *liquid-based cell* to study the growth of $Pt(0)_n$ nanoparticles from $Pt(acetylacetonate)_2$. Their studies revealed both monomer addition and bimolecular aggregation [114], albeit without a support present. A limitation exposed via that study is that the TEM electron beam is involved in inducing the nanoparticle formation reaction either directly, through solvated electrons, or possibly via an oleylamine-assisted pathway, oleylamine being present as the solvent [114]. In one additional in situ TEM study worth noting, the detection of several intermediate phases from amorphous $LiFePO_4$ en route to crystalline $LiFePO_4$

[7] Also worth mentioning here are the recent advances in electron sources, dampening and aberration correction that have improved resolution [136].

[115] demonstrated the ability of TEM to directly image intermediate nanoparticle phases en route to the final product.

Overall then, environmentally controlled TEM cells [112,136][7] promise to make additional contributions to our understanding of how supported-nanoparticle heterogeneous catalysts form.

2.1.3. Conclusions

Clearly, each of the precatalyst preparation steps—that is, precursor/support contact, calcination and reduction—has the potential to influence the supported-nanoparticle heterogeneous catalyst formation speciation and resultant kinetics. Overall, speciation-controlled, supported-metal precatalysts are needed for the next generation syntheses of supported-nanoparticles as well as for reliable kinetic studies of their formation reaction(s).

A variety of advanced techniques, including EXAFS, XANES, total high-energy X-ray scattering and PDF analysis as well as in situ TEM are emerging as viable, often complimentary options for following the stoichiometries and the kinetics of supported-nanoparticle heterogeneous catalyst formation. In addition, any technique capable of in situ, or better operando,[5] measurements can in principle be used to follow the stoichiometries and kinetics, thereby helping deduce the mechanism(s) of supported-nanoparticle heterogeneous catalyst formation reactions.

IR spectroscopic and H_2 uptake studies are the two-quicker/easier methods that have been used to date to follow supported-nanoparticle formation reactions. Care must be taken in such indirect studies to ensure that the desired supported-nanoparticle heterogeneous catalyst formation reaction is what is actually being monitored.

Overall however, *there is still a need to develop more routine, "available-in-any-lab" methods to follow supported-nanoparticle formation stoichiometries and kinetics*. A broader availability of more routine, ideally direct methods would ensure that only the

most important systems are thereby indentified and developed, so that only those “best” systems can then be subjected to the more expensive and time-consuming, but more powerful and direct techniques, including XAFS, high energy total X-ray scattering plus PDF analysis and in situ TEM. Furthermore, the inherently complex nature of supported-nanoparticle heterogeneous catalyst formation problem demands the use of multiple, complimentary physical methods to follow the stoichiometries, kinetics and thereby deduce reliable mechanisms of those supported-nanoparticle formation reactions.

2.2. Kinetic and Mechanistic Studies of Practical Supported-Nanoparticle Heterogeneous Catalyst Formation at the Gas-Solid Interface

2.2.1. Brief Overview of the Primary Literature at the Gas-Solid Interface

Table S1 of the Supporting Information is a compilation of 39 primary literature references reporting kinetic and mechanistic studies of supported-nanoparticle formation at the *gas-solid* interface [29-67]. For what follows we have chosen four representative systems, organized by the supported-metal precatalyst used and covered in 25 of the 39 references in Table S1, four systems which provide a good overview of the best-studied systems in the literature. Those 25 papers are shown in Table 2 along with: (i) the experimental details regarding the preparation of the supported metal precatalyst and then the supported-nanoparticle heterogeneous catalyst formation reaction; (ii) information on whether the study contains kinetic data (and if so, the physical method employed); and if kinetic data were obtained, (iii) information on whether they were collected isothermally or non-isothermally. While classical chemical kinetics are traditionally performed isothermally, non-isothermal kinetic measurements are common in the supported-nanoparticle formation literature, the precise interpretation, and hence the resultant exact meaning and value, of which are currently being actively debated

[137,138,139,140,141].[8] Also given in Table 2 is (iv) whether the stoichiometry of the supported-nanoparticle heterogeneous catalyst formation reaction was explicitly demonstrated (and if so, how that stoichiometry was obtained as a guide for future studies); and (v) the rate equations and proposed mechanism as given by the original authors (if available).

Before discussing each of the four case studies in detail, a brief overview of Table 2 is quite informative and reveals several insights into the state of mechanistic knowledge for supported-nanoparticle heterogeneous catalyst formation. Specifically, while 24 of the 25 studies in Table 2 contain kinetic data, 9 of those 24 studies were done under non-isothermal reduction conditions.137 In addition, only 10 of the 25 studies rigorously demonstrated the supported-nanoparticle heterogeneous catalyst formation *stoichiometry*—the first, key step in any reliable mechanistic study, since that stoichiometry is what the proposed mechanistic steps must sum to! Perhaps most strikingly, only 3 of the 25 studies in Table 2 contain rigorous, chemical-reaction-based mechanisms (i.e., vs. their less useful word-only or picture-based mechanisms[9]).

[8] One sub-goal of kinetic studies is to obtain the Arrhenius parameters for the chemical reaction of interest—that is, the activation energy (E_a) and pre-exponential factor (A). This is commonly done by collecting a series of isothermal kinetic curves (i.e., the change in the reactants or products with time), from which rate constants, k, are extracted. A subsequent plot of the ln k vs. 1/T then yields the well-known E_a (the slope of the line equals $-E_a/R$) and A (the y-intercept equals ln(A)). Another possibility is to measure the kinetic curve during a temperature ramp, that is non-isothermally. This approach is attractive as, at least in principle, the E_a, A and k can be determined from a single experiment [138]. Hence, the heterogeneous catalysis community has utilized such non-isothermal kinetic measurements to try and understand the mechanisms of supported-nanoparticle formation [137], as Table 2 makes apparent. *However*, the utility and treatment of non-isothermal kinetic data, particularly for understanding mechanism, is under current debate. Galwey has argued that is simply not possible, in general, to obtain the E_a, A and k from a single non-isothermal kinetic experiment [141]. Galwey and Brown have also noted that the isothermal treatment of kinetic data "requires fewer assumptions and results appear to be more consistent and reliable" [138].

[9] Chemical-reaction-based mechanisms have been the hallmark of rigorous mechanistic chemistry in, for example, physical organic [24], organometallic chemistry [25,26] and inorganic chemistry [27,28]. That said, and as we have noted elsewhere [282] "At times, a word or picture-only mechanism may be useful to describe what would otherwise be a

Chemical-reaction-based mechanisms are the hallmark of rigorous mechanistic chemistry in physical organic [24], organometallic chemistry [25,26] and inorganic chemistry [27,28], for example. From this brief overview alone of the literature in Table 2 one can conclude that the present state of knowledge, of how supported-nanoparticle catalysts form, is still in a somewhat crude state.

very complex set of equations (that may not be tested or even testable due to their associated mathematical complexity). But, as such they do not lead to precise kinetic equations and corresponding differential equations (and then, ideally, their integrated counterparts), such differential-kinetic equations being required to test the mechanism vs. the experimental kinetic data. Another serious issue arises when a word or picture-only mechanism is proposed along with (different or other) equation(s) that cannot be derived from that (word or picture) mechanism: *a disconnect then results between the mechanism proposed and the differential equation(s) given*, which in turn *leads to the use of rigorously undefined, if not simply wrong, concepts and words for the physical phenomena at hand*. In rigorous mechanistic studies, balanced chemical equations define *both the rate constant* and the *words and concepts* that one can use" [282].

Table 2. The twenty-five primary case studies, of four main systems, investigated herein regarding the kinetics and mechanisms of formation of supported-nanoparticle catalysts at the gas-solid interface. A full list of the 39 presently available studies, from which these 25 case-studies were chosen, is available in Table S1 of the Supporting Information.

Entry [Reference]	***Authors***	***System Studied***	***Kinetic Data (Physical Method Employed)***	***Isothermal Kinetic Data***	***Stoichiometry (Physical Method Employed)***	***Proposed Mechanism(s) and Rate Equations as Written by the Original Authors (If Available)***
$M(NH_3)_4^{2+}$ Based Systems						
1 [29]	Dalla Betta, R. A. Boudart, M.	5-wt% $Pt(NH_3)_4Cl_2$ was ion-exchanged onto zeolite Y and reduced under H_2 from 25 to 350 ºC. The effects of calcination and H_2O were also investigated.	Yes (IR spectroscopy)	No	Yes (H_2 uptake)	*Proposed Mechanism.* Aggregation is proposed to be due to "the unstable neutral, hence mobile, hydride (i.e, Pt–H), (which) leads to Pt agglomeration", as shown in Scheme 3 in this review.
2 [39]	Tzou, M. S.; Sachtler, W. M. H.	7.4-wt% $Pt(NH_3)_4Cl_2$ was ion-exchanged onto zeolite NaY. The resultant precatalyst was calcined between 360 and 550 °C and reduced under H_2 at 500 °C.	Yes (H_2 chemisorption)	Yes	No	*Proposed Mechanism of Subnanometer $Pt(0)_n$/Zeolite–Y Formation.* Calcination at 360 °C afforded Pt^{2+} ions in the zeolite supercages, which are easily reduced with H_2 between -15 and 150 °C. "Growth" kinetics were obtained by monitoring the change in the Pt dispersion by H_2 chemisorption. The H_2 chemisorption data "favor the mechanism of particle growth by migration and coalescence of particles rather than Ostwald ripening, that is by

					atomic migration". *Proposed Mechanism of 10-50 nm $Pt(0)_n$/Zeolite–Y Formation.* Calcination at 550 °C afforded Pt^{2+} ions in the sodalite cages. The Pt^{2+} ions are reduced and driven to a location where $Pt(0)_n$ particles can form. "Two stages can be discerned: (a) nucleation, and (b) growth of particles". The Pt(0) atoms can migrate to the surface of the zeolite.
3 [41]	Homeyer, S. T.; Sachtler, W. M. H.	2–7-wt% $[Pd(NH_3)_4](NO_3)_2$ was ion-exchanged onto zeolite NaY. The sample was calcined at 250 and 500 °C and then reduced under a temperature ramp from -80 to 350 °C.	No	Yes (H_2 Uptake)	*Proposed Mechanism when Pd Ions are in the Supercages.* "Pd ions migrate to an activated nucleus where they are reduced, forming primary particles. These migrate through the supercage network until they either contact another primary or secondary particle. Once all the primary particles are used up, further growth of the secondary particles occurs via a different mechanism, possibly involving Ostwald ripening or local collapse of the zeolite matrix". *Proposed Mechanism when Pd Ions are in the Sodalite Cages.* "Pd atoms are released into the supercage network at higher temperatures, where they form secondary particles either

						through migration and coalescence or by trapping Pd atoms as they leave the sodalite cages".
4 [47]	Oudenhuijzen, M. K.; Kooyman, P. J.; Tappel, B.; van Bokhoven, J. A.; Koningsberger, D. C.	1-wt% $[Pt^{2+}(NH_3)_4](NO_3^-)_2$ was impregnated onto SiO_2 by incipient wetness. The precatalyst was dried under N_2 for 1 h at room temperature, followed by 8 h at 80 °C. The precatalyst is then reduced with H_2 under a temperature ramp from room temperature to 400 °C.	Yes (XANES & EXAFS)	No	No	*Proposed Mechanism.* The final size of the Pt particles (when reduced under H_2) is controlled by two parameters, the nucleation rate and the growth rate. "Since the formation of metal–metal bonds adds significantly to the stability of Pt atoms, the reduction of the $Pt^{2+}(NH_3)_x$ complex must involve migration and collision of the Pt^{2+} species with either an earlier formed metallic Pt nucleus or several other Pt^{2+} complexes and reduced at the same moment". The authors propose that a highly mobile Pt–H species is responsible for the nanoparticle growth, analogous to that reported by Dalla Betta and Boudart [29].
5 [50]	Okumura, K.; Yoshimoto, R.; Uruga, T.; Tanida, H.; Kato, K.; Yokota, S.; Niwa, M.	0.4-wt% $Pd(NH_3)_4Cl_2$ was ion-exchanged onto zeolite Na–ZSM-5, H–ZSM-5 and Y-mordenite. The samples were oxidized at 773 K and then reduced in H_2 up to 750 K.	Yes (EXAFS)	No	No	No mechanism was proposed for the supported-nanoparticle heterogeneous catalyst formation reaction.

6 [58]	Okumura, K.; Kato, K.; Sanada, T.; Niwa, M.	0.4 and 0.8-wt% Pd $Pd(NH_3)_4Cl_2$ was ion-exchanged onto zeolite H-USY. The samples were calcined under O_2 at 773 K for 4 h and reduced with H_2 under a temperature ramp from room temperature to 773 K.	Yes (EXAFS)	No	Yes (XANES)	No mechanism was proposed for the supported-nanoparticle heterogeneous catalyst formation reaction.
7 [62]	Okumura, K.; Honma, T.; Hirayama, S.; Sanada, T.; Niwa, M.	0.4 and 0.8-wt% $Pd(NH_3)_4Cl_2$ was ion-exchanged onto zeolite H-USY. The samples were dried at 323 K under atmospheric conditions and reduced under H_2 at 300 K.	Yes (XANES & EXAFS)	Yes	Yes (XANES)	No mechanism was proposed for the supported-nanoparticle heterogeneous catalyst formation reaction.
8 [63]	Okumura, K.; Matsui, H.; Sanada, T.; Arao, M.; Honma, T.; Hirayama, S.; Niwa, M.	0.4-wt% $Pd(NH_3)_4Cl_2$ was ion-exchanged onto zeolite H-USY, dried at 323 K under atmosphere and reduced under H_2 at 300 K. Precatalysts containing $PdCl_2$, $Pd(OAc)_2$ and $Pd(NH_3)_4(NO_3)_2$ on zeolite H-USY were also investigated.	Yes (XANES & EXAFS)	Yes	Yes (XANES)	No mechanism was proposed for the supported-nanoparticle heterogeneous catalyst formation reaction.

H_2PtCl_6 Based Systems						
9 [38]	Dexpert, H.	H_2PtCl_6 was impregnated onto Al_2O_3. The samples were reduced under H_2 at room temperature or 200 ºC.	Yes (XANES & EXAFS)	Yes	No	*Proposed Mechanism.* A summary of the author's word-based mechanism for the "decomposition of the isolated $PtCl_6^{2-}$ complexes" is: (i) oxygen starts to replace the chlorine atoms; (ii) a chlorinated Pt dimer is formed, and (iii) the dimer grows as the reduction continues.
10 [40]	Le Normand, F.; Bazin, D.; Dexpert, H.; Lagarde, P.; Bournonville, J. P.	H_2PtCl_6 was impregnated onto γ -Al_2O_3. The catalyst was dried @ 120 °C and reduced under H_2 at 300 °C.	Yes (XANES & EXAFS)	Yes	No	No mechanism was proposed, but qualitatively the authors state that: (i) "*the reduction rate tends to increase with the time of isothermal reduction*", which may be due to spillover, and (ii) that "*the isothermal reduction is associated with the growth of Pt clusters*".
11 [56]	Chupas, P. J.; Chapman, K. W.; Jennings, G.; Lee, P. L.; Grey, C. P.	5-wt% H_2PtCl_6 was deposited on TiO_2 via incipient wetness. The samples were dried overnight at 60 °C and reduced under H_2 at 100, 150 and 200 °C.	Yes (Total high energy X-ray scattering + PDF analysis)	Yes	No	No mechanism was proposed for the supported-nanoparticle heterogeneous catalyst formation reaction.
12 [65]	Shishido, T.; Asakura, H.; Amano, F.; Sone, T.;	H_2PtCl_6 was impregnated on TiO_2 or γ -Al_2O_3 (5-wt%), dried at 353 K and	Yes (XANES)	Yes	Yes (XANES)	No mechanism was proposed for the supported-nanoparticle heterogeneous catalyst formation reaction.

	Yamazoe, S.; Kato, K.; Teramura, K.; Tanaka, T.	calcined at 773K. Subsequently the samples were pulsed with 5 mL of H_2 for 20 s at 473 K.				
13 [66]	Chupas, P. J.; Chapman, K. W.; Chen, H.; Grey, C. P.	2.5–7.5-wt% H_2PtCl_6 were impregnated onto TiO_2 and dried at 60 ºC overnight. Some of the samples were calcined at 200 ºC for 2 h under O_2. The kinetic data were collected while the sample was being reduced in H_2 from 0 to 227 ºC.	Yes (High energy total X-ray scattering + PDF analysis)	No	No	*Proposed Mechanism.* "The initial Pt nanoparticles that form are ~1 nm in size, while by 200 °C are larger and more crystalline. This suggests a mechanism for particle growth where the initial particles that form are small (<1 nm) then agglomerate into ensembles of many small particles and lastly anneal to form larger well-ordered particles".
			$Ag(NO)_3$ Zeolite Based Systems			
14 [32]	Beyer, H.; Jacobs, P. A.; Uytterhoeven, J. B.	$AgNO_3$ is ion-exchanged on zeolite NaY and reduced under H_2. Prior to reduction the samples were out gassed and calcined at 373, 473 and 623 K and subsequently reduced under H_2 isothermally between 298 and 623 K.	Yes (H_2 uptake)	Yes	Yes (H_2 uptake)	*Observed Rate Law: Low Temperature (≤ 430 K).* $$\frac{dc}{dt} = k' P \frac{(C_0' - C)}{C}$$ P = H_2 pressure, C_0' = Initial Ag^+, C = the reduced form of Ag^+ at time t *Proposed Mechanism #1 (Low Temperature): H_2 Activation on Ag^+*

						$H_2 + Ag^+ \rightleftharpoons (Ag^+H^-) + H^+$ $(Ag^+H^-) \xrightarrow{RDS} (Ag^0H)$ $Ag^+ + (Ag^0H) \rightleftharpoons H^+ + Ag_2$ *Proposed Mechanism #2 (Low Temperature): H_2 Activation at Some Surface Site, S* $H_2 + S \rightleftharpoons (SH\text{-}H)$ $(SH\text{-}H) + Ag^+ \rightleftharpoons (SH\text{-}Ag) + H^+$ $(SH\text{-}H) + Ag+ \xrightarrow{RDS} S + H^+ + 2\ Ag$ *Observed Rate Law: High Temperature >430 K).* $\frac{dc}{dt} = k_1(C_0 - C)$ C_0 = Initial Ag^+, C = the reduced form of Ag^+ at time t *Proposed Mechanism (High Temperature).* The reduction is "rate-controlled by the *migration of Ag^+ ions*" to activated H_2 somewhere within the zeolite.
15 [36]	Hermerschmidt, D.; Haul, R.	$AgNO_3$ was ion-exchanged onto zeolites X and A. The samples were dehydrated under O_2 at 400 °C and reduced under H_2 isothermally between -50 and 400 ºC.	Yes (ESR)	Yes	No	No mechanism was proposed for the supported-nanoparticle heterogeneous catalyst formation reaction.

16 [37]	Beyer, H. K.; Jacobs, P. A.	$Ag(NO)_3$ was ion-exchanged onto the chabsite zeolite. The samples were isothermally reduced under H_2 at varying temperatures between 295 and 613K.	Yes (H_2 uptake)	Yes	Yes (H_2 uptake)	*Observed Rate Law* $\frac{d[Ag^+]}{dt} = k[Ag^+]^2[P_{H_2}]^{\frac{1}{2}}$ *Proposed Mechanism* $H_2 \rightleftharpoons 2\,H\bullet$ $H\bullet + Ag^+ \rightleftharpoons [Ag(0)H^+]$ $[Ag(0)H^+] + Ag^+ \overset{RDS}{\rightleftharpoons} Ag_2^+ + H^+$
17 [42]	Schoonheydt, R. A.; Leeman, H.	$AgNO_3$ was ion-exchanged onto zeolite NaA. The samples were calcined at 673 K and reduced under H_2 between 253 and 298 K. All manipulations were carried out in the dark.	Yes (ESR)	Yes	No	*Proposed Mechanism* $Ag + Ag \rightarrow Ag_2 \rightarrow Ag_3$, etc…
18 [57]	Shimizu, K.-I.,; Sugino, K.; Kato, K.; Yokota, S.; Okumura, K.; Satsuma, A.	$AgNO_3$ was ion-exchanged onto zeolite H-MFI. The sample was dried at 383 K for 24 h, calcined at 823 K for 2 h and reduced under H_2 at 573 K.	Yes (EXAFS & UV-Vis)	Yes	Yes (H_2 uptake)	No mechanism was proposed for the supported-nanoparticle heterogeneous catalyst formation reaction.
			Supported-Organometallic Systems			
19	Nasher, M. S.;	1–2-wt%	Yes	No	No	*Proposed Mechanism.* "…the

[45]	Frenkel, A. I.; Somerville, D.; Hills, C. W.; Shaplye, J. R.; Nuzzo, R. G.	$PtRu_5C(CO)_{16}$ was deposited on carbon black via incipient wetness from THF. The sample was allowed to dry in air for 1 h and evacuated for 1 h and reduced under H_2 from 150 to 773 K.	(XANES & EXAFS)			initial nucleation of a compact (Pt-rich) structure (is) followed by the inversion of the intraparticle distribution of the Pt and Ru atoms upon continued high-temperature annealing. In this inversion, the core-segregated Pt atoms exchange with Ru surface atoms to form a surface Pt shell structure".
20 [48]	Fiddy, S. G.; Newton, M. A.; Campbell, T.; Dent, A. J.; Harvey, I.; Salvini, G.; Turin, S.; Evans, J.	5-wt% $Pt(acac)_2$ was slurried onto SiO_2 from toluene. The solvent was then removed by rotary evaporation and reduced under H_2 from 300 to 673 K. The authors also looked at a bimetallic system of $Pt(acac)_2$ plus $GeBu_4$.	Yes (EXAFS)	No	No	*Proposed Mechanism.* "…an initial decomposition of a small fraction of the supported $Pt(acac)_2$ leading to the formation of a low level of small Pt particles….(which are) active for rapid H_2 dissociation and subsequent spillover of atomic hydrogen"
21 [51]	Li, F.; Gates, B. C.	1-wt% $Ir(CO)_2(acac)$ was deposited on zeolite NaY from a pentane solution. The solvent was removed by evacuation and put under CO at 40 °C.	Yes (IR Spectroscopy)	Yes	No	No specific mechanism was proposed for the formation of $Ir_4(CO)_{12}$.
22 [58]	Uzun, A.; Gates, B. C.	1-wt% $Ir(C_2H_4)_2(acac)$ was contacted onto	Yes (XANES, EXAFS & IR	No	No	*Proposed Mechanism.* A model was proposed for the formation of $Ir_4(ligand)_x$/zeolite–Y that

		dealuminated zeolite–Y from a *n*-pentane slurry. The solvent was removed under vacuum and the sample was reduced under H_2 in a temperature ramp from 298-353 K.	Spectroscopies)			goes through a $Ir_2(ligand)_x$/zeolite–Y intermediate. A pictorial representation, as proposed by the original authors, is given in this review, Scheme 10.
23 [61]	Liang, A. J.; Gates, B. C.	1-wt% $Rh(C_2H_4)(acac)$ was contacted onto dealuminated zeolite–Y from a *n*-pentane slurry. The solvent was removed under vacuum and the sample was reduced under H_2 at 298 K.	Yes (XANES, EXAFS & IR Spectroscopies)	Yes	No	No mechanism was proposed for the supported-nanoparticle heterogeneous catalyst formation reaction.
24 [64]	Kulkarni, A.; Gates, B. C.	1-wt% of each $Os_3(CO)_{12}$ and $Ru_3(CO)_{12}$ (by metal) were simultaneously deposited onto MgO from pentane. The solvent was removed under vacuum and reduced under H_2 in a temperature ramp from 298 to 423 K.	Yes (XANES, EXAFS & IR Spectroscopies)	No	No	*Proposed Mechanism.* "First, the decarbonylation of triruthenium clusters (occurs) starting at 333 K (with the triosmium carbonyl clusters still being coordinatively saturated and intact). The coordinatively unsaturated ruthenium species were reactive, and at 333 K, had aggregated substantially so that the average ruthenium cluster was larger than trirutheim. When the temperature had been raised to about 358 K, the triosmium clusters began to

						undergo decarbonylation, and at approximately 398 K the triosmium clusters had lost enough CO ligands to become sufficiently coordinatively unsaturated to allow migration and reaction with Ru atoms of neighboring species".
25 [67]	Nassreddine, S.; Bergeret, G.; Jouguet, B.; Geantet, C.; Piccolo, L.	1.0-wt% $Ir(acac)_3$ was contacted with amorphous silica–alumina (ASA) from toluene. The sample was dried at 120 °C overnight and reduced in flowing H_2 at 350 ºC for 6 h.	Yes (In Situ XRD)	Yes	Yes (Mass Spectrometry)	No mechanism was proposed for the supported-nanoparticle heterogeneous catalyst formation reaction.

2.2.2. Kinetic and Mechanistic Case Studies

2.2.2.1. System I: $M(NH_3)_4^{2+}$ Based Systems (Where M = Pt and Pd)

Interest in $Pt(0)_n$ and $Pd(0)_n$ zeolite–supported-nanoparticle catalysts derives from their use as shape-selective isomerization, hydrogenation and hydrocracking catalysts [3,98,142,143]. Jacobs has insightfully noted that; "the solid-state transformations of Pt and Pd ions in zeolites are understood qualitatively…however, the detailed chemical reactions involved have not been elucidated quantitatively" [155]. He also noted and that "in order to establish the dispersion of metals in zeolite cages, it is necessary to understand the reduction mechanism" [153]. We have found eight papers in the literature [29,39,41,47,50,58,62,63], detailed in Table 2 as entries 1–8, that focus on the kinetics and mechanisms of $M(0)_n$/support supported-nanoparticle heterogeneous catalyst formation starting from the $M(NH_3)_4^{2+}$/support precatalyst (or from closely related derivatives such as $M(NH_3)_{4-x}(H_2O)_x$).

In a classic 1973 paper, shown in Entry 1 of Table 2, Dalla Betta and Boudart investigated the formation of $Pt(0)_n$/zeolite–Y nanometer and subnanometer sized particles from $Pt(NH_3)_4^{2+}$ supported on zeolite–Y [29]. The $Pt(0)_n$/zeolite–Y products were analyzed via H_2 chemisorption measurements; approximately[10] 14 nm $Pt(0)_n$/zeolite–Y nanoparticles were found when the precatalyst was reduced under H_2 using a temperature ramp from 25 to 350 ºC. In contrast, much smaller, approximately[10] 0.9 nm $Pt(0)_n$ nanoparticles were found when the sample was first calcined in O_2 at 350

[10] Dalla Betta and Boudart actually reported the dispersion of the $Pt(0)_n$/zeolite-Y catalyst based on H_2 chemisorption measurements [29]. Herein we estimate the supported-nanoparticle diameter empirically using a formula from the literature: diameter = 108/(% dispersion) [3]. This formula can be derived by considering that the dispersion is equal to the number of surface metal atoms divided by the total number of atoms present with the particle, assuming a particle geometry (e.g., spherical), and taking into consideration the planar area of the metal atom of interest, all as derived in [3]. For example, the dispersion of the $Pt(0)_n$/zeolite-Y catalyst reduced directly under H_2 was experimentally measured to be 8%. Therefore, 108/8 = 13.5 nm or approximately 14 nm $Pt(0)_n$ nanoparticles supported on zeolite-Y.

ºC and then reduced in a H_2 temperature ramp from 25 to 400 ºC. The observed, varying, $Pt(0)_n$/zeolite–Y product provides one specific example of how the precatalyst preparation conditions can significantly affect the resultant supported-nanoparticle products.

The structural evolution of the decomposition of the $Pt(NH_3)_4$/zeolite–Y precatalyst, during the temperature ramp under H_2, was qualitatively followed over time via IR spectroscopy by monitoring the loss of $–NH_3$ and –NH stretches. Dalla Betta and Boudart proposed that the "unstable neutral, hence mobile, hydride", $Pt(NH_3)_2H_2$ (Scheme 3), led to the formation of large 13–14 nm $Pt(0)_n$ nanoparticles supported on zeolite–Y when the precatalyst was reduced under H_2 without the calcination treatment [29]. However, no evidence was obtained for the presence of the putative $Pt(NH_3)_2H_2$ intermediate, nor was any kinetic or other evidence given for how $Pt(NH_3)_2H_2$ evolves to form the supported-nanoparticle product, $Pt(0)_n$/zeolite–Y.

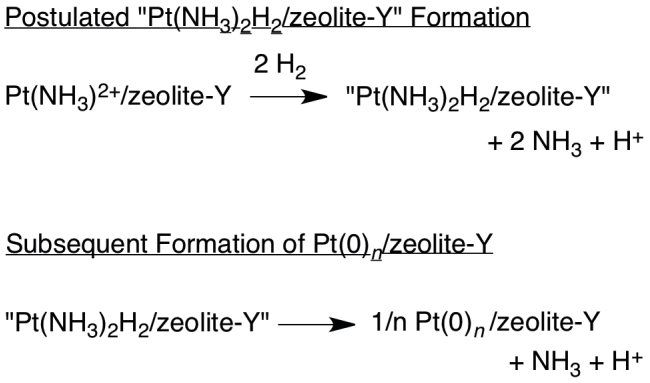

Scheme 3. Formation of Dalla Betta and Boudart's postulated "unstable neutral, hence mobile, hydride" (top) which is proposed to cause aggregation to $Pt(0)_n$/zeolite–Y supported-nanoparticles [29].

In a subsequent study, Mashchenko and coworkers [144] did obtain IR spectroscopy stretching frequencies consistent with a $Pt–H^+$/zeolite–Y intermediate under H_2; such a species may be related to the putative $Pt(NH_3)_2H_2$ intermediate proposed by Dalla Betta

and Boudart [29]. *However*, kinetic competence for the Pt–H^+/zeolite–Y intermediate en route to $Pt(0)_n$/zeolite–Y has yet to be demonstrated (i.e., observable species are often more stable and can, therefore, be detected only since they are off the kinetically dominant pathway). While it is conceivable that the putative $Pt(NH_3)_2H_2$ intermediate may be responsible for the formation of the lower dispersed ~14 nm $Pt(0)_n$/zeolite–Y products under H_2, one precedented, alternative hypothesis [106] is that the varying precatalyst preparation steps have led to the formation of different supported-Pt precatalyst species (i.e., the different conditions of direct reduction under H_2 vs. calcination followed by reduction under H_2). Indeed, precedence exists in the extant, $M(NH_3)_4^{2+}$/support preparation literature [106,145,146,147,148,149,150,151] for the formation of: (i) $(PtO_2)_n$ particles, (ii) Pt^{2+}-based ions (ligand composition unknown), or (iii) $Pt(0)_n$ particles (formed via autoreduction137). Each of these species would then have their own, different rates and mechanisms of supported-nanoparticle heterogeneous catalyst formation [47]. Relevant, excellent accounts of the insights into the effects of the precatalyst/support contact and calcination steps can be found in several key papers [147,151], reviews [152,153,154] and a book chapter [155]. Clearly, then, this is a classic example of where direct in situ (or better operando[5]) characterization of each precatalyst preparation step would be enormously helpful in elucidating the precatalyst speciation and then the resultant mechanism(s) of formation of the supported-nanoparticle catalyst(s). The bottom line here is that additional kinetic and other characterization studies are needed, under Dalla Betta and Boudart's precise experimental conditions, to confirm or refute the important $Pt(NH_3)_2H_2$ intermediate hypothesis.

In 1988, Sachtler and co-workers also studied the formation of $Pt(0)_n$/zeolite–Y under H_2 from the same $Pt(NH_3)_4^{2+}$/zeolite–Y precursor, Entry 2, Table 1 [39]. Again the $Pt(0)_n$ dispersion/particle size was found to be dependent on the calcination temperature.

More specifically, lower calcination temperatures (e.g., 360 ºC) lead to subnanometer $Pt(0)_n$ nanoparticles while higher calcination (e.g., 550 ºC) temperatures led to much larger, 10-50 nm $Pt(0)_n$ nanoparticles supported on zeolite–Y. Because of the widely varying supported-nanoparticle products, two different supported-nanoparticle formation mechanisms were proposed (as described in Table 2, entry 39), namely particle growth via migration and coalescence (for the subnanometer $Pt(0)_n$ nanoparticles) and nucleation and growth (for the 10–50 nm $Pt(0)_n$ nanoparticles). Unfortunately, these word-based mechanisms were not accompanied by the chemical equations necessary to define the underlying elementary reaction steps. The authors did obtain ex situ growth kinetics for the sample calcined at 360 ºC by monitoring the Pt dispersion (i.e., the Pt/H ratio) via H_2 chemisorption. Also unfortunate is that the H_2 chemisorption data were not fit to any series of specific reactions and their associated kinetic equations to support, or refute, the author's proposed mechanistic hypothesis.

In a subsequent study (Entry 3, Table 2), Sachtler and co-workers examined the closely related system, $Pd(NH_3)_4^{2+}$/zeolite–Y, which was calcined at either 250 or 500 ºC and then reduced under H_2 during a temperature ramp [41]. Both "Ostwald ripening and coalescence growth" mechanisms were proposed, albeit again without supporting kinetic data. In addition, neither study addressed the kinetics of the crucial nucleation step postulated [39] in the formation of their $Pd(0)_n$/zeolite–Y products. In short, specific, chemical-based mechanisms supported by kinetic studies are not available from these early, important studies of the M = Pt, Pd, $M(NH_3)_4^{2+}$ precursor to $M(0)_n$/zeolite systems [39,41].

More recently, in 2002 Koningsberger and co-workers studied the temperature-ramped H_2 reduction of $[Pt(NH_3)_4](NO_3)_2/SiO_2$ to yield 1.8 nm $Pt(0)_n$ nanoparticles supported on SiO_2 [47], Entry 4, Table 2. Several $[Pt(NH_3)_4](NO_3)_2/SiO_2$ precatalyst decomposition pathways were elucidated via temperature-programmed mass

spectrometry; however and unfortunately, the stoichiometry of the supported-nanoparticle formation reaction was not rigorously demonstrated. Insights into the $Pt(0)_n/SiO_2$ supported-nanoparticle formation reaction were obtained from non-isothermal reduction kinetics monitored via EXAFS of both the Pt–N bond loss and the Pt–Pt bond formation. The resultant kinetic data provide direct evidence for a simultaneous, rapid decrease in the Pt–N coordination number along with a concomitant increase in the Pt–Pt coordination number between 150 and 200 ºC. Building off Dalla Betta and Boudart's work [29], Koningsberger and co-workers postulated that a $Pt(NH_3)_2H_2$ intermediate was responsible for the formation of $Pt(0)_n/SiO_2$. However, again direct evidence for the postulated $Pt(NH_3)_2H_2$ hydride intermediate is lacking. In addition, XANES was used to follow the decreasing Pt L_{III} edge intensity as the supported-nanoparticle catalyst was being formed. The authors proposed that the final $Pt(0)_n/SiO_2$ particle size is "governed by the ratio of the growth-rate and nucleation rate". However, no mechanism was proposed for the $[Pt(NH_3)_4](NO_3)_2/SiO_2$ to $Pt(0)_n/SiO_2$ supported-nanoparticle heterogeneous catalyst formation reaction.

The authors turn out to be correct, however, in their statement that the nanoparticle size depends on the nucleation (k_1) and (autocatalytic) growth (k_2) rate constants. A quantitative expression for nanoparticle size as a function of the k_1 (nucleation), k_2 (growth) and precatalyst concentration (call it [A]) now exist from studies of the formation of nanoparticles in solution [156; see also 157], specifically the 2-step A → B slow, continuous nucleation (rate constant k_1) and then A + B → 2B autocatalytic surface growth (rate constant k_2) mechanism established for nanoparticle formation in solution, where B is the growing, $M(0)_n$ nanoparticle surface [156,157], vide infra.

Between 2004 and 2009 Okumura and coworkers have extensively studied the formation under H_2 of $Pd(0)_n$ nanoparticles supported on a variety of zeolites, including Na–ZSM-5, H–ZSM-5, H–mordenite and H–USY [50,58,62,63]. In an important initial

study (Entry 5, Table 2), Okumura and coworkers used XAFS to follow the calcination (heating from 523 K to 773 K in O_2) of $Pd(NH_3)_4^{2+}$ supported on the zeolites Na–ZSM-5, H–ZSM-5 and H–mordenite [50]. A key finding is that the calcination step yields $(PdO)_n$ clusters supported on Na–ZSM-5, but highly dispersed Pd^{2+}–$O_{zeolite}$ ions on the H–ZSM-5 and H–mordenite zeolites as revealed, respectively, by the presence or lack of Pd–O–Pd contributions in the EXAFS spectra. While not rigorously investigated or discussed by the authors [50], the change in the Pd–Pd coordination number over time (and with increasing temperature) was, as expected, observed to be qualitatively quite different for each zeolite and for the reduction of $(PdO)_n$ and Pd^{2+}–$O_{zeolite}$ [50]—that is, one expects that the mechanisms of formation of supported $Pd(0)_n$ will be quite different for the $(PdO)_n$ clusters vs. the more highly dispersed Pd^{2+}–$O_{zeolite}$ ions. The observed, different Pd–Pd coordination number changes are consistent with the hypothesis presented herein that different supported-precatalysts, $(PdO)_n$ and Pd^{2+}–$O_{zeolite}$ in the present case (and plausibly $(PtO_2)_n$, Pt^{2+} and $Pt(0)_n$ supported-precatalysts in the work of Dalla Betta and Boudart discussed earlier [29]), are expected to have different intimate mechanisms for their supported-nanoparticle heterogeneous catalyst formation reactions. Hence, further kinetic and mechanistic studies of this "$Pd(NH_3)_4^{2+}$"/support system (and of the classic "$Pt(NH_3)_4^{2+}$"/support system [29] as well) are needed to determine the precise mechanisms of the supported-nanoparticle formation reactions for these different, $Pd(0)_n$ (and $Pt(0)_n$) systems.

Building off their aforementioned studies [50], Okumura and co-workers studied the formation of $Pd(0)_n$/H–USY [58], Entry 6, Table 2. Characterization of the 773 K calcined $Pd(NH_3)_4^{2+}$/H–USY precatalyst via EXAFS spectroscopy indicated the formation of highly dispersed Pd^{2+}–$O_{zeolite}$ ions supported on H–USY. When the highly dispersed Pd^{2+}–O/H–USY ions were reduced with H_2 under an initial temperature programmed reduction (300 to 773 K under H_2), the supported-nanoparticle catalyst was found to be

$Pd(0)_{\sim 55}$/H–USY. The metal component of the reaction stoichiometry was confirmed via XANES spectroscopy in that all of the Pd^{2+} was converted to Pd(0) under H_2 by the time 500 K was reached. Interestingly, subsequent calcination/reduction treatments led to the formation of smaller, more highly dispersed, $Pd(0)_{\sim 4}$ and $Pd(0)_{\sim 13}$ clusters supported on the H–USY zeolite. In each case, EXAFS was used to follow the kinetics of the loss of Pd–O and the formation of Pd–Pd. Unfortunately and despite these very valuable direct kinetic studies from Okumura and co-workers, no detailed mechanism was proposed for the formation of the $Pd(0)_n$/H–USY supported-nanoparticle catalyst.

More recently, Okumura and co-workers revealed conditions where they could study the formation of $Pd(0)_{\sim 13}$/H–USY from $Pd(NH_3)_4^{2+}$ supported on H–USY [62,63] (Entries 7 and 8, Table 2). Two notable differences from the aforementioned studies [50,58], differences which gave rise to varying supported-precatalysts, include that the $Pd(NH_3)_4^{2+}$/H–USY precatalyst sample was dried under the milder conditions of 323 K in air (vs. 773 K under O_2) and that the reduction under H_2 to $Pd(0)_{\sim 13}$/H–USY was carried out isothermally at 300 K (vs. 300–773 K under H_2). EXAFS analysis of the supported-precatalyst species suggests some form(s) of $Pd(NH_3)_{4-x}(H_2O)_x$/H–USY are present; however, it is difficult to distinguish between the Pd–N and Pd–O contributions in the EXAFS spectrum and, therefore, is problematic to definitively assign the x value of the composition from the XAFS alone. Clearly, however, the precatalyst is different from either the $(PdO)_n$ clusters or the highly dispersed Pd^{2+}–$O_{zeolite}$ ions previously observed by EXAFS [50,58]. The metal component of the reaction stoichiometry was again confirmed by XANES spectroscopy, data which indicated complete reduction of $Pd(NH_3)_4^{2+}$ to $Pd(0)_{\sim 13}$ within 20 minutes. The authors studied the kinetics of the loss of Pd^{2+}/H–USY (via the XANES region) and the concomitant formation of $Pd(0)_n$/H–USY (via the EXAFS region). Plots of $\ln(C_0/C)$ (where $C_0 = Pd(0) + Pd^{2+}$ and $C = Pd^{2+}$) for both processes were linear, consistent with first-order behavior (i.e., $-d[Pd^{2+}]/dt = [Pd^{2+}]^1$

and +d[Pd–Pd]/dt = [Pd–Pd]^{1}), yielding apparent rate constants of k = 0.28 min^{-1} and k = 0.35 min^{-1} respectively.[11] Okumura and co-workers also investigated the effects of the H_2 partial pressure (from 0.6–50% by volume of H_2 in He), on the $Pd(0)_{\sim 13}$/H–USY supported-nanoparticle formation reaction [63]. A plot of the ln k vs. ln P(H_2) plot was almost linear, with only a slight slope of 0.08, indicating that the "partial pressure of H_2 hardly affected the reduction rate of Pd^{2+}", that is implying a near-zero order dependence on hydrogen, $[H_2]^{0.08}$. Overall, Okumura and co-workers studies contain the only quantitative kinetic data to date for the $Pd(NH_3)_4^{2+}$/support to $Pd(0)_n$/support system (and for the $Pt(NH_3)_4^{2+}$/support to $Pt(0)_n$/support system). However, they did not propose a mechanism for how the $Pd(0)_{\sim 13}$/H–USY supported-nanoparticles form, so that is done next.

Three conceivable mechanisms for the $Pd(0)_{\sim 13}$/H–USY supported-nanoparticle formation system are given in Scheme 4, possible mechanisms which we emphasize are deliberately minimal and offered solely to stimulate the required additional investigations attempting to disprove them.[12] The observation of a first order dependence on both the loss of the precursor and formation of the $Pd(0)_{\sim 13}$/H–USY supported-nanoparticle catalyst, -d[Pd^{2+}]/dt = [Pd^{2+}]^{1} and +d[$Pd(0)_{\sim 13}$]/dt = [Pd–Pd]^{1}, requires one to write a mechanism with only *one* Pd in the rate-determining-step.

---

[11] It should be noted that the reported rate constants from the EXAFS analysis (e.g., $k_{obsPd-Pd}$ = 0.35 min^{-1}) were not corrected by the required statistical factor for the reaction stoichiometry of 2 Pd^{2+} → 1 Pd–Pd; that is the XANES monitors the loss of 1 Pd^{2+} (-d[Pd^{2+}]/dt/1) species while the EXAFS monitors the formation of Pd–Pd (+d[Pd–Pd]/dt/2). Hence, 2 $k_{obsPd-Pd}$ is equivalent to 1 $k_{obsPd2+}$ so that $k_{obsPd-Pd}$/2 =0.35/2 = 0.18 min^{-1}.

[12] (a) Reaction mechanisms, like science in general, progress only via conclusive disproof of multiple alternative hypotheses, as Platt[12b] has emphasized. Platt has further noted that "for exploring the unknown, there is no faster method". (b) We strongly recommend the following, classic paper to all scientists. J. R. Platt Science 146 (1964) 347-353. It is one of our favorite papers in all of science.

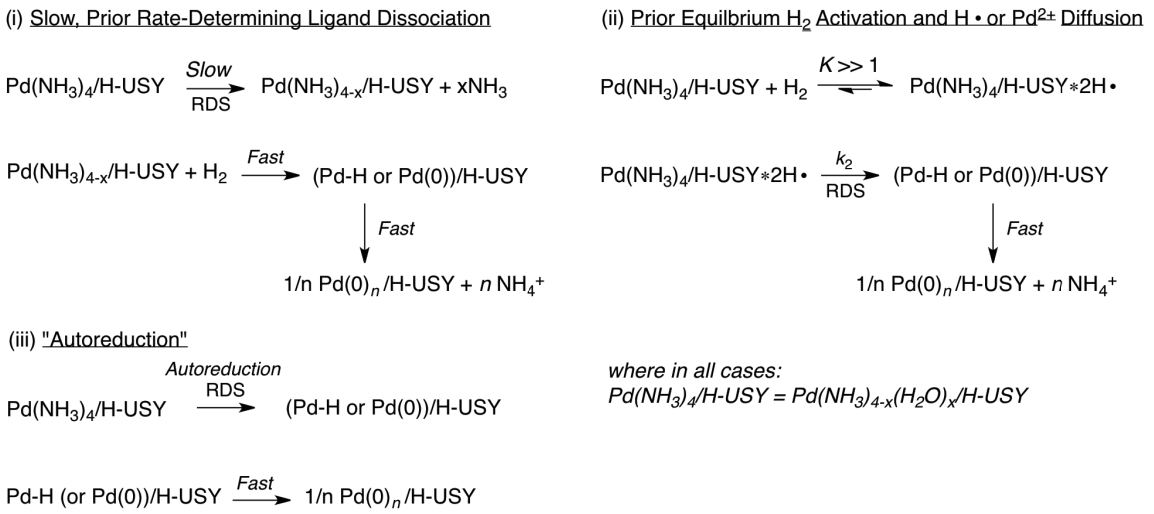

Scheme 4. Three plausible, deliberately minimal mechanisms proposed herein to account for the observed $Pd(0)_{\sim 13}$/H–USY supported-nanoparticle formation kinetics obtained by Okumura and co-workers [62,63]. The proposed mechanisms include: (i) a slow, prior rate-determining step such as ligand dissociation; (ii) a mechanism where H_2 is activated on the zeolite with $K >> 1$ and then diffusion occurs as part of the rate-determining step; and (iii) an "autoreduction"[2] mechanism. In the autoreduction possibility, (iii), the (non-obvious), ostensibly NH_3-based decomposition products are not shown.

The mechanistic postulates are: (i) a slow, rate determining step (top left, Scheme 4), such as ligand dissociation, to some "intermediate" species, followed by the fast activation of H_2 and subsequent formation $Pd(0)_{\sim 13}$/H–USY; (ii) H_2 activation by a K >> 1 prior equilibrium, on for example the zeolite surface, followed by slow diffusion of two H• to the Pd^{2+} species and or diffusion of Pd^{2+} to the activated H• as part of the rate determining step, followed by fast agglomeration of the resultant Pd–H or Pd(0) species (top right, Scheme 4); or (iii) some autoreduction[2] process (bottom left, Scheme 4) that generates reducing equivalents, an autoreduction that the observed kinetics require would have to be slow and rate-determining (i.e., and relative to the subsequent, faster, supported-nanoparticle formation steps under H_2). The autoreduction mechanism can likely be ruled out given the lower temperature (300 K) reaction conditions since the reducing equivalents, generated from autoreduction for supported $M(NH_3)_4^{2+}$ complexes,

are not typically observed until somewhat higher, 373 to 473 K, temperatures [149]. Overall, then, the implications are that the rate-controlling ligand dissociation or H• (or $Pd(NH_3)_4^{2+}$) migration steps are obscuring the supported-nanoparticle heterogeneous catalyst formation kinetics. To summarize, additional kinetic studies are needed in order to obtain the full rate law and distinguish between the prior equilibrium and H_2 activation mechanisms shown in Scheme 4 for this otherwise classic $Pd(NH_3)_4^{2+}$/support system [62,63].

2.2.2.2. System II: H_2PtCl_6/Support Based Systems

$Pt(0)_n$ nanoparticles supported on γ-Al_2O_3, as well as bimetallic derivatives such as $(Pt–Re)_n$, are commonly used in catalytic reforming reactions [3,36,40,158,159,160,161]. One of the most common metal precursors for the preparation of $Pt(0)_n$/γ-Al_2O_3 is H_2PtCl_6. However, and again, much less is known about the kinetics and mechanisms of the supported-nanoparticle heterogeneous catalyst formation step for such Pt-based systems. Five studies, which are summarized in Entries 9–13 of Table 2, start from a H_2PtCl_6-based supported metal precatalyst.

In 1986 and 1988 Dexpert and co-workers [38,40] studied the formation of ~1 nm $Pt(0)_n$ nanoparticles supported on γ-Al_2O_3, at 200 °C under H_2, from an ill-defined $Pt(OH)_x(Cl)_y$/γ-Al_2O_3 precursor. In their first study [38], the first 10 minutes of the supported-nanoparticle formation were qualitatively followed via EXAFS and XANES. A word-based mechanism, summarized in Entry 9 of Table 2, was proposed for the formation of small Pt_xCl_y clusters. However, the kinetic data collected were not fit to the proposed mechanism to thereby support, or refute, the proposed mechanism. In a subsequent report [40], the loss of Pt–O and Pt–Cl bonds in the supported precursor complex, as well as the formation of Pt–Pt bonds, were followed by EXAFS at 180 °C. No additional mechanistic details were proposed for the formation of the $Pt(0)_n$/γ-Al_2O_3 supported-nanoparticle catalyst [40].

In 2007 Chupas and co-workers used the direct and powerful method of total high-energy X-ray scattering along with PDF analysis to study the kinetics of $Pt(0)_n/TiO_2$ supported-nanoparticle formation [56,66], Entry 11 (Table 2). While the stoichiometry of the supported-nanoparticle formation reaction was not rigorously demonstrated, the $Pt(0)_n/TiO_2$ products were found to be 1-5 nm depending on the reduction temperature. In their initial study, in situ X-ray scattering was used to directly follow both the loss of Pt–Cl bonds and the formation of Pt–Pt bonds at 100, 150 and 200 °C. The kinetic data of the loss of the Pt–Cl bonds were well fit to a zero-order process, which was dependent on the reduction temperature—the activation energy of the zero-order reaction was found to be 50.17 kJ/mol, apparently the activation energy of a diffusion controlled process (vide infra). Unfortunately, no mechanism was proposed for the supported-nanoparticle formation reaction; the observed zero-order kinetics (i.e. $-d[H_2PtCl_6/TiO_2] \propto [H_2PtCl_6]^0$) imply a diffusion controlled process to the observed $Pt(0)_n/TiO_2$ products as detailed next.

The intriguing linear loss of H_2PtCl_6/TiO_2 and implied zero-order dependence, $[H_2PtCl_6]^0$, sparked Mondloch, Finke and co-workers to postulate a mechanism that could describe such a dependence for the $Pt(0)_n/TiO_2$ system and since those were also studying this same system, albeit in contact with solution [72]. Following collaborative discussions with the Chupas group, a mechanism was postulated that is consistent with the observed kinetic data, as shown in Scheme 5. The proposed mechanism consists of rate determining H_2 activation on TiO_2, followed by fast H• diffusional transfer to the active site (not shown, where H_2PtCl_6 is reduced) and then supported-nanoparticle formation (i.e., which must be fast compared to the rate-determining H_2 activation/diffusion and in order to explain the observed, zero-order kinetics). It is also plausible that a second, also diffusion-limited mechanism is operating here, one where the diffusion of non-dissociated H_2 to the Pt^{4+} precatalyst is slow and the subsequent H_2

activation and supported-nanoparticle formation steps are fast. Consistent in a general way with the presence of a diffusion-limited process, Mondloch, Finke and co-workers [56] reported conditions for $Pt(0)_n/TiO_2$ supported-nanoparticle formation *in contact with solution* (i.e., at the gas-liquid-solid interface) where a H_2 gas-to-solution, diffusion-limited mechanism was also found to be operating under certain conditions (vide infra, Section 3.2.2.3).

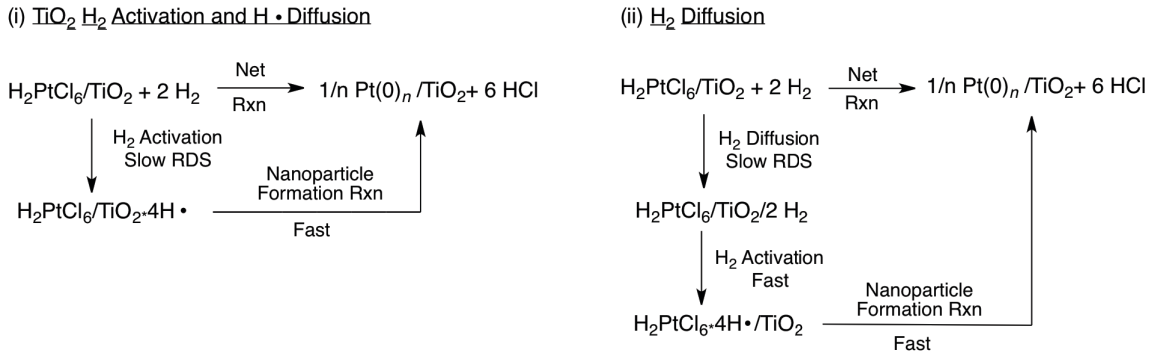

Scheme 5. Shown left is a proposed stoichiometry (top) and accompanying mechanism (bottom) [72] containing a slow rate-determining H_2 activation step to account for the observed, linear, apparently zero-order Pt–Cl and Pt–Pt kinetics observed in the formation of $Pt(0)_n/TiO_2$ [56]. Shown right is an alternative mechanism containing a slow H_2 diffusion step that could also account for the observed kinetics [56].

In a follow up study, Chupas and co-workers [66] studied the change in the Pt–Pt contributions as the temperature was ramped from 0 to 227 °C (Table 2, Entry 11). Three distinct regimes were observed, from which the authors proposed that the "…initial particles that form are small (<1 nm) then agglomerate into ensembles of many small particles and lastly anneal to form larger well-ordered particles". These ground breaking, first-of-their-kind, total high-energy X-ray scattering/PDF analysis methods from the Chupas team promise to provide significant insights into the mechanisms of supported-nanoparticle heterogeneous catalyst formation once the best, well-defined systems are studied. It will be important in those studies to couple the X-ray

scattering/PDF method to experimentally determined, balanced reaction stoichiometries and to other complimentary kinetic monitoring methods.

In 2009, Shishido et al. investigated the formation of $Pt(0)_n$ nanoparticles supported on TiO_2 and γ-Al_2O_3 from a PtO_x/TiO_2(γ-Al_2O_3) precatalyst, Table 2, Entry 12. The observation of PtO_x by EXAFS is indicative of either highly dispersed atomic Pt^{4+} ions or the presence of supported-PtO_2 monomers. Evidence against the formation of aggregated $(PtO_2)_n$ particles, post the precatalyst calcination step, is given by a lack of long range Pt–O–Pt contributions in the EXAFS analysis (a control EXAFS showed that such long range Pt–O–Pt contributions were observable in a bulk PtO_2 standard). To start, the authors monitored the change in the Pt L_{III} white line[13] XANES edge over time for the PtO_x/TiO_2 sample by admitting a pulse of 200 μL of H_2 into their gas-solid cell. At 473 K the reduction of Pt^{4+} to Pt(0) was linear and complete within 1 s with no observable induction period (i.e., further pulses of H_2 did not change the XANES white-line intensity, meaning that no additional PtO_x was being reduced to Pt(0)). These observations are consistent with Chupas and co-workers observed linear kinetics for the formation of $Pt(0)_n/TiO_2$ at 200 °C (which had not been calcined, i.e., the Chupas team started from the chloro complex $PtCl_6^{2-}$ supported on TiO_2) [56]. In addition, isosbestic points were observed in the XANES data at 473 K, suggesting that a direct transition from Pt^{4+} to Pt(0) occurred with no observable intermediate. Unfortunately, Shishido et al. did not attempt to fit their data to zero- or first-order plots. Another important point is that the temperature of the reduction drastically affected the observed changes in the white-line intensity over time; at room temperature the white line intensity effectively

[13] (a) The white-line at the L_3-edge is an element-specific quantum mechanical transition arising from the excitation of core-level $2p_{3/2}$ electrons into unoccupied $5d_{5/2}$ and $5d_{3/2}$ states above the Fermi level.[13b] Practically, the white-line intensity at the L_3-edge is a spectroscopic fingerprint that can be used, for example, to follow the loss of a supported metal precatalyst species. (b) J. J. Rehr, R. C. Albers Rev. Mod. Phys. 72 (2000) 621-654.

remained constant after two, 200 μL pulses of H_2, and did fully decrease until the third pulse (after which no change was seen with subsequent pulses of H_2). Although not discussed by the authors, the lack of an observable change in the XANES white line intensity with upon exposure to H_2 implies that an induction period is present under the milder room temperature reduction conditions.

Next, the authors changed the support from TiO_2 to γ-Al_2O_3 and examined the reduction of PtO_x/γ-Al_2O_3 by monitoring the XANES Pt L_{III}-edge and using the same H_2-pulse procedure. Interestingly, the PtO_x/γ-Al_2O_3 precatalyst could not be reduced (i.e., the XANES white-line intensity did not change) with H_2 at room temperature over the course of 100 s, revealing that the reduction of the PtO_x/γ-Al_2O_3 is slower than that observed for of the PtO_x/TiO_2 sample. The results provide *prima facie evidence that the support plays a major role in the rates of supported-nanoparticle formation*, at least in the PtO_x/TiO_2 and PtO_x/γ-Al_2O_3 systems. No mechanism was proposed for this interesting, supported-nanoparticle heterogeneous catalyst formation system, however, so it is hereby identified as an important system for additional kinetic and mechanistic investigations.

Noteworthy here is that Mondloch, Finke and co-workers observed very similar support effects for the reduction of H_2PtCl_6 on γ-Al_2O_3 and TiO_2, but now with these catalysts in contact with solution (i.e., at the gas-solid-solution interface) [72], vide infra, Section 3.2.2.3. That connection (i.e., of the H_2PtCl_6 on γ-Al_2O_3 or TiO_2 at the gas-solid interface vs. these same systems in contact with solution) and the connection between the Chupas [56] and the Mondloch, Finke [72] studies of H_2PtCl_6/TiO_2 (specifically the diffusion limited kinetics seen for both under certain conditions) are important connections/insights. Those comparisons suggest that the mechanistic insights obtained from such studies of supported heterogeneous catalyst formation in contact with solution [72,74,75] will at least sometimes connect back to, and perhaps be

transferable to, the formation of supported-nanoparticle catalysts at the gas-solid interface (more here in section 3.2.2.4, vide infra).

One final topic that merits discussion is the speciation of H_2PtCl_6 that can occur during the metal/support impregnation step. The speciation of H_2PtCl_6 in H_2O [162], and in contact with γ -Al_2O_3 [163,164,165,166], has been extensively studied, is quite complex, and varies according to the conditions employed during the impregnation step [162-166]. The literature is clear that the following species exist *in aqueous solution as a starting, reference point*: $[PtCl_6]^{2-}$, aquo species such as $[PtCl_5(H_2O)]^-$, and aquahydroxo species such as $[PtCl_4(OH)(H_2O)]^-$; in addition, their relative concentrations pH dependent [162-166] as one might expect. Hence, the exact interaction of the species formed from H_2PtCl_6 in aqueous solutions and in contact with γ -Al_2O_3 remains a complex, controversial subject [163,164]. Regalbuto has suggested that when fresh H_2PtCl_6 solutions are prepared, the major species present in solution is $[PtCl_3(H_2O)_3]^+$, and it is repelled from the protonated $[\gamma\text{-}Al_2O_3]^+$ surface at low pH [162]. However, the major species present in aged H_2PtCl_6 solutions at a pH of 5-9 is actually $[PtCl_2(OH)_2(H_2O)_2]^0$ [162], a neutral species that should more readily interact with the γ-Al_2O_3 support.

Also worth noting here is that speciation has also been documented for other chloro precursors, such as $AuCl_3$ [52,59,167,168]. Interestingly, recent work with the discrete metal oxides known as polyoxometalates reveals that metal chlorides, such as $RuCl_3$ [169] or $PtCl_4^{2-}$ [170,171] (with their strong metal–ligand bond strengths), are often inferior to, for example and in the platinum case, $Pt^{II}(OH)_6^{2-}$ [172,173] for inserting second or especially third-row transition metals into metal-vacancy containing (i.e., into so-called lacunary) polyoxometalates. The connection here is that insights from discrete metal oxides such as polyoxometalates can probably be use to synthesize better solid-oxide-supported catalysts.

The bottom line, then, of this subsection on H_2PtCl_6 derived catalysts is that until and unless care is taken to minimize the speciation present, the resultant supported-metal precatalysts will both be ill-defined, likely exist as multiple species, and in turn yield multiple mechanisms that yield a broad size distribution, mixed shape as well as compositionally disordered supported-nanoparticles! Hence, a central topic en route to spreparing the next generation of supported-nanoparticle $Pt(0)_n$ (and other!) catalysts, one that will require its own extensive studies to unravel, is the nature of the precise Pt speciation when H_2PtCl_6 (and other) metals are placed on supports such as γ-Al_2O_3. Once that speciation is in hand, *then* the kinetic contribution of each species to the formation of the supported $Pt(0)_n$ nanoparticles can be elucidated.[14]

2.2.2.3. System III: Ag^+/Zeolite Supported Systems

Interest in $Ag(0)_n$ zeolite–supported (commonly zeolite A, X and Y) catalysts arises from their potential use for hydrocarbon oxidation and the dimerization of alkenes [174]. Much is known about the precatalyst preparation steps when starting from $Ag(NO_3)$ and a zeolite (i.e., the metal/support ion-exchange, drying and then calcination steps). A key point, again, is that a broad range of speciation is present, including Ag^+, Ag_n^{x+} clusters and other precedented species [174,175,176,177,178,179,180,181,182, 183,184,185,186,187,188]. Much less is known about the supported-nanoparticle formation step, however. Entries 14–18 in Table 2 highlight the five papers [32,36,37,42,57] in the literature that address the kinetics and mechanisms of $Ag(0)_n$/zeolite supported-nanoparticle heterogeneous catalyst formation.

In a classic 1976 paper, Jacobs and co-workers studied the formation of a putative, $Ag(Ag_3)^+$ subnanometer cluster on zeolite–Y from a Ag^+/zeolite–Y precatalyst over the

[14] Highly relevant here is the observation by Mondloch, Finke and co-workers that the kinetics of $Pt(0)_n/\gamma$-Al_2O_3 formation, in contact with EtOH are quite variable and irreproducible [72], *presumably* due such uncontrollable speciation, vide infra, Section 3.2.2.3.

temperature range of 298 to 623 K [32], Table 2 (Entry 14). Complete reduction of Ag^+ to Ag(0) was observed only above 556 K. The stoichiometry of the reduction reaction was proposed to occur via equation 3 (where the zeolite support has been omitted, although it likely plays a role in trapping the proton, vide infra); H_2 uptake measurements confirmed the Ag^+, H_2 and Ag(0) portions of that stoichiometry, equation 3.

$$2Ag^+ + H_2 \rightarrow 2Ag(0) + 2H^+ \qquad (3)$$

Equation (3) is an example of what organometallic chemists have studied extensively and know as heterolytic H_2 activation [25,26]. As such, it requires a base (B) to accept the protons (as $B–H^+$), the strength of the base typically having a large effect on the observed rate. In the present case the base is likely a zeolite–O^- site, which when protonated yields the hydroxyl species zeolite–OH (a site not experimentally verified for the $Ag(0)_n$ supported-nanoparticle formation systems in Entries 14–18 of Table 2). The $Ag(0)_n$/zeolite–Y supported-nanoparticle products were probed using powder X-ray diffraction; below 473 K the products are $Ag(0)_n$ particles <3.5 nm (as indicated by the lack of a Ag(111) reflection in the XRD spectrum). Above 423 K, the XRD data reveal that the $Ag(0)_n$ zeolite–Y supported-nanoparticles are 21 nm.

The authors used H_2 uptake measurements to follow the kinetics of the Ag^+ reduction; two distinct, temperature-dependent kinetic regimes were observed. Since no mechanism was proposed for the high temperature regime (i.e., > 430 K), in what follows the focus will be on the kinetic data obtained at lower temperatures (i.e., ≤ 430 K). The kinetics at ≤ 430 K were first-order with respect to Ag^+ and H_2, showed an inverse-first-order dependence with respect to the “reaction product concentration” [32] (i.e., $-d[H_2]/dt$

α $[Ag^+]^1$, $[H_2]^1$ and $[H^+$ or $Ag(0)]^{-1}$, respectively)[15] and yielded an apparent activation energy of 40 kJ/mol. The authors proposed two mechanisms, Scheme 6, that are claimed to be consistent with the observed kinetic data.

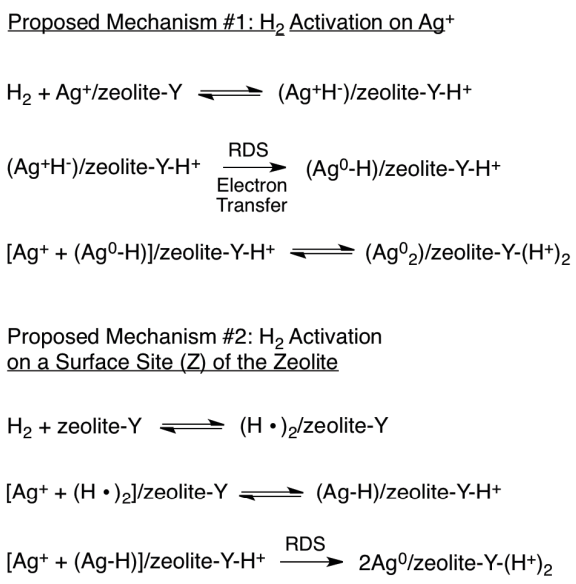

Scheme 6. The two mechanisms proposed by Jacobs and co-workers for the H_2 reduction of Ag^+/zeolite–Y to Ag^0/zeolite–Y at ≤ 430 K [32]. The first mechanism (top) entails H_2 activation on Ag^+ followed by a rate-determining electron transfer step, while the second mechanism involves H_2 activation on the zeolite and a rate-determining regeneration of the zeolite (Z) support site ("zeolite–Y", has been added for clarity to the author's original mechanisms [32]). However, only the first mechanism appears to be consistent with the authors observed kinetics and as discussed in the main text.

In the author's first proposed mechanism (top), H_2 is activated on Ag^+ followed by a slow rate-determining electron transfer step. In the second postulated mechanism (Scheme 6, bottom), H_2 is activated on some surface site of the zeolite (Z), followed by the diffusion of Ag^+ to that activated H•–Z and finally rate-determining regeneration of that surface site. Jacobs and co-workers favor the second mechanism (bottom) and

[15] A key kinetic plot in Jacobs' and co-workers paper [32] is their Figure 5 which establishes both a $[H_2]^1$ and a "c^{-1}" (i.e., a $[H^+]^{-1}$ or $[Ag(0)]^{-1}$) dependence, all from the H_2-uptake kinetics, plus the stoichiometry $C_0 - C_i' = [Ag^+]_i - [Ag^+]_t = [Ag(0)]_t = [H^+]_t$, a clever example of how much information can be obtained from just H_2 uptake kinetic measurements coupled with a balanced reaction stoichiometry.

argue that electron transfer in the first mechanism (top) should not be rate determining. However, the differential equation describing their second mechanism was not provided and attempts, at least in our hands, to derive a differential equation consistent with the observed kinetic data (i.e., to $-d[H_2]/dt \propto [Ag^+]^1$, $[H_2]^1$ and $[H^+$ or $Ag(0)]^{-1}$) have not been successful. As predicted by inspection of the second mechanism, such derivations yield a predicted $[Ag^+]^2$ dependence. However, derivations of the rate law corresponding to the first mechanism (Scheme 5, left) are consistent with the kinetic data, as stated by Jacobs' and co-workers [32]. Hence, the observed kinetic data favor the first mechanism, where by H_2 is heterolytically activated by Ag^+ plus a basic zeolite site. Also noteworthy is that while the diffusion of Ag^+ on the zeolite surface is possible, well-known H• diffusion (i.e., H• spillover) could also be part of the Ag^+ plus H• surface reaction [189]. In short, while the final detailed mechanism remains to be established, illustrative here is what Jacobs' and co-workers were able to obtain from just the reaction stoichiometry and H_2-uptake kinetic data. Their results argue strongly for the increased use of H_2 uptake experiments to screen and establish the initial steps of supported-nanoparticle formation, at least when and where such H_2 uptake experiments are possible.

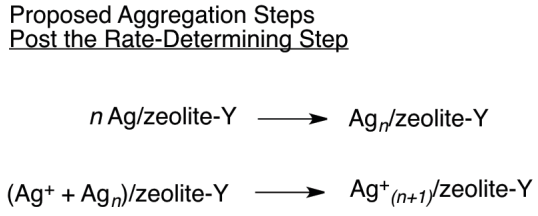

Scheme 7. The fast, post rate-determining (i.e., post the proposed steps in Schemes 5 and 6) aggregation steps proposed by Jacobs and co-workers, steps proposed to account for the observed formation of the aggregated $Ag(0)_n$/zeolite-Y products [32].

Finally, to account for the formation of their aggregated $Ag(0)_n$/zeolite–Y products, Jacobs and co-workers proposed the post-rate-determining, aggregation steps shown in Scheme 7 (albeit of course without any kinetic evidence for those steps since they are hidden kinetically by being after, and thus faster than, the rate-determining steps in Scheme 6) [32]. Based on two aggregation steps now precedented in solution nanoparticle chemistry [190,191,192], one can propose that analogous B + B → C (bimolecular) and B + C → 1.5C (autocatalytic) aggregation steps are actually a part of the aggregation/agglomeration of $Ag(0)_n$ in the Ag^+/zeolite–Y system, where B is $Ag(0)_n$, and C is aggregates of B The broader, more general point here is that there is a need to mesh the literature of formation of $Ag(0)_n$/solid-supports (Table 2, Entries 14–18) with both the established mechanistic steps of nanoparticles in solution [190,191,192,193,194] where applicable. A second, important future goal is to mesh those areas with the extensive literature of ligand-stabilized $Ag(0)_n$–L_x nanoparticle formation in solution [195,196,197,198].

In 1980 Hermerschmidt et al. studied the formation of <5 nm $Ag(0)_n$/zeolite–A supported-nanoparticles under H_2 by ESR spectroscopy (albeit from an uncharacterized, Ag supported-precatalyst), Entry 15, Table 2. A intermediate Ag_6^+/zeolite–A supported-cluster detectable by ESR was shown to be kinetically competent for the formation of <5 nm $Ag(0)_n$ nanoparticles supported on zeolite–A. Although kinetic data were collected, Hermerschmidt et al. acknowledge that "…the rate of formation of the silver clusters can be (and were) measured from ESR signal intensities below room temperature; (however) no evaluation of kinetic data was attempted since a simple kinetic model can not be proposed for the complex mechanisms involved in the reduction, migration, and aggregation processes". This 1980 statement is notable, a general testament to the difficulty in studying the kinetics and deriving a consistent and plausible elementary-step-

based mechanism for such supported-nanoparticle heterogeneous catalyst formation reactions. Nevertheless, and as pointed out by Jacobs [153], "Hermerschmidt et al. established that the loss of Ag_6^+/zeolite–A and the formation of $Ag(0)_n$/zeolite–A occur concurrently".

Following up their earlier work [32], in 1982 Jacobs and co-workers studied the reduction of Ag^+ supported on the chabsite zeolite (Entry 16, Table 2) to yield a sub-nanometer, $(Ag_2^+)_m$/chabsite product (where *m* is assumed/proposed by the authors, albeit without any experimental evidence, to be 2 to yield an overall Ag_4^{2+} cluster) [37]. Again, a significant amount of kinetic information was extracted via H_2 uptake measurements, data revealing that the reaction is second-order in Ag^+ and half-order with respect to the H_2 pressure (i.e., $-d[Ag^+]/dt = k[Ag^+]^2[H_2]^{1/2}$). An apparent activation energy of 49 kJ/mol was also reported. The authors proposed the mechanism shown in Scheme 8, where the "zeolite" has again been added clarity. The mechanism for their

$$1/2\ \{H_2 + \text{zeolite} \rightleftharpoons (H\bullet/\text{zeolite})_2\}$$

$$[Ag^+ + (H\bullet)]/\text{zeolite} \rightleftharpoons [Ag^0H^+]/\text{zeolite}$$

$$[Ag^0H^+ + Ag^+]/\text{zeolite} \xrightarrow{\text{RDS}} Ag_2^+/\text{zeolite-}H^+$$

$$\text{SUM: } [1/2\ H_2 + 2\ Ag^+]/\text{zeolite} \longrightarrow Ag_2^+/\text{zeolite-}H^+$$

Scheme 8. The mechanism proposed by Jacobs and co-workers [37] for the formation of Ag_2^+ on the chabsite zeolite. Modifications added herein for clarity include: the addition of the zeolite support ("zeolite", above), the ½ { } to balance the reaction, and the final summed stoichiometry.

stated "first reduction step" now requires homolytic H_2 activation (which presumably occurs on the zeolite surface or an impurity such as Fe^{x+} on the zeolite), followed by the formation of a putative protonated Ag(0), "Ag^0H^+", species (that an organometallic chemist would write *formally* as a little precedented, high energy Ag^{II} species, $[Ag^{II}–H]^+$).

Then a rate-determining step of Ag^+ ion migration to that "Ag^0H^+" was proposed. Unfortunately, the differential equation corresponding to the mechanism shown in Scheme 8 was again not derived [37], but appropriate derivations confirm that the proposed mechanism will account for the $-d[Ag^+]/dt = k[Ag^+]^2[H_2]^{1/2}$ rate law. That said, unequivocal demonstration of the net reaction stoichiometry, along with further kinetic and mechanistic work, are needed to support this proposed, classic study. Further study is also needed to understand why the mechanism and rate law have changed from that in equation 3 and Scheme 6 [32]; understanding the origin of that change promises to be an important insight into this area.

Moving to a 1989 study, Schoonheydt and co-workers also studied the kinetics of the formation of Ag_6^+/zeolite–A, from a putative Ag^+/zeolite–A precatalyst, under H_2 and over the temperature range of 258–298 K [42], Table 2, Entry 17. ESR was used to follow the formation of Ag_6^+ on zeolite–A (via the most intense, central line of the ESR spectra). The resultant kinetic data were not fit to any mechanism, but appear first-order in most instances. At each temperature, the initial rate (i.e., $[+d[Ag_6^+/zeolite–A]/dt]_i$) was extracted, and the log of the initial rate was plotted vs. 1/T to obtain an apparent activation energy of 47-60 kJ/mol (which depended strongly on the amount of ion-exchanged Ag^+).

Schoonheydt et al. also investigated the role of the zeolite counter cation on the formation of Ag_6^+/zeolite–A by ESR (e.g., K^+ was exchanged for Na^+). The idea here is that if the diffusion of Ag^+ is a crucial step in the Ag_6^+/zeolite–A formation reaction, then the presence of different cations should affect the resultant kinetics. The kinetic curves are clearly different in the presence of K^+ cations (vs. Na^+), appearing sigmoidal when K^+ is present (vs. the linear kinetics observed for the Na^+ sample). Hence, the presence of other cations besides Ag^+ matters. Finally, the authors note that Fe-based impurities (either discrete Fe^{3+} or Fe_2O_3) also affected the kinetics of Ag_6^+/zeolite–A formation.

From this information the authors hypothesize that "the rate-determining step for the formation of the Na^+-exchanged Ag_6^+/zeolite–A is the diffusion of Ag^+ cations" [42]—again we see that slow, M^{x+} cation diffusion on supports and/or H• diffusion is a common, albeit still not well-understood, step in the proposed mechanism of formation of supported-nanoparticle catalysts. The mechanism of the Ag_6^+ cluster formation consists, then, of at least two steps according to the authors: (i) "the formation of reduced centers, and (ii) the migration of Ag^+ toward these (reduced) centers" [42] (or, again we would add H• migration). "The reduced centers cannot be the Ag(0) atoms" [42]. In addition, the authors also suggest, "that the cluster formation is a series of consecutive reactions" given by $Ag + Ag \rightarrow Ag_2 \rightarrow Ag_3$ and so on to the Ag_6^+ product. The authors argue that diffusion of Ag^+, rather than of Ag(0), is rate-limiting based on the fact that the measured activation energy (40–67 kJ/mol) is within the range of known monovalent cation diffusion E_a values in zeolite–A [42]. However, additional studies are needed to rule out a mechanism containing diffusion of Ag(0) (or possibly of Ag–H) as well as the possibility of H• migration. In addition, the activation energy measured for the putative Ag^+ migration step is at best a composite of the undetermined mechanism of Ag_6^+/zeolite–A formation, making both interpretation of the 40–67 kJ/mol values, and its comparisons to the literature values, problematic at present [199,200].[16]

Finally, in Figure 7 we show previously unpublished results revealing that the K^+-based Ag_6^+/zeolite–A kinetics can be fit to a simplified, 2-step nanoparticle formation

[16] The authors measure the formation of Ag_6^+/zeolite–A, that is more rigorously something like $[+d[Ag_6^+/\text{zeolite–A}]/dt]_i = k_{obs}[Ag^+]_i^a[H_2]_i^b[\text{unknown species}]_i^c$. The Arrhenius equation is given by $k_{obs} = A*\exp(-E_a/RT)$ and the typical plot of $\ln(k_{obs})$ vs. $1/T$ yields the (composite) activation energy (E_a). The problem is that the rigorous interpretation of such composite activation energies relies on knowledge of the precise mechanism of formation of Ag_6^+/zeolite–A. For a detailed example and derivation of how activation parameters propagate for composite steps, see elsewhere [199,200].

mechanism that will be detailed in Section 3.[17] These results suggest that a different mechanism is operating in the presence of K^+. The simplified, 2-step mechanism, is that developed by Finke and Watzky for ligand-stabilized nanoparticle formation in solution [193] and has the general form of A → B (i.e., slow continuous nucleation, where A is either Ag or Ag^+, and B is the higher molecularity Ag_n and $Ag^+_{(n+1)}$ species), followed by A + B → 2B (i.e., autocatalytic surface growth). This minimal, 2-step nucleation and autocatalytic growth mechanism was developed while studying soluble [156,193], ligand-stabilized nanoparticle formation kinetics. It has also recently been shown to apply to the kinetics of formation of supported-nanoparticle formation in contact with solution [72,74,75], vide infra. It is by no means completely clear at present what the fit shown in Figure 7 to the 2-step mechanism precisely means in the present case—that is, Figure 7 is just a lead worthy of further investigation. It is clear, however, that the presence of K^+ has changed the kinetics of the underlying nanoparticle formation mechanism [42].

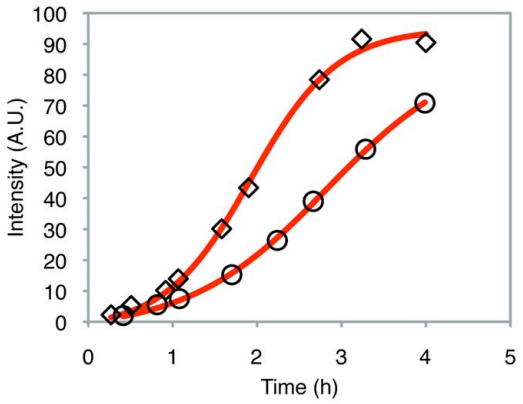

Figure 7. The kinetics of Ag_6^+/zeolite–A(K^+) supported-(sub)nanoparticle formation measured by ESR at 273 K (circles) and 278 K (diamonds) [42]. The red lines are fits to the two-step mechanism of A → B and A + B → 2B [193], where A is Ag^+, and B is the higher molecularity Ag_n or $Ag^+_{(n+1)}$ product(s). Adapted with permission from [42]. Copyright (1989) American Chemical Society.

[17] The previously published kinetic data from Schoonheydt and co-workers [42] were digitized using Engauge Digitizer 2.12. The data were fit by the integrated analytical

In 2007, Shimizu and co-workers studied the formation of Ag_4^{2+} clusters on zeolite MFI from Ag^+/MFI under H_2 via EXAFS and UV-Vis spectroscopy [57], Entry 18, Table 2. Pseudo first-order rate constants were obtained from diffuse-reflectance UV-Vis spectroscopy measurements over the temperature range of 573 to 913 K. Apparent activation energies were calculated from an Arrhenius plot and found to be the seemingly low value of 10 kJ/mol. Unfortunately, no specific mechanism was proposed making interpretation of the (apparent, composite) activation energy problematic. Note that this 10 kJ/mol activation energy is considerably smaller than the previous values obtained by Jacobs and co-workers [32,37] or by Schoonheydt et al. [42] (10 kJ/mol vs. 97.6, 49 and 47-60 kJ/mol, respectively). The range of activation energies suggests to us that one or more of these disparate values: (i) are suffering from so-called artifactual E_a vs. A (i.e., $\Delta H^{\ddagger}$ vs. $\Delta S^{\ddagger}$) compensation (in which, basically, the temperature range employed is insufficient to deconvolute $\Delta H^{\ddagger}$ from $\Delta S^{\ddagger}$) [201]; or (ii) are composites and need to be deconvoluted into the $\Delta H^{\ddagger}$ and $\Delta S^{\ddagger}$ values for their underlying steps to be meaningful [199,200].[16] Also possible here is (iii) that the different zeolites are playing a significant role in the supported-nanoparticle formation mechanism, or (iv) conceivably some combination of the above possibilities could be occurring. In any event, the need for further research on the Ag^+/support systems is apparent.

2.2.2.4. System IV: Compositionally Well-Defined Supported-Organometallic Complexes

So-called "single-site", compositionally well-defined, supported-organometallic complexes [202,203,204], along with various supported-organometallic clusters, are known, active catalysts for olefin polymerizations [205,206] and hydrogenations [100,207]. Furthermore, they can also be used as *speciation controlled precatalysts* en route to supported-nanoparticles [74,75]. In addition, such supported-organometallic

---

equation given elsewhere, corresponding to the two-step mechanism of A → B and A + B → 2B [193].

precatalysts are particularly attractive for understanding the mechanisms of supported-nanoparticle heterogeneous catalyst formation as detailed in what follows. Speciation-controlled, supported-organometallics also typically contain organic ligands that can often be used as additional handles to monitor the decomposition of supported-precatalysts which, when combined with a direct technique for following M–M bond formation (or net $M(0)_n$ nanoparticle formation), can be powerful en route to the required balanced reaction for the nanoparticle formation reaction. Seven kinetic and mechanistic studies of the formation of supported-nanoparticles from supported-organometallic complexes are listed as Entries 19–25 in Table 2 [45,48,51,60,61,64,67]. These studies are covered next.

In 1998, Nuzzo and co-workers studied the "nucleation and growth" of 1.5 nm $(Pt–Ru)_n$ nanoparticles from the well-defined $PtRu_5C(CO)_{16}$/activated-carbon precursor [45], Table 2, Entry 19. A narrow (but non-reported) size distribution and atomically precise (1:5 Pt:Ru metal content) supported-nanoparticle product, $(Pt–Ru)_n$ supported on activated-carbon, resulted [101]. The structural evolution of the formation of $(Pt–Ru)_n$/activated-carbon under H_2 (from 150 to 773 K) was followed via XANES and EXAFS. The EXAFS structural evidence is consistent with the author's proposed picture (Scheme 9) and word mechanism, in which "the initial nucleation of a compact (Pt-rich) structure (is) followed by the inversion of the intraparticle distribution of the Pt and Ru atoms upon continued high-temperature annealing". The authors further state "In this inversion, the core-segregated Pt atoms exchange with Ru surface atoms to form a surface Pt shell structure", all as depicted in Scheme 9. Nuzzo and co-workers' study, Scheme 9, is an important case history, one which sets a solid foundation for further investigations [157,208].[18] An important goal of those additional studies should be to

[18] An important point here is the emerging role of the ligands present in bi- or higher-multimetallic nanoparticles in determining which metal winds up on the surface vs. in the

provide a set of chemical-based equations that echo the authors' picture and word-based mechanism, so that the proposed mechanism can be tested kinetically.

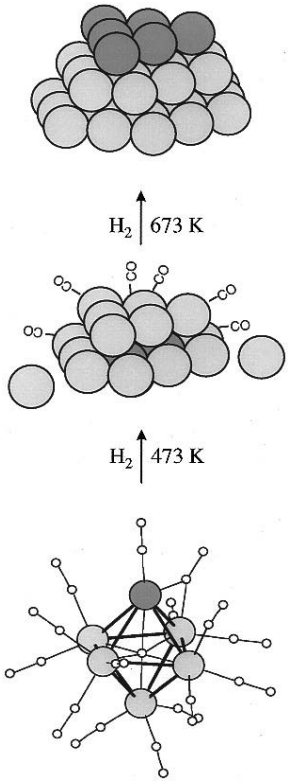

Scheme 9. Nuzzo and co-workers proposed pictorial mechanism for the conversion of $PtRu_5C(CO)_{16}$/activated-carbon into $(Pt–Ru)_n$/activated-carbon under H_2 (and a temperature ramp from 150 to 773 K) [45]. The light gray spheres represent Ru atoms, while the dark gray spheres represent Pt atoms. Reprinted with permission from [45]. Copyright (1998) American Chemical Society.

core. Normally, one expects the "heavier" metal, with its higher M–M bond strengths and associated higher $\Delta H_{vaporization}$ [157] to reside in the core of a multimetallic nanoparticle or "nano-onion", where a greater number of those stronger M–M bonds can be achieved. Good evidence of this expectation exists, see footnotes 38 and 39 elsewhere [157]. However, the ligands present, along with the stronger metal–ligand bond energies for the heavier metal, can draw that heavier metal to the surface [208]. In short, the extensive but still evolving literature of bimetallic and higher multimetallic nanoparticles is currently working to understand these and other competing factors that determine the structures of ligated, bimetallic and higher multimetallic nanoparticles, so that the interested reader is referred to that separate literature.

In 2002, Newton and co-workers studied the formation of $Pt(0)_n$ supported-nanoparticles on SiO_2 from a $Pt(acac)_2/SiO_2$ precursor (where acac = acetylacetonato) under H_2, and separately N_2, environments from 300 to 673 K (Table 2, Entry 20) [48]. The presence of a reducing environment clearly changes the resultant products—"larger" $Pt(0)_n/SiO_2$ nanoparticles (based on the Pt–Pt coordination number obtained from EXAFS) were observed under H_2 vs. N_2. EXAFS was used to follow the kinetics of the Pt–Pt bond formation under both the H_2 and N_2 environments. As just one example, the kinetic data (for the formation of $Pt(0)_n/SiO_2$) reveals that the Pt–Pt coordination number increased from 0 to about 9 over a very short temperature range of 15 K, starting at approximately 350 K. The authors suggest that this is "indicative of some form of autocatalysis", which is corroborated by the sigmoidal shape of their kinetic data. The authors attribute this autocatalysis to "an initial decomposition of a small fraction of the supported $Pt(acac)_2$ leading to the formation of a low level of small Pt particles….(which are) active for rapid H_2 dissociation and subsequent spillover of atomic hydrogen". In other words the authors hypothesize that H• spillover is the cause of the formation of the larger $Pt(0)_n/SiO_2$ particles under H_2 vs. N_2. However, very similar kinetics are observed for the decomposition of $Pt(acac)_2/SiO_2$ under N_2, data that seem inconsistent with this latter, specific hypothesis. One attractive alternative hypothesis here is that mobile hydride species (e.g., $[Pt–H]^0$), such as those proposed by Dalla Betta and Boudart [29] are present, a hypothesis consistent with the prior literature [29,72,74,75]. Again an important goal of the needed additional work here is to write rigorous chemical-based mechanisms followed by attempts to disprove those and the other, alternative mechanistic hypotheses.

In 2004, Gates and co-workers studied the formation of $Ir_4(CO)_{12}$/zeolite–Y from a $Ir(CO)_2(acac)$/zeolite–Y precatalyst under CO [51] (Table 2, Entry 21). The progress of the reaction was qualitatively followed using IR spectroscopy, the important, classic

spectroscopic handle for metal carbonyl complexes and clusters. A ν_{CO} stretching frequency at 1818 cm^{-1}, indicative of edge-bridging CO ligands, was assigned to a $Ir_2(CO)_8$/zeolite–Y intermediate en route to the $Ir_4(CO)_{12}$/zeolite–Y product. The assignment of the $Ir_2(CO)_8$ intermediate was corroborated by ex situ EXAFS analysis which revealed the presence of Ir–Ir scatterers. Gates and co-workers suggested that the formation of the $Ir_4(CO)_{12}$/zeolite–Y product occurs in a similar manner to known solution-based carbonyl chemistry [209] as shown in equations 4 and 5. This, then, is another valuable, classic system where detailed kinetic investigation promise to prove informative.

$$IrCl_3 + 3CO + H_2O \rightarrow [Ir(CO)_2Cl_2]^- + Cl^- + 2H^+ + CO_2 \quad (4)$$

$$4[Ir(CO)_2Cl_2]^- + 6CO + 2H_2O \rightarrow Ir_4(CO)_{12} + 2CO_2 + 4H^+ + 8Cl^- \quad (5)$$

Subsequently, starting from a well-defined $Ir(C_2H_4)_2$/zeolite–Y precursor, Gates and co-workers studied the formation of $Ir_4(ligand)_x$/zeolite–Y [60] (where the ligand structure was proposed to contain ethylidyne and di-σ-bonded ethylene) under H_2 from 298 to 353 K (Entry 22, Table 2) [210,211]. The $Ir(C_2H_4)_2$/zeolite–Y precursor was thoroughly characterized via IR and EXAFS spectroscopies [210] and, later, via aberration-corrected high-angle annular dark-field scanning TEM (HAADF STEM) [211]. Importantly in this well-executed study, a beautiful combination of complimentary physical techniques of XANES, EXAFS and IR spectroscopies were used to follow the loss of the $Ir(C_2H_4)_2$/zeolite–Y precursor and the formation of the $Ir_4(ligand)_x$/zeolite–Y product [60]. The XANES data at the Ir L_{III} edge indicated five identifiable isosbestic points, which are consistent with the transformation of the $Ir(C_2H_4)_2$/zeolite–Y into (just)

the $Ir_4(ligand)_x$/zeolite–Y. The time-resolved EXAFS data show the formation of Ir–Ir contributions and the loss of Ir–low Z contributions (i.e., Ir–ligand loss). The final Ir–Ir coordination number ($N_{Ir–Ir}$) was found to be approximately 3, which is consistent with the formation of Ir_4 clusters supported on zeolite–Y. The IR spectroscopy data also indicate the formation of di-σ-bonded ethylene ligands at the onset of Ir–Ir bond formation, data further consistent with the formation of the $Ir_4(ligand)_x$/zeolite–Y. One proposed mechanism for the formation of the $Ir_4(ligand)_x$/zeolite–Y supported cluster is pictorially reproduced in Scheme 10. Gates and co-workers caution that the proposed structures are "simplified" and were careful to note that there is "no direct evidence of the dinuclear intermediate species". Interestingly, the $Ir_4(ligand)_x$/zeolite–Y undergoes fragmentation *back* to the mononuclear $Ir(C_2H_4)_2$/zeolite–Y precatalyst under C_2H_4.

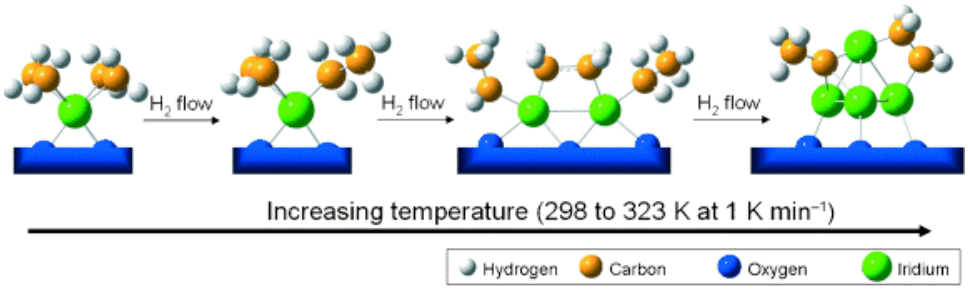

Scheme 10. Gates and co-workers proposed pictorial mechanism for the formation of $Ir_4(ligand)_x$/zeolite–Y under H_2 and a 298 to 323 K temperature ramp [60]. Copyright (2008) Wiley-VCH Verlag GmbH & Co. KGaA. Reproduced with permission from [45].

Gates and co-workers also studied the reduction of the analogous $Rh(C_2H_4)_2$/zeolite–Y precatalyst using the same methodology (Table 2, Entry 23)—the largest difference was that a $Rh_{2-3}(ligand)_x$/zeolite–Y product was formed during isothermal reduction at 298 K in H_2 [61] (i.e. and in comparison to the temperature ramp from 298 to 323 K for the $Ir(C_2H_4)_2$/zeolite–Y to $Ir_4(ligand)_x$/zeolite–Y zeolite system [60]). Significantly, the precise nuclearity of the subnanometer catalysts present, for both the Rh [212] and Ir

[213] systems, proved highly dependent on the reactive environment and specifically on the H_2/C_2H_4 ratio: higher H_2 ratios favor multinuclear clusters, while higher C_2H_4 ratios favor the mononuclear form [61,213].

To summarize, all of the data for the $Ir(C_2H_4)_2$/zeolite–Y to $Ir_4(ligand)_x$/zeolite–Y supported-cluster formation are consistent with Gates' et al.'s proposed pictorial mechanism, Scheme 9. Indeed, this example from the Gates' group is illustrative of how establishing "just" the balanced reaction is both very powerful mechanistically for supported-nanoparticle formation studies (and for materials chemistry in general). This example also illustrates that getting "just" that balanced stoichiometry often takes considerable, focused effort using multiple physical tools. The system in Scheme 9 is, therefore, a prime candidate for the next level of kinetics and associated chemical-reaction-based mechanistic studies. Some collaborative efforts towards this goal are currently underway [214].

In 2009, Gates and co-workers also studied the formation of the bimetallic $[H_2Os_3Ru(CO)_{13}]$/MgO cluster from $[Ru_3(CO)_{12}]$ and $[Os_3(CO)_{11}]^{2-}$ supported on MgO under H_2 and over the temperature range of 298 to 423 K [64], Entry 24, Table 2. Again a powerful combination of complimentary physical techniques, XANES, EXAFS and IR spectroscopy were used to follow the loss of the precursors and formation of $(Ru_xOs_y)_n$/MgO. Because of the multiple methods used, the authors were able to show that the supported product still contains some of both of the $[Ru_3(CO)_{12}]$ and $[Os_3(CO)_{11}]^{2-}$ precatalysts. The IR spectroscopy also indicates that the bimetallic product closely resembles $[H_2Os_3Ru(CO)_{13}]$/MgO, and the EXAFS data are consistent with that interpretation. The authors suggest that the mechanism of $[H_2Os_3Ru(CO)_{13}]$/MgO occurs, as pictorially described in Scheme 11, via "first, the decarbonylation of triruthenium clusters starting at 333 K (with the triosmium carbonyl clusters still being coordinatively saturated and intact)". The authors also note that "The coordinatively

unsaturated ruthenium species were reactive and, at 333 K, had aggregated substantially so that the average ruthenium cluster was larger than triruthenium. When the temperature had been raised to about 358 K, the triosmium clusters began to undergo decarbonylation, and at approximately 398 K the triosmium clusters had lost enough CO ligands to become sufficiently coordinatively unsaturated to allow migration and reaction with Ru atoms of neighboring species". Overall, this is another important system, developed by the Gates group, that merits additional kinetic and mechanistic studies en route to fully understanding bimetallic nanoparticle formation from well-defined, supported-organometallic complexes, metal carbonyl clusters in this latter case.

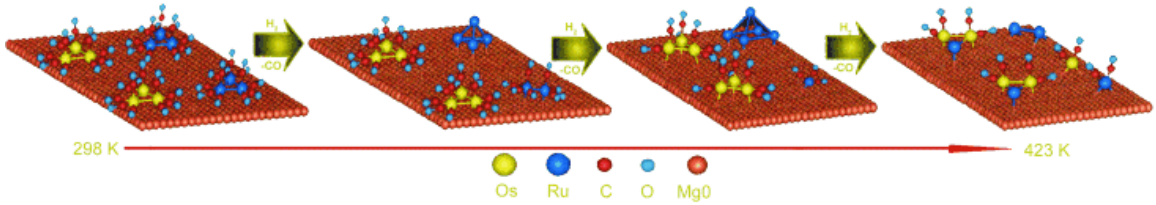

Scheme 11. Gates' and co-workers' proposed pictorial model for bimetallic $(Ru_xOs_y)_n$/MgO cluster formation from $[Ru_3(CO)_{12}]$ and $[Os_3(CO)_{11}]^{2-}$ supported on MgO under H_2 (and a temperature ramp from 298 to 423 K) [64]. In this scheme, the yellow spheres are O, the dark blue spheres Ru, the red spheres C, the light blue spheres O and the orange spheres are the MgO support. Copyright (2009) Wiley-VCH Verlag GmbH & Co. KGaA. Reproduced with permission from [45].

Finishing with very recent work, in 2010 Nassreddine et al. studied the formation of 1.2 nm $Ir(0)_n$ nanoparticles supported on amorphous silica alumina (ASA) from a $Ir(acac)_3$/ASA precursor under H_2 [67]. The formation of $Ir(0)_n$/ASA was followed by in situ XRD from 0 to 700 °C. The authors found that the $Ir(0)_n$/ASA particle size grows gradually from 0 to 300 °C and then slows down and remains constant at 1.2 nm above 500 °C. However, considering that the $Ir(0)_n$ particles can not be detected until 200 °C, it is not clear if the particle size truly increases linearly below 200 °C. No mechanism was proposed for the formation of the $Ir(0)_n$/ASA product.

2.2.3. Conclusions

The eight $M(NH_3)_4^{2+}$ ($M = Pt^{2+}$, Pd^{2+}) case studies reveal that $M(0)_n$, M^{x+} or $(M_xO_y)_n$ species can form on the support during the precatalyst preparation steps and that those (different) species can have different kinetics of supported-nanoparticle formation [50,58,62,63]—results that reiterate the importance of precisely controlling the precatalyst speciation, ideally in *all* future syntheses of heterogeneous catalysis. While kinetic studies are in hand for the $M(NH_3)_4^{2+}$/support systems, no rigorous chemical-reaction-based mechanisms have been proposed for the formation of the resultant $M(0)_n$ supported-nanoparticle products. Dalla Betta and Boudart [29], as well as Koningsberger and co-workers [47], have suggested that a neutral "$Pt(NH_3)_2H_2$" intermediate is responsible for the formation of $Pt(0)_n$ nanoparticles supported on zeolite–Y and SiO_2, although, no compelling—and certainly no direct—evidence for that putative Pt–H intermediate exists at present. Hence, further studies attempting to detect "$Pt(NH_3)_2H_2$" are hereby identified as an important, future research goal. Okumura and co-workers demonstrated that the $Pd(0)_{\sim 13}$/H–USY supported-nanoparticle formation kinetics from Pd^{2+}/H–USY are first order in Pd^{2+} and Pd–Pd (i.e., $-d[Pd^{2+}]/dt \propto [Pd^{2+}]^1[Pd–Pd]^1$) [62,63]; three deliberately minimal mechanisms have been suggested herein (and were shown back in Scheme 4), mechanisms that can account for the observed kinetic data and which employ the aforementioned, putative Pd–H intermediate. The fact that the kinetics are separately first-order in both Pd^{2+} and Pd–Pd, and not bimolecular in any Pd species (e.g., $-d[Pd^{2+}]/dt = k_{obs}[Pd^{2+}]$, but not $-d[Pd^{2+}]/dt = k_{obs}[Pd^{2+}][Pd–Pd]$), demands that some of the supported-nanoparticle formation steps occur post the rate-determining step and are, therefore, kinetically hidden. Hence, conditions that unmask those later steps are an additional important goal for future research.

Inspection of the five H_2PtCl_6 case studies reveals that the known speciation of H_2PtCl_6 in aqueous solution, as well as in the presence of metal-oxide supports [162-166], has been largely ignored in the extant kinetic and mechanistic literature of $Pt(0)_n$ supported-nanoparticle formation from the classic H_2PtCl_6 precursor. Chupas and co-workers demonstrated zero-order kinetics (i.e., $[H_2PtCl_6]^0$) for the H_2PtCl_6/TiO_2 to $Pt(0)_n/TiO_2$ system [56]. Two mechanisms, which can account for the observed zero-order H_2PtCl_6/TiO_2 kinetics, as well as the $Pt(0)_n/TiO_2$ supported-nanoparticle products, were shown back in Scheme 5. The observation that the kinetic data are zero-order in H_2PtCl_6/TiO_2, and not bimolecular in any supported Pt species, but still yield a Pt–Pt bonded, $Pt(0)_n/TiO_2$ product suggests that the nanoparticle formation steps are kinetically hidden. Hence, hereby identified as important steps in advancing our understanding of the formation of supported-nanoparticle catalysts, from the classic H_2PtCl_6 precatalyst (and once the speciation issues with this precatalyst are resolved first), are: continuing to write out specific balanced reactions corresponding to the proposed mechanistic steps, being sure those reaction steps add up to the observed, experimentally demonstrated reaction stoichiometry, and then executing the needed kinetic studies that unmask the desired supported-nanoparticle formation steps from any diffusion-limited processes present.

The five $Ag(NO_3)$ case studies contain, by far, the most-detailed chemical-reaction-based mechanisms to date for supported-nanoparticle formation at the gas-solid interface. Importantly, Jacobs and co-workers were able to rigorously demonstrate the supported-nanoparticle formation stoichiometry by using H_2 uptake measurements [32,33,37]. In addition, the classic studies of Jacobs and co-workers focused on the reduction step for those Ag^+/zeolite based systems. The accompanying kinetic studies reveal that the supported-nanoparticle formation steps are again masked by diffusion of H• and Ag^+ towards each other. Three different chemical-reaction-based mechanisms,

Schemes 6 and 8, were proposed for the formation of Ag(0) or Ag_n^{x+} species [32,33,37]. Hence, future studies that unmask those important supported-nanoparticle formation steps are highly desirable. *The insight that diffusion-limited processes are common in the mechanisms of supported-nanoparticle formation reactions at the gas-solid interface is important*. It means that consideration of diffusion-limitations needs to be undertaken in the design of future kinetic and mechanistic studies of supported-nanoparticle formation reactions at the gas-solid interface.

The seven kinetic and mechanistic studies starting from supported-organometallic precursors demonstrate that well-defined, speciation-controlled precatalysts can be and have been synthesized. Additional benefits when starting from well-defined, speciation-controlled, supported organometallics include: (i) the presence of organic ligands, which offer additional handles such as IR spectroscopy for following kinetics, and in favorable cases, (ii) systems which have precedented solution-based chemistry that can yield otherwise unobtainable insights. Unfortunately, to date no rigorous kinetic and mechanistic studies, starting from well-defined supported organometallic complexes, have been reported. However, many of the supported organometallic systems, in particular Gates and co-workers $M(C_2H_4)_2$/zeolite (M = Ir, Rh) systems [60,61], are prime systems for the desired kinetic and mechanistic studies.

In short, the above case studies of the $M(NH_3)_4^{2+}$ ($M = Pt^{2+}$, Pd^{2+}), H_2PtCl_6, $Ag(NO)_3$ and supported-organometallic systems makes apparent that a good foundation of work exists upon which to build. However, much remains to be done. Recommended focal points include: (i) controlling the precatalyst speciation, ideally to one supported species; (ii) determining experimentally the complete, balanced supported-nanoparticle formation stoichiometry, including trace products where possible; (iii) ensuring that diffusion is not masking the desired supported-nanoparticle formation kinetics if at all possible; (iv) writing chemical-reaction-based mechanisms,[9] rather than the word- and picture-based

schemes or cartoons as currently dominate the supported-nanoparticle formation literature, so that those mechanisms can be tested kinetically and then (v) disproving multiple alternative mechanisms/hypotheses[12] rather than asserting a single mechanism emphasizing the author's preferences/beliefs.

There is also arguably a need to bridge the practical gas-solid mechanistic systems discussed herein with the cleaner, better-studied, UHV counterparts where available, assuming their associated temperature, pressure and materials gaps [76-79] can be bridged/overcome. The eventual goal is to have a uniform, cohesive mechanistic picture of heterogeneous catalyst formation, and their resultant catalysis, a picture that spans the knowledge available from UHV to that from practical supported-nanoparticle science to what is known in organic, organometallic and inorganic chemistry. The goal of that merging of existing areas of knowledge is to yield insights sufficient to drive the synthesis of the next generation of composition-, size- and shape-controlled supported-nanoparticle catalysts. This includes heterogeneous catalysts synthesized in contact with solution, as discussed next.

3. Studies of Supported-Nanoparticles at the Gas-Liquid-Solid Interface

Recent advances in solution-based nanoparticle syntheses [134,215,216,217,218,219,220,221,222,223] have resulted in vastly improved control over the resultant nanoparticle composition [224,225,226,227,228,229,230], size [156,231] and shape [232,233,234,235]. A number of mechanistic insights have also been obtained [114,193-194,236,237,238,239,240], in no small part due to the greater ease of full product, balanced stoichiometry, and kinetic and mechanistic studies for solution reactions vs. those in the solid-state. Indeed, what follows makes a strong case that the synthetic and mechanistic insights available from a relative short period of solution nanoparticle syntheses are all ready comparable to those generated from all the aforementioned studies at the gas-solid interface. Hence, an important goal in modern

heterogeneous catalysis is to transfer the synthetic and mechanistic insights from the modern revolution in nanoparticle synthesis and mechanistic study *in solution*, to the synthesis of supported-nanoparticle *heterogeneous catalysts*.

3.1. Fundamental Background Information Regarding Supported-Nanoparticle Heterogeneous Catalyst Formation at the Gas-Liquid-Solid Interface

Before reviewing the kinetic and mechanistic studies of supported-nanoparticle heterogeneous catalyst formation in contact with solution—that is at the gas-liquid-solid interface—it will prove useful to describe, first and briefly, the synthetic methods for preparing supported-nanoparticles at the liquid-solid and gas-liquid-solid interfaces. The physical methods for following the kinetics of those reactions will also be briefly summarized to start, all as an aid to the reader in understanding what follows.

3.1.1. Emerging Synthetic Strategies Based on the Solution Nanoparticle Literature

Two limiting routes have emerged using solution-prepared transition metal nanoparticles en route to supported-nanoparticle heterogeneous catalysts, Scheme 12. The first method attempts to take advantage of the nanoparticle communities' ability to make stabilized transition-metal nanoparticles in solution (often with polymer or other ligands that are required to prevent nanoparticle aggregation [215-223]). Those stabilized nanoparticles are then typically isolated, redispersed and subsequently deposited onto a support [241,242,243,244,245,246,247,248]. Unfortunately however, *the polymer or other bulky, often massive stabilizers are unavoidably co-deposited*. Complete removal of the stabilizing polymer or other ligands—as is required for the most coordinatively unsaturated and, hence facile catalysts [249]—has proven difficult to impossible [247,248,250,251,252,253,254,255,256,257,258,259,260,261,262]. Extensive treatments such as thermal activation in N_2, H_2 and O_2 environments [250-252], UV/ozone [253-256], O_2/plasma [256] and even neutron sputtering [257] have been largely unsuccessful in completely removing all the polymeric or other organic ligand

"debris". The resultant, partially poisoned, supported-nanoparticles are then, and in turn, also rendered compositionally ill defined. The supported-nanoparticle's size and shape can also be altered by the harsh thermal, oxidative, reductive or other treatments attempting to fully remove the poisoning ligands or polymers [250-262].

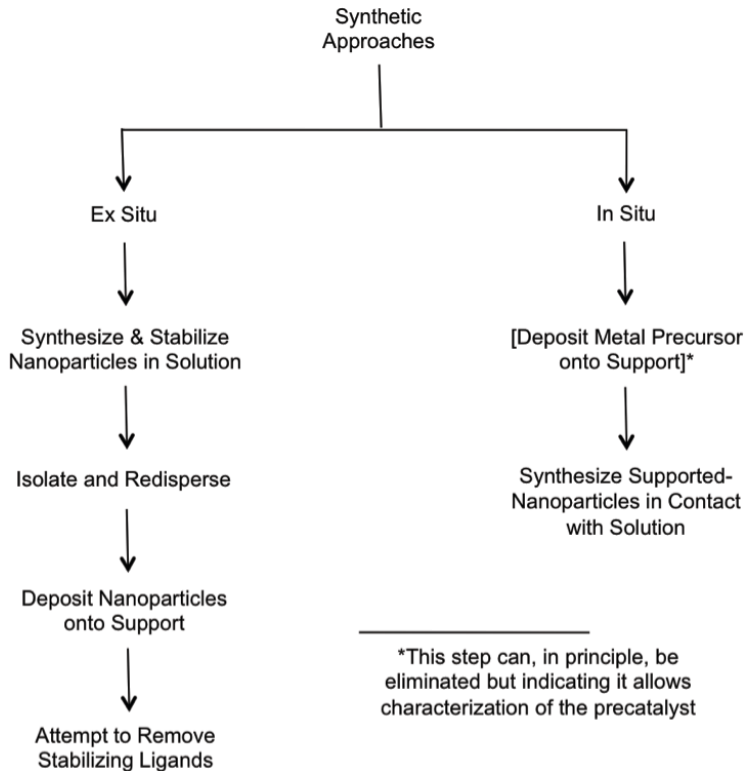

Scheme 12. Two emerging, limiting synthetic approaches for the preparation of supported-nanoparticle heterogeneous catalysts based on nanoparticle solution syntheses.

A second, arguably more attractive synthetic approach—one now attracting increasing attention [263,264,265,266,267,268,269,270,271,272,273,274,275,276,277]—is to start from supported molecular precursors and then synthesize the supported-nanoparticles in situ, that is, *in contact with solution,* ideally with only the desired catalytic reaction substrates or other desired ligands present during the synthesis in order to lead to what has been termed "weakly ligated/labile ligand nanoparticles"

[104,223,278,279].[19] In principle, this in situ method can provide good control over the supported-nanoparticle composition, size and shape since one can readily add desired solvents, ligands or other additives at will during the synthesis—assuming that a careful, preferred selection of ligands and solvents can be achieved en route to composition controlled, non-ligand-poisoned, "weakly ligated/labile ligand" [104,223,279] supported-nanoparticles.

3.1.2. Characterization Methods for Following the Kinetics of Supported-Nanoparticle Heterogeneous Catalyst Formation at the Gas-Liquid-Solid Interface

In principle, each of the physical methods capable of following the kinetics of supported-nanoparticle formation at the gas-solid interface (Table 1) could also be utilized at the gas-liquid-solid interface. Despite this, no direct, operando (or in situ) methods have yet been utilized to follow the kinetics of supported-nanoparticle formation at the gas-liquid-solid interface; to date, only H_2 uptake and ex situ TEM and AFM have been utilized for following the kinetics of supported-nanoparticle formation.

3.1.3. Conclusions

The synthesis of supported-nanoparticles at the gas-liquid-solid interface is attractive since it has the potential to allow the synthetic and mechanistic insights, from the modern revolution in nanoparticle syntheses in solution (including control over the nanoparticle size, shape and composition), to be transferable to the synthesis of supported-nanoparticles, at least in principle. Moreover, many of the physical methods listed back in Table 1 should be applicable to studies of the gas-liquid-solid interface. However, to date the use of direct, operando (or in situ) techniques to follow supported-

[19] "Weakly ligated/labile ligand" nanoparticles are simply nanoparticles where only weakly coordinated ligands plus the desired reactants are present [104]. Related topics, which we have addressed elsewhere include "putative cation-only stabilized nanoparticles" [223] and "putative solvent-only stabilized nanoparticles" [279], neither of which appear to actually exist [104,223,279].

nanoparticle formation kinetics at the gas-liquid-solid interface have not been reported, so that providing such operando studies is an obvious, needed area of future research.

3.2. Kinetic and Mechanistic Studies at the Gas-Liquid-Solid Interface

3.2.1. Brief Overview of the Primary Literature at the Gas-Liquid-Solid Interface

Table 3 is a compilation of the eight available studies striving to understand the mechanisms of supported-nanoparticle heterogeneous catalyst formation at the gas-liquid-solid interface. Table 3 details: (i) the experimental preparation and nanoparticle formation conditions; (ii) whether the study contains kinetic data and, if so, by which method(s) those data were obtained; (iii) whether the stoichiometry of the supported-nanoparticle formation reaction was obtained, and is so how; and finally (iv) the proposed mechanism and rate equations as given by the original authors, if available.

As with Table 2, a brief inspection of Table 3 is quite informative and reveals several global insights into the state of mechanistic knowledge for supported-nanoparticle heterogeneous catalyst formation at the gas-liquid-solid interface. First, there are only 8 studies at the gas-liquid-solid interface (versus the 39 at the gas-solid interface) demonstrating that the gas-solid interface has been studied almost 5 times more frequently to date. In 7 of the 8 studies kinetic data has been collected, but as already noted no study has used a direct method that is also at least in situ. However, in 3 of the 8 cases a supported-nanoparticle heterogeneous catalyst formation stoichiometry has been explicitly demonstrated, kinetic data collected and a chemical-reaction-based mechanism proposed that is both consistent with that kinetic data and where one or more alternative mechanistic pathways has been disproved.[12] Finally, the first gas-liquid-solid study in Table 3 was reported in 2004, two of the studies in 2006, with the remaining 5 studies of the 8 total from the period 2009–2011. Clearly the study of supported-nanoparticle formation, in contact with solution is a much younger, still wide-open area of investigation.

Table 3. The kinetic and mechanistic studies of supported-nanoparticle heterogeneous catalyst formation at the gas-liquid-solid interface.

Entry [Reference]	*Authors*	*System of Study*	*Kinetic Data (Physical Method)*	*Stoichiometry (Physical Method)*	*Proposed Mechanism(s) and Rate Equations as Written by the Original Authors (If Available)*
1 [68]	Singh, A.; Luening, K.; Brennan, S.; Homma, T.; Kubo, N.; Pianetta, P.	Si wafers were dipped into a Cu-2% nitric acid matrix.	Yes (AFM)	No	*Proposed Mechanism.* The authors believe that the Cu grows via an Ostwald-ripening mechanism.
2 [69]	Wang, Y.; Xu, X.; Tian, Z.; Zong, Y.; Cheng, H.; Lin, C.	50-wt% H_2PtCl_6, ethylene glycol (as the solvent and reducing agent), carbon nanotubes (CNTs), and sodium dodecyl sulfate (SDS) were mixed together and sonicated, and then heated and stirred.	No	No	*Proposed Mechanism.* "Salt effects increase the barrier towards homogeneous nucleation, such that heterogeneous nucleation becomes more favorable. Once the critical nucleus size is attained, autocatalytic growth of the particle rapidly depletes the Pt-monomer concentration in solutions, thereby effectively depressing homogeneous nucleation", that is pathway 2B in Scheme 13 in this review.
3 [70]	Marre, S.; Cansell, F.; Aymonier, C.	$Cu(hfac)_2•H_2O$ was mixed with SiO_2 spheres, in isopropyl alcohol, CO_2 and H_2 and brought to supercritical conditions.	Yes (Ex Situ TEM)	No	*Proposed Mechanism.* The author's (word-based) mechanism consists of (i) homogenous decomposition to Cu nuclei, which are then (ii) deposited onto the SiO_2 surface, followed by (iii) direct growth of the nuclei on the SiO_2 surface.
4	Marre, S.;	$Cu(hfac)_2•H_2O$	Yes	No	*Proposed Mechanism.* The authors suggest a

[71]	Erriguible, A.; Perdomo, A.; Cansell, F.; Marias, F.; Aymonier, C.	reduced in situ with SiO_2 spheres.	(Ex Situ TEM)		mechanism consisting of homogeneous nucleation followed by heterogeneous growth, as depicted in Scheme 14 in this review.
5 [72]	Mondloch, J. E.; Yan, X.; Finke, R. G.	1.96-wt% H_2PtCl_6 was slurried with either γ-Al_2O_3 or TiO_2 in a solution of ethyl acetate. The solution was taken to dryness under vacuum. The precatalyst was reduced in EtOH plus cyclohexene under 40 psig of H_2 at 22 °C.	Yes (H_2 uptake—Cyclohexene reporter reaction [a])	Yes ($pH_{apparent}$ measurements)	*Proposed Mechanism* $A \xrightarrow{k_1} B$ (Nucleation) $\quad n\,Pt^{IV} \xrightarrow{H_2} Pt(0)_n$ $A + B \xrightarrow{k_2} 2B$ (Autocatalytic Surface Growth) $\quad Pt^{IV} + Pt(0)_n \xrightarrow{H_2} Pt(0)_{n+1}$ where A is the supported precatalyst H_2PtCl_6/Al_2O_3 and B is the growing $Pt(0)_n$ nanoparticle surface *Integrated Rate Equation* $[A]_t = \frac{\frac{k_1}{k_2} + [A]_0}{1 + \frac{k_1}{k_2[A]_0} * \exp^{(k_1 + k_2[A]_0)t}}$
6 [73]	Rossi, L. M.; Nangoi, I. M; Costa, N. J. S.	Between 1.34 to 1.76-wt% $Pd(acetate)_2$ was slurried onto ligand-modified SiO_2 spheres (e.g., modified with (3-aminopropyl)triethoxy-silane) from toluene. The sample was washed with ethanol and acetone and dried	Yes (H_2 uptake—Cyclohexene reporter reaction [b])	No	No mechanism was proposed by the authors; however, they did note that “additional experiments and control arrangements are in progress in order to elucidate the mechanism of supported-nanoparticle formation”.

		under vacuum. The precatalyst was placed in toluene and reduced under H_2 (6 atm) at 75 °C.			
7 [74]	Mondloch, J. E.; Finke, R. G.	$[Ir(1,5\text{-COD})Cl]_2$ was slurried with γ-Al_2O_3 in ethyl acetate and taken to dryness under vacuum. The Ir(1,5-COD)Cl/γ-Al_2O_3 precatalyst was reduced under H_2 in acetone at 22 °C.	Yes (H_2 uptake—cyclohexene reporter reaction [a])	Yes (H_2 uptake, cyclooctane evolution)	*Proposed Mechanism* 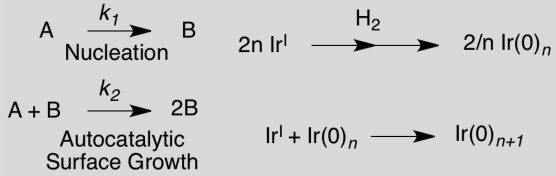 where A is the supported precatalyst Ir(1,5-COD)Cl/γ-Al_2O_3 and B is the growing $Ir(0)_n$ nanoparticle surface. *Integrated Rate Equation* $$[A]_t = \frac{\frac{k_1}{k_2} + [A]_0}{1 + \frac{k_1}{k_2[A]_0} * \exp^{(k_1 + k_2[A]_0)t}}$$
8 [75]	Mondloch, J. E.; Finke, R. G.	$[Ir(1,5\text{-COD})Cl]_2$ was slurried with γ-Al_2O_3 in ethyl acetate and taken to dryness under vacuum. The Ir(1,5-COD)Cl/γ-Al_2O_3 precatalyst was reduced under H_2 in acetone (and acetone plus cyclohexane) at 22 °C.	Yes (H_2 uptake—cyclohexene reporter reaction [a])	Yes (H_2 uptake, cyclooctane evolution)	*Proposed Mechanism* [c]

$$Ir^{I}/Al_2O_3 + solvent \overset{K_{Diss}}{\rightleftharpoons} Ir^{I}{*}solvent + Al_2O_3$$

$$Ir^{I}{*}solvent \xrightarrow[2.5\ H_2]{k_1'} Ir(0)_{soln} + solvent$$

$$Ir^{I}/Al_2O_3 + solvent \overset{K_{Diss}}{\rightleftharpoons} Ir^{I}{*}solvent + Al_2O_3$$

$$Ir(0)_{soln} + Al_2O_3 \xrightarrow{Fast} Ir(0)/Al_2O_3$$

$$Ir^{I}{*}solvent + Ir(0)/Al_2O_3 \xrightarrow[2.5\ H_2]{k_2''} 2\,[Ir(0)/Al_2O_3] + solvent$$

$$\text{SUM: } [Ir^{I}/Al_2O_3]_{sus} \xrightarrow[2.5\ H_2]{k_{obs}''} [Ir(0)/Al_2O_3]_{sus}$$

where Ir^{I}/Al_2O_3 is Ir(1,5-COD)Cl/γ-Al_2O_3, solvent is acetone and $Ir^{I}{*}$solvent is Ir(1,5-COD)Cl(solvent) and the rate and equilibrium constants are defined in Scheme 17 in this review.

Integrated Rate Equation [d]

$$[A]_t = \frac{\frac{k_1}{k_2} + [A]_0}{1 + \frac{k_1}{k_2[A]_0} * \exp^{(k_1 + k_2[A]_0)t}}$$

where k_{1obs} and k_{2obs} are given by

$$k_{1obs} = \frac{k_1' K_{Diss}[solvent]_t}{[Al_2O_3]_{sus,t} + K_{Diss}[solvent]_t}$$

$$k_{2obs} = \frac{k_2'' K_{Diss}[solvent]_t}{[Al_2O_3]_{sus,t} + K_{Diss}[solvent]_t}$$

[a] The appropriate [cyclohexene]^0 control reaction was demonstrated to ensure that the reporter reaction was functioning properly. [b] The appropriate [cyclohexene]^0 control reaction was not demonstrated to ensure that the reporter reaction was functioning properly. [c] This mechanism applies only rigorously to the supported-

nanoparticle formation reactions carried out in acetone. A slightly modified mechanism (with, however, the same general form) accounts for the mixed solvent case of acetone plus cyclohexane [75]. [d] These rate equations only apply rigorously to the supported-nanoparticle formation reactions carried out in acetone. Slightly modified rate equations (with, however, the same general form) were provided to account for the mixed solvent case of acetone plus cyclohexane [75].

3.2.2. Kinetic and Mechanistic Case Studies

3.2.2.1. Wang et al.'s Study of the Formation of Pt(0)$_n$ on Carbon Nanotubes

In 2006 Wang et al. studied the formation of Pt(0)$_n$ on carbon nanotubes (CNTs) from a mixture of H_2PtCl_6 in ethylene glycol, sodium dodecyl sulfate (SDS) and CNTs [69] (Table 3, Entry 2). The authors were able to control the Pt(0)$_n$/CNT nanoparticle size over a range of 2.3 to 9.6 nm (with 12 to 44% dispersities) by varying the concentration of H_2PtCl_6, the temperature and the reducing agent. It is likely that the use of the organic solvent helps minimize the H_2PtCl_6 speciation and allows the formation of the near-monodisperse (i.e., ≤ ±15% [215]) 2.3 ± 0.3 Pt(0)$_n$/CNT catalyst—although the precise speciation of the H_2PtCl_6 precatalyst is once again an issue. Wang et al. proposed a mechanism of supported-nanoparticle heterogeneous catalyst formation consisting of "…heterogeneous nucleation (which becomes favorable) once the critical nucleus size is attained, autocatalytic growth of the particle rapidly depletes the Pt-monomer concentration in solution, thereby effectively depressing homogeneous nucleation", as summarized pictorially in Scheme 13.

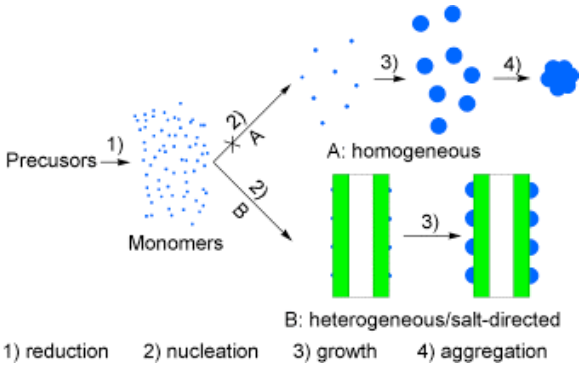

Scheme 13. Pictorial mechanisms proposed by Wang et al. [69] for the formation of Pt(0)$_n$/CNT in contact with solution. The authors favor the bottom pathway consisting of heterogeneous nucleation and growth a pathway that is, however, not supported by the one available kinetic study (of a different, Ir-based system [75]). Copyright (2006) Wiley-VCH Verlag GmbH & Co. KGaA. Reproduced with permission.

Unfortunately, the needed kinetic studies were not performed to support or refute the authors' proposed mechanistic hypothesis. In the one case where solid-support-based (i.e., heterogeneous) nucleation vs. solution (i.e., homogeneous) nucleation has been kinetically tested [75], *homogeneous* nucleation was observed, Scheme 17 (vide infra), not the heterogeneous nucleation proposed in Scheme 13. Hence, at present and until the needed kinetic studies are done, Scheme 13 must be considered as a proposed, but kinetically unverified, picture-based mechanism.

3.2.2.2 Marre at al.'s Studies of the Formation of $Cu(0)_n$ on SiO_2 Spheres

In 2006 and then in 2009, Marre et al. studied the formation of $Cu(0)_n/(SiO_2)_n$ (where $(SiO_2)_n$ are silica spheres) starting from $Cu(hfac)_2$ (where hfac = hexafluoroacetylacetonate) in supercritical CO_2/alcohol/H_2 mixtures [70,71], Entries 3 and 4, Table 3. Ex situ TEM kinetic data were collected, monitoring the change in size of the $Cu(0)_n/(SiO_2)_n$ product with time. The authors proposed a model, Scheme 14, for the formation of $Cu(0)_n/(SiO_2)_n$ that accounts for the generation of nuclei due to precursor decomposition (i.e., "mode (1)" in Scheme 14), and then particle growth by coagulation and coalescence (i.e., "mode (2)" in Scheme 14), that is "homogeneous nucleation followed by heterogeneous growth", to quote the authors [71]. The authors claim that "The model allows the description of the particle size evolution by the variation of four variables: the nuclei volume concentration of mode 1 N_1, the particle volume concentration of mode 2 N_2, the volumetric concentration of the aggregates V_2, and the particle surface area concentration of mode 2 A_2". However and unfortunately, the proposed model was not fit to the observed experimental $Cu(0)_n$ diameter vs. residence time data (as it contains four parameters and only 3 data points were collected), see Figure 11 in reference [71]. Hence and while valuable initial work identifying a good system for more detailed study, several issues become apparent from a critical look at this system [70,71], vide infra.

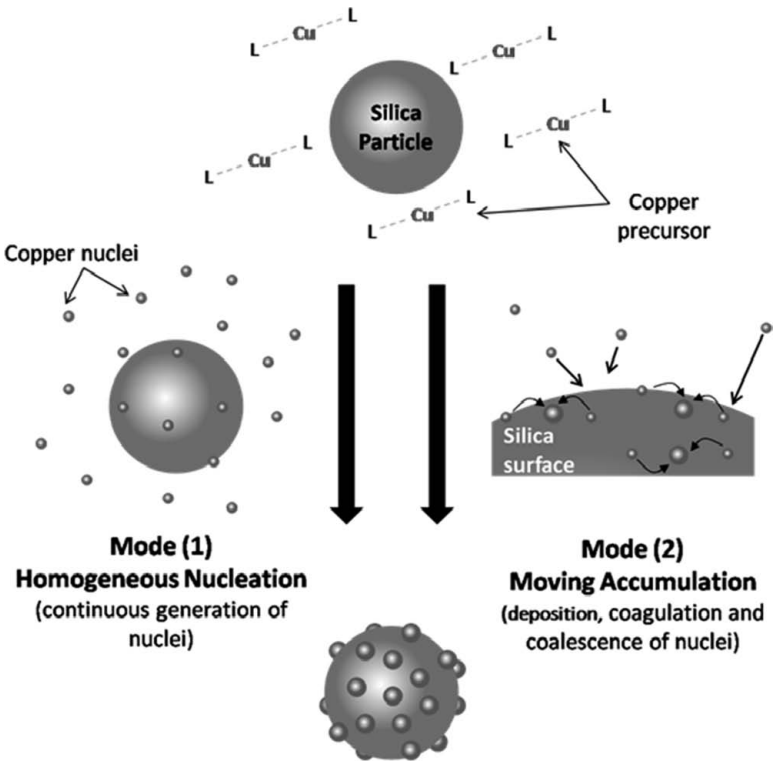

Scheme 14. A pictorial mechanism proposed by Marre et al. for the formation of $Cu(0)_n$ on SiO_2 spheres [71]. Reprinted with permission from [71]. Copyright (2009) American Chemical Society.

To start, the model, originally developed by Choi and co-workers for the formation of aerosols [280], was used, one which assumes a monodisperse particle size distribution. However, the -$(SiO2)_n$-supported $Cu(0)_n$ nanoparticles are not monodisperse; instead they show a size dispersion ranging from 29-55% based on the average and standard deviation of the diameters given in reference [71]. Second and perhaps most importantly (as examples elsewhere further detail [281,282][9]), an insidious disconnect exists here as it does with all other picture- or word-only based mechanisms: the words used have (a) no connection to balanced equations that rigorously and correctly *define* those words, and (b) *connects them to the differential equation and hence to the measured kinetic data.* Those predicted differential (kinetic) equations are, of course, essential for testing and thereby supporting, or refuting, the proposed mechanistic

equations and *hence their associated words and pictures*. A look at the complex, confused literature of solid-state kinetics, where such disconnects between the words/concepts and the differential equations/kinetics is at present rampant, will convince the skeptical reader that such disconnects are a very serious, insidious problem indeed [138-141,281], one future work must strive to avoid.

3.2.2.3 Mondloch, Finke and Co-Workers Studies of the Formation of $Pt(0)_n$ on γ-Al_2O_3 and TiO_2

In 2009, Mondloch, Finke and co-workers recently studied the formation of $Pt(0)_n$/γ-Al_2O_3 starting from 1.96-wt% H_2PtCl_6/γ-Al_2O_3 in EtOH (and cyclohexene) under H_2 [72], Table 3, Entry 5. The stoichiometry of the supported-nanoparticle formation, Scheme 15 (top reaction), was confirmed via $pH_{apparent}$ measurements of the reaction solution post the supported-nanoparticle formation reaction (i.e., and in comparison to a sample containing 6 equivalents of authentic HCl plus the appropriate amount of γ-Al_2O_3). Those experiments yielded an identical pH within experimental error [72], thereby verifying the 6 HCl part of the stoichiometry in the top line of Scheme 15.

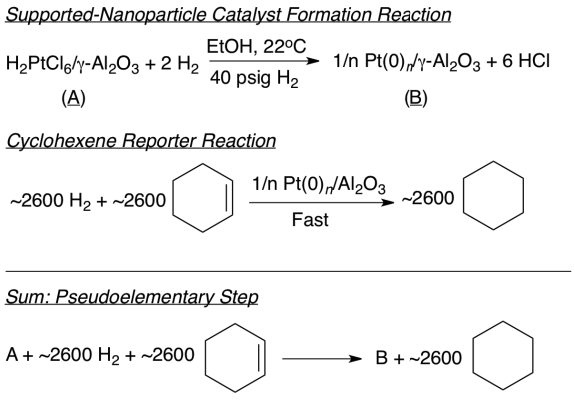

Scheme 15. The H_2PtCl_6/γ-Al_2O_3 to $Pt(0)_n$/γ-Al_2O_3 supported-nanoparticle formation reaction stoichiometry, cyclohexene reporter reaction and associated sum/pseudoelementary step [72].

The kinetics of the $Pt(0)_n/\gamma\text{-}Al_2O_3$ supported-nanoparticle formation reaction (Figure 8, black diamonds), were well-fit to a 2-step mechanism (Figure 8, red line) consisting of slow continuous nucleation (A → B, rate constant k_1), followed by fast autocatalytic surface growth (A + B → 2B, rate constant k_2), a mechanism originally discovered for solution nanoparticle formation in 1997 by Finke and Watzky [193], Figure 8 (right). In these equations and Figure 8 A is $H_2PtCl_6/\gamma\text{-}Al_2O_3$ and B is $Pt(0)_n/\gamma\text{-}Al_2O_3$. The 2-step

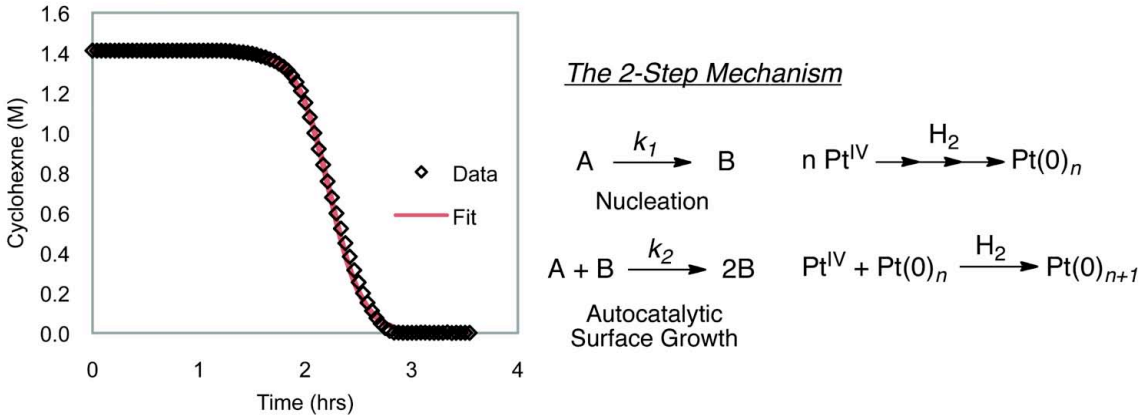

Figure 8. $H_2PtCl_6/\gamma\text{-}Al_2O_3$ to $Pt(0)_n/\gamma\text{-}Al_2O_3$ supported-nanoparticle formation kinetics (black diamonds) in contact with EtOH, cyclohexene and H_2 (shown left) and fit to the 2-step mechanism (red line). Shown to the right is the 2-step mechanism used to fit the observed kinetic data [72]. Reprinted with permission from [72]. Copyright (2009) American Chemical Society.

mechanism is a minimal, "Ockham's razor" [283], mechanism that has been widely used to extract *average* nucleation (k_1) and *average* autocatalytic surface growth (k_2) rate constants using the integrated analytical equation (shown in entry 5 of Table 3) corresponding to the 2-step mechanism. Average rate constants for nucleation ($k_1 \approx 10^{-5.5(7)}$ h^{-1}) and autocatalytic surface growth ($k_2 = 1.2(2) \times 10^4$ h^{-1} M^{-1}) were obtained so long as a prestirring/pre-equilibration period of 2–7 h was employed when starting from the $H_2PtCl_6/\gamma\text{-}Al_2O_3$ precatalyst in contact with EtOH—very likely an equilibration period needed to control/minimize the "H_2PtCl_6"/$\gamma\text{-}Al_2O_3$ speciation. Without this

preequilibration period the observed nucleation rate constant, k_1, *varies by a range of ~10^5*, as reflected in the varyied supported-nanoparticle formation curves shown in Figure 9. Although the detailed reason(s) for the interesting ~10^5 range in k_1 remain to be established, one very plausible hypothesis is that just noted: that a variable H_2PtCl_6 speciation, for the impregnation of H_2PtCl_6 onto metal oxides (recall section 2.2.2.2), is responsible for the ~10^5 range in the rate constant for nucleation of the supported $Pt(0)_n$ nanoparticle synthesis when in contact with EtOH solvent. Noteworthy here is that ~10^5 variation in k_1 directly causes a significant variation in the particle size (i.e., and in the size distribution) since k_1, k_2 and the starting $[H_2PtCl_6]_{initial}$ are three key factors in the equation governing nanoparticle size published for the 2-step mechanism [156].

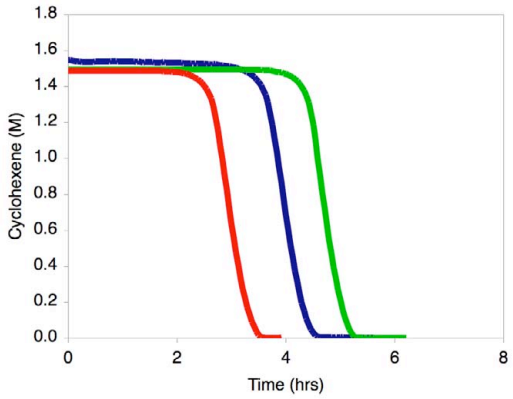

Figure 9. Observed variation in the kinetics of the $Pt(0)_n/\gamma\text{-}Al_2O_3$ supported-nanoparticle heterogeneous catalyst formation system if a pre-equilibrium stirring period (in the EtOH reaction medium) is not employed. The resultant k_1 nucleation rate constant for these curves varies from ~10^{-8}–10^{-13} h^{-1}, that is by a range of ~10^5 [72]. Reprinted with permission from [72]. Copyright (2009) American Chemical Society.

In order to fully appreciate how the $Pt(0)_n/\gamma\text{-}Al_2O_3$ supported-nanoparticle formation kinetic data were collected (e.g. Figure 8), it is necessary to understand the indirect—but rapid, quantitative, and now well-precedented [193,190-192]—cyclohexene hydrogenation reporter reaction method. Experimentally, the supported-nanoparticle

formation reaction is monitored by following the loss of H_2 pressure via a high pressure (± 0.01 psig) computer-interfaced pressure transducer, which is then converted into cyclohexene loss via the experimentally verified (by ^{1}H NMR) [193] 1:1 H_2:cyclohexene stoichiometry. The cyclohexene reporter reaction (Scheme 15, middle reaction) takes advantage of the fact that the catalytic activity of the nanoparticle surface is proportional to the concentration of the active metal, B [193]. The sum/pseudo-elementary step [284,285,286][20] is given in Scheme 15 (bottom reaction), so that the overall reaction stoichiometry is then given by -d[A]/dt/1 = -d[H_2]/dt/2600 = -d[cyclohexene]/dt/2600 = +d[B]/dt/1 = + d[cyclohexane]/dt/2600. The power of the pseudoelementary step is that it allows one to measure the loss of H_2 or cyclohexene (or formation of cyclohexane) and relate that to the loss of A (or formation of B) by the above equation, for example -d[A]/dt/1 = -d[H_2]/dt/2600. An important point is that the use of the cyclohexene reporter reaction demands that the hydrogenation of cyclohexene be fast in comparison to the nanoparticle formation steps. This assumption is easily experimentally tested by changing the concentration of cyclohexene and plotting it vs. the H_2 uptake rate; the H_2 uptake rate should reach a regime where its a constant with increasing cyclohexene concentrations (i.e., should reach a limiting zero-order dependence on cyclohexene, [cyclohexene]^0), as observed in Figure 10, thereby verifying that cyclohexene reporter reaction is fast relative to the slower steps that one wants to measure kinetically (i.e., A $\rightarrow$ B and A + B $\rightarrow$ 2B in the present example). In short, by following the loss of H_2 (or equivalently the loss of cyclohexene), and as long as the cyclohexene reduction reaction is fast relative to the supported-nanoparticle formation reaction, one can measure the

[20] A pseudoelementary step is the summation of one or more, slow elementary kinetic steps, to which one can add one or more fast steps, the overall (summed) pseudoelementary step by definition being establishable by determining the overall reaction stoichiometry. Noyes formally introduced the concept of the pseudoelementary step in the 1970s when studying complex oscillating reactions [284-286], although kineticists have used it and been aware of it probably long before Noyes' important labeling of the pseudoelementary step concept.

desired supported-nanoparticle nucleation, A → B, and autocatalytic growth, A + B → 2B, steps, all while employing the pseudoelementary-step stoichiometric relationships.

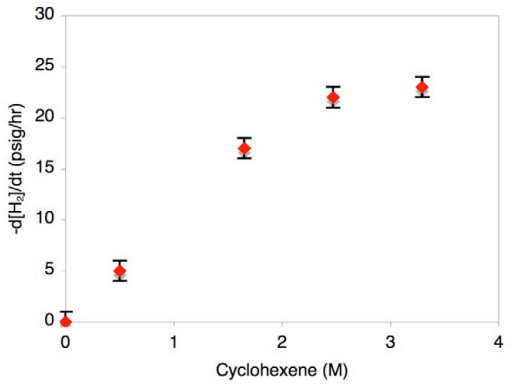

Figure 10. A plot of the H_2 uptake rate (-d[H_2]/dt extracted from the linear portion of the supported-nanoparticle formation reaction, Figure 8) vs. the cyclohexene concentration. The kinetics reach a zero-order plateau in cyclohexene above 1.65 M [72]. Reprinted with permission from [72]. Copyright (2009) American Chemical Society.

In their 2009 study, Mondloch, Finke and co-workers also investigated the a conversion of a more heavily metal loaded, 5-wt% H_2PtCl_6/TiO_2 precatalyst to $Pt(0)_n/TiO_2$ in EtOH (and cyclohexene) under H_2 [72]. The observed kinetics are now *linear* (Figure 11, red diamonds left), in dramatic contrast to the sigmoidal kinetics observed when starting from the lower loading, 2.0-wt% $H_2PtCl_6/\gamma\text{-}Al_2O_3$ precatalyst (Figure 8). Interestingly and importantly, those linear kinetics are the same as Chupas and co-workers observed for their formation of 5-wt% H_2PtCl_6/TiO_2 to $Pt(0)_n/TiO_2$, but in their studies at the gas-solid interface [56]. Stirring rate, and H_2PtCl_6 weight percent control experiments in the Mondloch et al. study revealed that the linear kinetic curves (at the gas-liquid-solid interface) are due to H_2 gas-to-solution mass transfer limitations (MTL). Figure 11 (left) demonstrates that when the stirring rate is increased from 600 to 1000 rpms, the cyclohexene uptake rate (or H_2 uptake) increases from 42.2 psig H_2/h to 66.8 psig H_2/h, that is a 66% increase leads to a 58% increase in the reaction rate, prima

facie evidence for H_2 gas-to-solution MTL [287]. Further evidence consistent with the presence of H_2 gas-to-solution MTL is given by varying the weight percent of H_2PtCl_6 on TiO_2, and then plotting that vs. the measured H_2 uptake rate, Figure 11 (right). In short, the kinetics for the higher, 5-wt% H_2PtCl_6/TiO_2 are *diffusion limited*, and not chemical-reaction limited, kinetic evidence that is invaluable to knowing if the $Pt(0)_n$ nanoparticles are being synthesized under optimum conditions. Here they are not due to the established effects of H_2 gas-to-solution MTL that broaden the nanoparticle dispersion (vide infra) [287].

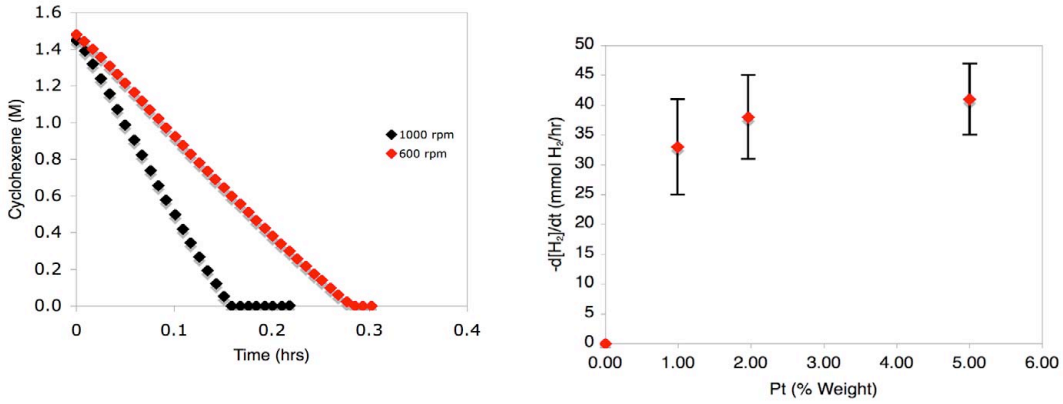

Figure 11. Linear kinetics observed for the 5-wt% H_2PtCl_6/TiO_2 system in contact with EtOH, cyclohexene and H_2 at 600 and 1000 rpms [72] (shown left). Rate of H_2 loss as a function of the Pt-wt%, which demonstrates that the reaction approaches zero-order kinetics (i.e., approaches the H_2 gas-to-solution MTL regime) even by 2-wt% (right) [72]. Reprinted with permission from [72]. Copyright (2009) American Chemical Society.

The negative affects of MTL conditions nanoparticle formation (and syntheses) in solution have been demonstrated in the literature [287], Scheme 16—an example of the ≥8 mechanistic insights now available from kinetic and mechanistic studies of nanoparticle formation in solution [281]. Specifically, since aggregation to *polydisperse nanoparticles* occurs under such MTL conditions (Scheme 16, bottom half) since that aggregation kinetically out competes the H_2-requiring surface autocatalytic growth that

would otherwise yield near-monodisperse nanoparticles (i.e., ± ≤15% [193]) at sufficient H_2 pressures (Scheme 16, top half).

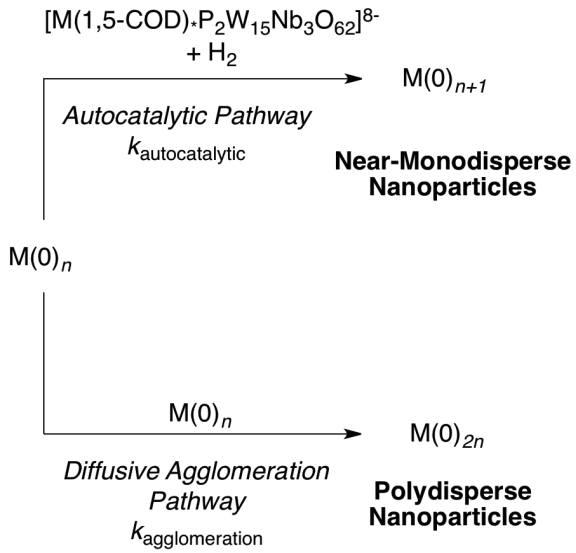

Scheme 16. The two, parallel nanoparticle growth pathways originally demonstrated during the formation, in solution, of polyoxoanion-stabilized $M(0)_n$ nanoparticles from a $[M(1,5\text{-COD})\bullet P_2W_{15}Nb_3O_{62}]^{8-}$ (M = Rh, Ir) precursor (i.e., $P_2W_{15}Nb_3O_{62}^{8-}$ is the polyoxoanion that was employed) [287]. As demonstrated elsewhere [287], insufficient H_2 (i.e., H_2 gas-to-solution MTL) yields polydisperse nanoparticles since diffusive agglomeration (bottom) kinetically outcompetes surface autocatalytic growth (top) when insufficient H_2 is present in solution.

However and importantly, by using the cyclohexene reporter reaction method it was possible to screen rapidly and find conditions that avoid the undesired linear (MTL) kinetic regime for the H_2PtCl_6/TiO_2 system [72]. Specifically, when a lower loading, 0.99-wt% H_2PtCl_6/TiO_2 precatalyst was employed, the kinetics changed from linear to sigmoidal. While those 0.99-wt% H_2PtCl_6/TiO_2 kinetics were shown to still contain some MTL,[21] the lower catalyst loading is having the desired effect of moving away from the MTL-regime and into the desired chemical-reaction-limited regime.

[21] The observation that the lower 0.99-wt% H_2PtCl_6 loading *on TiO_2* still has MTL effects, despite being at 2-fold lower loading than the γ-Al_2O_3 case, shows (a) the significant effect of the support on the catalyst formation kinetics, and (b) argues for different

In summary, kinetic and mechanistic studies of $H_2PtCl_6/\gamma\text{-}Al_2O_3$ in contact with EtOH solvent and using the cyclohexene/H_2 to cyclohexane reporter reaction method have demonstrated: (i) a balanced reaction stoichiometry; and (ii) sigmoidal kinetic curves which can be fit by a 2-step, slow, continuous nucleation and then fast autocatalytic surface growth mechanism—so the words/concepts of "slow, continuous nucleation" and then "fast autocatalytic surface growth" [193] can be used rigorously and with confidence.[9] Also demonstrated for the H_2PtCl_6/TiO_2 system were: (iii) H_2 gas-to-solution MTL kinetics, from which polydisperse nanoparticles form as a result of those MTL effects, and (iv) conditions that largely avoid such undesirable MTL effects. Perhaps especially important, also reported were (v) that there is a ~10^5 range in k_1 for the $H_2PtCl_6/\gamma\text{-}Al_2O_3$ system unless one pre-equilibrates the system with the EtOH solvent, and (vi) the suggestion that the H_2PtCl_6 speciation is the underlying cause of the ~$10^{\pm}$ variation in k_1, an important hypothesis that remains to be further tested and thereby supported or refuted.

3.2.2.4. Mondloch, Finke and Co-Workers Studies of the Formation for the Conversion of $Ir(1,5\text{-}COD)Cl/\gamma\text{-}Al_2O_3$ to $Ir(0)_{\sim 900}/\gamma\text{-}Al_2O_3$: Development of a Prototype System in Contact with Solution

The speciation issues in the classic H_2PtCl_6/support system [72] lead to the definition, then development, of a so-called "prototype" system for the study of the synthesis and kinetics and mechanism of the formation of supported-nanoparticles in contact with solution. Specifically, 8 criteria were defined, which [74]: (i) should start from a compositionally and structurally well-defined supported precatalyst; (ii) should be in contact with solution and formed under low temperature conditions; and (iii) should

---

speciation on, or in the presence of, these two supports (with a more active species toward Pt(0) formation being present on TiO_2). Such support effects have also been observed in the gas-solid supported-nanoparticle formation literature [32,37,42], but their detailed origin remains obscure.

contain an establishable, balanced stoichiometry for a supported-nanoparticle formation reaction, a reaction that should also lead to a well-characterized supported-nanoparticle catalyst. In addition, a prototype system: (iv) should yield an active and long-lived catalyst, so that (v) the desired/necessary kinetic and mechanistic studies are worth the effort. The prototype system (vi) should also yield reproducible and quantitative kinetic data, so that quantitative conclusions and mechanistic insights can be drawn, ideally all in comparison to a kinetically and mechanistically well-studied nanoparticle formation system in solution [193,288], for the insights that such a little-precedented comparison might reveal. Once that prototype system is in hand, one would also like to (viii) systematically vary key synthetic variables (such as the support, the solvent and the metal precursor) to reveal their affects on the supported-nanoparticle formation reaction in contact with solution. Other attributes of a prototype system are surely possible, but to start these 8 attributes were the goal [74].

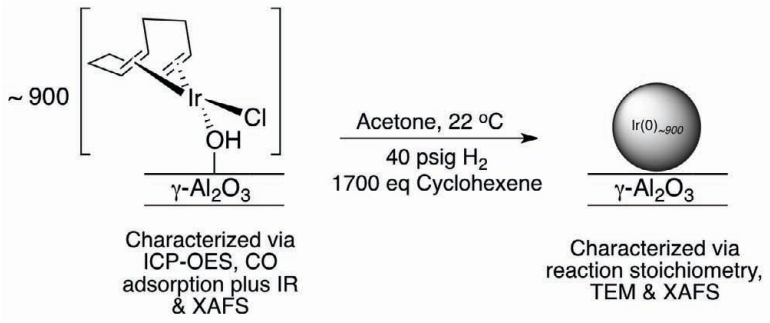

Scheme 17. The recently developed [74] Ir(1,5-COD)Cl/γ-Al_2O_3 to $Ir(0)_{\sim 900}$/γ-Al_2O_3 supported-nanoparticle catalyst formation system in contact with solution.

Hence, in a 2010 and also a 2011 paper, Mondloch, Finke and co-workers studied the formation of a well-defined, putatively prototype Ir(1,5-COD)Cl/γ-Al_2O_3 to $Ir(0)_{\sim 900}$/γ-Al_2O_3 supported-nanoparticle catalyst formation system [74,75] (Table 3, Entries 7 and 8). The Ir(1,5-COD)Cl/γ-Al_2O_3 to $Ir(0)_{\sim 900}$/γ-Al_2O_3 supported-nanoparticle formation

system in contact with solution satisfies the first 7 of 8 prototype criteria as defined above. The speciation-controlled Ir(1,5-COD)Cl/γ-Al_2O_3 precatalyst was thoroughly characterized via inductively coupled plasma optical emission spectroscopy, CO trapping plus IR, and XAFS spectroscopies. The $Ir(0)_{\sim 900}$/γ-Al_2O_3 product was formed in contact with acetone, cyclohexene and H_2, Scheme 17 and then fully characterized via reaction stoichiometry (confirmed via cyclooctane evolution and H_2 uptake measurements), TEM and XAFS spectroscopy revealing a near-monodisperse [215], non-aggregated 2.9±0.4 nm $Ir(0)_{\sim 900}$/γ-Al_2O_3 catalyst (Figure 12). The resultant $Ir(0)_{\sim 900}$/γ-Al_2O_3 is a highly active (turnover frequency of 8200 turnover/h) and long-lived (≥ 220,000 total turnovers) cyclohexene hydrogenation catalyst [74] ensuring that the subsequent, time-consuming kinetic and mechanistic studies were worth the effort.

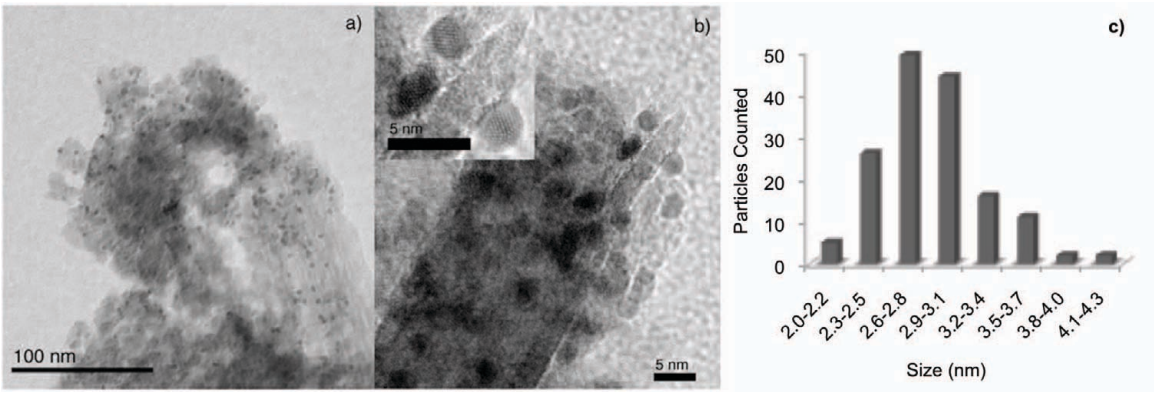

Figure 12. TEM imaging and particle size histogram of the prototype $Ir(0)_{\sim 900}$/γ-Al_2O_3 supported-nanoparticle catalyst showing 2.9±0.4 nm, and, hence a near-monodisperse size distribution [74]. (a) A large-area view (scale bar 100 nm) reveals that the nanoparticles are well-dispersed on the support. (b) A close-up view (scale bar 5 nm) reveals that the supported-nanoparticles are crystalline. (c) The associated particle size histogram. Reprinted with permission from [74]. Copyright (2010) American Chemical Society.

The observed $Ir(0)_{\sim 900}$/γ-Al_2O_3 supported-nanoparticle formation kinetics (Figure 13, left), again monitored via the cyclohexene reporter reaction (analogous to the one shown

in Scheme 15), are sigmoidal, Figure 13. Those kinetics are well-fit to the 2-step mechanism of slow continuous nucleation (A → B, rate constant k_1), followed by fast autocatalytic surface growth (A + B → 2B, rate constant k_2), where in this case A is the Ir(1,5-COD)Cl/γ-Al_2O_3 precatalyst and B is the growing $Ir(0)_n$ nanoparticle surface [74]. The resultant, well-defined rate constants are k_1 = 1.5(1.1) × 10^{-3} h^{-1} and k_2 = 1.6(2) × 10^4 h^{-1} M^{-1} for nucleation and autocatalytic surface growth, respectively—note that control over the Ir(1,5-COD)Cl/γ-Al_2O_3 speciation has allowed reproducible k_1 and k_2 rate constants along with formation of a near monodisperse (i.e., ± ≤15%) 2.9±0.4 nm $Ir(0)_{\sim 900}$/γ-Al_2O_3 supported-nanoparticle catalyst.

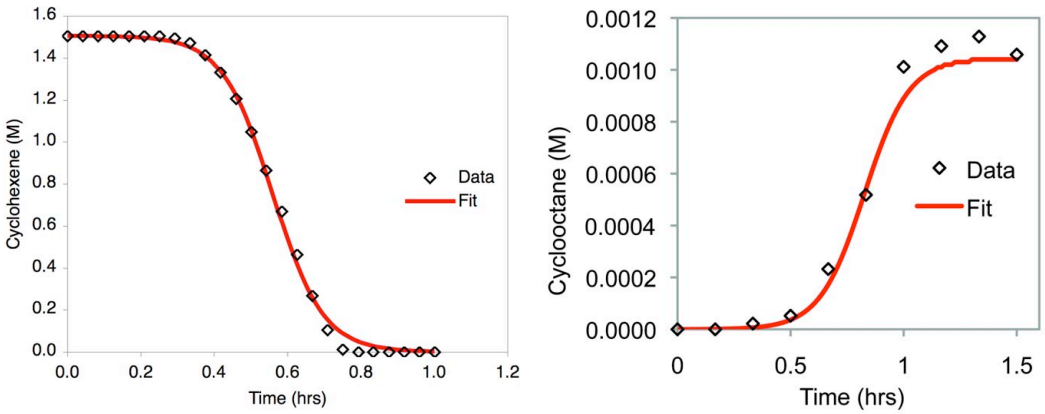

Figure 13. The sigmoidal kinetics obtained via the cyclohexene reporter reaction method and fit to the 2-step mechanism (left), plus the control of directly monitoring the evolution of cyclooctane via GLC (right) all for the Ir(1,5-COD)Cl/γ-Al_2O_3 to $Ir(0)_{\sim 900}$/γ-Al_2O_3 supported-nanoparticle formation reaction in contact with solution. The k_1 and k_2 rate constants obtained independently from the two kinetic monitoring methods agree within experimental error [74] (i.e., and after correction for the pseudoelementary step derived -d[A]/dt/1 = -d[H_2]/dt/2600 stoichiometry), nicely confirming each method and the underlying kinetic derivations and pseudoelementary step method. Reprinted with permission from [74]. Copyright (2010) American Chemical Society.

The choice of the Ir(1,5-COD)Cl/γ-Al_2O_3 precatalyst allows for an additional, valuable kinetic monitoring method performed as a control. By using gas-liquid-chromatography (GLC), the authors directly monitored the cyclooctane evolution kinetics (i.e., the loss of

A, Ir(1,5-COD)Cl, by the formation of the cyclooctane hydrogenated product of the starting 1,5-cyclooctadiene ligand), Figure 13 (right). Importantly, the nucleation (k_{1GLC} = 1.2(2) × 10^{-3} h^{-1}) and autocatalytic surface growth (k_{2GLC} = 1.2(2) × 10^{4} h^{-1} M^{-1}) rate constants obtained by the more direct, but slow and imprecise, GLC monitoring method provides independent verification of the kinetics obtained by the fast and precise, but indirect, cyclohexene reporter reaction method (k_1 = 1.5(1.1) × 10^{-3} h^{-1} and k_2= 1.6(2) × 10^{4} h^{-1} M^{-1}). The comparison of the GLC vs. H_2-pressure transducer obtained kinetics also experimentally and independently verifies the -d[A]/dt/1 = -d[H_2]/dt/2600 relationship [74]. The results make apparent the ease, precision, power and validity of the of the cyclohexene reporter reaction method for following the kinetics of supported-nanoparticle formation in contact with solution, at least in such favorable cases and when the proper [cyclohexene]^0 controls are performed [74,193].

In a follow up study [75], the authors addressed the important question of whether the nucleation and growth steps, for the formation of the non-aggregated Ir(0)$_{\sim 900}$/γ-Al_2O_3 supported-nanoparticle formation reaction, *occur primarily in solution, on the support, or possibly in both phases for one or more of the catalyst formation steps.* That is, what is the intimate kinetic mechanism for this prototype system in contact with solution? The possible solid-oxide-based, solution-based and a mixed nucleation and growth pathways to the Ir(0)$_{\sim 900}$/γ-Al_2O_3 product are shown in Scheme 18. The bolded pathway shows the mechanism that has been uncovered by the kinetic studies performed [75], vide infra.

In the kinetic treatment, and the expressions provided next (and as originally derived elsewhere [75]), the Ir(1,5-COD)Cl/γ-Al_2O_3 precatalyst (abbreviated [Ir^I/Al_2O_3]$_{sus}$) and γ-Al_2O_3 (abbreviated [Al_2O_3]$_{sus}$) were necessarily approximated as being “homogeneously

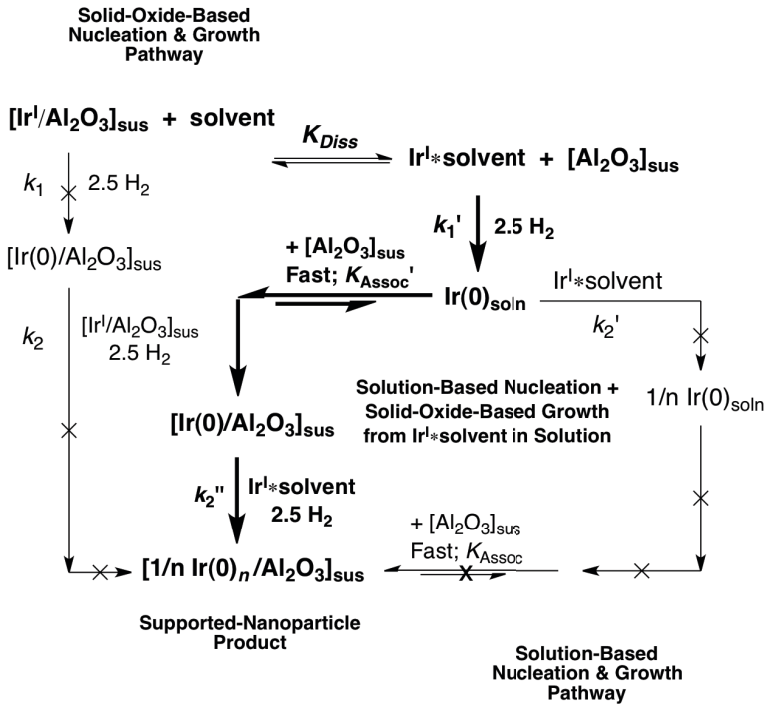

Scheme 18. The a priori, plausible solid-oxide only (left), solution-only (right), and mixed (bolded; the kinetically observed) pathways for conversion of Ir(1,5-COD)Cl/γ-Al_2O_3 to $Ir(0)_{\sim 900}$/γ-Al_2O_3 in contact with solution [75].

suspended in solution",[22] as depicted by the "sus" subscripts. The bold mechanism in Scheme 18 consists of Ir(1,5-COD)Cl(solvent) dissociation from the γ-Al_2O_3 support (i.e., from Ir(1,5-COD)Cl/γ-Al_2O_3), then solution-based nucleation from that dissociated Ir(1,5-COD)Cl(solvent) species, subsequent fast $Ir(0)_n$ nanoparticle capture by γ-Al_2O_3 and then solid-oxide-based nanoparticle growth by $Ir(0)_n$/γ-Al_2O_3 with Ir(1,5-COD)Cl(solvent). For that bold pathway, the relevant kinetic equations can be derived by starting from the 2-step mechanism, equation 6.

$$\frac{\mathrm{d}[\mathrm{Ir}^{\mathrm{I}}/\mathrm{Al_2O_3}]_{\mathrm{sus}}}{\mathrm{dt}} = k_1'[\mathrm{Ir}^{\mathrm{I}} * \mathrm{solvent}]_t + k_2''[\mathrm{Ir}^{\mathrm{I}} * \mathrm{solvent}]_t[\mathrm{Ir}(0)_n/\mathrm{Al_2O_3}]_{\mathrm{sus},t} \qquad (6)$$

[22] More specifically, the hypothetical "concentrations" of active "Ir(1,5-COD)Cl" binding sites of the suspended γ-Al_2O_3 were treated as if they increase linearly when in contact with solution (or, really, with the amount of solvent-exposed γ-Al_2O_3 surface area) [75].

In equation 6 and the equations that follow, $Ir^{I}*$solvent is the dissociated complex, Ir(1,5-COD)Cl(solvent), the subscript "i" represents initial concentrations, while the subscript "*t*" denotes each species as a function of time. Solving the dissociative equilibrium equation (K_{Diss}), equation 7, for $[Ir^{I}*solvent]_t$ followed by subsequent substitution in the mass balance equation, equation 8, are key steps in the derivation.

$$K_{\mathrm{Diss}} = \frac{[\mathrm{Ir}^{\mathrm{I}} * \mathrm{solvent}]_t [\mathrm{Al_2O_3}]_{\mathrm{sus},t}}{[\mathrm{Ir}^{\mathrm{I}} / \mathrm{Al_2O_3}]_{\mathrm{sus},t} [\mathrm{solvent}]_t} \tag{7}$$

$$[\mathrm{Ir}^{\mathrm{I}} / \mathrm{Al_2O_3}]_{\mathrm{sus,i}} = [\mathrm{Ir}^{\mathrm{I}} / \mathrm{Al_2O_3}]_{\mathrm{sus},t} + [\mathrm{Ir}^{\mathrm{I}} * \mathrm{solvent}]_t \tag{8}$$

Substitution of the resultant $[Ir^{I}/Al_2O_3]_{sus}$ equation back into equation 6 yields equation 9, where the resultant rate constants are given by equations 10 and 11 respectively.

$$\frac{\mathrm{d}[\mathrm{Ir}^{\mathrm{I}} / \mathrm{Al_2O_3}]_{\mathrm{sus}}}{\mathrm{dt}} = k_{1\mathrm{obs}} [\mathrm{Ir}^{\mathrm{I}} / \mathrm{Al_2O_3}]_{\mathrm{sus,i}} + k_{2\mathrm{obs}} [\mathrm{Ir}^{\mathrm{I}} / \mathrm{Al_2O_3}]_{\mathrm{sus,i}} [\mathrm{Ir}(0)_n / \mathrm{Al_2O_3}]_{\mathrm{sus},t} \tag{9}$$

$$k_{1\mathrm{obs}} = \frac{k_1' K_{\mathrm{Diss}} [\mathrm{solvent}]_t}{[\mathrm{Al_2O_3}]_{\mathrm{sus},t} + \mathrm{K}_{\mathrm{Diss}} [\mathrm{solvent}]_t} \tag{10}$$

$$k_{2\mathrm{obs}} = \frac{k_2'' K_{\mathrm{Diss}} [\mathrm{solvent}]_t}{[\mathrm{Al_2O_3}]_{\mathrm{sus},t} + \mathrm{K}_{\mathrm{Diss}} [\mathrm{solvent}]_t} \tag{11}$$

The mechanism in Scheme 18 (bold), along with equations 10 and 11, predict that both the γ-Al_2O_3 and solvent "concentrations" should affect the nucleation and growth rate constants.

To start, the effects of the suspended γ-Al_2O_3 on the $Ir(0)_{\sim 900}$/γ-Al_2O_3 nucleation and growth kinetics [75] were investigated, Figure 14. Consistent with the mechanism in Scheme 18 (bold) both k_{2obs} and k_{1obs} qualitatively decrease with increasing γ-Al_2O_3 (black circles). That trend is explained by the increased γ-Al_2O_3 shifting the K_{Diss} equilibrium in Scheme 18 to the left, resulting in less Ir(1,5-COD)Cl(solvent) in solution, and a corresponding decrease in both k_{2obs} and k_{1obs}. Importantly, equation 11 could be used to quantitatively fit the k_{2obs} vs. γ-Al_2O_3 data shown in Figure 14 (red line, left), yielding values of $k_2'' = 4(1) \times 10^{-4}$ h^{-1} M^{-1} and $K_{Diss} = 1.3(6) \times 10^{-2}$.

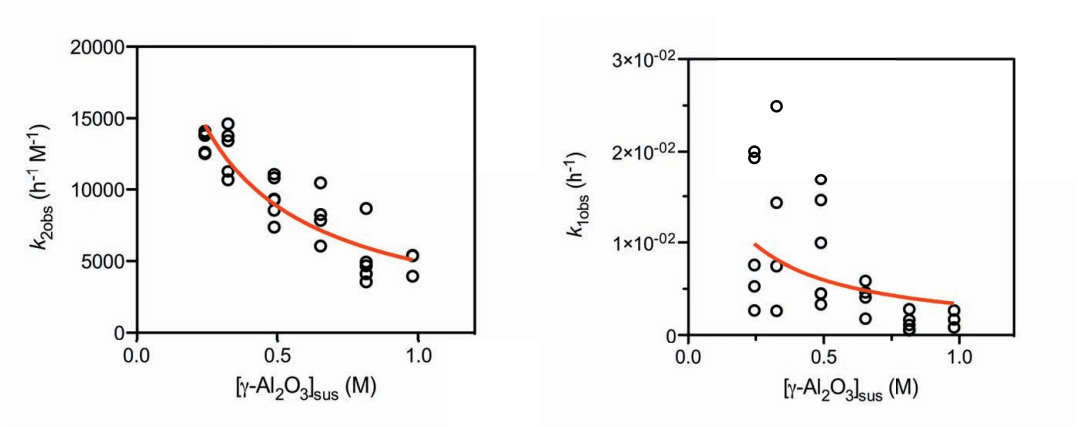

Figure 14. Dependence of the k_{2obs} (left, black circles) and k_{1obs} (right, black circles) rate constants on the [γ-Al_2O_3]$_{sus}$ "concentration". Also shown are the fits (red lines) to equations 11 and 10 respectively [75]. Reprinted with permission from [75]. Copyright (2011) American Chemical Society.

The K_{Diss} equilibrium was *independently verified* by hydrogenating the dissociated/equilibrated Ir(1,5-COD)Cl(solvent) in solution and quantifying the amount of cyclooctane in solution via GLC. In addition, utilizing $K_{Diss} = 1.3(6) \times 10^{-2}$, equation 10 could roughly account for the rough shape of the k_{1obs} vs. γ-Al_2O_3 data also shown in

Figure 14 (red line, right)—note that the $10^{\pm 1}$ scatter in that data is as expected, nucleation and growth even in solution of $Ir(0)_{\sim 300}$ nanoparticles from a Ir(1,5-COD)•$P_2W_{15}Nb_3O_{62}^{8-}$ polyoxoanion (i.e., single species) precursor similarly shows a $10^{1.2}$ variability [289] for reasons that are partially understood [193,288]. The steeper rise of the data vs. the computed curve in the right-hand, k_1 vs. $[\gamma\text{-}Al_2O_3]_{sus}$ plot in Figure 14 may be evidence for bimolecular nucleation, a point under investigation.

In order to investigate the affects of the acetone/solvent "concentration" on the Ir(1,5-COD)Cl/γ-Al_2O_3 to $Ir(0)_n/\gamma$-Al_2O_3 kinetics, a mixed solvent system of cyclohexane plus acetone was used [75]. One key difference is that $[Ir(1,5\text{-}COD)Cl]_2$ was now the dominant species observable in solution via UV-visible spectroscopy. While a slightly modified mechanism, and forms of equations 10 and 11, was derived in that original publication [75], the qualitative results are easily explainable in terms of Scheme 17 and equations 10 and 11, and thus that modified mechanistic scheme and its associated rate equations are not reproduced here. The k_{2obs} and k_{1obs} vs. [acetone] data are shown in Figure 15; qualitatively both k_{2obs} and k_{1obs} increase with increasing acetone concentration as the mechanism back in Scheme 18 predicts. Again, this is easily explained by shifting the dissociative equilibrium in Scheme 18 to the right, resulting in more Ir(1,5-COD)Cl(solvent) (really $[Ir(1,5\text{-}COD)Cl]_2$ in this mixed solvent case) in solution and a concomitant increase in both k_{2obs} and k_{1obs}. Again, the general forms of equations 11 and 10 could be used to quantitatively fit the k_{2obs} vs. [acetone] data. Once the K_{Diss} equilibrium for the mixed solvent system was determined, the k_{1obs} vs. [acetone] data could also be accounted for at least semiquantitatively (i.e., and in light of the inherent experimental error in the data), Figure 15 right. The higher data above the curve-fit line in the right-hand k_{1obs} vs. $[acetone]^1$ plot may, again, be indicating a bimolecular nucleation mechanism.

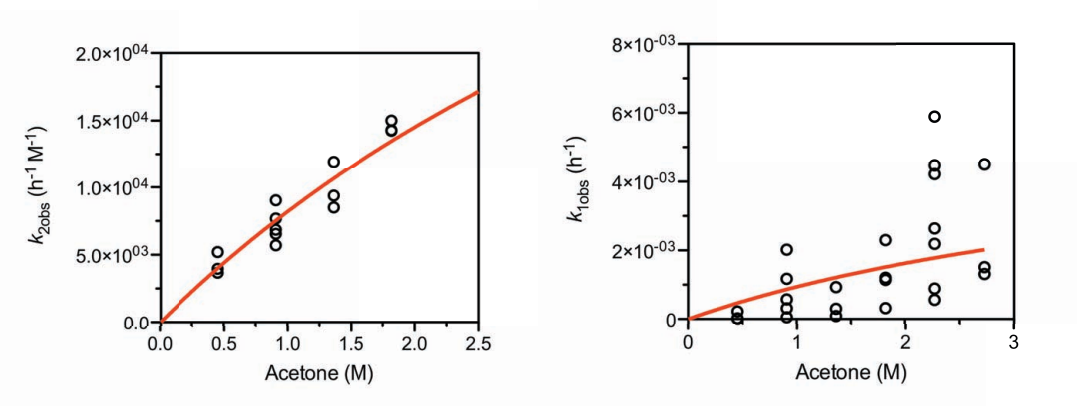

Figure 15. Dependence of the k_{2obs} (left, black circles) and k_{1obs} (right, black circles) rate constants on the [acetone] "concentration". Also shown are the fits (red lines) to equations that have the same general form as equations 11 and 10 respectively [75]. Reprinted with permission from [75]. Copyright (2011) American Chemical Society.

The Ir(1,5-COD)Cl/γ-Al_2O_3 to $Ir(0)_{\sim 900}$/γ-Al_2O_3 supported-nanoparticle formation nucleation and growth rate constants also have a general solvent dependence in acetone, propylene carbonate, CH_2Cl_2 and cyclohexane: k_{1obs} varies by ~3000-fold and k_{2obs} varies by ~70-fold. Finally, that solvent variation-, γ-Al_2O_3- and acetone-dependent kinetic data, along with UV-visible spectroscopic and GLC data could also be used to rule out the all-heterogeneous (solid-oxide-based) and all-homogeneous (solution-based) nucleation and growth mechanisms also shown in Scheme 18 (and as detailed in the original paper [75]).

Maybe most importantly these studies (and analogous ones) suggest that the ≥8 available synthetic insights from the soluble, ligand-stabilized, nanoparticle formation literature should be transferable to the syntheses of supported-nanoparticle heterogeneous catalysts. Those insights include [281]: (i) that autocatalysis separates nucleation and growth in time, which in turn is why near-monodisperse (≤ ±15%) size distributions of typically "magic-number" sized [157] supported-nanoparticles are formed; (ii) that rational size control is possible via a recently developed nanoparticle size vs. time equation that relates k_1, k_2 and the precursor ([A]) concentration to the final

nanoparticle average size [156]; (iii) that additional size control is possible via olefin or other ligand additives [288]; (iv) that rational seeded-growth methods are predicted by the surface autocatalytic growth step, including the rational syntheses of all possible geometric isomers of multimetallic "nano-onions" [157]; (v) that rational catalyst shape control is predicted, via preselected ligands attaching to the growing nanoparticle faces, thereby preventing autocatalytic surface growth at those facets [232-235]; (vi) that the negative effects ofH_2 gas-to-solution mass-transfer limitations in nanoparticle syntheses are expected (vide supra) [287], along with insights into how to avoid such effects; (vii) that specific, nanoparticle lattice-matching ligands can provide additional nanoparticle stability if desired [223,290]; and finally (viii) the possibility of nanoparticle size-dependent surface metal-to-ligand bond energies exist—plus all that very important preliminary finding implies for catalysis [191,192].

3.2.3. Conclusions

The above survey (i.e., Table 3) of the kinetic and mechanistic studies of supported-nanoparticle formation at the gas-liquid-solid interface makes clear that such studies have occurred ≥ 5 times less frequently than those at the gas-solid interface. While word- and picture based mechanisms dominated the earlier literature [69-71], there is a clear trend towards more rigorous, chemical reaction-based, supported-nanoparticle formation mechanisms in the gas-liquid-solid based nanoparticle formation systems [72,74,75]. A 2-step mechanism consisting of slow, continuous nucleation A → B (rate constant k_1) followed by fast autocatalytic surface growth, A + B → 2B (rate constant k_2), has been shown to quantitatively account for both $Pt(0)_n/\gamma\text{-}Al_2O_3$ and $Ir(0)_n/\gamma\text{-}Al_2O_3$ supported-nanoparticle formation in contact with solution [72,74,75]. Furthermore, it has been demonstrated that when solution is present, nucleation occurs in solution from Ir(1,5-COD)Cl(solvent) for the $Ir(1,5\text{-COD})Cl/\gamma\text{-}Al_2O_3$ to $Ir(0)_{\sim 900}/\gamma\text{-}Al_2O_3$ system, the one case examined to date [75]. One expects the finding of solution-based nucleation to be

more general for other coordinatively saturated (e.g., d^8 square planar), or high-valent (e.g., Ir(III), Rh(III), Au(III)), supported organometallic species that do not have facile reduction mechanisms to $M(0)_n$ under H_2 (i.e., and while on the support) [291]. Additionally, diffusion-based mechanisms (more specifically H_2 gas-to-solution MTL) were also revealed for $Pt(0)_n/TiO_2$ supported-nanoparticle formation from 5-wt% H_2PtCl_6/TiO_2 [72]; hence, care must be taken to minimize such effects even when employing the gas-liquid-solid interface. Finally, a very important insight for future studies—one that makes physical sense in hindsight—is *that diffusion limitations present in gas-solid catalyst formation systems can be overcome in favorable cases by going to a gas-liquid-solid system*. This potential advantage, argues, by itself, for much greater investigation of gas-liquid-solid systems.

The future appears bright for synthetic, kinetic and mechanistic studies of supported-nanoparticle formation in solution from, ideally, speciation-controlled, supported organometallics and other single-species precatalysts. In those studies it will continue to be important to establish regimes where chemical-reaction-based kinetics are occurring, rather than diffusion-limited conditions. Establishing fully the supported-nanoparticle formation stoichiometry and resultant products will continue to be important stepping stones, as those stoichiometries must be the sum of the proposed mechanistic steps. Overall, the results suggest that synthetic and mechanistic insights, from the modern revolution in nanoparticle syntheses and study in solution, can now begin to be transferred to the syntheses of improved, size, shape and surface-composition controlled supported-nanoparticles and their catalysis.

4. Summary

Key points from the introduction section include:

- Key catalytic properties—such as selectivity, activity and lifetime—of supported-nanoparticle catalysts depend of course on the size, structure and composition of the supported nanoparticles.
- Unfortunately, rational, mechanistically guided syntheses of the desired size, structure and compositionally controlled supported-nanoparticle catalysts are generally still lacking.
- One major reason for this gap, despite the technological and commercial importance of supported-nanoparticle catalysts, is the present poor understanding of the mechanisms that govern supported-nanoparticle formation.

Key points from the fundamental background information at the gas-solid interface include:

- Methods such as XAFS and total high-energy X-ray scattering plus PDF analysis are direct, powerful physical methods capable of following supported-nanoparticle formation in real time.
- However, and despite the emergence and use of such powerful spectroscopic methods, additional, more routine complimentary kinetic monitoring methods are needed to screen systems and to ensure that only the most important and well-defined systems are subject to the more expensive and time-consuming synchrotron X-ray methods mentioned above. Restated, there is a need to couple cheap, quick and easy (albeit sometimes indirect) methods with the more expensive, slower (but more direct and thereby powerful) kinetic monitoring methods in the future.
- The complex nature of the mechanisms of formation of supported-nanoparticles will demand the use of multiple, complimentary physical methods (e.g., XAFS plus total high-energy X-ray scattering plus PDF analysis).

Key points from the kinetic and mechanistic studies at the gas-solid interface include:

- The $M(NH_3)_4^{2+}$ (M = Pt^{2+}, Pd^{2+}) H_2PtCl_6, $Ag(NO_3)$, and supported-organometallic systems provide a solid foundation of work upon which to build. However, much remains to be done including studies that, at a minimum, rigorously demonstrate the following: (i) the supported-precatalyst composition and structure—that is, the precise speciation present, (ii) the supported-nanoparticle products, and (iii) the overall balanced stoichiometry of the nanoparticle formation reaction.
- Control over the supported-precatalyst speciation is particularly crucial as the supported-nanoparticle formation kinetics are governed by the rates of evolution of those species (e.g., their nucleation (k_1) and growth (k_2) rate constants). Supported-organometallic precatalysts offer one good, precedented, and arguably more broadly applicable way to control the precatalyst speciation.
- Once speciation-controlled precatalysts are in hand, diffusional and other unwanted processes need to be looked for and then eliminated when present so that chemical-reaction-based kinetic regimes can studied en route to the synthesis of more active, more selective, long-lived and precisely ligated supported-nanoparticle catalysts.
- Indeed, the finding of diffusion-limited processes in supported-nanoparticle formation in gas-solid systems is arguably a major limitation of those systems, and unless conditions which eliminate such diffusion-controlled limitations can be found.
- Chemical-reaction-based mechanisms (rather than the currently dominant word- and picture-based) mechanisms, and notably the disproof of multiple alternative mechanisms (hypotheses) en route to a thereby supported mechanism, are needed if such mechanistic knowledge of supported-nanoparticle formation is to advance smoothly, more quickly and *reliably*.

- There is arguably a need to bridge the known supported-nanoparticle formation mechanistic knowledge from the studies reviewed herein, with the knowledge from the UHV community, as well as with the knowledge now available from the soluble ligand-stabilized nanoparticle formation community as well as the organometallic community.

Key points from the fundamental background information at the gas-liquid-solid interface include:

- Supported-nanoparticles synthesized at the gas-liquid-solid interface is an attractive, emerging area, one where the synthetic and mechanistic insights, from the modern revolution in nanoparticle synthetic and mechanistic studies in solution, can probably be transferred to the synthesis of supported-nanoparticle catalysts and their resultant catalysis.
- Direct, operando techniques for following the kinetics of supported-nanoparticle formation need to be emphasized in the future.

Key points from the kinetic and mechanistic studies at the gas-liquid-solid interface include:

- In terms of volume, kinetic and mechanistic studies at the gas-liquid-solid interface are presently 5-fold less common than those at the gas-solid interface—indicating that much remains to be done with gas-liquid-solid systems.
- Despite the lower volume of work to date, headway has been made into understanding supported-nanoparticle formation at the gas-liquid-solid interface. In particular, the overall kinetics in several systems can be fit by a chemical-reaction-based mechanism consisting of slow, continuous, nucleation (A $\rightarrow$ B, rate constant k_1) followed by fast autocatalytic surface growth (A + B $\rightarrow$ 2B, rate constant k_2).

- In one case, a putative prototype system, Ir(1,5-COD)Cl/γ-Al_2O_3, has been prepared and shown to evolve to a well-defined, $Ir(0)_{\sim 900}$/γ-Al_2O_3 supported-nanoparticle catalyst via a demonstrated, balanced reaction stoichiometry.
- In the Ir(1,5-COD)Cl/γ-Al_2O_3 to $Ir(0)_{\sim 900}$/γ-Al_2O_3 system, nucleation has been demonstrated to occur in solution, followed by a fast $Ir(0)_n$ nanoparticle capture step and then subsequent support-based nanoparticle growth between $Ir(0)_n$/γ-Al_2O_3 plus Ir(1,5-COD)Cl(solvent) from solution.

Overall, it is clear that kinetic and mechanistic insights into supported-nanoparticle heterogeneous catalyst formation greatly lags both the importance, as well as the prior preparative chemistry, of these practical, industrially relevant catalysts. However, a convergence appears to be emerging between the knowledge of solution nanoparticle syntheses, mechanistic studies of nanoparticle formation in solution, improved speciation-controlled synthesis of supported precatalysts, plus the use of powerful physical methods (such as XAFS and the total high-energy X-ray scattering and PDF analysis). Complimentary, quicker and easier, but less direct methods for following nanoparticle formation reactions are also finding use. A synergism of these subareas, along with a combination of the knowledge of the heterogeneous catalysts, UHV and organometallic communities as noted earlier, appears to be occurring.

Despite the above advances, much remains to be done to achieve the lofty goal of synthesizing the next generation of size, size dispersion, shape and surface-composition-controlled supported-nanoparticle heterogeneous catalysts. It is hoped the present review of the current state of knowledge, and additional research needs, will help fuel the needed, synergistic efforts!

Acknowledgement

We gratefully acknowledge support from the Chemical Sciences, Geosciences and Biosciences Division, Office of Basic Energy Sciences, Office of Science, U.S. Department of Energy, Grant DE-FG02-03ER15453.

Supporting Information. Supplementary Data

Table S1 contains all 39 studies of supported-nanoparticle formation at the gas-solid interface.

References

[1] H. Heinemann, Handbook of Heterogeneous Catalysis, Vol. 1, VCH: Weinham, 1997.

[2] J.M. Thomas, Angew. Chem. Int. Ed. 27 (1988) 1673-1691.

[3] C.H. Bartholomew, R.J. Farrauto, Fundamentals of Industrial Catalytic Processes, second ed., John Wiley & Sons, Hoboken, 2006.

[4] B.C. Gates, G.W. Huber, C.L. Marshall, P.N. Ross, J. Siirola, Y. Wang, MRS Bull. 33 (2008) 429-435.

[5] B.C. Gates, Catalytic Chemistry, John Wiley & Sons, New York, 1992.

[6] A.T. Bell, Science 299 (2003) 1688-1691.

[7] R. Schlögl, S.B. Abd Hamid, Angew. Chem. Int. Ed. 43 (2004) 1628-1637.

[8] M. Che, C.O. Bennett, Adv. Catal. 36 (1989) 55-172.

[9] R.A. van Santen, Acc. Chem. Res. 42 (2006) 57-66.

[10] G. Leendert Bezemer, J.H. Bitter, H.P.C.E. Kuipers, H. Oosterbeek, J.E. Holewijn, X. Xu, F. Kapteijn, A. Jos van Dillen, K.P. de Jong, J. Am. Chem. Soc. 128 (2006) 3956-3964.

[11] G.A. Somorjai, Catal. Lett. 7 (1990) 169-182.

[12] K.M. Bratlie, H. Lee, K. Komvopoulos, P. Yang, G.A. Somorjai, Nano Lett. 7 (2007) 3093-3101.

[13] I. Lee, F. Delbecq, R. Morales, M.A. Albiter, F. Zaera, Nat. Mater. 8 (2009) 132-138.

[14] D.J. Sajkowski, M. Boudart, Catal. Rev.-Sci. Eng. 29 (1987) 325-360.

[15] G.C. Bond, Acc. Chem. Res. 26 (1993) 490-495.

[16] H.-S. Oh, J.H. Yang, C.K. Costello, Y.M. Wang, S.R. Bare, H.H. Kung, M.C. Kung, J. Catal. 210 (2002) 375-386.

[17] L.V. Tiep, M. Bureau-Tardy, G. Bulgi, G. Djega-Maridassou, M. Che, G.C. Bond, J. Catal. 99 (1986) 449-460.

[18] G.A. Somorjai, K. McCrea, Appl. Catal., A 222 (2001) 3-18.

[19] G.A. Somorjai, J.Y. Park, Angew. Chem. Int. Ed. 47 (2008) 9212-9228.

[20] Z. Ma, F. Zaera, in: B.R. King (Ed.), Heterogeneous Catalysis by Metals, John Wiley & Sons Ltd, West Sussex, 2005, pp. 1768-1784.

[21] S.H. Joo, J.Y. Park, C.-H. Tsung, Y. Yamada, P. Yang, Nat. Mater. 8 (2009) 126-131.

[22] J.M. Thomas, J. Chem. Phys. 128 (2008) 182502.

[23] G.J. Hutchings, J. Mater. Chem. 19 (2009) 1222-1235.

[24] E.V. Anslyn, D.A. Dougherty, Modern Physical Organic Chemsitry, University Science Books, Sausalito, CA, 2006.

[25] J.P. Collman, L.S. Hegedus, J.R. Norton, R.G. Finke, Principles and Applications of Organotransition Metal Chemistry, second ed., University Science Books, Sausalito, CA, 1987.

[26] J. Hartwig, Organotransition Metal Chemistry: From Bonding to Catalysis, University Science Books, Sausalito, CA, 2010.

[27] J. H. Espenson, Chemical Kinetics and Reaction Mechanisms, second ed. McGraw-Hill, New York, 2002.

[28] R. G. Wilkins, Kinetics and Mechanism of Reactions of Transition Metal Complexes second ed. VCH Publishers Inc., New York, 1991.

[29] R.A. Dalla Betta, M. Boudart, Well-Dispersed Platinum on Y Zeolite: Preparation and Catalytic Activity *5th Intern. Congr. Catal.* 1 (1973) pp. 1329-1341.

[30] A.C. Herd, C.G. Pope, J. Chem. Soc. Faraday Trans. 69 (1973) 833-838.

[31] M. Kermarec, M. Briend-Faure, D. Delafosse, J. Chem. Soc. Chem. Comm. 8 (1975) 272-273.

[32] H. Beyer, P.A. Jacobs, J.B. Uytterhoeven, J. Chem. Soc. Faraday Trans. 72 (1976) 674-685.

[33] P.A. Jacobs, M. Tielen, J.-P. Linart, J.B. Uytterhoeven, H. Beyer, J. Chem. Soc. Faraday Trans. 72 (1976) 2793-2804.

[34] M. Briend-Faure, D. Delafosse, J. Chem. Soc. Faraday Trans. 73 (1977) 905-912.

[35] M Briend-Faure, J. Jeanjean, M. Keramerec, D. Delafosse, J. Chem. Soc. Faraday Trans. 74 (1978) 1538-1544.

[36] D. Hermerschmidt, R. Haul, Ber. Bunsenges. Phys. Chem. 84 (1980) 902-907.

[37] H.K. Beyer, P.A. Jacobs, Stud. Surf. Sci. Catal. 12 (1982) 95-102.

[38] Dexpert, H., J. Phys-Paris 47 (1986) 219-226.

[39] M.S. Tzou, W.M.H. Sachtler, Stud. Surf. Sci. Catal. 38 (1988) 233-241.

[40] F. Le Normand, D. Bazin, H. Dexpert, P. Lagarde, J.P. Bournonville, in, Structural Genesis of Supported Platinum Particles Followed by EXAFS Spectroscopy, 1988, pp. 1401-1409.

[41] S.T. Homeyer, W.M.H. Sachtler, J. Catal. 118 (1989) 266-274.

[42] R.A. Schoonheydt, H. Leeman, J. Phys. Chem. 93 (1989) 2048-2053.

[43] D. Bazin, H. Dexpert, J.P. Bournonville, J. Lynch, J. Catal. 123 (1990) 86-97.

[44] M. Che, Z.X. Cheng, C. Louis, J. Am. Chem. Soc. 117 (1995) 2008-2018.

[45] M.S. Nashner, A.I. Frenkel, D. Somerville, C.W. Hills, J.R. Shapley, R.G. Nuzzo, J. Am. Chem. Soc. 120 (1998) 8093-8101.

[46] A. Yamaguchi, T. Shido, Y. Inada, T. Kogure, K. Asakura, M. Nomura, Y. Iwasawa, Catal. Lett. 68 (2000) 139-145.

[47] M.K. Oudenhuijzen, P.J. Kooyman, B. Tappel, J.A. van Bokhoven, D.C. Koningsberger, J. Catal. 205 (2002) 135-146.

[48] S.G. Fiddy, M.A. Newton, T. Campbell, A.J. Dent, I. Harvey, G. Salvini, S. Turin, J. Evans, Phys. Chem. Chem. Phys. 4 (2002) 827-834.

[49] M.K. Neylon, C.L. Marshall, A.J. Kropf, J. Am. Chem. Soc. 124 (2002) 5457-5465.

[50] K. Okumura, R. Yoshimoto, T. Uruga, H. Tanida, K. Kato, S. Yokota, M. Niwa J. Phys. Chem. B 108 (2004) 6250-6255.

[51] F. Li, B.C. Gates, J. Phys. Chem. B 108 (2004) 11259-11264.

[52] J.H. Yang, J.D. Henao, M.C. Raphulu, Y. Wang, T. Caputo, A.J. Groszek, M.C. Kung, M.S. Scurrell, J.T. Miller, H.H. Kung, J. Phys. Chem. B 109 (2005) 10319-10326.

[53] P. Li, J. Liu, N. Nag, P.A. Crozier, Surf. Sci. 600 (2006) 693-702.

[54] B.J. Hwang, C.-H. Chen, L.S. Sarma, J.M. Chen, G.-R. Wang, M.-T. Tang, D.-G. Liu, J.-F. Lee, J. Phys. Chem. B 110 (2006) 6475-6482.

[55] H. Tanaka, M. Uenishi, M. Taniguchi, I. Tan, K. Narita, M. Kimura, K. Kaneko, Y. Nishihata, J. Mizuki, Catal. Today 117 (2006) 321-328.

[56] P.J. Chupas, K.W. Chapman, G. Jennings, P.L. Lee, C.P. Grey, J. Am. Chem. Soc. 129 (2007) 13822-13824.

[57] K.-I. Shimizu, K. Sugino, K. Kato, S. Yokota, K. Okumura, A. Satsuma, J. Phys. Chem. C 111 (2007) 1683-1688.

[58] K. Okumura, K. Kato, T. Sanada, M. Niwa, J. Phys. Chem. C 111 (2007) 14426-14432.

[59] E. Bus, R. Prins, J.A. van Bokhoven, Phys. Chem. Chem. Phys. 9 (2007) 3312-3320.

[60] A. Uzun, B.C. Gates, Angew. Chem. Int. Ed. 47 (2008) 9245-9248.

[61] A.J. Liang, B.C. Gates, J. Phys. Chem. C 112 (2008) 18039-18049.

[62] K. Okumura, T. Honma, S. Hirayama, T. Sanada, M. Niwa, J. Phys. Chem. C 112 (2008) 16740-16747.

[63] K. Okumura, H. Matsui, T. Sanada, M. Arao, T. Honma, S. Hirayama, M. Niwa, J. Catal. 265 (2009) 89-98.

[64] A. Kulkarni, B.C. Gates, Angew. Chem. Int. Ed. 48 (2009) 9697-9700.

[65] T. Shishido, H. Asakura, F. Amano, T. Sone, S. Yamazoe, K. Kato, K. Teramura, T. Tanaka, Catal. Lett. 131 (2009) 413-418.

[66] P.J. Chupas, K.W. Chapman, H. Chen, C.P. Grey, Catal. Today 145 (2009) 213-219.

[67] S. Nassreddine, G. Bergeret, B. Jouguet, C. Geantet, L. Piccolo, Phys. Chem. Chem. Phys. 12 (2010) 7812-7820.

[68] A. Singh, K. Luening, S. Brennan, T. Homma, N. Kubo, P. Pianetta, Aip. Conf. Proc. 705 (2004) 1086-1089.

[69] Y. Wang, X. Xu, Z. Tian, Y. Zong, H. Cheng, C. Lin, Chem. Eur. J. 12 (2006) 2542-2549.

[70] S. Marre, F. Cansell, C. Aymonier, Nanotechnology 17 (2006) 4594-4599.

[71] S. Marre, A. Erriguible, A. Perdomo, F. Cansell, F. Marias, C. Aymonier, J. Phys. Chem. C 113 (2009) 5096-5140.

[72] J.E. Mondloch, X. Yan, R.G. Finke, J. Am. Chem. Soc. 131 (2009) 6389-6396.

[73] L.M. Rossi, I.M. Nangoi, N.J.S. Costa, Inorg. Chem. 48 (2009) 4640-4642.

[74] J.E. Mondloch, Q. Wang, A.I. Frenkel, R.G. Finke J. Am. Chem. Soc. 132 (2010) 9701-9714.

[75] J.E. Mondloch, R.G. Finke, J. Am. Chem. Soc. 133 (2011) 7744-7756.

[76] C.T. Campbell, Surf. Sci. Rep. 27 (1997) 1-111.

[77] C.R. Henry, Surf. Sci. Rep. 31 (1998) 231-325.

[78] H. Poppa, Catal. Rev.-Sci. Eng. 35 (1993) 359-398.

[79] J.A. Venables in: W.K. Liu, M.B. Santos (Eds.) Thin films: Heteroepitaxial Systems, Series on Directions in Condensed Matter Physics-Vol. 15, World Scientific Publishing, Singapore, 1999, pp. 1-53.

[80] D.W. Goodman, J. Phys. Chem. 100 (1996) 13090-13102.

[81] P.L.J. Gunter, J.W. Niemantsverdriet, F.H. Riberio, G.A. Somorjai, Catal. Rev-Sci. Eng. 39 (1997) 77-168.

[82] G. Ertl, H.-J. Freund, Phys. Today 52 (1999) 32-38.

[83] R. Imbihl, R.J. Behm, R. Schlögl, Phys. Chem. Chem. Phys. 9 (2007) 3459-3459.

[84] G.A. Somorjai, R.L. York, D. Butcher, J.Y. Park, Phys. Chem. Chem. Phys. 9 (2007) 3500-3513.

[85] M.A. Newton, Chem. Soc. Rev. 37 (2008) 2644-2657.

[86] M.M. Günter, B. Bems, R. Schlögl, T. Ressler, J. Synchrotron Radiat. 8 (2001) 619-621.

[87] M.A. Newton, S.G. Fiddy, G. Guilera, B. Jyoti, J. Evans, Chem. Commun. (2005) 118-120.

[88] R. Imbihl, G. Ertl, Chem. Rev. 95 (1995) 697-733.

[89] For example see: J.A. Rodriguez, J.Y. Kim, J.C. Hanson, M. Perez, A.I. Frenkel, Catal. Lett. 85 (2003) 247-254.

[90] Examples of kinetic studies of photodeposited supported-nanoparticles include: (a) H. Yoneyama, N. Nishimura, H. Tamura J. Phys. Chem. 85 (1981) 268-272. (b) J.-M. Herrmann, J. Disdier, P. Pichat J. Phys. Chem. 90 (1986) 6028-6034. (c) E. Borgarello, N. Serpone, G. Emo, R. Harris, E. Pelizzetti, C. Minero Inorg. Chem. 25 (1986) 4499-4503. (d) A. Fernández, A. Caballero, A. R. González-Elipe J. Phys. Chem. 99 (1995) 3303-3309. (e) K. Teramura, S.-I. Okuoka, S. Yamazoe, K. Kato, T. Shishido, T. Tanaka J. Phys. Chem. C 112 (2008) 8495-8498. (f) J. Ohyama, K. Teramura, S.-I. Okuoka, S. Yamazoe, K. Kato, T. Shishido, T. Tanaka Langmuir 26 (2010) 13907-13912.

[91] I. Yordanov, R. Knoerr, V. De Waele, M. Mostafavi, P. Bazin, S. Thomas, M. Rivallan, L. Lakiss, T. H. Metzger, S. Mintova J. Phys. Chem. C 114 (2010) 20974-20982.

[92] M. Che, O. Clause, C. Marcilly, in: G. Ertl, H. Knözinger, J. Weitkamp (Eds.), Preparation of Solid Catalysts, WILEY–VCH, Weinheim, 1999, pp. 315-526.

[93] See several chapters in the recent book: Catalyst Preparation Science and Engineering, Regalbuto, J. R. (Eds.) CRC Press, Boca Raton, 2007.

[94] Many interesting individual reports can also be found in a series of proceedings dedicated to the subject titled *International Symposium on Scientific Bases for the Preparation of Heterogeneous Catalysts,* which was originally edited by B. Delmon and is available through Elsevier.

[95] C. Perego, P. Villa, Catal. Today 34 (1997) 281-305.

[96] M. Komiyama, Catal. Rev.-Sci Eng. 27 (1985) 341-372.

[97] J.W. Geus, A.J. van Dillen, in: G. Ertl, H. Knözinger, J. Weitkamp (Eds.), Preparation of Solid Catalysts, WILEY–VCH, Weinheim, 1999, pp. 460-487.

[98] W.M.H. Sachtler, in: G. Ertl, H. Knözinger, J. Weitkamp (Eds.), Handbook of Heterogeneous Catalysis, VCH, Weinheim, 1997, pp. 365-374.

[99] B.C. Gates, Chem. Rev. 95 (1995) 511-522.

[100] J.M. Thomas, B.F.G. Johnson, R. Raja, G. Sankar, P.A. Midgley, Acc. Chem. Res. 36 (2003) 20-30.

[101] M.S. Nashner, A.I. Frenkel, D.L. Adler, J.R. Shapley, R.G. Nuzzo, J. Am. Chem. Soc. 119 (1997) 7760-7771.

[102] G. Schmid (Ed.), Clusters and Colloids: From Theory to Applications, VCH Publishers, Inc. New York, NY, 1994.

[103] R.G. Finke, in: D.L. Feldheim, C.A. Foss Jr., (Eds.), Metal Nanoparticles: Synthesis, Characterization and Applications, Marcel Dekker, Inc. New York, 2002.

[104] E. Bayram, M. Zahmakıran, S. Özkar, R.G. Finke, Langmuir 26 (2010) 12455-12464.

[105] G. Schmid, D. Fenske, Philos. T. R. Soc. A 368 (2010) 1207-1536.

[106] J.A. Schwarz, C. Contescu, A. Contescu, Chem. Rev. 95 (1995) 477-510.

[107] B.M. Weckhuysen, Phys. Chem. Chem. Phys. 5 (2003) 4351-4360.

[108] M.A. Bañares, Catal. Today 100 (2005) 71-77.

[109] S.J. Tinnemans, J.B. Mesu, K. Kervinen, T. Visser, T.A. Nijhuis, A.M. Beale, D.E. Keller, A.M.J. van der Eerden, B.M. Weckhuysen, Catal. Today 113 (2006) 3-15.

[110] F. Meunier, M. Daturi, Catal. Today 113 (2006) 1-2.

[111] M.A. Bañares, Top. Catal. 52 (2009) 1301-1302.

[112] J.M. Thomas, J.-C. Hernandez-Garrido, Angew. Chem. Int. Ed. 48 (2009) 2-6.

[113] J.F. Creemer, S. Helveg, G.H. Hoveling, S. Ullmann, A.M. Molenbroek, P.M. Sarro, H.W. Zandbergen, Ultramicroscopy 108 (2008) 993-998.

[114] H. Zheng, R.K. Smith, Y.-W. Jun, C. Kisielowski, U. Dahmen, A.P. Alivisatos, Science 324 (2009) 1309-1312.

[115] S.-Y. Chung, Y.-M. Kim, J.-G. Kim, Y.-J. Kim, Nat. Phys. 5 (2009) 68-73.

[116] M. Bauer, H. Bertagnolli ChemPhysChem 10 (2009) 2197-2200.

[117] D.C. Koningsberger, R. Prins (Eds.), X-Ray Abosrption: Principles, Applications, Techniques of EXAFS, SEXAFS and XANES, John Wiley & Sons, New York, 1988.

[118] D. C. Koningsberger, B. L. Mojet, G. E. van Dorssen, D. E. Ramaker, Top. Catal. 10 (2000) 143-145.

[119] D. Bazin, J.J. Rehr, J. Phys. Chem. B 107 (2003) 12398-12402.

[120] K. Chao, A.C. Wei, J. Electron. Spectrosc. 119 (2001) 175 and references therein.

[121] J.J. Rehr, A.L. Ankudinov, Coord. Chem. Rev. 249 (2005) 131-140.

[122] B.C. Gates, Handbook of Heterogeneous Catalysis, vol. 2, pp. 793 and M. Vaarkamp, D.C. Koninsberger, Handbook of Heterogeneous Catalysis vol. 2, pp. 475.

[123] A.I. Frenkel, C.W. Hills, R.G. Nuzzo, J. Phys. Chem. B 105 (2001) 12689-12703.

[124] A. Kulkarni, R. J. Lobo-Lapidus, B. C. Gates Chem. Commun. 46 (2010) 5997-6015.

[125] L. Nagy, T. Yamaguchi, K. Yoshida, Struct. Chem. 14 (2003) 77-84.

[126] T. Egami, S.J.L. Billinge, Underneath the Bragg Peaks: Structural Analysis of Complex Materials, Elsevier, Oxford, 2003.

[127] S.J.L. Billinge, in: R.E. Dinnebier, S.J.L. Billinge (Eds.), Powder Diffraction: Theory and Practice, RSC, London, 2008.

[128] S.J.L. Billinge, J. Solid State Chem. 181 (2008) 1695-1700.

[129] S.J.L. Billinge, M.G. Kanatzidis, Chem. Commun. (2004) 749-760.

[130] S.J.L. Billinge, I. Leven, Science 316 (2007) 561-565.

[131] R.S. Drago, Physical Methods in Chemistry, W. B. Saunders Company, Philadelphia, 1977.

[132] D.C. Harris, M.D. Bertolucci, Symmetry and Spectroscopy: An Introduction to Vibrational and Electronic Spectroscopy, Oxford University Press Inc., New York, 1978.

[133] J.C. Fierro-Gonzalez, S. Kuba, Y. Hao, B.C. Gates, J. Phys. Chem. B 110 (2006) 13326-13351.

[134] J.D. Aiken, R.G. Finke, J. Mol. Catal. A: Chem. 145 (1999) 1-44.

[135] D.B. Williams, C.B. Carter, Transmission Electron Microscopy, Plenum Press, New York, 1996, Ch. 4.

[136] M. Jacoby C&E News 86 (2008) 31-34.

[137] H. Knözinger, in: G. Ertl, H. Knözinger, J. Weitkamp (Eds.), Handbook of Heterogeneous Catalysis, vol.2, VCH, Weinham, 1997, pp. 676-689.

[138] A. K. Galwey, M. E. Brown Thermochim. Acta. 269 (1995) 1-25.

[139] M.E. Brown, J. Therm. Anal. 49 (1997) 17-32.

[140] A.K. Galwey, Thermochim. Acta 413 (2004) 139-183.

[141] A.K. Galwey, J. Therm. Anal. Calorim. 92 (2008) 967-983.

[142] R.M. Dessau, J. Catal. 77 (1982) 304-306.

[143] F. Ribeiro, C. Marcilly, M. Guisnet, J. Catal. 78 (1982) 275-280.

[144] A.I. Mashchenko, O.D. Bronnikov, R.V. Dmitriev, V.I. Garanin, V.B. Kazanskii,

K.M. Minachev, Kinet. Catal. 15 (1974) 1418-1419.

[145] W.J. Reagan, A.W. Chester, G.T. Kerr, J. Catal. 69 (1981) 89-100.

[146] D. Exner, N. Jaeger, K. Moller, G. Schulz-Ekloff, J. Chem. Soc. Faraday Trans. 78 (1982) 3537-3544.

[147] W.M.H. Sachtler, M.S. Tzou, F.J. Jiang, Solid State Ionics 26 (1988) 71-76.

[148] M.S. Tzou, B.K. Teo, W.M.H. Sachtler, J. Catal. 113 (1988) 220-235.

[149] S.T. Homeyer, W.M.H. Sachtler, J. Catal. 117 (1989) 91-101.

[150] A. Paez-Munoz, D.C. Koningsberger, J. Phys. Chem. 99 (1995) 4193-4204.

[151] A.C.M. van den Broek, J. van Grondelle, R.A. van Santen, J. Catal. 167 (1997) 417-424.

[152] J.B. Uytterhoeven, Acta. Phys. Chem. 24 (1978) 53-69.

[153] P.A. Jacobs, Stud. Surf. Sci. Catal. 12 (1982) 71-85.

[154] D. Delafosse, J. Chim. Phys. 83 (1986) 791-799.

[155] P.A. Jacobs, Carboniogenic Activity of Zeolites, Elsevier Scientific Publishing Company, New York, 1977, pp. 184-227.

[156] M.A. Watzky, E.E. Finney, R.G. Finke, J. Am. Chem. Soc. 130 (2008) 11959-11969.

[157] M.A. Watzky, R.G. Finke, Chem. Mater. 9 (1997) 3083-3095.

[158] H.L. Coonradt, F.G. Ciapetta, W.E. Garwood, W.K. Leaman, J.N. Miale, Ind. Eng. Chem. 53 (1961) 727-732.

[159] M.J. Sterba, V. Haensel, Ind. Eng. Chem., Prod. Res. Dev. 15 (1976) 2-17.

[160] C.N. Satterfield, Heterogeneous Catalysis in Practice, McGraw-Hill Inc., New York, 1980.

[161] L.R. Gellens, W.J. Mortier, J.B. Uytterhoeven, Zeolites 1 (1981) 85-90.

[162] W.A. Spieker, J. Liu, J.T. Miller, A.J. Kropf, J.R. Regalbuto, Appl. Catal. A 232 (2002) 219-235.

[163] W.A. Speiker, J. Liu, J.T. Miller, A.J. Kropf, J.R. Regalbuto, Appl. Catal. A 243 (2003) 52-66.

[164] B.N. Shelimov, J.-F. Lambert, M. Che, B. Didillon, J. Mol. Catal. A: Chem. 158 (2000) 91-99.

[165] T. Mang, B. Breitshceidel, P. Polanek, H. Knözinger, Appl. Catal. A 106 (1993) 239-258.

[166] J.P. Brunelle, Pure Appl. Chem. 50 (1978) 1211-1229.

[167] M. Haruta, Cattech 6 (2002) 102-115.

[168] S. Wang, K. Qian, X. Bi, W. Huang, J. Phys. Chem. C 113 (2009) 6505-6510.

[169] A.M. Morris, O.P. Anderson, R.G. Finke, Inorg. Chem. 48 (2009) 4411-4420.

[170] T.M. Anderson, W.A. Neiwert, M.L. Kirk, P.M.B. Piccoli, A.J. Schultz, T.F. Koetzle, D.G. Musaev, K. Morokuma, R. Cao, C.L. Hill, Science 306 (2004) 2074-2077.

[171] R. Cao, T.M. Anderson, D.A. Hillesheim, P. Kögerler, K.I. Hardcastle, C.L. Hill, Angew. Chem. Int. Ed. 47 (2008) 9380-9382.

[172] U. Lee, H.-C. Joo, K.-M. Park, S. S. Mal, U. Kortz, B. Keita, L. Nadjo, Angew. Chem. Int. Ed. 47 (2008) 793-796.

[173] U. Kortz, U. Lee, H.-C. Joo, K.-M. Park, S.S. Mal, M.H. Dickman, G.B. Jameson, Angew. Chem. Int. Ed. 47 (2008) 9383-9384.

[174] G.A. Ozin, M.D. Baker, J. Godber, J. Phys. Chem. 88 (1984) 4902-4904.

[175] P.A. Jacobs, J.B. Uytterhoeven, H.K. Beyer, J. Chem. Soc. Faraday Trans. 75 (1979) 56-64.

[176] Y. Kim, K. Seff, J. Am. Chem. Soc. 99 (1977) 7055-7057.

[177] Y. Kim, K. Seff, J. Am. Chem. Soc. 100 (1978) 175-180.

[178] R. Kellerman, J. Texter, J. Chem. Phys. 70 (1979) 1562-1563.

[179] L.R. Gellens, W.J. Mortier, R.A. Schoonheydt, J.B. Uytterhoeven, J. Phys. Chem. 85 (1981) 2783-2788.

[180] L.R. Gellens, W.J. Mortier, J.B. Uytterhoeven, Zeolites 1 (1981) 11-18.

[181] G.A. Ozin, F. Hugues, J. Phys. Chem. 87 (1983) 94-97.

[182] J. Michalik, L. Kevan, J. Am. Chem. Soc. 108 (1986) 4247-4253.

[183] J. Texter, R. Kellerman, T. Gonsiorowski, J. Phys. Chem. 90 (1986) 2118-2124.

[184] N.D. Cvjeticanin, N.A. Petranovic, Zeolites 14 (1994) 35-41.

[185] T. Sun, K. Seff, Chem. Rev. 94 (1994) 857-870.

[186] R. Schollner, H.K. Beyer, Zeolites 4 (1984) 61-66.

[187] M.D. Baker, G.A. Ozin, J. Godber, J. Phys. Chem. 89 (1985) 305-311.

[188] M.D. Baker, J. Godber, G.A. Ozin, J. Phys. Chem. 89 (1985) 2299-2304.

[189] W. C. Conner, Jr, J. L. Falconer, Chem. Rev. 95 (1995) 759-788.

[190] B.J. Hornstein, R.G. Finke, Chem. Mater. 16 (2004) 139-150. (see also: Chem. Mater. 16 (2004) 3972).

[191] C. Besson, E.E. Finney, R.G. Finke, J. Am. Chem. Soc. 127 (2005) 8179-8184.

[192] C. Besson, E.E. Finney, R.G. Finke, Chem. Mater. 17 (2005) 4925-4938.

[193] M.A. Watzky, R.G. Finke, J. Am. Chem. Soc. 119 (1997) 10382-10400.

[194] A recent review of the kinetic and mechanistic studies of transition-metal nanoparticle nucleation and growth, with an emphasis on the nucleation process, has appeared. E.E. Finney, R.G. Finke, J. Colloid Interface Sci. 317 (2008) 351-374.

[195] A. Henglein, M. Giersig, J. Phys. Chem. B 103 (1999) 9533-9539.

[196] J. Wang, H.F.M. Boelens, M.B. Thatagar, G. Rothenberg, ChemPhysChem 5 (2004) 93-98.

[197] R. Patakfalvi, S. Papp, I. Dékány, J. Nanoparticle Res. 9 (2007) 353-364.

[198] M. Harada, E. Katagiri, Langmuir 26 (2010) 17896-17905.

[199] T. Koenig, R.G. Finke, J. Am. Chem. Soc. 110 (1988) 2657-2658.

[200] T.W. Koenig, B.P. Hay, R.G. Finke, Polyhedron 7 (1988) 1499-1516.

[201] D.H. Leung, R.G. Bergman, K.N. Raymond, J. Am. Chem. Soc. 130 (2008) 2798-2805.

[202] J. Evans, in: J.-M. Basset, B.C. Gates, J.-P. Candy (Eds.), Surface Organometallic Chemistry: Molecular Approaches to Surface Catalysis, Kluwer, Dordrecht, 1988, pp. 47-73.

[203] H.H. Lamb, B.C. Gates, H. Knozinger, Angew. Chem. Int. Ed. 27 (1988) 1127-1144.

[204] J.-M. Basset, F. Lefebvre, C. Santini, Coord. Chem. Rev. 178-180 (1998) 1703-1723.

[205] T.J. Marks, Acc. Chem. Res. 25 (1992) 57-65.

[206] J.F. Walzer Jr., U.S. Patent 5,643,847 1997.

[207] A. Uzun, D.A. Dixon, B.C. Gates, Chem. Cat. Chem. 3 (2011) 95-107.

[208] K.J.J. Mayrhofer, V. Juhart, K. Hartl, M. Hanzlik, M. Arenz, Angew. Chem. Int. Ed. 48 (2009) 3529-3531.

[209] R. Dellapergola, L. Garlaschelli, S. Martinengo, Inorg. Synth. 28 (1990) 245-247.

[210] A. Uzun, V. A. Bhirud, P. W. Kletnieks, J. F. Haw, B. C. Gates J. Phys. Chem. C 111 (2007) 15064-15073.

[211] V. Ortalan, A. Uzun, B. G. Gates, N. D. Browning Nature Nanotechnology 5 (2010) 506-510.

[212] P. Serna, B. C. Gates J. Am. Chem. Soc. 133 (2011) 4714-4717.

[213] A. Uzun, B.C. Gates, J. Am. Chem. Soc. 131 (2009) 15887-15894.

[214] E. Bayram, J. Lu, C. Aydin, A. Uzun, N.D. Browning, B.C. Gates, R.G. Finke, "*Investigation of the Catalytically Active Species when Starting with Well-Characterized, Site-Isolated [Ir(C_2H_4)$_2$]/zeolite-Y Complex in Contact with Solution via the Cyclohexene Hydrogenation Reporter Reaction and Post-Kinetic Structural Analyses via EXAFS and HAADF-STEM*" (Tentative Title).

[215] J.D. Aiken, Y. Lin, R.G. Finke, J. Mol. Catal. A: Chem. 114 (1996) 29-51.

[216] A.C. Templeton, W.P. Wuelfing, R.W. Murray, Acc. Chem. Res. 33 (2000) 27-36.

[217] R.M. Crooks, M. Zhao, L. Sun, V. Chechik, L.K. Yeung, Acc. Chem. Res. 34 (2001) 181-190.

[218] H. Bönnemann, R.M. Richards, Eur. J. Inorg. Chem. (2001) 2455-2480.

[219] A. Roucoux, J. Schulz, H. Patin, Chem. Rev. 102 (2002) 3757-3778.

[220] B.L. Cushing, V.L. Kolesnichenko, C.J. O'Connor, Chem. Rev. 104 (2004) 3893-3946.

[221] D. Astruc, F. Lu, J.R. Aranzaes, Angew. Chem. Int. Ed. 44 (2005) 7852-7872.

[222] J.P. Wilcoxon, B.L. Abrams, Chem. Soc. Rev. 35 (2006) 1162-1194.

[223] L.S. Ott, R.G. Finke, Coord. Chem. Rev. 251 (2007) 1075-1100.

[224] E.G. Mednikov, M.C. Jewell, L.F. Dahl, J. Am. Chem. Soc. 129 (2007) 11619-11630. Also see the extensive references therein for similar nanosized clusters, "nanoclusters".

[225] P.D. Jadzinsky, G. Calero, C.J. Ackerson, D.A. Bushnell, R.D. Kornberg, Science 318 (2007) 430-433.

[226] M.W. Heaven, A. Dass, P.S. White, K.M. Holt, R.W. Murray, J. Am. Chem. Soc. 130 (2008) 3754-3755.

[227] H. Qian, R. Jin, Nano Lett. 9 (2009) 4083-4087.

[228] H. Qian, W.T. Eckenhoff, Y. Zhu, T. Pintauer, R. Jin, J. Am. Chem. Soc. 132 (2010) 8280-8281.

[229] J.F. Parker, C.A. Fields-Zinna, R.W. Murray, Acc. Chem. Res. 43 (2010) 1289-1296.

[230] Y. Levi-Kalisman, P.D. Jadzinsky, N. Kalisman, H. Tsunoyama, T. Tsukuda, D.A. Bushnell, R.D. Kornberg, J. Am. Chem. Soc. 133 (2011) 2976-2982.

[231] B. Corain, G. Schmid, N. Toshima (Eds.), Metal Nanoclusters in Catalysis and Materials Science: The Issue of Size Control, Elsevier, Amsterdam, 2008.

[232] T.S. Ahmadi, Z.L. Wang, T.C. Green, A. Henglein, M.A. El-Sayed, Science 272 (1996) 1924-1926.

[233] C. Burda, X. Chen, R. Narayanan, M.A. El-Sayed, Chem. Rev. 105 (2005) 1025-1102.

[234] A.R. Tao, S. Habas, P. Yang, Small 4 (2008) 310-325.

[235] Y. Xia, Y. Xiong, B. Lim, S.E. Skrabalak, Angew. Chem. Int. Ed. 48 (2009) 60-103.

[236] C.B. Murray, Science 324 (2009) 1276-1277.

[237] M. Harada, Y. Inada, Langmuir 25 (2009) 6049-6061.

[238] J. Polte, T.T. Ahner, F. Delissen, S. Sokolov, F. Emmerling, A.F. Thunemann, R. Kraehnert, J. Am. Chem. Soc. 132 (2010) 1296-1301.

[239] J. Polte, R. Erler, A.F. Thunemann, S. Sokolov, T.T. Ahner, K. Rademann, F. Emmerling, R. Kraehnert, ACS Nano 4 (2010) 1076-1082.

[240] T. Yao, Z. Sun, Y. Li, Z. Pan, H. Wei, Y. Xie, M. Nomura, Y. Niwa, W. Yan, Z. Wu, Y. Jiang,Q. Liu, S. Wei, J. Am. Chem. Soc. 132 (2010) 7696-7701.

[241] Z. Kónya, V.F. Puntes, I. Kiricsi, J. Zhu, J.W. Ager III, M.K. Ko, H. Frei, P. Alivisatos, G.A. Somorjai, Chem. Mater. 15 (2003) 1242-1248.

[242] N. Zheng, G.D. Stucky, J. Am. Chem. Soc. 128 (2006) 14278-14280.

[243] I. Lee, R. Morales, M.A. Albiter, F. Zaera, Proc. Natl. Acad. Sci. 105 (2005) 15241-15246.

[244] X. Huang, C. Guo, J. Zuo, N. Zheng, G.D. Stucky, Small 5 (2009) 361-365.

[245] M. Boualleg, J.-M. Basset, J.-P. Candy, P. Delichere, K. Pelzer, L. Veyre, C. Thieuleux, Chem. Mater. 21 (2009) 775-777.

[246] Y. Zhu, H. Qian, B.A. Drake, R. Jin, Angew. Chem. Int. Ed. 49 (2010) 1295-1298.

[247] R.M. Rioux, H. Song, J.D. Hoefelmeyer, P. Yang, G.A. Somorjai, J. Phys. Chem. B 109 (2005) 2192-2202.

[248] H. Song, R.M. Rioux, J.D. Hoefelmeyer, R. Komor, K. Niesz, M. Grass, P. Yang, G.A. Somorjai, J. Am. Chem. Soc. 128 (2006) 3027-3037.

[249] L.S. Ott, B.J. Hornstein, R.G. Finke, Langmuir 22 (2006) 9357-9367.

[250] H. Eniaga, M. Harada, Langmuir 21 (2005) 2578-2584.

[251] R.M. Rioux, B.B. Hsu, M.E. Grass, H. Song, G.A. Somorjai, Catal. Lett. 126 (2008) 10-19.

[252] Y.L. Borodko, L. Jones, H. Lee, H. Frei, G.A. Somorjai, Langmuir 25 (2009) 6665-6671.

[253] S. Pang, Y. Kurosawa, T. Kondo, T. Kawai, Chem. Lett. 34 (2005) 544-545.

[254] W. Chen, J. Kim, S. Sun, S. Chen, Phys. Chem. Chem. Phys. 8 (2006) 2779-2786.

[255] J.Y. Park, C. Aliaga, J. Russell-Renzas, H. Lee, G.A. Somorjai, Catal. Lett. 129 (2009) 1-6.

[256] C. Aliaga, J.Y. Park, Y. Yamada, H. Sook Lee, C.-H. Tsung, P. Yang, G.A. Somorjai, J. Phys. Chem. C 113 (2009) 6150-6155.

[257] A.S. Eppler, J. Zhu, E.A. Anderson, G.A. Somorjai, Top. Catal. 13 (2000) 33-41.

[258] H. Lang, R. A. May, B.L. Iversen, B.D. Chandler, J. Am. Chem. Soc. 125 (2003) 14832-14836.

[259] D. Liu, J. Gao, C.J. Murphy, C.T. Williams, J. Phys. Chem. B 108 (2004) 12911-12916.

[260] A. Singh, B.D. Chandler, Langmuir 21 (2005) 10776-10782.

[261] D.S. Deutsch, A. Siani, P.T. Fanson, H. Hirata, S. Matsumoto, C.T. Williams, M.D. Amiridis, J. Phys. Chem. C 111 (2007) 4246-4255.

[262] M.A. Albiter, F. Zaera, Langmuir 26 (2010) 16204-16210.

[263] K.P. De Jong, J.W. Geus, Appl. Catal. A: General 4 (1982) 41-51.

[264] G.C. Bond, A.F. Rawle, J. Mol. Catal. A: Chem. 109 (1996) 261-271.

[265] E.A. Sales, B. Benhamida, V. Caizergues, J.-P. Lagier, F. Fievet, F. Bozon-Verduraz, Appl. Catal. A: General 172 (1998) 273-283.

[266] Y. Guari, C. Thieuleux, A. Mehdi, C. Reyé, R.J.P. Corriu, S. Gomez-Gallardo, K. Philippot, B. Chaudret, R. Dutartre, Chem. Commun. (2001) 1374-1375.

[267] G. Marconi, P. Pertici, C. Evangelisti, A.M. Caporusso, G. Vitulli, G. Capannelli, M. Hoang, T.W. Turney, J. Organomet. Chem. 689 (2004) 639-646.

[268] V. Hulea, D. Brunel, A. Galarneau, K. Philippot, B. Chaudret, P.J. Kooyman, F. Fajula, Micropor. Mesopor. Mater. 79 (2005) 185-194.

[269] Y. Jiang, Q. Gao, J. Am. Chem. Soc. 128 (2006) 716-717. (i) L.-S. Zhong, J.-S. Hu, Z.-M. Cui, L.-J. Wan, W.-G. Song, Chem. Mater. 19 (2007) 4557-4562.

[270] M. Zawadzki, J. Okal, Mater. Res. Bull. 43 (2008) 3111-3121.

[271] M. Boutros, A. Denicourt-Nowicki, A. Roucoux, L. Gengembre, P. Beaunier, A. Gedeon, F. Launay, Chem. Commun. (2008) 2920-2922.

[272] R. Xing, Y. Liu, H. Wu, X. Li, M. He, P. Wu, Chem. Commun. (2008) 6297-6299.

[273] M.A. Elmoula, E. Panaitescu, M. Phan, D. Yin, C. Richter, L.H. Lewis, L. Menon, J. Mater. Chem. 19 (2009) 4483-4487.

[274] Y. Xie, K. Ding, Z. Liu, R. Tao, Z. Sun, H. Zhang, G. An, J. Am. Chem. Soc. 131 (2009) 6648-6649.

[275] E. Besson, A. Mehdi, C. Reye, R.J.P. Corriu, J. Mater. Chem. 19 (2009) 4746-4752.

[276] M. Zahmakiran, S. Özkar, Langmuir 25 (2009) 2667-2678.

[277] M. Zahmakiran, S. Özkar, J. Am. Chem. Soc. 132 (2010) 6541-6549.

[278] S. Özkar, R. G. Finke J. Am. Chem. Soc. 127 (2005) 4800-4808.

[279] L. Starkey Ott, R. G. Finke Inorg. Chem. 45 (2006) 8382-8393.

[280] J.I. Jeong, M. Choi, Aerosol Sci. 34 (2003) 965-976.

[281] E.E. Finney, R.G. Finke, Chem. Mater. 21 (2009) 4692-4705.

[282] A.M. Morris, M.A. Watzky, R.G. Finke, Biochim. Biophys. Acta 1794 (2009) 375-397.

[283] William of Ockham, 1285-1349, as cited by E. A. Moody in, The Encyclopedia of Philosophy, vol 7, McMillan, 1967.

[284] R.J. Field, E. Koros, R.M. Noyes, J. Am. Chem. Soc. 94 (1972) 8649-8664.

[285] R.J. Field, R.M. Noyes, J. Chem. Phys. 60 (1974) 1877-1884.

[286] R.J. Field, R.M. Noyes, Acc. Chem. Res. 10 (1977) 214-221.

[287] J.D. Aiken III, R.G. Finke, J. Am. Chem. Soc. 120 (1998) 9545-9554.

[288] Y. Lin, R.G. Finke, Inorg. Chem. 33 (1994) 4891-4910.

[289] J.A. Widegren, M.A. Bennett, R.G. Finke, J. Am. Chem. Soc. 125 (2003) 10301-10310.

[290] R.G. Finke, S. Özkar, Coord. Chem. Rev. 248 (2004) 135-146.

[291] J.A. Widegren, J.D. Aiken III, S. Özkar, R.G. Finke, Chem. Mater. 13 (2001) 312-324.

Supporting Information for:

A Review of the Kinetics and Mechanisms of Formation of Supported-Nanoparticle Heterogeneous Catalysts

Joseph E. Mondloch, Ercan Bayram and Richard G. Finke

Table S1 is a compilation of the 39 primary references regarding practical supported-nanoparticle heterogeneous catalyst formation at the gas-solid interface. 25 of the 39 papers are given in Table 2 of the main text, but are reproduced here so that those 39 references are neatly contained in one Table. Table S1 is listed in chronological order, dating from 1972 to present and contains: (i) the experimental details regarding the preparation of the supported metal precatalyst and then on the generation of the supported-nanoparticle heterogeneous catalyst; (ii) information on whether the study contains kinetic data (and if so, the physical method by which that kinetic data were obtained); and (iii) if kinetic data were obtained, was it collected isothermally or non-isothermally (see the main text, and footnote 8 also of the main text, for a more detailed discussion regarding this point). Also given in Table S1 is (iv) whether the stoichiometry of the supported-nanoparticle heterogeneous catalyst formation reaction was explicitly demonstrated (and if so, how that stoichiometry was obtained); and (v) if available the rate equations and proposed mechanism, as given by the original authors. Note that unless stated, the mechanisms are written as proposed originally by the authors as to avoid confusion.

Table S1. Listed chronologically are the 39 papers within the literature regarding the kinetics and mechanisms of the formation of supported-nanoparticle heterogeneous catalysts at the gas-solid interface.

Entry [Reference]	*Authors*	*System Studied*	*Kinetic Data (Physical Method Employed)*	*Isothermal Kinetic Data*	*Stoichiometry (Physical Method Employed)*	*Proposed Mechanism(s) and Rate Equations as Written by the Original Authors (If Available)*
1 [1]	Dalla Betta, R. A. Boudart, M.	5-wt% $Pt(NH_3)_4Cl_2$ was ion-exchanged onto zeolite Y and reduced under H_2 from 25 to 350 ºC. The effects of calcination and H_2O were also investigated.	Yes (IR spectroscopy)	No	Yes (H_2 uptake)	*Proposed Mechanism.* Aggregation is proposed to be due to "the unstable neutral, hence mobile, hydride (i.e, Pt–H), (which) leads to Pt agglomeration", as shown in Scheme 3 of the main text.
2 [2]	Herd, A. C.; Pope, G. C.	$Ni(NO_3)_2$ ion-exchanged on zeolite NaX, and reduced under H_2 between 638 and 793 K	Yes (H_2 uptake)	Yes	Yes (H_2 uptake)	*Proposed Mechanism.* (i) Chemisorption of H_2 on Ni^{2+} ions (ii) Reduction of the Ni ions and simultaneous back reaction (shown below) (iii) Migration and aggregation of Ni atoms. 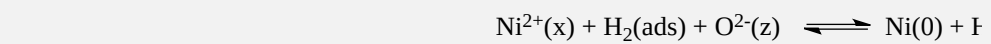 *Proposed Rate Law.* $-\frac{dP}{dt} = k_1(kP^{\alpha})[Ni_x^{2+}] - k_2[Ni^0][H_2O(z)]$ where P is the H_2 pressure, $P\alpha$ the chemisorbed H_2, k_1 and k_2 the surface reaction rate constants and $[Ni_x^{2+}]$ the concentration of nickel ions at site x.
3	Kermarec,	Ni^{2+} ion-exchanged	Yes	Yes	Yes	*Proposed Rate Equation/Model.*

[3]	M.; Briend-Faure, M.; Delafosse, D.	on zeolite NaX and a silica magnesia gel and reduced under H_2 at temperatures between 498 and 653 K.	(H_2 uptake)			$\frac{3}{(1-\alpha)^{\frac{1}{3}}} + \log(1-\alpha) = kt$ where α is the degree of precursor reduction
4 [4]	Beyer, H.; Jacobs, P. A.; Uytterhoeven, J. B.	$AgNO_3$ is ion-exchanged on zeolite NaY and reduced under H_2. Prior to reduction the samples were out gassed and calcined at 373, 473 and 623 K and subsequently reduced under H_2 isothermally between 298 and 623 K.	Yes (H_2 uptake)	Yes	Yes (H_2 uptake)	*Observed Rate Law: Low Temperature (≤ 430 K).* $\frac{dc}{dt} = k' P \frac{(C_0' - C)}{C}$ P = H_2 pressure, C_0' = Initial Ag^+, C = the reduced form of Ag^+ at time t *Proposed Mechanism #1 (Low Temperature): H_2 Activation on Ag^+* $H_2 + Ag^+ \rightleftharpoons (Ag^+H^-) + H^+$ $(Ag^+H^-) \xrightarrow{RDS} (Ag^0H)$ $Ag^+ + (Ag^0H) \rightleftharpoons H^+ + Ag_2$ *Proposed Mechanism #2 (Low Temperature): H_2 Activation at Some Surface Site (S)* $H_2 + S \rightleftharpoons (SH\text{-}H)$ $(SH\text{-}H) + Ag^+ \rightleftharpoons (SH\text{-}Ag) + H^+$ $(SH\text{-}H) + Ag+ \xrightarrow{RDS} S + H^+ + 2\,Ag$ *Observed Rate Law: High Temperature >430 K).* $\frac{dc}{dt} = k_1(C_0 - C)$ C_0 = Initial Ag^+, C = the reduced form of Ag^+ at time t

						Proposed Mechanism (High Temperature). The reduction is "rate-controlled by the *migration of* Ag^+ *ions*" to activated H_2 somewhere within the zeolite.
5 [5]	Jacobs, P. A.; Tielen, M.; Linart, J.-P.; Uytterhoeven, J. B.; Beyer, H.	$CuCl_2$ was non-stoichiometrically ion-exchanged onto zeolite NaY, dehydrated under vacuum at 673 K and reduced under H_2 at 400 K. (Other conditions were also investigated but did not lead to Cu(0) formation).	Yes (H_2 uptake)	Yes [6]	Yes (H_2 uptake)	*Inferred Observed Rate Law (Not Explicitly Written by Jacobs and Co-Workers).* $$-\frac{d[Cu^+]}{dt} = k[Cu^+]^2$$ No mechanism was proposed for the Cu^{2+} to Cu(0) supported-nanoparticle heterogeneous catalyst formation reaction.
6 [7]	Briend-Faure, M.; Delafosse, D.	Ni^{2+} substituted on a silica-magnesia gel (*not described in detail*) and reduced under H_2 from 613 to 753 K.	Yes (H_2 uptake)	Yes	Yes (H_2 uptake)	*Observed Rate Equation/Model.* $$[-\log(1-\alpha)] = Kt^n$$ where α is the degree of precursor reduction and *n* is a fractional number, the value of which depends on the presence of chemisorbed H_2O. *Proposed Mechanism.*

						$H_2 + Site \underset{k'_1}{\overset{k_1}{\rightleftharpoons}} 2H/Site$ $2H/Site + 2\ Ni^{2+} \underset{k'_2}{\overset{k_2}{\rightleftharpoons}} H\text{-}OH/Site + Ni($ $H_2O/Site \underset{k'_3}{\overset{k_3}{\rightleftharpoons}} H_2O + Site$ Where steps two and three were proposed to be co-rate-determining and "site" has been added for clarity.
7 [8]	Briend-Faure, M.; Jeanjean, J.; Kermarec, M.; Delafosse, D.	$Ni(NO_3)_2 \bullet 6H_2O$ was ion-exchanged onto zeolites NaX and NaY, heated to 773 K for 15 h under vacuum and reduced under H_2 between 473 and 873 K.	Yes (H_2 uptake)	Yes	Yes (H_2 uptake)	*Proposed Rate Equation/Model.* $\frac{3}{(1-\alpha)^{\frac{1}{3}}} + \log(1-\alpha) - 3 = kt$ where α is the degree of precursor reduction. *Proposed Mechanism.* The above model "expresses a diffusion mechanism in the case where there is steady state formation of a reaction front, with a diffusion coefficient *D*".
8 [9]	Hermer-schmidt, D.; Haul, R.	$AgNO_3$ was ion-exchanged onto zeolites X and A. The samples were dehydrated under O_2 at 400 °C and reduced under H_2 isothermally between -50 and	Yes (ESR)	Yes	No	No mechanism was proposed for the supported-nanoparticle heterogeneous catalyst formation reaction.

		400 ºC.				
9 [10]	Beyer, H. K.; Jacobs, P. A.	$Ag(NO)_3$ was ion-exchanged onto the chabsite zeolite. The samples were isothermally reduced under H_2 at varying temperatures between 295 and 613K.	Yes (H_2 uptake)	Yes	Yes (H_2 uptake)	*Observed Rate Law* $\frac{d[Ag^+]}{dt} = k[Ag^+]^2[P_{H_2}]^{\frac{1}{2}}$ *Proposed Mechanism* $H_2 \rightleftharpoons 2\,H\bullet$ $H\bullet + Ag^+ \rightleftharpoons [Ag(0)H^+]$ $[Ag(0)H^+] + Ag^+ \overset{RDS}{\rightleftharpoons} Ag_2^+ + H^+$
10 [11]	Dexpert, H.	H_2PtCl_6 was impregnated onto Al_2O_3. The samples were reduced under H_2 at room temperature or 200 ºC.	Yes (XANES & EXAFS)	Yes	No	*Proposed Mechanism.* A summary of the author's word-based mechanism for the "decomposition of the isolated $PtCl_6^{2-}$ complexes" is: (i) oxygen starts to replace the chlorine atoms; (ii) a chlorinated Pt dimer is formed, and (iii) the dimer grows as the reduction continues.
11 [12]	Tzou, M. S.; Sachtler, W. M. H.	7.4-wt% $Pt(NH_3)_4Cl_2$ was ion-exchanged onto zeolite NaY. The resultant precatalyst was calcined between 360 and 550 °C and reduced under H_2 at 500 °C.	Yes (H_2 chemisorption)	Yes	No	*Proposed Mechanism of Subnanometer $Pt(0)_n$/Zeolite–Y Formation.* Calcination at 360 °C afforded Pt^{2+} ions in the zeolite supercages, which are easily reduced with H_2 between -15 and 150 °C. "Growth" kinetics were obtained by monitoring the change in the Pt dispersion by H_2 chemisorption. The H_2 chemisorption data "favor the mechanism of particle growth by migration and coalescence of particles rather than Ostwald ripening, that is by atomic migration".

						Proposed Mechanism of 10-50 nm $Pt(0)_n$/Zeolite–Y Formation. Calcination at 550 °C afforded Pt^{2+} ions in the sodalite cages. The Pt^{2+} ions are reduced and driven to a location where $Pt(0)_n$ particles can form. "Two stages can be discerned: (a) nucleation and (b) growth of particles". The Pt(0) atoms can migrate to the surface of the zeolite.
12 [13]	Le Normand, F.; Bazin, D.; Dexpert, H.; Lagarde, P.; Bournonville, J. P.	H_2PtCl_6 was impregnated onto γ-Al_2O_3. The catalyst was dried @ 120 °C and reduced under H_2 at 300 °C.	Yes (XANES & EXAFS)	Yes	No	No mechanism was proposed, but qualitatively the authors state that: (i) "*the reduction rate tends to increase with the time of isothermal reduction*", which may be due to spillover, and (ii) that "*the isothermal reduction is associated with the growth of Pt clusters*".
13 [14]	Homeyer, S. T.; Sachtler, W. M. H.	2–7-wt% $[Pd(NH_3)_4]$ $(NO_3)_2$ was ion-exchanged onto zeolite NaY. The sample was calcined at 250 and 500 °C and then reduced under a temperature ramp from -80 to 350 °C.	No		Yes (H_2 Uptake)	*Proposed Mechanism when Pd Ions are in the Supercages.* "Pd ions migrate to an activated nucleus where they are reduced, forming primary particles. These migrate through the supercage network until they either contact another primary or secondary particle. Once all the primary particles are used up, further growth of the secondary particles occurs via a different mechanism, possibly involving Ostwald ripening or local collapse of the zeolite matrix". *Proposed Mechanism when Pd Ions are in the Sodalite Cages.* "Pd atoms are released into the supercage network at higher temperatures, where they form secondary particles either through migration and coalescence or by trapping

						Pd atoms as they leave the sodalite cages".
14 [15]	Schoonheydt, R. A.; Leeman, H.	$AgNO_3$ was ion-exchanged onto zeolite NaA. The samples were calcined at 673 K and reduced under H_2 between 253 and 298 K. All manipulations were carried out in the dark.	Yes (ESR)	Yes	No	*Proposed Mechanism.* 
15 [16]	Bazin, D.; Dexpert, H.; Bournonville, J. P.; Lynch, J.	H_2PtCl_6 and NH_4ReO_4 or H_2PtCl_6 and $RhCl_3 \cdot 3H_2O$ were deposited onto γ-Al_2O_3 via successive impregnation. The samples were dried and calcined and reduced under H2 during a temperature ramp from 22–100 °C.	Yes (XANES & EXAFS)	No	No	No mechanism was proposed for the supported-nanoparticle heterogeneous catalyst formation reaction.
16 [17]	Che, M; Cheng, Z. X.; Louis, C.	The basic preparation of the precatalyst contains two steps: (i) cation exchange of $[Ni(NH_3)_6]^{2+}$	No	No	No	*Proposed Mechanism.* The authors believe that Ni particles form via nucleation and growth and consider two mechanisms of $Ni(0)_n/SiO_2$ formation: (i) reduction of Ni^{2+} to Ni(0) and subsequent formation of $Ni(0)_n$ and (ii) formation of

		(generated *in situ*) on SiO_2 or cation exchange of $[Ni(en)_3]^{2+}$ onto SiO_2 followed by (ii) a subsequent impregnation of $Ni(NO_3)_2$. Samples were typically dried and calcined in O_2 between the ion-exchange and impregnation steps and reduced under H_2 after the impregnation step in a temperature ramp from room temperature to 700 °C.				$(NiO)_n$ followed by reduction to $Ni(0)_n$. The authors favor mechanism (ii) based on product evidence post the drying and calcination treatments.
17 [18]	Nasher, M. S.; Frenkel, A. I.; Somerville, D.; Hills, C. W.; Shaplye, J. R.; Nuzzo, R. G.	1–2-wt% $PtRu_5C(CO)_{16}$ was deposited on carbon black via incipient wetness from THF. The sample was allowed to dry in air for 1 h and evacuated for 1 h and reduced under H_2 from 150 to 773 K.	Yes (XANES & EXAFS)	No	No	*Proposed Mechanism.* "…the initial nucleation of a compact (Pt-rich) structure (is) followed by the inversion of the intraparticle distribution of the Pt and Ru atoms upon continued high-temperature annealing. In this inversion, the core-segregated Pt atoms exchange with Ru surface atoms to form a surface Pt shell structure".
18	Yamaguchi, A.; Shido, T.;	$Cu(NO_3)_2$ was ion-exchanged onto	Yes (XANES &	No	No	No mechanism was proposed for the supported-nanoparticle heterogeneous

[19]	Inada, Y.; Kogure, T.; Asakura, K.; Nomura M.; Iwasawa, Y.	zeolite ZSM-5. The samples were washed, dried and then calcined at 773 K prior to reduction with H_2 under a temperature ramp from ~300–600 K.	EXAFS)			catalyst formation reaction. These XAFS results also appeared elsewhere, [20,21,22] but no significant advances in understanding the $Cu(0)_n$ particle formation were made vs. Entry 20.
19 [23]	Oudenhuijzen, M. K.; Kooyman, P. J.; Tappel, B.; van Bokhoven, J. A.; Koningsberger, D. C.	1-wt% $[Pt^{2+}(NH_3)_4](NO_3^-)_2$ was impregnated onto SiO_2 by incipient wetness. The precatalyst was dried under N_2 for 1 h at room temperature, followed by 8 h at 80 °C. The precatalyst is then reduced with H_2 under a temperature ramp from room temperature to 400 °C.	Yes (XANES & EXAFS)	No	No	*Proposed Mechanism.* The final size of the Pt particles (when reduced under H_2) is controlled by two parameters, the nucleation rate and the growth rate. "Since the formation of metal–metal bonds adds significantly to the stability of Pt atoms, the reduction of the $Pt^{2+}(NH_3)_x$ complex must involve migration and collision of the Pt^{2+} species with either an earlier formed metallic Pt nucleus or several other Pt^{2+} complexes and reduced at the same moment". The authors propose that a highly mobile hydride species is responsible for the nanoparticle growth, analogous to that reported by Dalla Betta and Boudart [1].
20 [24]	Fiddy, S. G.; Newton, M. A.; Campbell, T.; Dent, A. J.; Harvey, I.; Salvini, G.; Turin, S.;	5-wt% $Pt(acac)_2$ was slurried onto SiO_2 from toluene. The solvent was then removed by rotary evaporation and reduced under H_2 from 300 to 673	Yes (EXAFS)	No	No	*Proposed Mechanism.* "…an initial decomposition of a small fraction of the supported $Pt(acac)_2$ leading to the formation of a low level of small Pt particles….(which are) active for rapid H_2 dissociation and subsequent spillover of atomic hydrogen"

	Evans, J.	K. The authors also looked at a bimetallic system of $Pt(acac)_2$ plus $GeBu_4$.				
21 [25]	Neylon, M. K.; Marshall, C. L.; Kropf, A. J	$Cu(NO_3)_2$ was ion-exchnaged onto the xeolite ZSM-5 from dilute aqueous solution (pH 8.0). The slurry was dried at 110 ºC and calcined in flowing air at 500 ºC for 3 h. The precatalyst was reduced in H_2 under a temperature ramp from 22–800 ºC.	Yes (XANES & EXAFS)	No	Yes (XANES)	No mechanism was proposed for the supported-nanoparticle heterogeneous catalyst formation reaction.
22 [26]	Okumura, K.; Yoshimoto, R.; Uruga, T.; Tanida, H.; Kato, K.; Yokota, S.; Niwa, M.	0.4-wt% $Pd(NH_3)_4Cl_2$ was ion-exchanged onto zeolite Na–ZSM-5, H–ZSM-5 and Y-mordenite. The samples were oxidized at 773 K and then reduced in H_2 up to 750 K.	Yes (EXAFS)	No	No	No mechanism was proposed for the supported-nanoparticle heterogeneous catalyst formation reaction.
23 [27]	Li, F.; Gates, B. C.	1-wt% $Ir(CO)_2(acac)$ was deposited on zeolite NaY from a	Yes (IR Spectroscopy)	Yes	No	No specific mechanism was proposed for the formation of $Ir_4(CO)_{12}$.

		pentane solution. The solvent was removed by evacuation and put under CO at 40 °C.				
24 [28]	Yang, J. H.; Henao, J. D.; Raphulu, M. C.; Wang ,Y.; Caputo, T.; Groszek, A. J.; Kung, M. C.; Scurrell, M. S.; Miller, J. T.; Kung, H. H.	$[AuO_x(OH)_{4-2x}]^{n-}$ /TiO_2 (Au/TiO_2) was prepared via deposition-precipitation from $HAuCl_4$ in aqueous solution. The $[AuO_x(OH)_{4-2x}]^{n-}$ /TiO_2 was reduced under pulses of H_2 gas at 298 K.	Yes (H_2 uptake)	No	Yes (XANES)	No mechanism was proposed for the supported-nanoparticle heterogeneous catalyst formation reaction.
25 [29]	Li, P; Liu, J.; Nag, N.; Crozier, P. A.	$Ni(NO_3)_2 \bullet 6H_2O$ was deposited on TiO_2 via t incipient wetness, dried in air at 120 °C and reduced under CO at 350 °C.	No	No	No	*Proposed Mechanism.* A nucleation and growth mechanism was assumed where by "*most Ni nanoparticles nucleate from the Ni* precursor uniformly coating the titania support". Nucleation occurs readily on both the anatase and rutile phases of the TiO_2. Growth occurs 3 dimensionally and "involves the diffusion of the Ni containing species to the surface of the growing metal particles".
26 [30]	Hwang, B. J.; Chen, C.-H.; Sarma, L. S.; Chen, J.-M.; Wang, G.-R.; Tang, M.-T.; Liu, D.-G.;	Separate solutions of H_2PtCl_6 and $RuCl_3$ were adjusted to pH 7 and 4. Both solutions were reduced using $NaHSO_3$, and H_2O_2	No	No	No	*Proposed Mechanism.* The authors propose that the species $H_2Pt(OH)_6$ and $Ru(OH)_4$ are formed prior to deposition onto the activated carbon support. Upon addition of the support a mixed $(PtRu(O)(OH))_n$ species was formed en route to the $(PtRu)_n$/carbon supported-

	Lee, J.-F.	was added. The two solutions were then mixed at pH 5 and the carbon support was added and stirred for 8 h at 100 °C. After washing with water the colloidal product was reduced with H_2 at 300 °C.				nanoparticles.
27 [31]	Tanaka, H.; M. Uenishi; M. Taniguchi; I. Tan; K. Narita; M. Kimura; K. Kaneko; Y. Nishihata; J. Mizuki	Pd ions were incorporated into the $LaFe_{0.95}Pd_{0.05}O_3$ perovskite structure through a solid-state synthesis. The sample was then reduced under H_2 at 400 °C.	Yes (EXAFS)	Yes	No	*Proposed Mechanism.* A picture-based mechanism was given within the paper, however it does not correspond to any rigorous chemical-based reaction mechanism and hence was not reproduced here.
28 [32]	Chupas, P. J.; Chapman, K. W.; Jennings, G.; Lee, P. L.; Grey, C. P.	5-wt% H_2PtCl_6 was deposited on TiO_2 via incipient wetness. The samples were dried overnight at 60 °C and reduced under H_2 at 100, 150 and 200 °C.	Yes (Total high energy X-ray scattering + PDF analysis)	Yes	No	No mechanism was proposed for the supported-nanoparticle heterogeneous catalyst formation reaction.
29	Shimizu, K.-I.,; Sugino,	$AgNO_3$ was ion-exchanged onto	Yes (EXAFS & UV-	Yes	Yes	No mechanism was proposed for the supported-nanoparticle heterogeneous

[33]	K.; Kato, K.; Yokota, S.; Okumura, K.; Satsuma, A.	zeolite H-MFI. The sample was dried at 383 K for 24 h, calcined at 823 K for 2 h and reduced under H_2 at 573 K.	Vis)		(H_2 uptake)	catalyst formation reaction.
30 [34]	Okumura, K.; Kato, K.; Sanada, T.; Niwa, M.	0.4 and 0.8-wt% Pd $Pd(NH_3)_4Cl_2$ was ion-exchanged onto zeolite H-USY. The samples were calcined under O_2 at 773 K for 4 h and reduced with H_2 under a temperature ramp from room temperature to 773 K.	Yes (EXAFS)	No	Yes (XANES)	No mechanism was proposed for the supported-nanoparticle heterogeneous catalyst formation reaction.
31 [35]	Bus, E.; Prins, R.; van Bokhoven, J. A.	$HAuCl_4$ was either impregnated or deposited/precipitated onto g-Al_2O_3 and TiO_2. The sample was reduced in H_2 at 293 K.	Yes (XANES)	Yes	Yes (XANES)	No mechanism was proposed for the supported-nanoparticle heterogeneous catalyst formation reaction.
32 [36]	Uzun, A.; Gates, B. C.	1-wt% $Ir(C_2H_4)_2(acac)$ was contacted onto dealuminated zeolite–Y from a *n*-pentane slurry. The solvent was	Yes (XANES, EXAFS & IR Spectro-scopies)	No	No	*Proposed Mechanism.* A model was proposed for the formation of $Ir_4(ligand)_x$/zeolite–Y that goes through a $Ir_2(ligand)_x$/zeolite–Y intermediate. A pictorial representation, as proposed by the original authors, is given in Scheme

		removed under vacuum and the sample was reduced under H_2 from 298-353 K.				10 of the main text.
33 [37]	Liang, A. J.; Gates, B. C.	1-wt% $Rh(C_2H_4)(acac)$ was contacted onto dealuminated zeolite–Y from a *n*-pentane slurry. The solvent was removed under vacuum and the sample was reduced under H_2 at 298 K.	Yes (XANES, EXAFS & IR Spectro-scopies)	Yes	No	No mechanism was proposed for the supported-nanoparticle heterogeneous catalyst formation reaction.
34 [38]	Okumura, K.; Honma, T.; Hirayama, S.; Sanada, T.; Niwa, M.	0.4 and 0.8-wt% $Pd(NH_3)_4Cl_2$ was ion-exchanged onto zeolite H-USY. The samples were dried at 323 K under atmospheric conditions and reduced under H_2 at 300 K.	Yes (XANES & EXAFS)	Yes	Yes (XANES)	No mechanism was proposed for the supported-nanoparticle heterogeneous catalyst formation reaction.
35 [39]	Okumura, K.; Matsui, H.; Sanada, T.; Arao, M.; Honma, T.; Hirayama, S.;	0.4-wt% $Pd(NH_3)_4Cl_2$ was ion-exchanged onto zeolite H-USY, dried at 323 K under atmoshpere and	Yes (XANES & EXAFS)	Yes	Yes (XANES)	No mechanism was proposed for the supported-nanoparticle heterogeneous catalyst formation reaction.

	Niwa, M.	reduced under H_2 at 300 K. Precatalysts containing $PdCl_2$, $Pd(OAc)_2$ and $Pd(NH_3)_4(NO_3)_2$ on zeolite H-USY were also investigated.				
36 [40]	Kulkarni, A.; Gates, B. C.	1-wt% of each $Os_3(CO)_{12}$ and $Ru_3(CO)_{12}$ (by metal) were simultaneously deposited onto MgO from pentane . The solvent was removed under vacuum and reduced under H_2 from 298 to 423 K.	Yes (XANES, EXAFS & IR Spectroscopies)	No	No -	*Proposed Mechanism.* "First, the decarbonylation of triruthenium clusters (occurs) starting at 333 K (with the triosmium carbonyl clusters still being coordinatively saturated and intact). The coordinatively unsaturated ruthenium species were reactive, and at 333 K, had aggregated substantially so that the average ruthenium cluster was larger than trirutheim. When the temperature had been raised to about 358 K, the triosmium clusters began to undergo decarbonylation, and at approximately 398 K the triosmium clusters had lost enough CO ligands to become sufficiently coordinatively unsaturated to allow migration and reaction with Ru atoms of neighboring species".
37 [41]	Shishido, T.; Asakura, H.; Amano, F.; Sone, T.; Yamazoe, S.; Kato, K.; Teramura, K.;	H_2PtCl_6 was impregnated on TiO_2 or g-Al_2O_3 (5-wt%), dried at 353 K and calcined at 773K. Subsequently the samples were	Yes (XANES)	Yes	Yes (XANES)	No mechanism was proposed for the supported-nanoparticle heterogeneous catalyst formation reaction.

	Tanaka, T.	pulsed with 5 mL of H_2 for 20 s at 473 K.				
38 [42]	Chupas, P. J.; Chapman, K. W.; Chen, H.; Grey, C. P.	2.5–7.5-wt% H_2PtCl_6 were impregnated onto TiO_2 and dried at 60 ºC overnight. Some of the samples were calcined at 200 ºC for 2 h under O_2. The kinetic data were collected while the sample was being reduced in H_2 from 0 to 227 ºC.	Yes (High energy total X-ray scattering + PDF analysis)	No	No	*Proposed Mechanism.* "The initial Pt nanoparticles that form are ~1 nm in size, while by 200 °C are larger and more crystalline. This suggests a mechanism for particle growth where the initial particles that form are small (<1 nm) then agglomerate into ensembles of many small particles and lastly anneal to form larger well-ordered particles".
39 [43]	Nassreddine, S.; Bergeret, G.; Jouguet, B.; Geantet, C.; Piccolo, L.	1.0-wt% $Ir(acac)_3$ was contacted with amorphous silica–alumina (ASA) from toluene. The sample was dried at 120 °C overnight and reduced in flowing H_2 at 350 ºC for 6 h.	Yes (*In Situ* XRD)	Yes	Yes (Mass Spectrometry)	No mechanism was proposed for the supported-nanoparticle heterogeneous catalyst formation reaction.

References

[1] R.A. Dalla Betta, M. Boudart, Well-Dispersed Platinum on Y Zeolite: Preparation and Catalytic Activity *5th Intern. Congr. Catal.* 1 (1973) pp. 1329-1341.

[2] A.C. Herd, C.G. Pope, J. Chem. Soc. Faraday Trans. 69 (1973) 833-838.

[3] M. Kermarec, M. Briend-Faure, D. Delafosse, J. Chem. Soc. Chem. Comm. 8 (1975) 272-273.

[4] H. Beyer, P.A. Jacobs, J.B. Uytterhoeven, J. Chem. Soc. Faraday Trans. 72 (1976) 674-685.

[5] P.A. Jacobs, M. Tielen, J.-P. Linart, J.B. Uytterhoeven, H. Beyer, J. Chem. Soc. Faraday Trans. 72 (1976) 2793-2804.

[6] R.G. Herman, J.H. Lunsford, H. Beyer, P.A. Jacobs, J.B. Uytterhoeven, J. Phys. Chem. 79 (1975) 2388-2394.

[7] M. Briend-Faure, D. Delafosse, J. Chem. Soc. Faraday Trans. 73 (1977) 905-912.

[8] M Briend-Faure, J. Jeanjean, M. Keramerec, D. Delafosse, J. Chem. Soc. Faraday Trans. 74 (1978) 1538-1544.

[9] D. Hermerschmidt, R. Haul, Ber. Bunsenges. Phys. Chem. 84 (1980) 902-907.

[10] H.K. Beyer, P.A. Jacobs, Stud. Surf. Sci. Catal. 12 (1982) 95-102.

[11] Dexpert, H., J. Phys-Paris 47 (1986) 219-226.

[12] M.S. Tzou, W.M.H. Sachtler, Stud. Surf. Sci. Catal. 38 (1988) 233-241.

[13] F. Le Normand, D. Bazin, H. Dexpert, P. Lagarde, J.P. Bournonville, in, Structural Genesis of Supported Platinum Particles Followed by EXAFS Spectroscopy, 1988, pp. 1401-1409.

[14] S.T. Homeyer, W.M.H. Sachtler, J. Catal. 118 (1989) 266-274.

[15] R.A. Schoonheydt, H. Leeman, J. Phys. Chem. 93 (1989) 2048-2053.

[16] D. Bazin, H. Dexpert, J.P. Bournonville, J. Lynch, J. Catal. 123 (1990) 86-97.

[17] M. Che, Z.X. Cheng, C. Louis, J. Am. Chem. Soc. 117 (1995) 2008-2018.

[18] M.S. Nashner, A.I. Frenkel, D. Somerville, C.W. Hills, J.R. Shapley, R.G. Nuzzo, J. Am. Chem. Soc. 120 (1998) 8093-8101.

[19] A. Yamaguchi, T. Shido, Y. Inada, T. Kogure, K. Asakura, M. Nomura, Y. Iwasawa, Catal. Lett. 68 (2000) 139-145.

[20] A. Yamaguchi, Y. Inada, T. Shido, K. Asakura, M. Nomura, Y. Iwasawa, J. Synchrotron Rad. 8 (2001) 654-656.

[21] A. Yamaguchi, T. Shido, Y. Inada, T. Kogure, K. Asakura, M. Nomura, Y. Iwasawa, Bull. Chem. Soc. Jpn. 74 (2001) 801-808.

[22] T. Shido, A. Yamaguchi, Y. Inada, K. Asakura, M. Nomura, Y. Iwasawa, Top. Catal. 18 (2002) 53-58.

[23] M.K. Oudenhuijzen, P.J. Kooyman, B. Tappel, J.A. van Bokhoven, D.C. Koningsberger, J. Catal. 205 (2002) 135-146.

[24] S.G. Fiddy, M.A. Newton, T. Campbell, A.J. Dent, I. Harvey, G. Salvini, S. Turin, J. Evans, Phys. Chem. Chem. Phys. 4 (2002) 827-834.

[25] M.K. Neylon, C.L. Marshall, A.J. Kropf, J. Am. Chem. Soc. 124 (2002) 5457-5465.

[26] K. Okumura, R. Yoshimoto, T. Uruga, H. Tanida, K. Kato, S. Yokota, M. Niwa J. Phys. Chem. B 108 (2004) 6250-6255.

[27] F. Li, B.C. Gates, J. Phys. Chem. B 108 (2004) 11259-11264.

[28] J.H. Yang, J.D. Henao, M.C. Raphulu, Y. Wang, T. Caputo, A.J. Groszek, M.C. Kung, M.S. Scurrell, J.T. Miller, H.H. Kung, J. Phys. Chem. B 109 (2005) 10319-10326.

[29] P. Li, J. Liu, N. Nag, P.A. Crozier, Surf. Sci. 600 (2006) 693-702.

[30] B.J. Hwang, C.-H. Chen, L.S. Sarma, J.M. Chen, G.-R. Wang, M.-T. Tang, D.-G. Liu, J.-F. Lee, J. Phys. Chem. B 110 (2006) 6475-6482.

[31] H. Tanaka, M. Uenishi, M. Taniguchi, I. Tan, K. Narita, M. Kimura, K. Kaneko, Y. Nishihata, J. Mizuki, Catal. Today 117 (2006) 321-328.

[32] P.J. Chupas, K.W. Chapman, G. Jennings, P.L. Lee, C.P. Grey, J. Am. Chem. Soc. 129 (2007) 13822-13824.

[33] K.-I. Shimizu, K. Sugino, K. Kato, S. Yokota, K. Okumura, A. Satsuma, J. Phys. Chem. C 111 (2007) 1683-1688.

[34] K. Okumura, K. Kato, T. Sanada, M. Niwa, J. Phys. Chem. C 111 (2007) 14426-14432.

[35] E. Bus, R. Prins, J.A. van Bokhoven, Phys. Chem. Chem. Phys. 9 (2007) 3312-3320.

[36] A. Uzun, B.C. Gates, Angew. Chem. Int. Ed. 47 (2008) 9245-9248.

[37] A.J. Liang, B.C. Gates, J. Phys. Chem. C 112 (2008) 18039-18049.

[38] K. Okumura, T. Honma, S. Hirayama, T. Sanada, M. Niwa, J. Phys. Chem. C 112 (2008) 16740-16747.

[39] K. Okumura, H. Matsui, T. Sanada, M. Arao, T. Honma, S. Hirayama, M. Niwa, J. Catal. 265 (2009) 89-98.

[40] A. Kulkarni, B.C. Gates, Angew. Chem. Int. Ed. 48 (2009) 9697-9700.

[41] T. Shishido, H. Asakura, F. Amano, T. Sone, S. Yamazoe, K. Kato, K. Teramura, T. Tanaka, Catal. Lett. 131 (2009) 413-418.

[42] P.J. Chupas, K.W. Chapman, H. Chen, C.P. Grey, Catal. Today 145 (2009) 213-219.

[43] S. Nassreddine, G. Bergeret, B. Jouguet, C. Geantet, L. Piccolo, Phys. Chem. Chem. Phys. 12 (2010) 7812-7820.

CHAPTER III

MONITORING SUPPORTED-NANOCLUSTER HETEROGENEOUS CATALYST FORMATION: PRODUCT AND KINETIC EVIDENCE FOR A 2-STEP, NUCLEATION AND AUTOCATALYTIC GROWTH MECHANISM OF $Pt(0)_n$ FORMATION FROM H_2PtCl_6 ON Al_2O_3 OR TiO_2

This dissertation chapter contains the manuscript of a paper published in the *Journal of the American Chemical Society* **2009,** *131,* 6389–6396 and is available online at http://dx.doi.org/10.1021/ja808980a. This chapter develops a kinetic monitoring method, namely a cyclohexene reporter reaction method, for following supported-nanocluster formation in contact with solution. The kinetics of H_2PtCl_6/Al_2O_3 to $Pt(0)_n/Al_2O_3$ and H_2PtCl_6/TiO_2 to $Pt(0)_n/TiO_2$ supported-nanocluster formation in contact with ethanol, cyclohexene and under H_2 were quantitatively followed and subsequently analyzed.

The experiments within this chapter were designed by Joseph E. Mondloch and Professor Richard G. Finke. Initial scouting experiments for monitoring the H_2PtCl_6/Al_2O_3 to $Pt(0)_n/Al_2O_3$ supported-nanocluster formation kinetics were performed by Xinhuan Yan. Joseph E. Mondloch completed all of the supported-nanocluster formation kinetic and other experimental work as well as the data analysis necessary to bring this work to publication. The manuscript was written by Joseph E. Mondloch and edited by Professor Richard. G. Finke.

CHAPTER III

MONITORING SUPPORTED-NANOCLUSTER HETEROGENEOUS CATALYST FORMATION: PRODUCT AND KINETIC EVIDENCE FOR A 2-STEP, NUCLEATION AND AUTOCATALYTIC GROWTH MECHANISM OF $Pt(0)_n$ FORMATION FROM H_2PtCl_6 ON Al_2O_3 OR TiO_2

This dissertation chapter contains the manuscript of a paper published in the *Journal of the American Chemical Society* **2009,** *131,* 6389–6396 and is available online at http://dx.doi.org/10.1021/ja808980a. This chapter develops a kinetic monitoring method, namely a cyclohexene reporter reaction method, for following supported-nanocluster formation in contact with solution. The kinetics of H_2PtCl_6/Al_2O_3 to $Pt(0)_n/Al_2O_3$ and H_2PtCl_6/TiO_2 to $Pt(0)_n/TiO_2$ supported-nanocluster formation in contact with ethanol, cyclohexene and under H_2 were quantitatively followed and subsequently analyzed.

The experiments within this chapter were designed by Joseph E. Mondloch and Professor Richard G. Finke. Initial scouting experiments for monitoring the H_2PtCl_6/Al_2O_3 to $Pt(0)_n/Al_2O_3$ supported-nanocluster formation kinetics were performed by Xinhuan Yan. Joseph E. Mondloch completed all of the supported-nanocluster formation kinetic and other experimental work as well as the data analysis necessary to bring this work to publication. The manuscript was written by Joseph E. Mondloch and edited by Professor Richard. G. Finke.

MONITORING SUPPORTED-NANOCLUSTER HETEROGENEOUS CATALYST FORMATION: PRODUCT AND KINETIC EVIDENCE FOR A 2-STEP, NUCLEATION AND AUTOCATALYTIC GROWTH MECHANISM OF $Pt(0)_n$ FORMATION FROM H_2PtCl_6 ON Al_2O_3 OR TiO_2

Joseph E. Mondloch, Xinhuan Yan and Richard G. Finke

Overview

A pressing problem in supported-metal-nanocluster heterogeneous catalysis—despite the long history and considerable fundamental as well as industrial importance of such heterogeneous catalysts—is how to monitor such catalysts' formation more routinely, rapidly and in real time. Such information is needed in order to better control the size, shape, composition and thus resultant catalytic activity, selectivity, and lifetime of these important catalysts. To this end, a study is reported of the formation of supported $Pt(0)_n$ nanoclusters by H_2 reduction of H_2PtCl_6 on Al_2O_3 (or TiO_2) to give 6 equivalents of HCl plus supported $Pt(0)_n/Al_2O_3$ (or $Pt(0)_n/TiO_2$), all while in contact with a solution of EtOH and cyclohexene. The HCl and $Pt(0)_n$ products were confirmed, respectively, by the stoichiometry of HCl formation using $pH_{apparent}$ measurements, appropriate standards, and by TEM and EDX measurements. The hypothesis of this research is that the kinetics of formation of this supported heterogeneous catalyst could be successfully monitored by a fast

cyclohexene hydrogenation catalytic reporter reaction method first worked out for monitoring transition-metal nanocluster formation in solution (Watzky, M. A.; Finke, R. G. *J. Am. Chem. Soc.* **1997**, *119*, 10382–10400). Significantly, sigmoidal kinetics of $Pt(0)_n/Al_2O_3$ catalyst formation were in fact successfully monitored by the catalytic hydrogenation reporter reaction method and then found to be well fit to the Finke–Watzky (hereafter F–W) 2-step, slow continuous nucleation and then autocatalytic surface growth mechanism, A → B (rate constant k_1) and A + B → 2B (rate constant k_2), respectively, in which A is the H_2PtCl_6 and B is the growing, catalytically active Pt(0) nanocluster surface. The finding that the F–W mechanism is applicable is significant in that it, in turn, suggests that the ≥8 insights from studies of the mechanisms of soluble nanocluster formation can likely also be applied to supported heterogeneous catalyst synthesis, including a recent equation that gives nanocluster size vs time in terms of k_1, k_2, $[A]_0$ and other parameters (Watzky, M. A.; Finney, E. E.; Finke, R. G., *J. Am. Chem. Soc.* **2008**, *130*, 11959-11969). Also presented are the use of the catalytic reporter reaction to reveal H_2 gas-to-solution mass-transfer-limitations (MTL) in the system of H_2PtCl_6 on TiO_2, results relevant to a recent communication in this journal. The use of the F–W 2-step nucleation and autocatalytic growth kinetic model to fit 3 literature examples of heterogeneous catalyst formation, involving H_2 reduction of both supported or bulk M_xO_y (i.e., and in gas–solid reactions), are also presented as part of the Supporting Information. A conclusion section is then provided summarizing the insights and caveats from the present work, as well as some needed future studies.

Introduction

Heterogeneous catalysts—often in the form of finely dispersed metal nanoclusters supported on inert materials[1]—are used in many important industrial catalytic processes.[2] However and despite the extensive literature on heterogeneous catalyst preparation,[3] relatively little is known about the mechanisms of formation of the active catalyst.[4] One main reason for this paucity of mechanistic information is the lack of experimental methods able to follow heterogeneous catalyst formation in real time.[4] Early studies in the 1970's and 1980's focused on the formation of nanoclusters in zeolites using primarily H_2 uptake data to obtain kinetics.[5] More recent studies have examined particle formation on both SiO_2[4b,6] and TiO_2,[4c] using extended X-ray absorption fine-structure analysis (EXAFS) along with more traditional techniques such as mass spectrometry (MS), transmission electron microscopy (TEM) and temperature programmed reduction (TPR). Gate's and co-worker's more recent studies[7] using the $[Ir(C_2H_4)(-O)_2]$ on dealuminated zeolite Y precatalyst (where $(-O)_2$ indicates the Ir complex is bonded to two surface oxygen atoms from the zeolite support), report that Ir_{2-4} clusters are formed upon exposure to H_2 via EXAFS and infrared spectroscopy.[7] These clusters contain both ethylidyne and di-σ-bonded ethylene ligands and undergo reversible breakup upon exposure to C_2H_4.[7]

Nevertheless, new kinetic monitoring methods for following heterogeneous catalyst formation are needed and would permit a better understanding of the mechanisms of formation of supported heterogeneous catalysts.[8] Such improved kinetic and mechanistic understanding is important in at least three ways:[9] (i) fundamentally, (ii) in order to gain better control over catalyst syntheses, as well as (iii) practically, since key catalytic properties—including selectivity,[10] activity,[11] lifetime and stability[11]—depend on the catalyst size,[12] surface composition,[13] and structure,[14] which in turn require greater control over heterogeneous-catalyst syntheses.

Especially relevant to our work is Chupas and co-worker's recent, interesting communication monitoring H_2 reduction of H_2PtCl_6 on TiO_2 to form supported $Pt(0)_n$ nanoclusters using in-situ time resolved high-energy X-ray scattering[15] data and the pair distribution function (PDF) method to follow directly the loss of Pt–Cl bonds and the formation of Pt–Pt bonds.[4c] Chupas and co-workers note in their communication that the "kinetics and mechanism of nanocluster formation and sintering in heterogeneous systems…is…an area that has been largely overlooked, due to the lack of adequate experimental methodology".[4c] Their communication triggered us to report our own, different but related results (vide infra) monitoring H_2PtCl_6 reduction under H_2 to $Pt(0)_n$ on Al_2O_3 or TiO_2. Our results offer an interesting advance in comparison to even that tour de force effort[4c,16] in that we: (i) employ a different, faster, highly convenient and hence much more easily employed, albeit less direct, cyclohexene hydrogenation catalytic reporter reaction monitoring method for following the formation of heterogeneous catalysts;[17] and (ii) study a non-traditional—but more flexible and potentially quite interesting—system where solvent and ligands are present during the supported-catalyst formation. This added flexibility in the supported nanocluster syntheses[18] offers possible greater control en route to size,[19] shape[20] or composition control over the resultant supported nanoclusters since nucleation and growth can now happen in solution as well as on the support and in the presence of soluble ligands or other additives. In addition, as detailed in what follows our results have allowed us: (iii) to examine quickly a broad range of conditions that uncover H_2 gas-to-solution mass transfer limitations (hereafter MTL) and other issues in the H_2PtCl_6/TiO_2 system (*vide infra*); (iv) to provide product and kinetic evidence consistent with the F–W 2-step mechanism of nanocluster formation, and hence our results allow us (v) to tap into the broadest studies and presently best understood solution–based mechanism of transition-metal particle formation and its more than 8 insights for synthesis.[17,21] That repository of

kinetic and mechanistic insights include a recent nanocluster size vs formation time equation that allows size to be controlled as a function of the nucleation (k_1) and growth (k_2) rate constants and the starting concentration of precatalyst, $[A]_0$.[19]

The results reported herein also bear on an interesting 2005 communication from Newton[22] and co-workers, as well as Weaver and co-workers' related studies,[23] monitoring the reduction of a solid 5-wt % Rh_2O_3/γ-Al_2O_3 precatalyst under H_2 gas as a function of temperature. Specifically, we show that the sigmoidal, gas–solid reduction curves reported by Weaver and co-workers can be fit by the F–W 2-step kinetic model (the curves of Newton are more complex and will be analyzed in detail separately). We also show that several literature data sets for the gas–solid reduction of $(CuO)_n$ by H_2 are also well fit by the F–W 2-step model. Those findings—ones summarized in the Supporting Information since the main focus of the present work is $Pt(0)_n$ catalyst formation on Al_2O_3 and TiO_2 and not $Rh(0)_n$—nevertheless still: (a) offer additional support for the greater generality of the F–W kinetic model for the formation of supported catalysts, and (b) providing deconvoluted nucleation (k_1) and growth ($k_2' = k_2[A]_o$) rate constants for those literature systems for the first time. Noteworthy here is that Newton also comments that "the paucity of such detailed kinetic measurements on (the formation of) real, highly dispersed supported catalysts bears testament to their difficulty".[22]

Experimental Section

Materials. All solvents and compounds used were stored in the drybox prior to use. Anhydrous ethanol (Aldrich, ≥ 99.5%, 200 proof) packed under nitrogen, ethyl acetate (Aldrich, 99.8%), cyclohexane (99.5%, anhydrous) and chloroplatinic acid hexahydrate (Aldrich, ≥37.5% Pt) were used as received. Cyclohexene (Aldrich, 99%) was freshly distilled over Na metal and under nitrogen. Acidic activated γ-Al_2O_3 (Aldrich), with a surface area of 155 m^2/g was dried at 160 °C in air for 24 h. A mixture of rutile and

anatase TiO_2 (Aldrich), with a BET surface area of <100 nm was dried at 160 °C in air for 24 hours. Nanopure 18 MΩ-cm H_2O was used from an in house purification system. H_2 gas purchased from General Air (> 99.5% purity) was passed through O_2 and H_2O scavenging traps (Trigon Technologies) before use.

Analytical Instrumentation and Procedures. Unless otherwise reported all reaction solutions were prepared under O_2 and moisture free conditions in a Vacuum Atmospheres N_2 filled drybox. The O_2 level (≤ 5 ppm) is continuously monitored by a Vacuum Atmospheres O_2 sensor. $pH_{apparent}$ measurements were conducted on a Corning pH meter 125 and with a Beckman (511050) dry, gel-filled electrode. (We denote $pH_{apparent}$ since the electrode was used, with calibration, in primarily EtOH but with some H_2O as well as cyclohexane present, vide infra.) TEM analysis was conducted at Clemson University with the expert assistance of JoAn Hudson and her staff. Dark field TEM analysis was done using a Hitachi HD-2000 microscope and bright field TEM analysis was done using both a Hitachi HD-2000 and Hitachi H7600T microscope. EDX analysis was performed on a Hitachi HD-2000 microscope.

Hydrogenation Apparatus and Data Handling. Hydrogenation experiments for monitoring the H_2 reduction of H_2PtCl_6 on Al_2O_3 or TiO_2 to $Pt(0)_n$ on Al_2O_3 or TiO_2 were carried out in a previously described[17,24,25] apparatus to monitor continuously H_2 pressure loss. The apparatus consists of a Fisher-Porter (FP) bottle modified with Swagelock TFE-sealed Quick-Connects to both a H_2 line and an Omega PX621 pressure transducer. The pressure transducer is interfaced to a PC through an Omega D1131 5V A/D converter with a RS-232 connection. Pressure uptake data were collected using LabView 7.1. The hydrogen uptake curves were converted to cyclohexene curves using the previously established 1:1 H_2/cyclohexene stoichiometry.[17,21,26] The data is also corrected for the EtOH solvent-vapor pressure using the previously established protocol.[26] Specifically one can either measure the EtOH vapor pressure independently

and subtract that curve (point-by-point) from the raw H_2 uptake data during the cyclohexene reporter reaction, or one can simply back extrapolate the experimental vapor pressure rise (seen in the induction period of the reaction).[26] Both methods yield the same k_1 and k_2 rate constants within a ±15% error. The k_2 values are corrected by the required 2600:1 cyclohexene/H_2PtCl_6 stoichiometry factor as required and previously done.[21] Reactions were run at a constant temperature by immersing the FP bottle in a 500 mL jacketed reaction flask containing dimethyl silicon fluid (Thomas Scientific), which was regulated by a thermostatted recirculating water bath (VWR).

Pre-Catalyst Preparation: H_2PtCl_6/γ-Al_2O_3 and H_2PtCl_6/TiO_2. Note that for what follows and throughout this paper, we use wt% defined as wt% = wt ($H_2PtCl_6 \bullet 6H_2O$)/((wt $H_2PtCl_6 \bullet 6H_2O$) + (wt Al_2O_3)) since that is what we experimentally measure out and, hence, know. Hence, our wt% values are different than the more common convention in heterogeneous catalysis of the wt% being the wt of the metal only (e.g. the wt of just Ir in the present case) divided by the total weight (as defined above), all x 100 to convert into a percentage.

All of the precatalysts were prepared in the drybox using pre-selected H_2PtCl_6/support weight-to-weight ratios. For example, a 2.0% weight-to-weight H_2PtCl_6/Al_2O_3 sample was prepared by adding 1.0 g Al_2O_3 to 20 mg H_2PtCl_6 (or TiO_2), corresponding to a 1.96-wt% sample, by the following procedure. The appropriate amount of H_2PtCl_6 was weighed out in a 20 mL scintillation vial. A new 5/8 in. × 5/16 in. Teflon-coated octagon shaped stir bar was added to the vial and the solid was dissolved in 15 mL of ethyl acetate. The appropriate amount of solid oxide (e.g., 1.0 g of Al_2O_3 for the 2 wt% Pt catalyst) was added by pouring the metal oxide into the vial (i.e., this order of addition is deliberate, along with an equilibration time that is important, vide infra) and the solution was stirred for 24 h to equilibrate the H_2PtCl_6 with the solid oxide and the solution. After

the 24 h period the reaction was taken to dryness in a drybox by placing the sample under vacuum for 8 hours at room temperature. The resulting supported precatalysts were stored in the drybox.

Formation of the Active Catalyst: Standard Conditions Reaction. In the drybox 0.05 g of the appropriate H_2PtCl_6/support catalyst precursor was weighed out into a 2 dram vial. Subsequently, 2.5 mL of ethanol and 0.5 mL of cyclohexene were added via gastight syringes to the 20 mL scintillation vial. A 5/8 in. × 5/16 in. Teflon-coated octagon shaped stir bar was added, the vial was capped and the solution was stirred for 2 hours (in catalyst batch #1) and for 7 hours (in catalyst batch #2) in the drybox. Catalyst batch #1 and #2 are two different (separately synthesized) batches of the 1.96-wt% H_2PtCl_6/Al_2O_3 precatalyst. The kinetics of the nanocluster formation were reproducible to the average k_1 and k_2 values reported in the main text after these equilibration periods (i.e., control reactions with longer stirring times did not change the kinetics). The solution was then transferred via a disposable polyethylene pipette into a new borosilicate culture tube (22 × 175 mm) with a new 5/8 in. × 5/16 in. Teflon-coated octagon shaped stir bar. The culture tube was sealed in the FP bottle, removed from the drybox, and attached to the H_2 line. The sealed, H_2-line attached FP bottle was placed into the temperature regulated water bath set at 22.0 ± 0.1 °C. The previously developed standard conditions purge cycle[17,27] was used to initiate the reaction, a series of H_2-flushing cycles in which the FP bottle is purged with H_2 every 15 seconds until 3 minutes and 30 seconds have passed (a total of 14 purges). The stir plate was started at 600 rpm, and the H_2 pressure was then set to 40 psig with the data recording started at four minutes after the purge cycle began (i.e., by definition t = 0 for the kinetics).

Determination of the Reaction Stoichiometry: $pH_{apparent}$ Measurements. The reaction stoichiometry was determined by measuring the $pH_{apparent}$ of the reaction solution in comparison to a standard solution containing the expected 6 equiv of

authentic HCl. First, a Standard Conditions supported nanocluster formation reaction was performed (vide supra). After the reaction was complete, H_2 from the FP bottle was vented and then the FP bottle was brought into the drybox. Next, 5.5 mL of EtOH was added to the reaction mixture and the sample was brought out of the drybox, where 0.5 mL of nanopure H_2O was also added to the solution. The $pH_{apparent}$ was then measured (i.e., the pH in the nanocluster formation solution which also contains EtOH, cyclohexane and added H_2O). Measurements of the $pH_{apparent}$ were also made on (i) a background solution containing 0.05 g Al_2O_3, 8.0 mL EtOH, 0.5 mL cyclohexane and 0.5 mL H_2O ("Alumina Background Control", Figure 1) and, importantly, on (ii) a standard consisting of 0.05 g Al_2O_3, 8.0 mL EtOH, 0.5 mL cyclohexane and 0.5 mL of H_2O containg 6.0 equivalents of HCl ("6 eq HCl added" control, Figure 1), 6 eq of HCl being the precise amount of acid expected to be generated in the nanocluster formation reaction. The results of these three $pH_{apparent}$ measurements are shown in Figure 1.

Preparation of TEM Grids. Following the preparation of a Standard Conditions supported nanocluster formation reaction, and approximately 2 h after the complete hydrogenation of cyclohexene (as monitored by the H_2 loss curve slowing to effectively

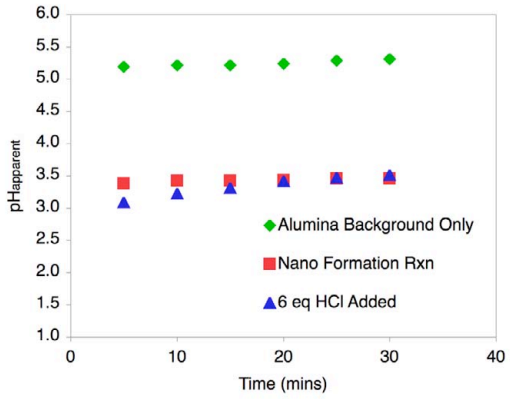

Figure 1. $pH_{apparent}$ measurements confirm the overall nanocluster formation stoichiometry (to within ±0.1 pH units or ±20%) for the H_2PtCl_6/Al_2O_3 system shown in Scheme 1.

zero), the FP bottle was transferred into the drybox. A 300 mesh, Formvar coated SiO_2 TEM grid was dipped in the sample for approximately 5 seconds and then allowed to dry. The grid was placed in a 2-dram vial, wax sealed and placed in a 20 mL scintillation vial. The TEM grids were sent to JoAn Hudson and her staff at the University of Clemson for TEM analysis.

Results and Discussion

H_2PtCl_6 on Al_2O_3: Precatalyst Synthesis and the Experimental Apparatus. To start, a H_2PtCl_6/Al_2O_3 precatalyst (1.96-wt%) was prepared in a drybox by the addition of Al_2O_3 to a H_2PtCl_6 ethyl acetate solution followed by vacuum drying and as described in the Experimental section. The H_2PtCl_6/Al_2O_3 was then placed in EtOH with ~2600 equivalents of cyclohexene (per equiv of Pt), the mixture sealed in a FP bottle equipped with swage lock quick connects, removed from the drybox, placed in a temperature-regulated water bath, attached to a O_2 and H_2O scrubbed H_2 line, interfaced to a pressure transducer (±0.01 psig) and computer, and stirred at 600 rpms. This now well-described apparatus[17,21,24,25,26,27] allows reduction of the H_2PtCl_6/Al_2O_3 precatalyst by H_2 while in contact with ethanol solvent and an olefin (cyclohexene, that is reduced to cyclohexane), Scheme 1, top reaction. This convenient experimental setup also permits the simultaneous, real-time monitoring of the H_2 pressure loss as a means to follow the nanocluster formation kinetics via the also well-established cyclohexene reporter reaction method,[17,21,24,25,26,27] Scheme 1, the bottom reaction. Noteworthy here is the contrast of the above (albeit not unprecedented[28]) system with its solid H_2PtCl_6/Al_2O_3 precatalyst in contact with solvent and any other additives such as the olefin cyclohexene, vs traditional heterogeneous catalyst formation systems and their typical H_2 gas–solid reaction.[3]

Scheme 1. Stoichiometry for the H_2PtCl_6/Al_2O_3 Nanocluster System and Cyclohexene Reporter Reaction Studied Herein.

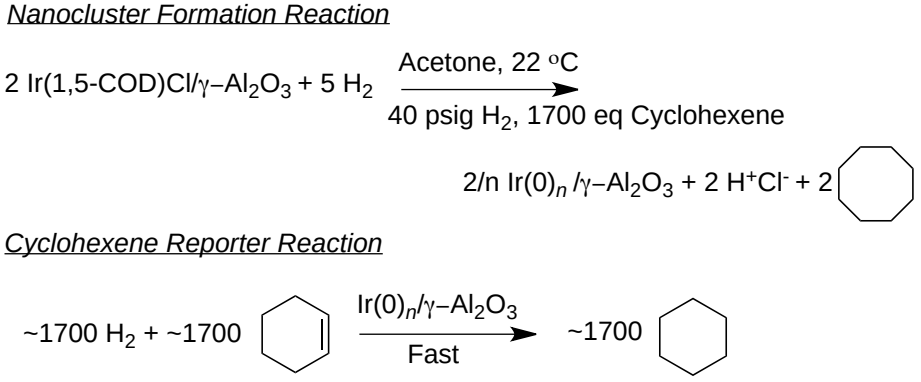

H_2PtCl_6 on Al_2O_3: The Reaction Stoichiometry and Product Characterization. A firm knowledge of the products and the balanced reaction stoichiometry is the first rule of reliable mechanistic studies; hence, this is where we began our studies and even though balanced reactions are typically less readily obtained for heterogeneous catalyst formation reactions. Specifically, the stoichiometry in the top of Scheme 1 was confirmed by measuring the H^+ produced (i.e. the $pH_{apparent}$ *vide infra*) and showing it matches (±20%, *vide infra*) a control experiment in which the expected 6 equivalents of HCl was added to the identical volume of a EtOH/cyclohexane solution also containing the same amount of Al_2O_3, Figure 1. Back calculating out the number of moles of H^+ in solution over the 6 data points in Figure 1 for the two, non-background samples confirms that the expected 6 equivalents of H^+ are formed (to within ±0.1 pH unit or ±20%). In short, the observed $pH_{apparent}$ and its overlap with the standard where 6 equivalents of authentic HCl is added confirms the anticipated HCl formation stoichiometry and is fully consistent with the reaction stoichiometry shown in Scheme 1.

The metal product obtained at the end of the nanocluster formation reaction is visible as a dark gray solid. Dark-field TEM images, Figure 2, and the EDX results shown in the Supporting Information (Figures SI 4 and 5) confirm the formation of 5–10 nm $Pt(0)_n$

nanoclusters supported on the Al_2O_3, particles that more than suffice for the present focus on their kinetics and mechanism of formation.

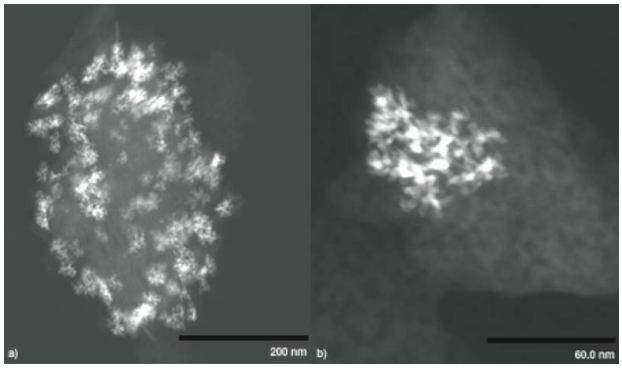

Figure 2. (a) The overall morphology (vs. a 200 nm scale bar) of the resultant $Pt(0)_n/Al_2O_3$ catalyst. (b) An expanded image (60 nm scale bar) suggesting that at least some of the observed large clusters in (a) may be formed from agglomerated smaller nanoclusters. Such 2-D images of 3-D supported particles can, of course, misrepresent apparently agglomerated particles as what can actually be individual particles stacked perpendicular to the grid.

A control experiment in which the Al_2O_3 is omitted and 0.63 mM H_2PtCl_6 in EtOH and with 1.65 M cyclohexene is run in solution under otherwise identical conditions (e.g., 40 psig H_2) shows different products (bulk metal and a colorless solution devoid, therefore, of significant amounts of H_2PtCl_6). Different kinetics are seen as well (Figure S6 of the Supporting Information) vs the sigmoidal ones seen in the next section for the Al_2O_3 containing system. This control shows that the Al_2O_3 support is as expected an essential part of the present system, without which the (supported) nanoclusters are not formed.

H_2PtCl_6 on Al_2O_3: Catalyst Formation Kinetic Studies. The formation kinetics of the supported $Pt(0)_n/Al_2O_3$ catalyst were obtained using cyclohexene hydrogenation as a precedented reporter reaction,[17,21,24,25,26,27] Scheme 2, in which A is the added precursor complex (H_2PtCl_6/Al_2O_3, or its Cl^- dissociated/solvated forms)[29,30] and B is the growing $Pt(0)_n$ nanocluster surface. It is known that the cyclohexene hydrogenation reaction will

accurately report on and amplifies the amount of $Pt(0)_n$ nanocluster hydrogenation catalyst, B, present:[17,21,25,26] (i) if there is no H_2 gas-to-solution mass transfer limitations[21b] (MTL), and (ii) when the rate of reduction of cyclohexene to cyclohexane is fast in comparison to the rate of nanocluster formation, k_{obs},[17,21] Scheme 2. The necessary stirring rate dependence plots (Figure S1, Supporting Information) reveal that H_2 gas-to-solution MTL effects are negligible; in addition, [cyclohexene] dependence plots (Figure S2, Supporting Information) approach zero-order in [cyclohexene] as was done before[17] to ensure that the cyclohexene hydrogenation reporter reaction is fast relative to the rate of the (slower) nanocluster formation k_1 and k_2 steps (vide infra). In short, these controls along with prior precedent[17] ensure that the nanocluster formation kinetics are being faithfully monitored.

Scheme 2. Illustration of the Cyclohexene Reporter Reaction in Which A is the Metal Precursor Complex (H_2PtCl_6 in the Presence of Al_2O_3) and B is Pt(0) on the Growing Nanocluster Surface.

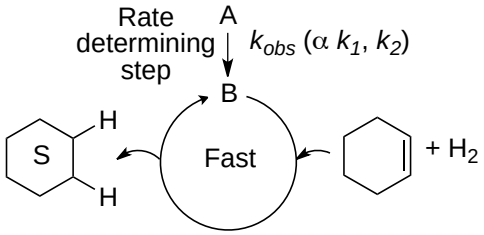

Experimentally, post monitoring the H_2 uptake with a high-precision (±0.01 psig) pressure transducer it is most convenient to convert and represent the data as cyclohexene consumption, Figure 3, using the known 1:1 H_2/cyclohexene stoichiometry.[17,21] The beauty of this fast, efficient kinetic method[17,21] is that it provides hundreds to thousands (if desired) of high precision data points for the catalyst formation, more—as well as more precise—data than obtainable by other present methods, to our knowledge.

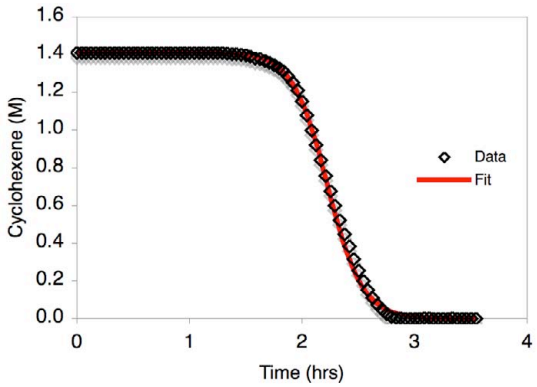

Figure 3. Reproducible kinetics associated with the formation of $Pt(0)_n/Al_2O_3$ and the corresponding excellent fits (R^2 = 0.9996) to the F-W 2-step kinetic model of nucleation plus autocatalytic surface growth, Scheme 3.

The resultant kinetics for the formation of $Pt(0)_n$ nanoclusters on Al_2O_3, Figure 3, are interesting. Specifically, sigmoidal kinetics for the $Pt(0)_n/Al_2O_3$ formation reaction are seen and closely fit by the F–W 2-step, nucleation and autocatalytic growth mechanism of nanocluster formation, Scheme 3, first worked out in 1997 for soluble nanocluster formation.[17] The average rate constants (from 8 independent kinetic runs) for nucleation ($k_1 \sim 10^{-5.5(7)}$ h^{-1}) and autocatalytic growth (k_2 = 1.2(2) x 10^4 h^{-1} M^{-1}) from the $Pt(0)_n/Al_2O_3$ supported nanoclusters are obtained from a nonlinear least-squares fit to the analytic integrated rate equation derived from the 2-step kinetic model (shown in the Supporting Information). Importantly, the observed kinetics are reproducible to the given error bars[31] from batch-to-batch of freshly synthesized H_2PtCl_6/Al_2O_3 precatalyst, so long as one employs a pre-stirring/pre-equilibration period of ca. 2–7 hrs at 22 ^oC in which the H_2PtCl_6 or its Cl^- dissociated/solvated[29,30] forms become equilibrated with the Al_2O_3 support and solution. Shown in the Supporting Information are the different curves that one can obtain if insufficient equilibration times are used, results that readily reveal this important-for-synthesis, pre-equilibration time.

Scheme 3. F–W 2-step Mechanism and Its Implied More Detailed Steps (Right) for the 1.96-wt% H_2PtCl_6/Al_2O_3 Precatalyst (A) System En Route to the Supported $Pt(0)_n$ Nanoclusters (B).

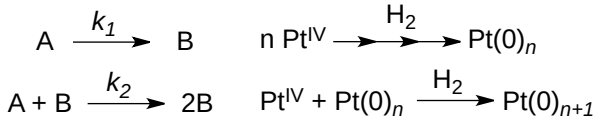

The observed kinetics and excellent fit to the F–W 2-step mechanism[17,21] are on one hand not entirely unexpected,[17,21,32,33] but are still quite significant. For starters, the fit to the 2-step model and the resultant nucleation (k_1) and autocatalytic growth (k_2) rate constants imply that all of ≥8 available insights into soluble nanocluster synthesis and stabilization[17,21] should be applicable, at least in principle, to supported-nanocluster heterogeneous catalysts, insights which include: (i) understanding how to form routinely near-monodisperse (≤ ±15%) size distributions of typically "magic-number sized" (i.e., full shell)[21a] size distributions of supported nanoclusters; (ii) *rational size control* via a recently developed nanocluster size vs. time equation in terms of k_1, k_2 and the precatalyst concentration, $[A]_o$,[19] (iii) additional possible size control via olefin or other ligand dependence,[24,27] (iv) rational use of seeded-growth methods including the rational synthesis of all possible geometric isomers of multimetallic "nano-onions"[21a] (v) rational catalyst shape control via ligands capable of attaching to the growing nanocluster faces and thereby preventing autocatalytic surface growth of that facet;[20] (vi) knowledge of the negative effects of, and insights into how to avoid, H_2 gas-to-solution mass-transfer limitations (MTL) in nanocluster syntheses;[21b] (vii) knowledge of what added nanocluster surface ligands can provide additional nanocluster stability if desired;[34] and (viii) the possibility of nanocluster size-dependent surface metal-to-ligand bond energies–and all that preliminary finding implies for catalysis.[21e-g]

More immediately, however, we were able to apply the insight that the F–W 2-step mechanism fits the 1.96-wt% H_2PtCl_6/Al_2O_3 system, in order to gain insights about the

related, but interestingly different, system of H_2PtCl_6/TiO_2. Those observed differences must mirror the differences in the TiO_2 vs Al_2O_3 supports since that is the only difference between the two systems, vide infra.

H_2PtCl_6 on TiO_2: Catalyst Formation Kinetics. The knowledge that the 2-step F–W mechanism quantitatively accounts for the kinetics of conversion of H_2PtCl_6/Al_2O_3 to $Pt(0)_n/Al_2O_3$ caused us to re-examine—but now under our solution containing system and conditions—the interesting 5-wt% H_2PtCl_6/TiO_2 precatalyst plus H_2 system recently communicated to this journal, but which was examined under the more traditional conditions of reduction via a H_2 gas–solid interface.[4c] Specifically, the recently observed,[4c] intriguing linear loss and implied zero-order dependence on the H_2PtCl_6/TiO_2 precursor, $+d[Product]/dt \alpha [H_2PtCl_6/TiO_2]^0$, in the literature H_2 gas–solid precatalyst system caught our attention. Such a zero-order dependence, $[H_2PtCl_6/TiO_2]^0$, to an end $Pt(0)_n/TiO_2$ product, requires one to write a mechanism not involving H_2PtCl_6 in the rate-determining step. Rate-determining H_2 activation on TiO_2 is about the only rational mechanism one can write, Scheme 4, and assuming facile H• diffusional transfer to the active site where H_2PtCl_6 is reduced.

The implication is that the rate-controlling H_2 activation (and/or or possibly a slow H• transfer) are obscuring the desired kinetics of nanocluster formation. While the direct monitoring of Pt–Cl loss and Pt–Pt formation is the power of the elegant high-energy X-ray scattering and pair distribution function (PDF) methods reported recently, those methods are relatively slow and expensive[16] so that studies under the chemically interesting conditions where the catalyst formation rate is not zero-order in $[H_2PtCl_6/TiO_2]$ have yet to be reported. Hence, it is of interest to examine the H_2PtCl_6/TiO_2 system by the reporter reaction methods developed herein so that a broader range of conditions can be more quickly examined. It is also of considerable interest to combine the present methods with more direct, powerful X-ray scattering methods[16]

Scheme 4. One Possible Mechanism Consistent with the Observed Linear $[H_2PtCl_6/TiO_2]^0$ Kinetics Seen for the Literature Gas–solid Catalysts Formation System.[4c] [a]

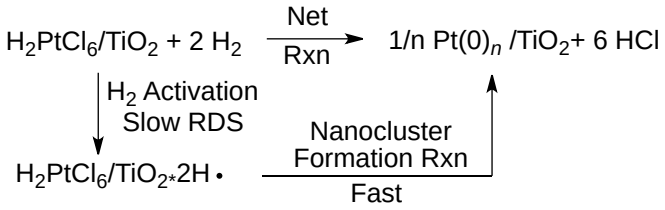

[a] The net reaction is shown on the top of the scheme and on the bottom H_2 activation is postulated as the slow, rate-determining step.

Intriguingly, under our solution-based conditions and using our catalytic reporter reaction monitoring method, we, too, see linear kinetics for the same 5-wt% H_2PtCl_6 on TiO_2,[4c] even though our system is not the gas–solid system but is in EtOH, 1.65 M cyclohexene, and has these reagents plus H_2 gas initially at 40 psig in contact with the stirred solution, Figure 4. The F–W 2-step mechanism does not fit the experimental data as expected since those data are basically a straight line. The observed zero-order kinetics for the H_2PtCl_6/TiO_2 system, Figure 4, and the implicated H_2 gas-to-solution MTL effects (vide infra), were further supported by the studies summarized in Figure 5, in which the observed H_2 uptake rate vs the Pt-wt% is plotted. Further confirmation of MTL effects for the 5-wt% H_2PtCl_6/TiO_2 system were obtained by the kinetic data in Figure 6, the loss of cyclohexene was measured as a function of stirring speed, 600 rpms and then 1000 rpms, respectively. The figure shows a large increase in the rate of cyclohexene uptake (or H_2 uptake) as a function of increasing stirring speed. Specifically the rate of H_2 uptake (calculated using the method of initial rates,[35] and then expressed in Figure 6 as its equivalent cyclohexene loss kinetic data) exhibits a significant dependence on stirring rate, 42.2 psig H_2/hr at 600 rpm vs a 58% higher 66.8 psig H_2/hr at a ca. 66% higher, 1000 rpm stirring rate. Overall, the above data are prima facie evidence consistent with unwanted H_2 gas-to-solution MTL effects in the 5-wt%

H_2PtCl_6/TiO_2 system. Such MTL effects of course obscure the desired, underlying nanocluster formation chemical mechanism.

However and importantly, the above evidence for MTL effects, plus our ability to rapidly screen conditions, allowed us to quickly find lower metal loading conditions (0.99-wt% H_2PtCl_6/TiO_2) *that unmask sigmoidal-type kinetics*, thereby revealing the desired nanocluster formation chemical kinetics. The 0.99-wt% H_2PtCl_6/TiO_2 data, along with the corresponding fit to the F–W nanocluster formation mechanism, is shown in Figure 7. The data and fit in Figure 7 also reveal that even the 0.99-wt% H_2PtCl_6/TiO_2 system still

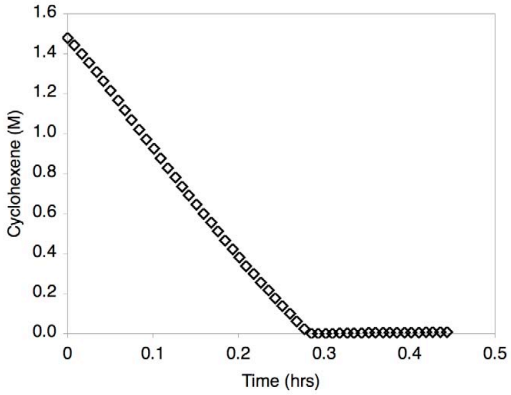

Figure 4. Linear kinetics observed for the 5-wt% H_2PtCl_6/TiO_2 system herein in contact with stirred EtOH and cyclohexene. The curve shows no discernable induction period; hence it is not fit to the F–W 2-step mechanism.

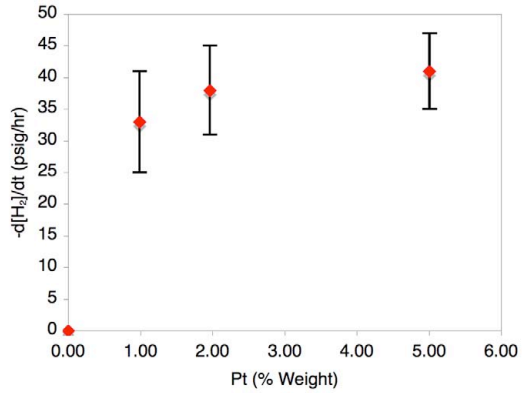

Figure 5. Rate of H_2 loss as a function of the Pt-wt%. The reaction approaches zero-order kinetics, and thus enters a H_2 gas-to-solution MTL regime, even by 2-wt% Pt (with complete MTL by 5-wt% Pt) for H_2PtCl_6/TiO_2 (and in our specific apparatus, stirring conditions, H_2 pressure, solvent, temperature and other conditions that influence MTL).

is under some MTL (results which are elaborated on in the SI for the interested reader). However, the sigmoidal features in Figure 7 make it clear the change to a lower catalyst loading is having the anticipated, desired effect of moving away from the chemically uninteresting MTL regime.

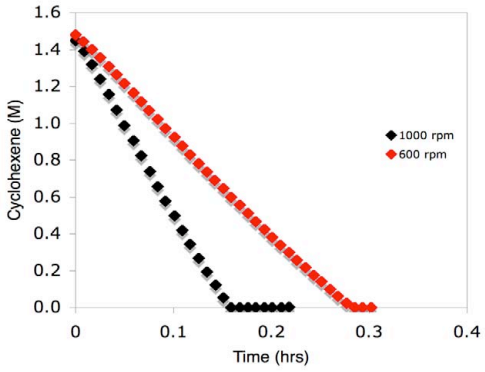

Figure 6. Comparison of the kinetics observed for the 5-wt% H_2PtCl_6/TiO_2 sample stirred at both 600 and 1000 rpms. Note the large increase in the reaction rate at 1000 rpms (66.8 mmols H_2/hr vs 42.2 mmols H_2/hr), indicating H_2 gas-to-solution MTL effects are present in this system.

The observation that the lower loading 0.99-wt% H_2PtCl_6/TiO_2 still has MTL effects, even though these are minimized for the somewhat higher loading 1.96-wt% H_2PtCl_6/Al_2O_3 precatalyst, is interesting. While not fully understood, this observation of less MTL in the Al_2O_3-supported precatalyst despite it being at nearly 2-times the metal loading: (a) shows the significant effect of the support on the catalyst formation kinetics, and (b) argues for different H_2PtCl_6 speciation on these two supports (with a more active species towards Pt(0) formation on TiO_2)[29] as one of the few, possible explanations that is apparent at present. This observation of the support effect on catalyst formation also makes clear that (c) such support effects are a topic that will merit a range of their own, in-depth studies to achieve a better understanding of such interesting, catalyst-synthesis-relevant, support effects.

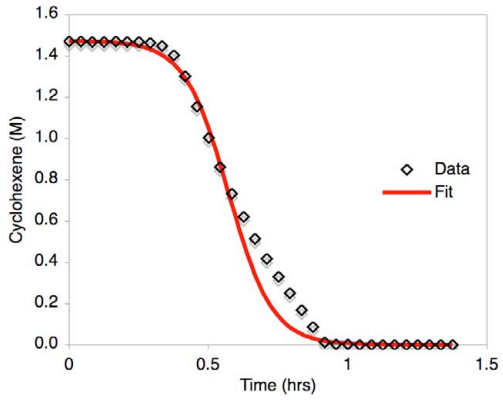

Figure 7. $Pt(0)_n$ on TiO_2 nanocluster formation kinetics for the 0.99-wt% H_2PtCl_6/TiO_2 system. One can see the sigmoidal kinetics-and the reasonable but not great fit to the F–W 2-step mechanism (R^2=0.9964). The lower catalyst loading conditions reveal the sigmoidal nucleation (k_1 = 1.8(9) x 10^{-2} h^{-1}) and autocatalytic growth (k_2 = 5.0(6) x 10^4 h^{-1} M^{-1}) nanocluster formation kinetics as compared to Figure 4.

The value of the methods reported herein, for rapidly screening kinetics of supported nanocluster formation under at least our solution-containing conditions, is noteworthy. In addition, our results already provide an important insight into the synthesis and formation of heterogeneous catalysts, namely the need to avoid MTL effects that are known to lead to broad distributions of nanoclusters.[21b] Exciting here is the collaboration we have initiated with the Argonne group[4c] to use the advantage of each of our separate methods, while minimizing exposure to each method's disadvantages,[16] in further studies of the H_2PtCl_6/TiO_2 and other supported nanocluster catalysts systems. Studies meriting additional scrutiny include the interesting comparison of the gas–solid vs gas–solution–solid based systems and studies of other supports and their effects.

Initial Application of the F–W 2-Step Kinetic Model to Other Heterogeneous Catalyst Formation Systems. Sigmoidal reduction kinetics have also been observed by Weaver and co-workers,[23] for the reduction of Rh_2O_3 thin films followed by surface-enhanced Raman spectroscopy (SERS), as well as by Newton and co-workers,[22] for the

H_2 reduction of Rh_2O_3 particles on γ-Al_2O_3 followed by the XANES edge. Sigmoidal curves are also common in the $(CuO)_n$ H_2 gas–solid reduction literature, for example in the reduction $(CuO)_n$ by H_2.[36] However, none of the sigmoidal kinetic curves in those studies were quantitatively fit, testament to the general lack until recently[17,37,38] of kinetic models able to fit the kinetics of such phase-change phenomenon with a chemical-mechanism-based equation.[17,37,38] In for example the 2005 study of the H_2 reduction of Rh_2O_3 particles on γ-Al_2O_3,[22] primarily the post-induction period part of the kinetic curve was analyzed and used to provide apparent activation parameters for the second part of the kinetic curve (that we know from the studies herein is largely the growth phase).

Using the F–W kinetic model, we have fit or attempted to fit the Rh_2O_3[22,23] data as well as the $(CuO)_n$[36] reduction data we mined from the literature. These data, provided in the Supporting Information for the interested reader, demonstrate sigmoidal M_xO_y reduction curves for *gas–solid* reactions can be fit in at least 2 of the 3 cases examined by the F–W 2-step mechanism and that k_1 nucleation and, now, k_2' (= $k_2[A]_o$; see the Supporting Information) autocatalytic growth rate parameters can be deconvoluted from those fits, previously unreported resutls. The importance of these fits to literature gas—solid heterogeneous catalyst formation kinetic data is they show the broader applicability of the F–W 2-step kinetic model to at least some H_2 gas–solid M_xO_y reduction systems.

Conclusions

In conclusion we have demonstrated: (i) the ability to monitor heterogeneous catalyst formation rapidly and in real time using the fast catalytic reporter reaction method developed previously;[17,21] (ii) that the formation kinetics are well fit by the F–W 2-step mechanism of slow, continuous nucleation followed by fast autocatalytic surface growth first worked out for soluble nanocluster formation;[17] and (iii) that the ≥8 insights available from solution based nanocluster mechanism of formation studies[17,21] should, therefore,

be applicable at least in principle en route to supported nanocluster heterogeneous catalysts with potentially rationally improved size, shape, multi-metallic nano-onion and other mechanism-based synthetic control. In addition, we: (iv) have studied a relatively little-investigated, flexible solution-solid heterogeneous catalyst formation system where added ligands, solvent and so on can be employed to gain additional control over the formation of the supported metal particles; and (v) have demonstrated the ability to screen rapidly supported heterogeneous catalyst formation, thereby allowing MTL effects in the H_2PtCl_6/TiO_2 precatalyst systems to be uncovered, in turn allowing lower [catalyst] loading conditions to be used to unmask the desired chemical kinetics and mechanism of nanocluster formation. Finally, we: (vi) have also shown that the weaknesses and strengths of the catalytic reporter reaction monitoring method are a good match for the, respectively, complimentary strength and weakness of the powerful, direct, high-energy X-ray scattering methods[4c] so that it is of considerable interest to use these two methods (or similar ones) *in tandem*; and (vii) have demonstrated the applicability of the F–W kinetic model to 2 of 3 sets of literature heterogeneous catalyst formation from Rh_2O_3 and $(CuO)_n$ gas–solid reductions, allowing nucleation and growth rate constants to be obtained from those data sets for the first time, results which demonstrate the broader applicability of the F–W kinetic model to at least some other, in those cases H_2 gas, M_xO_y solid, heterogeneous catalyst formation systems.[39]

It is our hope that others will employ the methods and kinetic model presented herein, but while keeping the limitations of the reporter reaction method and the minimalistic F–W model well in mind.[37,38] The results of our own additional studies of the present systems, as well as other metals and a range of different support materials, will be reported in due course.

Acknowledgement. We thank Dr. P. Chupas and co-workers for enlightening discussions of their interesting work.[4c] This work was funded by DOE Grant SE-FG02-03ER15453.

Supporting Information Available: MTL and zero-order cyclohexene plots; EDX; additional 1.96-wt% H_2PtCl_6/Al_2O_3 kinetics; un-supported H_2PtCl_6 reduction kinetics in EtOH, 0.99-wt% H_2PtCl_6/TiO_2 MTL data; and fits to 7 sets of H_2 plus M_xO_y gas—solid catalyst formation kinetic data by the F–W 2-step kinetic model. This material is available free of charge via the Internet at http://pubs.acs.org

References

[1] Gates, B. C., *Catalytic Chemistry*. John Wiley & Sons: New York, 1992.

[2] (a) Heinemann, H. Development of Industrial Catalysis. In *Handbook of Heterogeneous Catalysis*, Ertl, G.; Knözinger, H.; Weitkamp, J. VCH: Weinham, 1997; Vol. 1. 35-38. (b) Bartholomew, C. H.; Farrauto, R. J., *Fundamentals of Industrial Catalytic Processes*. 2 ed.; John Wiley & Sons: Hoboken, 2006.

[3] Preparation of Solid Catalysts; Ertl, G.; Knözinger, J.; Weitkamp, J. WILEY-VCH: Weinheim, 1999. (b) Catalyst Preparation Science and Engineering; Regalbuto, J. CRC Press: Boca Raton, 2007.

[4] (a) Lambert, J.-F.; Che, M. *J. Mol. Catal. A: Chemical* **2000**, *162*, 5-18. (b) Oudenhuijzen, M. K.; Kooyman, P. J.; Tappel, B.; van Bokhoven, J. A.; Koningsberger, D. C. *J. Catal.* **2002**, *205*, 135-146. (c) Chupas, P. J.; Chapman, K. W.; Jennings, G.; Lee, P. L.; Grey, C. P. *J. Am. Chem. Soc.* **2007**, *129*, 13822-13824.

[5] (a) Herd, A. C.; Pope, C. G. *J. Chem. Soc. Faraday Trans* **1973**, *69*, 833-838. (b) Kermarec, M.; Briend-Faure, M.; Delafosse, D. *J. Chem. Soc. Chem. Comm.* **1975**, *8*, 272-273. (c) Beyer, H.; Jacobs, P. A.; Uytterhoeven, J. B. *J. Chem. Soc. Faraday Trans* **1976**, *72*, 674-685. (d) Jacobs, P. A.; Tielen, M.; Linart, J.-P.; Uytterhoeven, J. B.; Beyer, H. *J. Chem. Soc. Faraday Trans* **1976**, *72*, 2793-2804.

[6] Che, M.; Cheng, Z. X.; Louis, C. *J. Am. Chem. Soc.* **1995**, *117*, 2008-2018.

[7] Uzun, A.; Gates, B. C. *Angew. Chem. Int. Ed. Engl.* **2008,** 47, 9245-9248.

[8] We have complied a table of the main prior kinetic and mechanistic studies of heterogeneous catalyst formation, and will report that in due course along with our other, in-progress studies. As stated in the main text a few of the conclusions from compiling that table are; (a) additional or improved experimental techniques for following

heterogeneous catalyst formation are needed, and (b) more in depth kinetic and mechanistic studies, including the balanced stoichiometry of the catalyst formation reaction, will be required en route to a better, mechanism-based understanding of how to control the syntheses of heterogeneous catalysts.

[9] For these reasons, the present research falls under one of DOE's current Grand Challenges in catalysis, namely the design and controlled synthesis of catalytic structures at the molecular and nanometer level, see: *Basic Research Needs: Catalysis for Energy*; PNNL-17214; Office of Basic Energy Sciences, U.S. Department of Energy; 2007 (http://www.sc.doe.gov/bes/reports/list.html).

[10] Somorjai, G. A.; Borodko, Y. G. *Catal. Lett.* **2001**, *76*, 1-5.

[11] Ma, Z.; Zaera, F. In *Encyclopedia of Inorganic Chemsitry*; 2nd ed.; King, B. R., Ed.; John Wiley & Sons Ltd: West Sussex, 2005; Vol. 3, p 1768-1784.

[12] Che, M.; Bennett, C. O. *Adv. Catal.* **1989**, *36*, 55-172.

[13] (a) Sajkowski, D. J.; Boudart, M. *Catal. Rev.-Sci. Eng.* **1987**, *29*, 325-360. (b) Bond, G. C. *Acc. Chem. Res.* **1993**, *26,* 490-495. (c) Oh, H.-S.; Yang, J. H.; Costello, C. K.; Wang, Y. M.; Bare, S. R.; Kung, H. H.; Kung, M. C. *J. Catal.* **2002**, *210*, 375-386. (d) Tiep, L. V.; Bureau-Tardy, M.; Bulgi, G.; Djega-Maridassou, G.; Che, M.; Bond, G. C. *J. Catal.* **1986**, *99*, 449-460.

[14] Somorjai, G. A. *Catal. Lett.* **1990**, *7*, 169-182.

[15] (a) Billinge, S. J. L.; Kanatzzidis, M. G. *Chem. Commun.* **2004**, 749-760 and references therein. (b) Billinge, S. J. L.; Foley, H. C.; Kantazidis, M. G.; Petkov, V.; Thorpe, M. F. *Structure of Nanocrystals*, available online at http://nirt.pa.msu.edu/ (accessed July 2008).

[16] The powerful, direct, high-energy X-ray scattering and pair distribution function (PDF) analysis methods have the large advantage of directly monitoring the loss of Pt–Cl bonds and the formation of Pt–Pt bonds.[4c] The primary disadvantage of these methods is that they are time and effort intensive, and thus relatively slow, with it possible to take even 1–2 years to analyze significant results. Hence, there is a pressing need to prescreen systems and then subject only the most interesting systems to those more direct and powerful, but also more expensive and slower, methods. Important in this regard is that advantages (fast; easy; cheap) and disadvantages (indirect) of the present, fast reporter reaction kinetic method are precisely the opposite of the high-energy X-ray scattering and pair distribution function (PDF) analysis methods (slower and expensive, but direct). Hence, the two methods are highly complimentary. For this reason, a collaboration with the Chupas team has been established in which the general plan is to screen systems with the fast kinetic methods reported herein and then subject the most interesting and important systems to the X-ray scattering methods.

[17] Watzky, M. A.; Finke, R. G. *J. Am. Chem. Soc.* **1997**, *119*, 10382-10400.

[18] (a) Aiken III, J. D.; Finke, R. G. *J. Mol. Catal. A: Chemical* **1999**, *145*, 1-44. (b) Roucoux, A.; Schulz, J.; Patin, H. *Chem. Rev.* **2002**, *102*, 3757-3778.

[19] Watzky, M. A.; Finney, E. E.; Finke, R. G. *J. Am. Chem. Soc.* **2008,** *130,* 11959-11969.

[20] (a) Wang, T.; Lee, C.; Schmidt, L. D. *Surf. Sci.* **1985**, *163*, 181-197. (b) Ahmadi, T. S.; Wang, Z. L.; Green, T. C.; Henglein, A.; El-Sayed, M. A. *Science* **1996**, *272*, 1924-1926. (c) Tao, A. R.; Habas, S.; Yang, P. *Small* **2008**, *4*, 310-325.

[21] (a) Watzky, M. A.; Finke, R. G. *Chem. Mater.* **1997,** *12*, 3083-3095. (b) Aiken III, J. D.; Finke, R. G. *J. Am. Chem. Soc.* **1998**, *120*, 9545-9554. (c) Widegren, J. A.; Aiken III, J. D.; Özkar, S.; Finke, R. G. *Chem. Mater.* **2001**, *13*, 312-324. (d) Hornstein, B. J.; Finke, R. G. *Chem. Mater.* **2004**, *16*, 139-150 (see also: *Chem. Mater.* **2004,** 16, 3972-3972). (e) Besson, C.; Finney, E. E.; Finke, R. G. *J. Am. Chem. Soc.* **2005**, *127*, 8179-8184. (f) Besson, C.; Finney, E. E.; Finke, R. G. *Chem. Mater.* **2005**, *17*, 4925-4938. (g) Finney, E. E.; Finke, R. G. *Chem. Mater.* **2008**, *20*, 1956-1970.

[22] Newton, M. A.; Fiddy, S. G.; Guilera, G.; Jyoti, B.; Evans, J. *Chem. Commun.* **2005**, 118-120.

[23] Williams, C. T.; Chen, E. K.-Y.; Takoudis, C. G.; Weaver, M. J. *J. Phys. Chem. B* **1998**, *102*, 4785-4794.

[24] Lin, Y.; Finke, R. G. *J. Am. Chem. Soc.* **1994**, *116*, 8335-8353.

[25] Aiken III, J. D.; Finke, R. G. *Chem. Mater.* **1999**, *11*, 1035-1047.

[26] Widegren, J. A.; Aiken III, J. D.; Özkar, S.; Finke, R. G. *Chem. Mater.* **2001**, *13*, 312-324.

[27] Lin, Y.; Finke, R. G. *Inorg. Chem.* **1994**, *33*, 4891-4910.

[28] (a) De Jong, K. P.; Geus, J. W. *Appl. Catal.* **1982**, *4*, 41-51. (b) Bond, G. C.; Rawle, A. F. *J. Mol. Catal. A: Chemical* **1996**, *109*, 261-271. (c) Sales, E. A.; Benhamida, B.; Caizergues, V.; Lagier, J.-P.; Fiévet, F.; Bozon-Verduraz, F. *Appl. Catal. A: General* **1998**, *172*, 273-283. (d) Bonet, F.; Grugeon, S.; Urbina, R. H.; Tekaia-Elhsissen, K.; Tarascon, J.-M. *Solid State Sicences* **2002**, *4*, 665-670. (e) Zawadzki, M.; Okal, J. *Mater. Res. Bull.* **2008**, *43*, 3111-3121. (f) Boutros, M.; Denicourt-Nowicki, A.; Roucoux, A.; Gengembre, L.; Beaunier, P.; Gédéon, A.; Launay, F. *Chem. Commun.* **2008**, 2920-2922.

[29] An important topic, one that will require its own extensive studies to unravel, is the nature of the precise Pt speciation when H_2PtCl_6 is placed on supports such as Al_2O_3 as well as the kinetic contribution of each species to $Pt(0)_n$ formation. There is literature on the speciation of H_2PtCl_6 in aqueous solutions as well as in the presence of Al_2O_3.[30] However, no real consensus exists at present on either the exact species present in solution or on the Al_2O_3 support. The literature is clear that $[PtCl_6]^{2-}$, aquo species such as $[PtCl_5(H_2O)]^-$, aquahydroxo species such as $[PtCl_4(OH)(H_2O)]^-$ along with many others exist in aqueous solutions, and that such speciation is highly pH dependent. The exact interaction of the species formed from aqueous H_2PtCl_6 with the Al_2O_3 support is also a controversial subject.[30b,c] Regalbuto[30a] suggests that when fresh H_2PtCl_6 solutions are

prepared the major species present in solution is $[PtCl_3(H_2O)_3]^+$, and it is repelled from the protonated $[Al_2O_3]^+$ surface at low pH. However the major species present in aged H_2PtCl_6 solutions in a mid-pH of 5-9 (as defined by those authors[30b]) is $[PtCl_2(OH)_2(H_2O)_2]^0$, and this species should more readily interact with the Al_2O_3 support. In the present studies, we use ethyl acetate for the H_2PtCl_6 impregnation step in a deliberate attempt to minimize any subsequent speciation and to emphasize support of the neutral, parent complex. However, during our kinetic runs the H_2PtCl_6/Al_2O_3 is in contact with the EtOH and cyclohexene solution, so that additional speciation is possible if not probable. Experimentally, we know that the kinetics of H_2PtCl_6 reduction in EtOH plus cyclohexene solutions (but without Al_2O_3 present) are different than the kinetics when Al_2O_3 is present; hence, the support must be playing a role in the observed catalyst formation kinetics. The good news here is that the ability of the catalytic reporter reaction method to rapidly monitor the kinetics of nanocluster formation will allow the needed survey of a range of supports, metal, and other conditions. Such experiments should yield insights into the Pt speciation and into many other unanswered questions regarding how to best prepare superior supported-nanocluster heterogeneous catalysts.

[30] (a) Spieker, W. A.; Liu, J.; Miller, J. T.; Kropf, A. J.; Regalbuto, J. R. *Appl. Catal. A: General* **2002,** *232,* 219-235. (b) Spieker, W. A.; Liu, J.; Miller, J. T.; Kropf, A. J.; Regalbuto, J. R. *Appl. Catal. A: General* **2003**, *243,* 53-66. (c) Shelimov, B. N.; Lambert, J.-F.; Che, M.; Didillon, B. *J. Mol. Catal. A: Chemical* **2000**, *158,* 91-99. (d) Mang, T.; Breitscheidel, B.; Polanek, P.; Knözinger, H. *Appl. Catal. A: General* **1993**, *106,* 239-258. (e) Brunelle, J. P. *Pure & Appl. Chem.* **1978**, *50,* 1211-1229.

[31] For the error limits in k_1 (~$\pm 10^{1.2}$ h^{-1}) and k_2 (~1(3) x 10^2 M^{-1} h^{-1}) observed in multiple investigator's hands over a 7+ year period for $P_2W_{15}Nb_3O_{62}^{9-}$ polyoxoanion-stabilized $Ir(0)_{\sim 300}$ nanocluster formation, see p. 10304 of: Widegren, J. A.; Bennett, M. A.; Finke, R. G. *J. Am. Chem. Soc.* **2003,** *125,* 10301-10310.

[32] (a) Although the 2-step F–W kinetic model is consistent with all of the present data as well as a considerable body of prior kinetics (more than 700 runs) of nanocluster formation under H_2,[17,21] it needs to be emphasized that the F–W kinetic model is a deliberately minimalistic, "Ockham's razor"-obtained model. As just one example of presently unknown details, the fuller mechanism presumably involves ligated nanocluster, M_a–L_b (M = metal), intermediates as well as possible nanocluster hydride, M_c–H_d, intermediates,[21c,g] since naked M(0) atoms are highly energetic and thus relatively unstable.[17,21c,g] Of interest in this regard is that metal-hydrides have been previously postulated to be the aggregating species in supported catalyst formation.[33] Elsewhere we discuss the limitations of the F–W model, limitations that derive ultimately from its minimalistic nature.[37,38]

[33] (a) Dalla Betta, R. A.; Boudart, M. In *International Congress on Catalysis (5th)*; North-Holland: Palm Beach, Fla, 1972; Vol. 5th Annual, p 1329-1341. (b) Reagan, W. J.; Chester, A. W.; Kerr, G. T. *J. Catal.* **1981**, *69*, 89-100.

[34] Ott, L. S.; Finke, R. G. *Coord. Chem. Rev.* **2007**, *251*, 1075-1110.

[35] Wilkins, R. G. *Kinetics and Mechanism of Reactions of Transition Metal Complexes.* 2 ed.; VCH: New York, 1991.

[36] Rodriguez, J. A.; Kim, J. Y.; Hanson, J. C.; Perez, M.; Frenkel, A. I. *Catal. Lett.* **2003**, *85*, 247-254.

[37] Sigmoidal kinetic curves for protein aggregation fit by the F–W 2-step kinetic model, papers that also contain a detailed discussion of the limitations of the F–W kinetic model (see also elsewhere for a general discussion of the limitations of models in science[38]) all types: (a) Morris, A. M.; Watzky, M. A.; Agar, J. N.; Finke, R. G. *Biochem.* **2008**, *47*, 2413-2427. (b) Watzky, M. A.; Morris, A. M.; Ross, E. D.; Finke, R. G. *Biochemistry* **2008**, *47*, 10790-10800. (c) Morris, A. M.; Finke, R. G. *Biophysical Chemistry* **2009**, *140,* 9-15.

[38] Finney, E. E.; Finke, R. G. *Chem. Mater.* **2009,** *21,* 4468-4479.

[39] The successful extension of the F–W model to solid-gas reactions is not surprising given that metal thin-film formation have been previously shown to follow the F–W model in at least the one case examined: Widegren J. A.; Bennett, M. A.; Finke, R. G. *J. Am. Chem. Soc.* **2003**, *125*, 10301-10310.

Supporting Information for:

Monitoring Supported-Nanocluster Heterogeneous Catalyst Formation: Product and Kinetic Evidence for a 2-Step, Nucleation and Autocatalytic Growth Mechanism of $Pt(0)_n$ Formation from H_2PtCl_6 on Al_2O_3 or TiO_2

Joseph E. Mondloch, Xinhuan Yan and Richard G. Finke

Additional Results and Discussion

H_2 Gas-to-Solution MTL Test Plots. H_2 gas-to-solution MTL have been shown to cause the undesired effect of producing bulk-metal products in the case of $Rh(0)_n$ formation, since diffusive aggregation of initially formed nanoparticles (which eventually yields bulk metal) competes kinetically with surface autocatalytic growth (to form near-monodisperse nanoparticles).[1] To test whether or not H_2 gas-to-solution MTL are affecting the observed nanocluster formation (k_1 and k_2) kinetics in the 1.96-wt% H_2PtCl_6/Al_2O_3 system presented in the main text, we looked at stirring-speed dependence plots, a classic test for the presence of MTL.[1] If the rate-determining step of the overall reaction is H_2 gas-to-solution mass-transfer limited, then an increase in the rate of the reaction as the stir speed is increased should be observed.

The data, Figure S1, show that only a small change in reaction rate is observed at higher stirring speeds under our experimental conditions (600 rpm). Specifically, increasing the stir speed from 600 to 1000 rpm changes the observed H_2 uptake by just 3 in 21 parts. This introduces an error of ≤15% into our observed kinetics, an error that is less than or equal to the experimental error in the rate constants. In short, the stirring rate controls in Figure S1 show that negligible MTL effects are present as desired in the 1.96-wt% H_2PtCl_6/Al_2O_3 system under the conditions reported and in our apparatus as described in the Experimental section of the main text.[2]

Testing the Cyclohexene Reporter Reaction for the Desired Zero-Order [Cyclohexene] Dependence. One of the necessary requirements when using the cyclohexene reporter reaction is that the rate of cyclohexene reduction must be fast (see Scheme 2 in the main text) in comparison to the supported nanocluster (i.e., heterogeneous catalyst) formation steps k_1 and k_2. This requirement is experimentally testable by looking at the [cyclohexene] dependence of the reaction and plotting it against the rate of the loss of H_2, as shown in Figure S2: if zero-order or approaching

zero-order kinetics in [cyclohexene] are seen, then the reporter reaction is working properly.

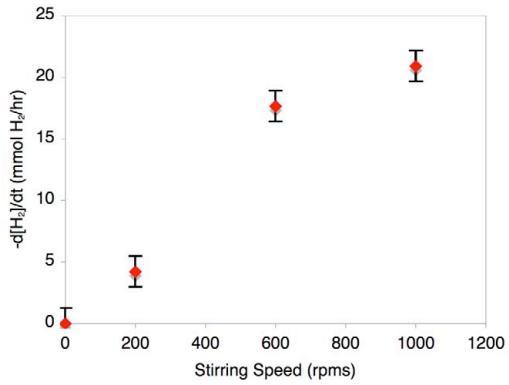

Figure S1. Stirring speed dependence for the 1.96-wt% H_2PtCl_6/Al_2O_3 system investigated as part of the present work and in our specific apparatus and other experimental conditions (as described in the Experimental section in the main text). This plot shows that H_2 gas-to-solution MTL effects are minimized when the stirring speed is above ca. 600 rpm; hence, that stirring speed was chosen for the present studies.

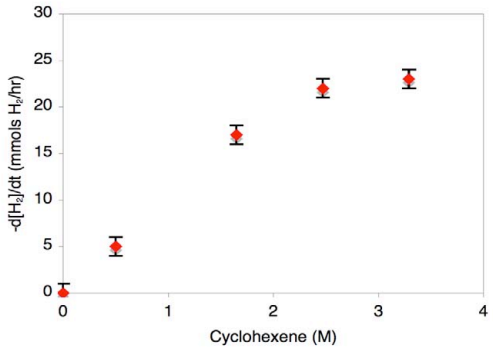

Figure S2. Cyclohexene dependent plots for the 1.96-wt% H_2PtCl_6/Al_2O_3 catalyst system shown in Scheme 1 of the main text. The observed near zero-order olefin reduction kinetics ensure that the cyclohexene reporter reaction is faster than the nanocluster formation rate, so that it is thereby properly reporting the nanocluster formation kinetics within the experimental error.[3]

Figure S2 shows that approaching zero-order kinetics in [cyclohexene] are in fact observed under our experimental conditions, which include 1.65 M cyclohexene. There is a slight increase of about 4 parts out of 22, introducing a quite tolerable error[2] of ≤18%

into the kinetics, an error again less than or equal to the intrinsic experimental error. However, an additional control experiment using higher olefin concentrations confirms the desired result that k_2 is identical within experimental error at higher olefin concentrations, k_2 (at 1.65M cyclohexene) = 1.3(1) x 10^4 h^{-1} M^{-1}, where as k_2 (at 2.47 M and 3.29 M cyclohexene) = 1.3 x 10^4 h^{-1} M^{-1}.

Effect of the Pre-Equilibration Time on the Reproducibility of the Kinetics of the 1.96-wt% H_2PtCl_6/Al_2O_3 System. During our studies, we noted that if one does not employ the 2-7 h pre-equilibration period cited in the Experimental and Results and Discussion sections in the main text, then irreproducible kinetics are obtained—very probably due to the different speciation of H_2PtCl_6 formed as a function of time (as discussed in the main text). The irreproducibility is largely observed in the induction period and hence in the resulting k_1 rate constant (since k_1 is roughly α $1/t_{induction}$).[3] As Figure S3 shows, the induction period can vary by several hours resulting in large k_1

variations from ~10^{-8} to 10^{-13} h^{-1}, that is $10^{\pm5}$ if the pre-equilibrium period is not used.

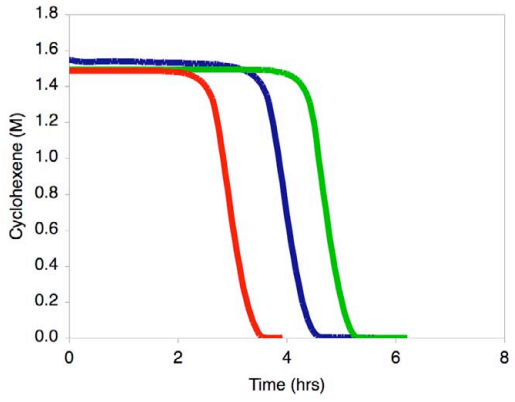

Figure S3. Observed variation in the kinetics of the 1.96-wt% $Pt(0)_n$ Al_2O_3 heterogeneous catalyst formation system if a pre-equilibrium stirring period (in the EtOH reaction medium) is not employed. The resultant k_1 for these curves varies from ~10^{-8}–10^{-13} h^{-1} (the smallest k_1 corresponding to the longest induction time), revealing the need to control and more fully understand the factors that influence k_1—which in turn is a key rate constant in controlling nanocluster *size*.[4]

Typical variations in k_1 (which is generally rather sensitive to conditions as discussed and listed elsewhere[2]) are $10^{\pm 1}$. This k_1, nucleation rate constant variation is an important experimental observation of this work as it shows that control of the precatalyst speciation and other variables (that need to be better understood) are having sizable effects on k_1.

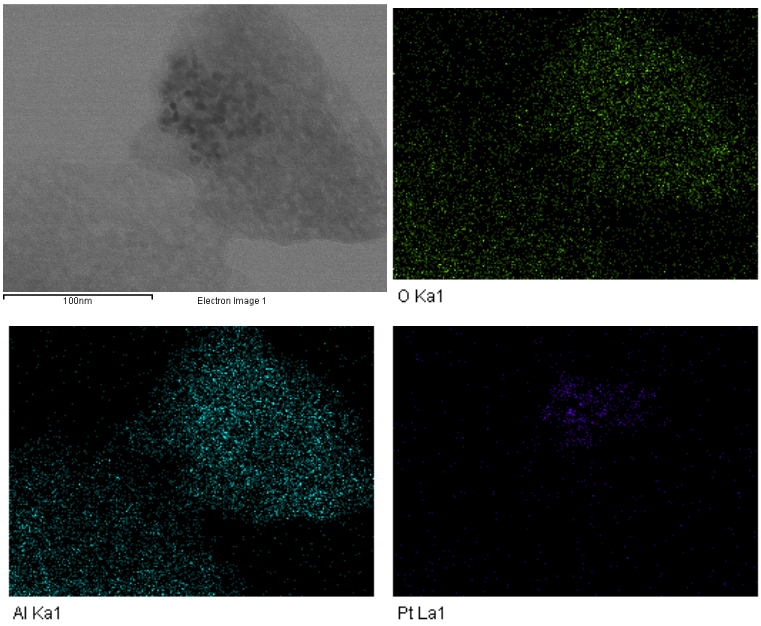

Figure S4. EDX mapping qualitatively confirms the presence of Pt on the Al_2O_3 support. The upper left shows a TEM image of the $Pt(0)_n$ nanoclusters on Al_2O_3. (Note the 100 nm scale bar at the bottom of the upper left image.) The EDX mapping image in the upper right and lower left confirm that the large structure in the TEM image does indeed contain Al and O. The EDX mapping image in the lower right shows the dark spots present on the Al_2O_3 support also contain Pt.

Integrated Rate Equation for the 2-Step, Finke-Watzky Nucleation and Autocatalytic Growth Mechanism. Equation S1 was first derived elsewhere[3] and is the equation employed in the nonlinear least-squares fitting of the concentration vs. time data.

$$[A]_t = \frac{\frac{k_1}{k_2} + [A]_0}{1 + \frac{k_1}{k_2[A]_0} * \exp^{(k_1 + k_2[A]_0)t}} \quad \text{(S1)}$$

EDX Mapping and Spectra of Pt(0)$_n$ Nanoclusters on Al_2O_3. The EDX mapping (Figure S4) and spectral (Figure S5) results confirm that Pt is in fact present on the Al_2O_3 surface; specifically, observed are the presence of the Pt L α edge (9.441 keV), Pt L-β edge (11.069 keV) and the Pt L-II absorbance edge (13.268 keV).[5]

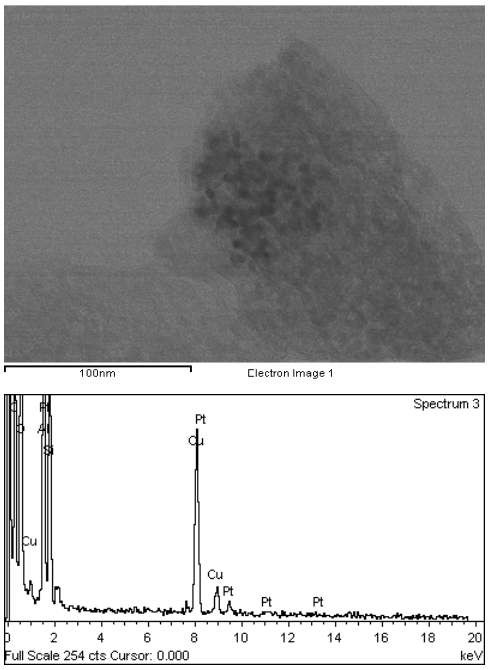

Figure S5. EDX spectra confirm the presence of the Pt L α edge (9.441 keV), Pt L-β edge (11.069 keV) and the Pt L-II absorbance edge (13.268 keV).[5] The top picture is again a TEM image of the resultant nanocluster formation products Pt(0)$_n$/Al_2O_3. The bottom image is the EDX spectrum demonstrating that the expected Pt(0) binding energies are observed.

Evidence for MTL Effects for 0.99-wt% H_2PtCl_6 on TiO_2. We also examined our 0.99-wt% H_2PtCl_6/TiO_2 sample for H_2 gas-to-solution MTL; the results of those

experiments are shown in Figure S6. One can see that even the 0.99-wt% sample is under significant H_2 gas-to-solution MTL since increasing the stirring speed from 600 to 1000 rpm results in a H_2 uptake increase from 33 psig of H_2/hr (at 600 rpm) to 50 psig of H_2/hr (at 1000 rpm). This is a ~52% increase in H_2 uptake for a 66% increase in stirring speed. However, the better fit to the F–W 2-step mechanism observed for the 1000 rpm stirred experiment is consistent with less MTL in that experiment as expected. The maximum stir speed of our apparatus is 1000 rpm so we were unable to experimentally verify whether or not a stirring rate of 1000 rpm is completely out of the H_2 gas-to-solution MTL regime.[1]

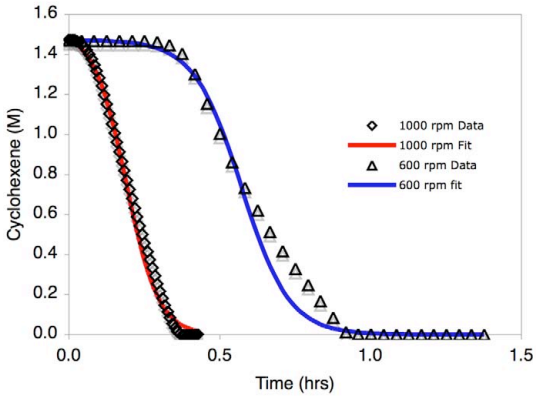

Figure S6. Comparison of the kinetics observed for the 0.99-wt% H_2PtCl_6/TiO_2 sample at 600 rpm and then 1000 rpm. Note the large increase in the reaction rate as well as the decrease in the induction period at 1000 rpm (50 psig H_2/hr @1000 rpm vs 33 psig H_2/hr @ 600 rpms), observations consistent with considerable H_2 gas-to-solution MTL at the slower 600 rpm stirring rate.[1] The improved fit to the F–W 2-step mechanism at the higher stirring rate is consistent with the move further away from the MTL regime at the higher, 1000 rpm stirring rate.

Control Experiment of H_2PtCl_6 Reduction in EtOH and Cyclohexene Solution in the Absence of Al_2O_3: Evidence for the Importance of the Al_2O_3 Component. To obtain direct evidence for (or against) the importance of the Al_2O_3 component, a reduction of H_2PtCl_6 in EtOH and cyclohexene solution, but in the absence of any Al_2O_3,

was done. Specifically, the conditions for this experiment were 0.63 mM H_2PtCl_6 (the same amount of Pt as in the Al_2O_3 supported run) in 2.5 mL of EtOH, 0.5 mL of cyclohexene and reduced under 40 psig of H_2; the results are shown in Figure S7. Again (as when Al_2O_3 *is* present) there is an induction period followed by a sharp turn-on during the formation of the final catalyst. $Pt(0)_n$ nanoclusters are formed when Al_2O_3 is present but bulk $Pt(0)_n$ is observed rather when Al_2O_3 is absent. The bottom line of this control experiment is that it provides prima facie evidence for the importance of the Al_2O_3 support in allowing the observed, supported-$Pt(0)_n$ nanocluster products to be formed, and before a good fit to the F–W 2-Step nucleation and growth mechanism can be obtained (see Figure S7).

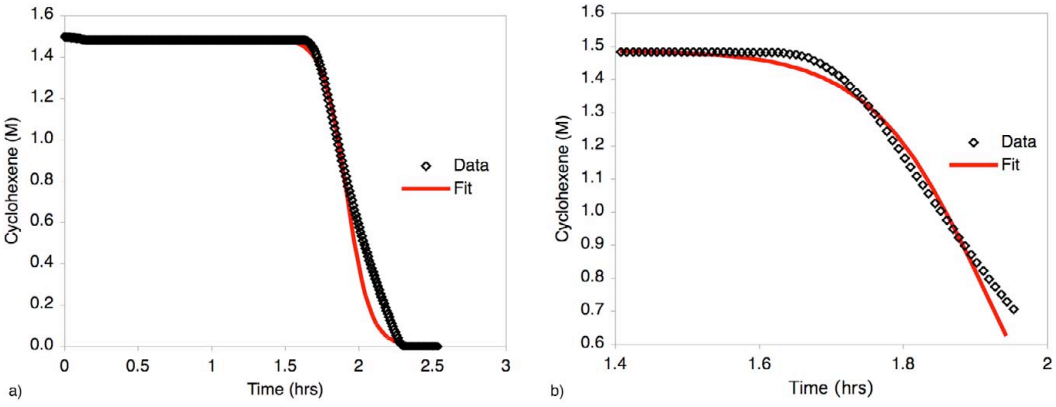

Figure S7. (a) Kinetics from the reduction of 0.63 mM H_2PtCl_6 in EtOH and cyclohexene and under 40 psig H_2, but without Al_2O_3 present, to form *bulk* $Pt(0)_n$ plus the attempted fit to the F–W 2-step mechanism. The fit to the F–W 2-step mechanism is relatively poor (R^2 = 0.9888), consistent with these kinetics (without Al_2O_3) being different than the 1.96-wt% H_2PtCl_6/Al_2O_3 kinetics—the main differences being in the sharp decrease post the induction period and what is probably agglomeration towards the end of the reduction curve (agglomeration needed to account for the bulk-metal product).

Scope of the H_2 Gas-Solid M_xO_y Reduction Problem. As noted in the main text, sigmoidal reduction curves have been observed in several H_2 gas-solid M_xO_y catalyst formation systems related to heterogeneous catalysts.[6] However the full sigmoidal

kinetic curves obtained from these studies have not been fully analyzed. We wondered if the F–W 2-step kinetic model could account for those observed sigmoidal kinetics. Specifically we have looked at both $Rh_2O_3/\gamma\text{-}Al_2O_3$[7a] supported nanoparticles and Rh_2O_3 thin films[7b] as well as bulk $(CuO)_n$[8] reduction, in what follows.

Derivation of a Form of the F–W 2-Step Kinetic Model Able to Fit the Fractional Product Conversion, a, of Solid-State Reactions. The 2-step F–W mechanism, and corresponding analytic equation (S1), was initially developed for solution-based kinetics. Since concentration is not a useful concept in the solid-state, one needs to convert eq. S1 into a form that measures the fractional conversion, α, for gas-solid catalyst formation or other solid-state reactions.[9] We need, therefore, to express equation S1 as a function of α, the extent of the reaction. This was previously done[10] by recognizing that $\alpha = ([A]_0\text{-}[A]_t)/[A]_0$ in the F–W 2-step kinetic model. Rearranging yields $[A]_t = [A]_0(1\text{-}\alpha)$, which was then substituted into S2. One also needs to define $k_2' = k_2[A]_0$ as first done elsewhere[10] to remove the concentration dependence in equation S1. The desired fractional form of our 2-step kinetic model, with no explicit concentration-dependent terms, is obtained as equation S2.

$$\alpha = 1 - \frac{k_1 + k_2'}{k_2' + k_1 \exp^{(k_1 + k_2')t}} \qquad \text{(S2)}$$

Also required for the fits presented next is a slightly rearranged form of equation S2 which allows one to follow the loss of starting material, $1\text{-}\alpha$, rather than the fractional growth of product, α. Rearranging equation S2 yields the desired $1\text{-}\alpha$ equation, S3.

$$1 - \alpha = \frac{k_1 + k_2'}{k_2' + k_1 \exp^{(k_1 + k_2')t}} \qquad \text{(S3)}$$

Literature M_xO_y Reduction Kinetics Data Analysis and Curve Fitting. The selected, previously published kinetic data were digitized from those literature papers and figures[7,8] using Engauge Digitizer 2.12. The data were fit to equation S2 when the fractional formation of the product, α, was followed, and to equation S3 when the loss of original precursor or phase, 1-α, was followed. Fits were obtained using the nonlinear least-squares curve-fitting program in Originlab Corporation's Origin version 7.0.

Initial Application of the Results Herein and the F–W 2-Step Kinetic Model to Other Heterogeneous Catalyst Formation Systems. In the applications of the F–W 2-step kinetic model which follow A is by definition the M_xO_y (either Rh_2O_3 or $(CuO)_n$ for the cases which follow) while B is the growing phase or zone of the reduced metal species, presumably $Rh(0)_n$ or $Cu(0)_n$, respectively.

Weaver, and co-workers Study on Rh_2O_3 Thin Film Reduction. In the first study re-examined herein, Weaver and co-workers studied the reduction of Rh_2O_3 thin films under H_2 by using Surface Enhanced Raman spectroscopy (SERS) from 50-100 °C.[7b] These authors observed the presence of an induction period while monitoring the ν_{Rh-O} oxide band intensity, and aptly suggested that this "can most readily be rationalized in terms of a nucleation/growth type of reaction mechanism". However, the authors did not fit their data to any specific nucleation and growth mechanism—undoubtedly since there was no chemical-equation-based mechanism and associated analytic equations available that had been used to fit such solid-state data. The F–W model was available,[3] but it had not yet been recognized that it could be used to analyze solid-state data[10] normally fit by the Avrami and related, non-chemical-mechanism-based, equations.

Employing the F–W 2-step model, eq S3, effectively fit both the 50 (k_1 = 5(2) x 10^{-5} s^{-1}, k_2' = 0.93(4) s^{-1}) and 100 ℃ (k_1 = 2(2) x 10^{-5} s^{-1}, k_2' = 1.8(2) s^{-1}) sets of data, Figure S8. The 50 and 100 ℃ data and associated fits confirm for the first time Weaver and co-workers hypothesis that their data "can most readily be rationalized in terms of a nucleation/growth type of reaction mechanism". The data taken at 150 ℃ can also be fit by the F–W 2-step kinetic model as shown in Figure S8, but the lack of an induction period means that nucleation is fast so that there is not really a good reason to use the 2-step model with its nucleation step based on this data 150 ℃ alone (although the good fits to the lower temperature data do provide some basis for using the 2-step model in even this case). The higher temperature data in Figure S8 are of some interest for a possible explanation they suggest in relation to the literature H_2PtCl_6/TiO_2 data[11] noted in the main text. Specifically the lack of induction in the literature H_2PtCl_6/TiO_2 could conceivably be at least in part due to the high temperatures employed.

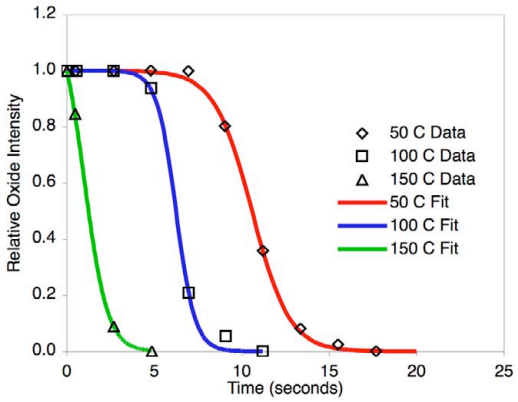

Figure S8. Digitized relative oxide intensity (ν_{Rh-O}) data for the reduction of Rh_2O_3 thin films followed by SERS,[7b] and the associated fits to the F–W 2-step kinetic model. The fits for the 50 ℃ and 100 ℃ data are well fit by the F–W 2-step kinetic model and yield k_1 = 5(2) x 10^{-5} s^{-1} and k_2' = 0.93(4) s^{-1} rate constants in the 50 ℃ case (R^2 = 0.993) and k_1 = 2(2) x 10^{-5} s^{-1} and k_2' = 1.8(2) s^{-1} rate constants in the 100 ℃ case (R^2 = 0.998). The data at 150 ℃ are also well fit to the F–W 2-step kinetic model; however, the lack of induction period means that the F–W 2-step model is not really appropriate for that higher temperature data. The lack of the expected temperature dependence on the k_1 rate constant for the 50 ℃ and 100 ℃ data is very likely due to the imprecision of the k_1 values, that imprecision in turn due to the relatively few datum points present in the (always hard to precisely determine[2]) induction period.

Newton et al.'s Rh_2O_3 Nanoparticle on γ-Al_2O_3 System: A Case Where Good Fits to the F–W 2-Step Mechanism are Not Always Seen. Newton et al.[7a] studied the reduction and oxidation behavior of Rh_2O_3 nanoparticles on γ-Al_2O_3 (5-wt%) using x-ray absorption near edge structure (XANES), from 373–573 K. Those authors observed an induction period and also claim, albeit without fitting their data to any kinetic expressions, that this "suggests a nucleation-growth mechanism".

To analyze this data we assigned a value of 1 to the highest intensity of the XANES spectra in Figure 1 of that paper[7a], and a value of 0 for the lowest intensity in that figure. The results for the 373, 473 and 573 K data are shown in Figures S9–S11.

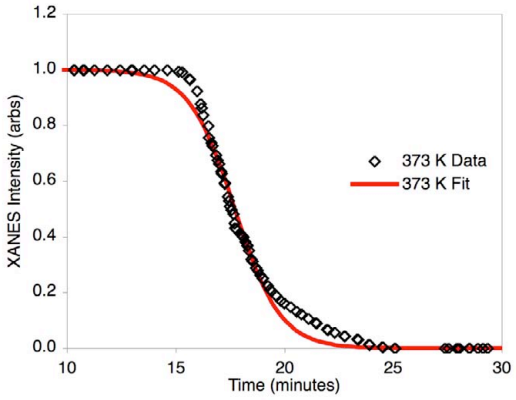

S9. Digitized Rh K edge data[7a] followed by XANES at 373 K and the corresponding attempted fit to the F–W 2-step kinetic model for the H_2 gas-solid reduction of Rh_2O_3 nanoparticles on γ-Al_2O_3. The F–W 2-step kinetic model cannot account for the kinetic data observed under these specific conditions, although it is probable that our 3- or 4-step models, which involve aggregation steps,[12] will, something we are testing as part of other work in progress.

Overall, one can see that F–W 2-step kinetic model only fits the data to some extent in the 473 K case, with significant deviations from the model at both lower (373 K) and higher temperature (573 K). Not shown are the 423 K and 523 K data, but the results are similar: the F–W 2-step model cannot adequately account for those kinetic curves, either. As noted above, it is quite possible that our 3- or 4-step mechanisms[12] may be

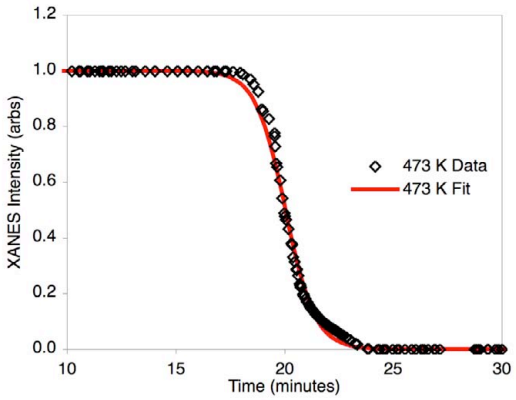

Figure S9. Digitized Rh K edge data[7a] followed by XANES at 473 K and the corresponding fit to the F-W 2-step kinetic model for the H_2 gas-solid reduction of Rh_2O_3 nanoparticles on γ-Al_2O_3. In this case the F–W 2-step model accounts reasonably well for the observed data and rate constants k_1 ~ 3(5) x 10^{-13} min^{-1} and k_2' = 1.5(1) min^{-1} can be obtained, effectively deconvoluting nucleation and growth. However, the poor fits for the lower (Figure S9) and higher (Figure S11) data suggest that the current fit is more accidental than real. The failure of the 2-step model to fit closely the sharp "turn-on" after the induction period even in the present 473 K data is another hint that the 2-step model is probably not appropriate for these curves. These are interesting findings, one we are exploring further.

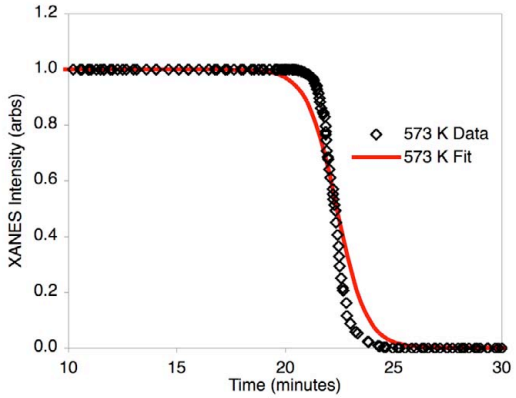

Figure S10. Digitized Rh K edge data[7a] followed by XANES at 573 K and the corresponding attempted fit to the F–W 2-step kinetic model for the H_2 gas-solid reduction of Rh_2O_3 nanoparticles on γ-Al_2O_3. Now again at higher temperature, the F-W 2-step kinetic model cannot account for the kinetic data observed under these specific conditions. Again, it is likely that our 3- or 4-step models involving aggregation steps[12] will fit this data, something that is under study. The curious part is that even if it does, the resulting aggregation steps—which make sense at this higher temperature since solid-state diffusion often has a higher activation enthalpy and thus is significantly thermally activated—do *not* also therefore make sense at the lower temperature in Figure S9. In short, the data in Figures S9-S11 are of considerable interest for a more detailed analysis than is beyond the scope of the present work, but one that is in progress as part of other studies.

able to account for this data, where the 3- and 4-step models are just the first 3, or all 4, of the steps which follow: A → B, A+B → 2B, 2B → C, and B + C → 1.5 C. Indeed, in preliminary studies (not shown) *the 4-step mechanism can fit both the 373 and 473 K data*; however, both the 4-step and 2-step mechanisms fail to account for the 573 K data indicating that further studies will be required. Moreover, whether or not the 4-step model (and its aggregation steps)[12] makes physical sense for the solid-state (and where concentration is not a useful concept) is an unresolved issue—again, further research is needed. Another issue with the above data and analyses—as in all kinetic studies—is (a) precisely what the method of following the reaction is measuring (the XANES in this case, or the XRD in the example below, especially in terms of any speciation present), and (b) then the need to express what is actually being followed correctly mathematically in terms of the specific kinetic model employed. The needed additional studies of this interesting set of data, and the insights they promised to provide, are in progress.

Rodriguez and Co-Workers $(CuO)_n$ Reduction System. Rodriguez and co-workers[8] used in situ time-resolved X-ray diffraction (XRD) to study both the H_2 reduction of $(CuO)_n$ and the simultaneous formation of $(Cu)_n$ at 200 °C. Induction periods in the H_2 reduction of $(CuO)_n$ have been observed for quite some time,[13] yet the mechanistic interpretation of such curves has been lacking. The results of the fit to the F–W 2-step kinetic model to the data are presented in Figure S12. One can see that pretty decent fits to both the loss of $(CuO)_n$ and the formation of $(Cu)_n$ are observed in this case. Rate constants for the loss of $(CuO)_n$ have been obtained for the first time from this data, k_1 = 1.5(1) x 10^{-3} min^{-1} and k_2' = 7.0(1) x 10^{-2} min^{-1}, as well as for the formation of $(Cu)_n$, k_1 = 2(1) x 10^{-5} min^{-1} and k_2' 1.70(9) x 10^{-1} min^{-1}. This is a telling data set regarding the errors in the resultant rate constants; we expect that the k_1 values are basically the same (and thus ~$10^{-4(\pm1)}$ min^{-1}) as are the k_2' values, ~(1.2 ± 0.5) x 10^{-1} min^{-1}. The important findings here are, then, three fold: (i) the fits provide the first kinetic evidence in the $(CuO)_n$ plus

H_2 system for the 2-step mechanism consisting of slow, continuous nucleation followed by fast autocatalytic growth;[3] (ii) the nucleation and growth rate constants have been deconvoluted from this sigmoidal kinetic data for the first time; and (iii) this particular data set is a good one since it follows both the loss of reactants and the formation of products, and therefore allows some idea of realistic error bars on the rate constants.

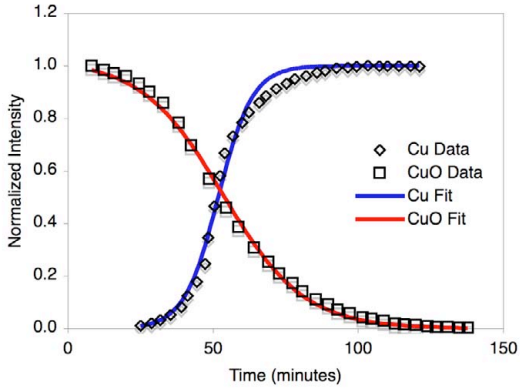

Figure S12. Digitized data following the H_2 reduction of $(CuO)_n$ and the formation of $(Cu)_n$ by time-resolved XRD at 200 ℃, and their associated fits to the F–W 2-step kinetic model. The resulting rate constants for $(CuO)_n$ loss are: k_1 = 1.5(1) x 10^{-3} min^{-1} and k_2' = 7.0(1) x 10^{-2} min^{-1}, while those for $(Cu)_n$ formation are k_1 = 2(1) x 10^{-5} min^{-1} and k_2' 1.70(9) x 10^{-1} min^{-1}.

Conclusions Regarding the Literature M_xO_y Reduction Kinetics Data Analysis and Curve Fitting. The take home message from these fits (or attempted fits in some cases) of literature M_xO_y reductions by traditional H_2 gas-solid reactions is that the F–W 2-step model can account nicely for some, *but not all*, of the literature *gas-solid* reaction data examined above. A chemical-mechanism-based nucleation and growth model has not been used to fit nor quantitatively analyze these heterogeneous catalyst formation kinetic data previously, but should be at least considered in the future (albeit considered with the above results and limitations in mind, as well as the limitations and caveats noted elsewhere[10] clearly in mind).

References

[1] Aiken III, J. D.; Finke, R. G. *J. Am. Chem. Soc.* **1998**, *120*, 9545-9554.

[2] (a) For the error limits observed in k_1 (~$10^{1.2}$ h^{-1}) and k_2 (~1(3) x 10^2 M^{-1} h^{-1}) in multiple investigator's hands over a seven-plus year period for $P_2W_{15}Nb_3O_{62}^{9-}$ polyoxoanion-stabilized $Ir(0)_{\sim 300}$ nanoparticle formation, see p. 10304 of: Widegren, J. A.; Bennett, M. A.; Finke, R. G. *J. Am. Chem. Soc.* **2003,** 125, 10301-10310. (b) See also that work and the references therein[2] for a list of variables that are known to affect nanocluster formation kinetics (such as H_2O in the solvent, acetone solvent impurities, the presence of any free $[(1,5\text{-COD})Ir(solvate)_2]^+$ not bound to the polyoxoanion, the possibility of heterogeneous nucleation sites, and so on.

[3] Watzky, M. A.; Finke, R. G. *J. Am. Chem. Soc.* **1997**, *119*, 10382-10400.

[4] Watzky, M. A.; Finney, E. E.; Finke, R. G., *J. Am. Chem. Soc.* **2008**, *130*, 11959-11969.

[5] Thompson, A. C.; Vaughn, D. *X-Ray Data Booklet*, 2 ed.; Kirz, J., Attwood, D., Gullikson, E. Lawrence Berkley National Laboratory: Berkley, 2001; Pg's 19, 38.

[6] Note one caveat here: we have not yet completed an exhaustive search of the gas-solid heterogeneous catalyst formation literature for useful kinetic curves. However, we do know that sigmoidal curves for phase-change behavior are very common in nature. This in turn implies that the sigmoidal curves analyzed as part of this Supporting Information are very probably representative of at least some heterogeneous catalyst formations involving H_2 as the reductant in gas-solid reactions.

[7] (a) Newton, M. A.; Fiddy, S. G.; Guilera, G.; Jyoti, B.; Evans, J. *Chem. Commun.* **2005**, 118-120. (b) Williams, C. T.; Chen, E. K.-Y.; Takoudis, C. G.; Weaver, M. J. *J. Phys. Chem. B* **1998**, *102*, 4785-4794.

[8] Rodriguez, J. A.; Kim, J. Y.; Hanson, J. C.; Perez, M.; Frenkel, A. I. *Catal. Lett.* **2003**, *85*, 247-254.

[9] Galeway, A. K., Brown, M. E., *Studies in Physical and Theoretical Chemistry: Thermal Decomposition of Ionic Solids.* Elsevier: Amsterdam, 1999.

[10] Finney, E. E.; Finke, R. G. *Chem. Mater.* **2009,** *21,* 4692-4705.

[11] Chupas, P. J.; Chapman, K. W.; Jennings, G.; Lee, P. L.; Grey, C. P. *J. Am. Chem. Soc.* **2007**, *129*, 13822-13824.

[12] (a) Besson, C.; Finney, E. E.; Finke, R. G. *J. Am. Chem. Soc.* **2005**, *127*, 8179-8184. (b) Besson, C.; Finney, E. E.; Finke, R. G. *Chem. Mater.* **2005**, *17*, 4925-4938.

[13] (a) Wright, C. *J. Chem. Soc. Transactions* **1879**, *35*, 475-524. (b) Voge, H. H.; Atkins, L. T. *J. Catal.* **1962**, *1*, 171-179.

CHAPTER IV

DEVELOPMENT PLUS KINETIC AND MECHANISTIC STUDIES OF A PROTOTYPE SUPPORTED-NANOPARTICLE HETEROGENEOUS CATALYST FORMATION SYSTEM IN CONTACT WITH SOLUTION: Ir(1,5-COD)Cl/γ-Al_2O_3 AND ITS REDUCTION BY H_2 TO $Ir(0)_n$/γ-Al_2O_3

This dissertation chapter contains the manuscript of a paper published in the *Journal of the American Chemical Society* **2010,** *132,* 9701–9714 and is available online at http://dx.doi.org/10.1021/ja1030062. This chapter develops eight prototype criteria for a well-defined supported-nanoparticle formation system in contact with solution, namely Ir(1,5-COD)Cl/γ-Al_2O_3 to $Ir(0)_{\sim 900}$/γ-Al_2O_3 in acetone, cyclohexene and H_2. Emphasis was placed on state-of-the-art characterization of the supported-precatalyst, the supported-nanoparticle catalyst and the stoichiometry of the conversion of Ir(1,5-COD)Cl/γ-Al_2O_3 to $Ir(0)_{\sim 900}$/γ-Al_2O_3. Initial kinetic studies of the supported-nanoparticle heterogeneous catalyst formation reaction were also performed.

The experiments within this chapter were designed by Joseph E. Mondloch and Professor Richard G. Finke. XAFS data was measured, processed and analyzed by our XAFS collaborators Qi Wang and Anatoly I. Frenkel. All remaining experiments (and data analysis) within this chapter were performed by Joseph E. Mondloch. The manuscript was written by Joseph E. Mondloch and edited by Professor Richard G. Finke, with proofreading at the galley stages by all authors.

DEVELOPMENT PLUS KINETIC AND MECHANISTIC STUDIES OF A PROTOTYPE SUPPORTED-NANOPARTICLE HETEROGENEOUS CATALYST FORMATION SYSTEM IN CONTACT WITH SOLUTION: Ir(1,5-COD)Cl/γ-Al_2O_3 AND ITS REDUCTION BY H_2 TO Ir(0)$_n$/γ-Al_2O_3

Joseph E. Mondloch, Qi Wang, Anatoly I. Frenkel and Richard G. Finke

Overview

An important question and hence goal in catalysis is how to best transfer the synthetic and mechanistic insights gained from the modern revolution in nanoparticle synthesis, characterization and catalysis, to prepare the next generation of improved, supported-nanoparticle heterogeneous catalysts. It is precisely this question and to-date somewhat elusive goal which are addressed by the present work. More specifically, the global hypothesis investigated herein is that the use of speciation-controlled, well-characterized, solid oxide supported-organometallic precatalysts *in contact with solution* will lead to the next generation of better *composition,* size, and shape-controlled, as well as highly active and reproducible, supported-nanoparticle heterogeneous catalysts—ones that can also be understood kinetically and mechanistically. Developed herein are eight criteria defining a prototype system for supported-nanoparticle heterogeneous catalyst formation in contact with solution. The initial prototype system explored is the precatalyst, Ir(1,5-COD)Cl/γ-Al_2O_3 (characterized via ICP, CO adsorption plus IR, and XAFS spectroscopies), and the

well-defined product, $Ir(0)_n/\gamma\text{-}Al_2O_3$ (characterized by reaction stoichiometry, TEM, and XAFS). The $Ir(0)_n/\gamma\text{-}Al_2O_3$ system proved to be a highly active and long-lived catalyst in the simple test reaction of cyclohexene hydrogenation and in comparison to two literature $Ir(0)_n/Al_2O_3$ heterogeneous catalysts examined under identical conditions. High activity (2.2–4.8 fold higher than that of the literature $Ir(0)_n/Al_2O_3$ catalysts tested under identical conditions) and good lifetime (≥220 000 total turnovers of cyclohexene hydrogenation) are observed, in part by design since only acetone solvent, cyclohexene, and H_2 are possible ligands in the resultant "weakly ligated/labile-ligand" supported nanoparticles. Significantly, the $Ir(1,5\text{-}COD)Cl/\gamma\text{-}Al_2O_3 + H_2 \rightarrow Ir(0)_n/\gamma\text{-}Al_2O_3$ heterogeneous catalyst formation kinetics were also successfully monitored using the cyclohexene hydrogenation reporter reaction method previously developed and applied to solution-nanoparticle formation. The observed sigmoidal supported-nanoparticle heterogeneous catalyst formation kinetics, starting from the $Ir(1,5\text{-}COD)Cl/\gamma\text{-}Al_2O_3$ precatalyst, are closely fit by the two-step mechanism of slow continuous nucleation ($A \rightarrow B$, rate constant $k_1 = 1.5(1.1) \times 10^{-3}\ h^{-1}$) followed by fast autocatalytic surface growth ($A + B \rightarrow 2B$, rate constant $k_2 = 1.6(2) \times 10^{4}\ h^{-1}\ M^{-1}$), where A is the $Ir(1,5\text{-}COD)Cl/\gamma\text{-}Al_2O_3$ precatalyst and B is the resultant $Ir(0)_n/\gamma\text{-}Al_2O_3$ catalyst. The kinetics are significant in establishing the ability to monitor the formation of supported-nanoparticle heterogeneous catalysts in contact with solution. They also suggest that the nine synthetic and mechanistic insights from the two-step mechanism of nanoparticle formation in solution should now apply also to the formation of supported-nanoparticle heterogeneous catalysts in contact with solution. The results open the door for new syntheses of supported-nanoparticle heterogeneous catalysts under nontraditional, mild, flexible conditions where supported organometallics and other precursors are in contact with solution, so that additional variables such as the solvent choice, added ligands, solution temperature and so on can be used to control the catalyst formation steps and,

ideally, the resultant supported-nanoparticle heterogeneous catalyst composition, size, and shape.

Introduction

Nanoparticles on metal-oxide supports constitute a large important subset of heterogeneous catalysts.[1] However, the synthesis of these industrially significant catalysts is still largely empirical, Schlögl, for example, recently noted that "catalysts are currently 'prepared' rather than synthesized".[2] In addition, relatively little is known about *the mechanisms of formation* of those industrially most significant catalysts.[3,4] This dearth of mechanistic information is largely due to a lack of experimental methods that would allow researchers to follow the catalyst formation kinetics easily and in real time.[5,6,7] Methods to more quickly, routinely, and precisely monitor supported-nanoparticle heterogeneous catalyst formation are expected to be significant in at least three ways: (i) mechanistically, resulting in an improved fundamental understanding of the mechanism(s) of heterogeneous catalyst formation; (ii) synthetically, allowing improved rational design and subsequent synthesis of heterogeneous catalysts, a significant challenge for the field;[8] and (iii) practically, since key catalytic properties[9]—such as selectivity,[10] activity,[9] lifetime and stability[11]—depend on the catalyst surface composition,[12] size,[13] and structure.[10]

Hence, an important but still largely unmet goal of modern catalysis is to transfer to heterogeneous catalysis the synthetic control[14] over nanoparticle composition,[15] size,[16] and shape,[17] as well as the mechanistic insights into nanoparticle formation,[18,19,20,21,22,23,24] which have resulted from the modern revolution in nanoparticle science. The hope is that transferring those insights will allow improved syntheses of, mechanistic understanding of, and catalysis by those composition-, shape-, and size-controlled supported-nanoparticles.

Relevant here is that surprisingly little is known for certain about the mechanisms of formation of supported-nanoparticle heterogeneous catalysts outside of high-vacuum studies (i.e. little is known about practical, "dirty/real-world" catalysts),[25,26,27] and there

are no kinetic studies of the formation of supported catalysts in contact with solution (as performed herein). A review of the literature of the kinetics and mechanism of heterogeneous catalyst formation is available elsewhere,[4] and some lead papers[28,29,30,31,32,33,34,35,36,37] and points from that review are summarized in a footnote[38] for the interested reader.

Controlling the resultant nanoparticle *surface composition* is, in our opinion, the most overlooked, yet crucial, aspect of nanoparticle catalysts.[14h] The literature teaches that there is a general problem with *completely* removing stabilizing ligands or polymers from ligand- or polymer-protected nanoparticles (i.e., ligands or polymers used during their synthesis to prevent aggregation).[39,40] This is closely related to what we have termed the "weakly ligated/labile-ligand" nanoparticle synthesis and stabilization problem,[41,42] that is the question of how can one prepare nanoparticles with *only* the desired, catalytically relevant ligands (or other ligands relevant to the desired physical property) present *from the start*?

Goals of the Present Studies. The overarching hypothesis of the present work is that developing the synthesis of supported-nanoparticle catalysts *formed in contact with solution*, while simultaneously studying the kinetics and mechanism under those identical conditions (i.e., in situ or ideally operando[43]), is an important way to both (a) prepare a next generation of supported-nanoparticle catalysts with composition, size and shape control and to (b) bring what has been developed in the modern "nanoparticle revolution"[14] to supported heterogeneous catalysts and their catalysis.

On reflection we realized it would help considerably to outline the needed studies in terms of what we define herein as a *prototype system* for the study of supported-nanoparticle heterogeneous catalysts *in contact with solution*. Specifically, a prototype system should be one in which the following 8 attributes have been achieved (seven of which are reported via the present studies, vide infra): (i) a compositionally and

structurally well-defined supported precatalyst is developed and employed; (ii) the system is in contact with solution, and a lower temperature reaction (at least to start) is employed with the goal of minimizing further speciation of the precatalyst;[6,36] and (iii) one both can and does establish the balanced stoichiometry of a supported-nanoparticle formation reaction to well-defined supported-nanoparticle products. In addition, a prototype system should be one in which (iv) an active and long-lived catalyst results (so that the time-consuming kinetic and mechanistic studies are worth the expense and effort); (v) a rapid, quantitative, real-time kinetic monitoring method can be applied to the forming supported-nanoparticle heterogeneous catalyst; and (vi) reproducible kinetic data are obtained so that reliable, quantitative conclusions can be drawn.[44] Ideally, (vii) a prototype system would also be one in which the supported heterogeneous catalyst system can be compared and contrasted with a kinetically and mechanistically well-studied—and ideally the prior best-studied—nanoparticle formation system in solution.[18,19,45,46,47] Once a prototype system is in hand, one would also like to (viii) systematically vary key synthetic variables such as the support, solvent and metal precursor to reveal their effects on the kinetics, mechanism(s), and synthesis of supported-nanoparticle heterogeneous catalyst formation in contact with solution.

Herein we describe our initial studies (a) synthesizing and characterizing a prototype system consisting of a compositionally and structurally well-defined Ir(1,5-COD)Cl/γ-Al_2O_3 precatalyst; (b) characterizing the $Ir(0)_n$/γ-Al_2O_3 product formed in contact with solution and under H_2 and cyclohexene reduction catalysis while also establishing a balanced nanoparticle formation reaction; and (c) determining the high activity and long lifetime of the resultant "weakly ligated/labile-ligand"[41] supported-nanoparticle catalyst, in which the γ-Al_2O_3 support, the solvent, and the desired reactants H_2 and cyclohexene are the *only ligands present* (since the reaction product HCl is a very poor ligand at best). Significantly, also provided are studies (d) successfully monitoring the

nanoparticle formation kinetics by our now well-precedented cyclohexene reporter reaction method (Scheme 1, top),[18-22,45,48,49] plus the appropriate control studies to ensure that the reporter reaction is performing reliably. Additionally provided are (e) evidence that the observed kinetic data are well-fit by a two-step mechanism of nanoparticle formation[18] in Scheme 1, plus (f) interesting comparative studies of the $[Ir(1,5\text{-}COD)Cl]_2$ precursor alone, that is, in the absence of $\gamma\text{-}Al_2O_3$, which reveal the role of the solid-support in stabilization the resultant $Ir(0)_{\sim 900}$ nanoparticles towards subsequent aggregation.

Scheme 1. The Cyclohexene Reporter Reaction Employed Herein to Follow $Ir(0)_n/\gamma\text{-}Al_2O_3$ Supported-Nanoparticle Heterogeneous Catalyst Formation in Contact with Solution [a] and the Two-Step Mechanism Hypothesis That Will Be Tested Herein [b]

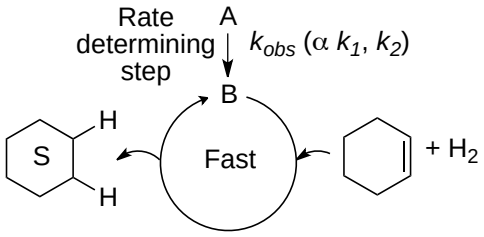

2-Step Mechanism

$A \xrightarrow{k_1} B$ (Nucleation)

$A + B \xrightarrow{k_2} 2B$ (Autocatalytic Surface Growth)

Implied Detailed Steps

$2n\ Ir^{I} \xrightarrow{H_2} 2/n\ Ir(0)_n$

$Ir^{I} + Ir(0)_n \longrightarrow Ir(0)_{n+1}$

[a] A is the $Ir(1,5\text{-}COD)Cl/\gamma\text{-}Al_2O_3$ precatalyst and B is the growing $Ir(0)_n$ surface. [b] See Figure 6, vide infra.

Overall, the results presented herein satisfy the first seven of eight attributes defined above for a prototype system for kinetic and mechanistic studies of supported-nanoparticle formation in contact with solution. As such, they begin to test the global hypothesis underlying this work: that quantitative studies of the kinetics and mechanisms

of heterogeneous catalyst formation *in contact with solution*[4] will allow exploration of an important, but to-date little investigated, subarea of heterogeneous catalyst synthesis[50] and the associated mechanistic studies and resultant knowledge. A key sub-hypothesis is that the necessary prototype systems must begin with well-defined, speciation-controlled precatalysts, while also demonstrating a balanced stoichiometry to an also well-characterized, ideally highly active catalyst. The overall goal is to use the resultant knowledge to guide new and improved syntheses of better composition-, size-, and shape-controlled supported-nanoparticle heterogeneous catalysts.

Results and Discussion

Ir(1,5-COD)Cl/γ-Al_2O_3: Precatalyst Synthesis and Characterization. Organometallic complexes such as $[M(1,5\text{-COD})Cl]_2$ (where M = Ir or Rh) provide a precedented[51] avenue for the preparation of well-defined oxide-supported-metal complexes.[52] They also have served as precursors for discrete polyoxoanion oxide-supported organometallics such as $[M(1,5\text{-COD})\bullet P_2W_{15}Nb_3O_{62}]^{8-}$ (M = Ir or Rh)[44,46] that evolve under H_2 and cyclohexene to the highly active,[44] yet stable and isolable,[44] as well as kinetically and mechanistically well-characterized,[18,19,45,46,47] soluble $Ir(0)_{\sim 300}\bullet(P_2W_{15}Nb_3O_{62}{}^{8-})_n{}^{-8n}$ nanoparticles.

For what follows and unless stated otherwise, a 2.0 wt % Ir(1,5-COD)Cl/γ-Al_2O_3 precatalyst was prepared and employed in the drybox by the addition of acidic γ-Al_2O_3 to an ethyl acetate solution of $[Ir(1,5\text{-COD})Cl]_2$ of the appropriate wt % (Scheme 2, top). The solid was then brought to dryness under vacuum, all as described in the accompanying Experimental Section. The resultant precatalyst is denoted Ir(1,5-COD)Cl/γ-Al_2O_3, consistent with our characterization data, vide infra.

The Ir content of the Ir(1,5-COD)Cl/γ-Al_2O_3 precatalyst was confirmed by inductively coupled plasma-optical emission spectroscopy (ICP-OES): theoretical 1.1% Ir, found

1.0% Ir. In addition we find that 1 equiv of cyclooctadiene per Ir is converted into 1 equiv of cyclooctane (i.e. the expected amount) by the end of the supported-nanoparticle heterogeneous catalyst formation reaction, vide infra. This result suggests that an intact $Ir^{I}(1,5\text{-COD})^{+}$ moiety is present on the $\gamma\text{-}Al_2O_3$ support, consistent with a 16 electron Ir(I) species and its strong preference for a square planar geometry.

Scheme 2. Synthesis of the $Ir(1,5\text{-COD})Cl/\gamma\text{-}Al_2O_3$ Precatalyst (Top) as Well as the CO Trapping Reaction for Subsequent IR Analysis (Bottom)

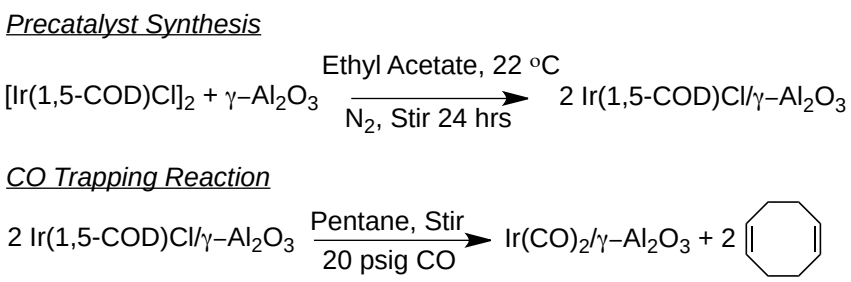

One precedent, valuable method for probing the nature of low-valent supported-metal complexes is to place the precatalyst under CO (Scheme 2, bottom), isolate the resultant material (a beige solid), and examine its IR spectrum in the CO stretch region.[53] The IR spectrum in Figure 1 (green line) shows ν(CO) stretches at 2076 and 2000 cm^{-1}, as expected for the symmetric and antisymmetric stretches, respectively, of a C_{2v}-symmetric $Ir^{I}(CO)_2/\gamma\text{-}Al_2O_3$ dicarbonyl species.[54] As a control, an authentic $Ir^{I}(CO)_2/\gamma\text{-}Al_2O_3$ dicarbonyl precatalyst sample was prepared by contacting $Ir^{I}(CO)_2(acac)$ with $\gamma\text{-}Al_2O_3$, revealing very similar bands at 2075 and 1998 cm^{-1} (Figure 1, red line), confirming the assignment of a supported $Ir(CO)_2^{+}$ moiety. Note that the presence of only two CO bands in the IR spectrum *is consistent with the $[Ir(1,5\text{-COD})Cl]_2$ dimer being split into the corresponding Ir(1,5-COD)Cl monomer during its support on $\gamma\text{-}Al_2O_3$*; if a dimeric $[Ir(1,5\text{-COD})\mu\text{–}O_{Support}]_2$ species had been present, then symmetry considerations along with literature precedent[51] suggest that three CO bands would have been seen (i.e., in that

case arising from the coupling of the *cis*-$Ir(CO)_2$ moieties[55]). Precedent for surface-induced cleavage of the bridging M–Cl bonds has been observed for the deposition of $[Rh(1,5\text{-}COD)Cl]_2$ onto partially dehydroxylated $\gamma\text{-}Al_2O_3$.[52]

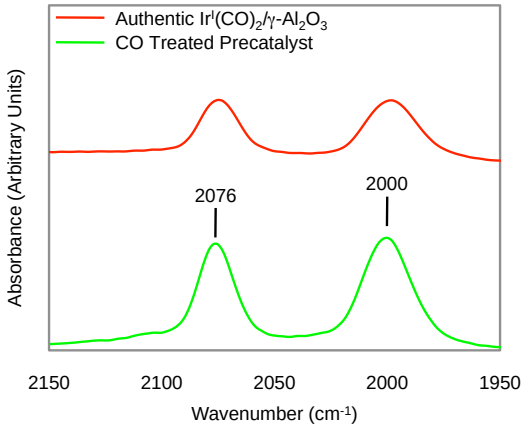

Figure 1. IR spectra of the $Ir(1,5\text{-}COD)Cl/\gamma\text{-}Al_2O_3$ precatalyst after reaction with CO (green line), ν(CO) = 2076 and 2000 cm^{-1} consistent with the assignment of $Ir(CO)_2/\gamma\text{-}Al_2O_3$. The red line is a sample of independently prepared $Ir(CO)_2/\gamma\text{-}Al_2O_3$, ν(CO) = 2075 and 1998 cm^{-1}.

X-ray absorption near-edge structure (XANES) and extended X-ray absorption fine structure (EXAFS) analyses were used to further probe the nature of the precatalyst structure and, ultimately, provide further strong support for a $Ir(1,5\text{-}COD)Cl/\gamma\text{-}Al_2O_3$ precatalyst composition and structure. The XANES spectrum of the $Ir(1,5\text{-}COD)Cl/\gamma\text{-}Al_2O_3$ precatalyst is shown in Figure 2a, in comparison to those of the well-known $[Ir(1,5\text{-}COD)Cl]_2$[56] and $[Ir(1,5\text{-}COD)\mu\text{-}OCH_3]_2$[57] reference compounds. The position and intensity as well as the shape of the Ir L_3-edge white-line are consistent with the precatalyst structure being formally in the Ir^{I} oxidation state (the white-line at the L_3-edge is an element-specific quantum mechanical transition arising from the excitation of core-

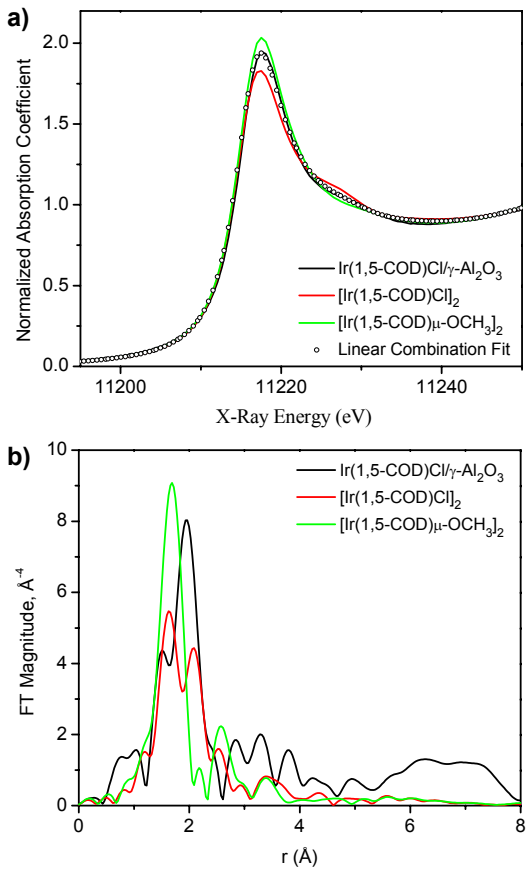

Figure 2. XAFS data comparison of the precatalyst Ir(1,5-COD)Cl/γ-Al_2O_3 to the reference compounds $[Ir(1,5\text{-COD})Cl]_2$ and $[Ir(1,5\text{-COD})\mu\text{-}OCH_3]_2$: (a) XANES spectra; (b) EXAFS data-Fourier transform magnitude of $k^3\chi(k)$ (k ranges 2 – 11.5 $Å^{-1}$). Error bars for the resultant coordination numbers are provided in Table 1.

level $2p_{3/2}$ electrons into unoccupied $5d_{5/2}$ and $5d_{3/2}$ states above the Fermi level[58]). In addition, the white-line intensity of the Ir(1,5-COD)Cl/γ-Al_2O_3 precatalyst is intermediate between those of the $[Ir(1,5\text{-COD})Cl]_2$ and $[Ir(1,5\text{-COD})\mu\text{-}OCH_3]_2$ reference compounds. This suggests partial substitution of the chloride ligands from the $[Ir(1,5\text{-COD})Cl]_2$ precursor with an oxo type ligand, an –OH from the γ-Al_2O_3 support being consistent with all our evidence, vide infra. This qualitative result was further confirmed by simulating the Ir(1,5-COD)Cl/γ-Al_2O_3 precatalyst spectrum as a linear combination of the $[Ir(1,5\text{-COD})Cl]_2$ and $[Ir(1,5\text{-COD})\mu\text{-}OCH_3]_2$ model compounds (Figure 2a, black circles): the precatalyst spectrum is well modeled by 47% $[Ir(1,5\text{-COD})Cl]_2$ plus 53% [Ir(1,5-

COD)μ-OCH_3]$_2$, *consistent with an Ir(1,5-COD)Cl/γ-Al_2O_3 structure in which the fourth ligand at Ir is an –OH or other overall neutral oxygen ligand donated by the γ-Al_2O_3 support.*

EXAFS was used to further elucidate the coordination environment around Ir in the Ir(1,5-COD)Cl/γ-Al_2O_3 precatalyst. The Fourier-transformed, k^3 weighted Ir-L_3 EXAFS data are plotted in Figure 2b, again alongside the two Ir reference compounds. Two distinct peaks at ~ 1.6 and ~ 2.1 Å are present in the [Ir(1,5-COD)Cl]$_2$ reference spectrum due to the Ir–C (i.e., cyclooctadiene ligand) and Ir–Cl scattering contributions. Each EXAFS spectrum was fit using theoretical signals modeled with FEFF6[59] (see the Supporting Information). The data were analyzed in the first nearest neighbor (hereafter 1NN) distance range only; details of the analysis are provided in the Experimental Section. The best-fit values of the 1NN structural parameters are listed in Table 1. The 1NN scattering parameter for [Ir(1,5-COD)Cl]$_2$, $N_{Ir–total}$, was constrained to 6 and yielded coordination numbers for Ir–C and Ir–Cl of 4.1 ± 0.5 and 1.9 ± 0.5 respectively. In contrast, only one dominant scattering peak is present at ~ 1.7 Å for the [Ir(1,5-COD)μ-OCH_3]$_2$ reference spectrum, arising from both the C (from cyclooctadiene) and O (from the bridging methoxy ligands) scatters since EXAFS is unable to distinguish between these two scatterers.

The Ir(1,5-COD)Cl/γ-Al_2O_3 precatalyst also contains split peaks, due to the presence of multiple ligands in the Ir coordination sphere. The partial replacement of chloride by oxo ligands from the γ-Al_2O_3 support is believed to account for the subtle change in peak position and amplitude relative to those for the [Ir(1,5-COD)Cl]$_2$ precursor. When the overall coordination number of the precatalyst structure was held constant at 6, $N_{Ir–C}$ and $N_{Ir–Cl}$ were found to be 3.6 ± 0.7 and 2.4 ± 0.7 respectively. In addition, theoretical modeling done without imposing such constraints (i.e., $N_{Ir–Total}$ = 6) for both the precatalyst and [Ir(1,5-COD)Cl]$_2$ reference compound reveals overall coordination

numbers of 6.1 ± 1.5 and 5.9 ± 0.9 respectively, consistent with the literature data.[51,56] The individual Ir–C and Ir–Cl pair coordination numbers also agree with those obtained by the constrained fit model, further confirming that the CN(Ir–1NN) = 6 model is a good approximation. Pleasingly, the EXAFS and the XANES analyses *independently confirm* the presence of chloride in the first coordination shell of Ir for the Ir(1,5-COD)Cl/γ-Al_2O_3 precatalyst structure. The two techniques complement each other in this work, giving a range of possible values of the Ir–Cl coordination numbers [between 1 Ir–Cl pair per Ir (by analysis of the XANES), and 2.4 Ir–Cl pairs per Ir (by analysis of the EXAFS)], thereby constraining the possible precatalyst structural models, vide infra.

Table 1. The best fit results obtained via EXAFS analysis for: Ir black, $Ir(0)_{\sim 900}/\gamma\text{-}Al_2O_3$, the precatalyst Ir(1,5-COD)Cl/γ-Al_2O_3, and for the reference compounds $[Ir(1,5\text{-}COD)Cl]_2$ and $[Ir(1,5\text{-}COD)\mu\text{-}OCH_3]_2$.[a]

	sample				
	Ir black	$Ir(0)_{\sim 900}/\gamma\text{-}Al_2O_3$	Ir(1,5-COD)Cl/γ-Al_2O_3	$[Ir(1,5\text{-}COD)Cl]_2$	$[Ir(1,5\text{-}COD)\mu\text{-}OCH_3]_2$
$N_{Ir–Ir}$	*12*[b]	9.2(2.8)			
$N_{Ir–Cl}$			2.4(7)[c]	1.9(5)[c]	
$N_{Ir–C}$			3.6(7)	4.1(5)	4[d]
$N_{Ir–O}$					2[d]
$N_{Ir–Total}$			6[c]	6[c]	6
$R_{Ir–Ir}$ (Å)	2.713(3)	2.68(2)			
$R_{Ir–Cl}$ (Å)			2.36(1)	2.41(1)	
$R_{Ir–C}$ (Å)			2.07(3)	2.10(1)	2.05(3)
$R_{Ir–O}$ (Å)					2.07(1)
$\sigma^2_{Ir–Ir}$ (Å^2)	0.0032(1)	0.0042(27)			
$\sigma^2_{Ir–Cl}$ (Å^2)			0.0031(16)	0.0048(19)	
$\sigma^2_{Ir–C}$ (Å^2)			0.0056(19)	0.0039(12)	0.0076(42)
$\sigma^2_{Ir–O}$ (Å^2)					0.0008(5)

[a] The actual fits are shown in the Supporting Information for the interested reader. [b] $N_{Ir–Ir}$ is fixed at 12 based on the crystallographically determined structure; [c] $N_{Ir–Total}$ is fixed at 6 and $N_{Ir–Cl}$ is constrained to vary as 6 - $N_{Ir–C}$; [d] $N_{Ir–O}$ and $N_{Ir–C}$ are fixed at 2 and 4, respectively, based on the known structure of this reference compound.[57]

In short, XANES and EXAFS confirm the CO trapping and subsequent IR analysis results by revealing that supporting the dimeric $[Ir(1,5\text{-}COD)Cl]_2$ on γ-Al_2O_3 results in splitting this precursor complex into monomeric units. The EXAFS data are consistent with the presence of 6 1NN scatterers around Ir in the precatalyst structure, as one would expect for an Ir^I, d^8 square planar complex with one 1,5-COD ligand (i.e., four 1NN C scatterers), one Cl, and one other O ligand, taken to be a surface hydroxyl, –OH, by charge balance. The XANES data are also consistent with a mixed chloro and oxo ligand environment around Ir, further supported by the fit to a linear combination of the $[Ir(1,5\text{-}COD)Cl]_2$ and $[Ir(1,5\text{-}COD)\mu\text{-}OCH_3]_2$ model compounds. Given that EXAFS provides an average result, we cannot unequivocally rule out by the XAFS a 1:1 mixture of $Ir(1,5\text{-}COD)Cl(–Cl–Al)_{Support}$ plus $Ir(1,5\text{-}COD)OH(–OH)_{Support}$, although chemically this—and in a precise 1:1 ratio—seems less plausible, as do other possibilities that do not fit our structural data.[52b] Such a mixture is also less consistent with the (just) two band $Ir(CO)_2$ IR data, vide supra. Overall, the data are fully consistent with and supportive of the precatalyst structure $Ir^I(1,5\text{-}COD)Cl(–OH)_{Support}$/γ-$Al_2O_3$, designated as Ir(1,5-COD)Cl/γ-Al_2O_3.[60] Significantly, consistent with the well-defined composition and structure of our Ir(1,5-COD)Cl/γ-Al_2O_3 precatalyst, we see highly reproducible supported-nanoparticle heterogeneous catalyst formation kinetics (vide infra), results pleasingly much more “homogeneous catalysis-like” than “heterogeneous catalysis-like”, probably in no small part due to control over the precatalyst speciation.

$Ir(0)_n$/γ-Al_2O_3 Supported-Nanoparticle Heterogeneous Catalyst Formation: Solution Synthesis, Resultant Stoichiometry, and Product Characterization. To convert the Ir(1,5-COD)Cl/γ-Al_2O_3 precatalyst into the active $Ir(0)_n$/γ-Al_2O_3 catalyst product, 50 mg of the precatalyst was placed in acetone along with ~1700 equiv of cyclohexene (per equivalent of Ir) (Scheme 3, top); note that the Ir(1,5-COD)Cl/γ-Al_2O_3 precatalyst is, then and therefore, in contact with acetone, cyclohexene and H_2 only (vide

infra). The mixture was sealed in a Fisher Porter (FP) bottle equipped with Swagelock Quick-Connects, removed from the drybox, placed in a temperature regulated water bath, attached to an O_2- and H_2O-scrubbed H_2 line, interfaced to a pressure transducer (that reports ±0.01 psig) and stirred at 600 rpm, all as done previously in our well-described kinetic/synthetic apparatus.[18-22] The reduction of cyclohexene to cyclohexane serves as a reporter reaction[18-22] (Scheme 1, vide supra), one able to monitor the formation of the $Ir(0)_n/\gamma\text{-}Al_2O_3$ catalyst, vide infra (Scheme 3, bottom reaction). As before,[18-22] we denote these conditions as "standard conditions" in the Experimental Section and throughout the rest of the paper.

Scheme 3. Supported-Nanoparticle Heterogeneous Catalyst Formation Reaction Stoichiometry Starting from the $Ir(1,5\text{-}COD)Cl/\gamma\text{-}Al_2O_3$ Precatalyst (Top), Along With the Cyclohexene Reporter Reaction (Bottom)

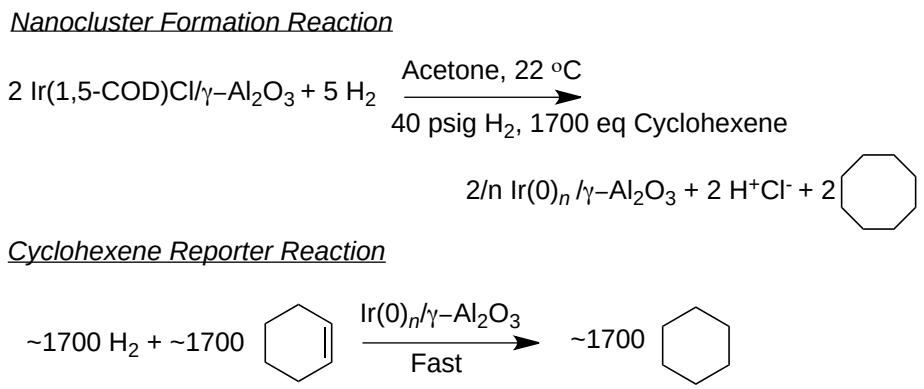

The designed $Ir(1,5\text{-}COD)Cl/\gamma\text{-}Al_2O_3$ precatalyst allows confirmation of the reaction stoichiometry (Scheme 3, top) via the evolution of the expected 1.0 equiv of cyclooctane [1.0 ± 0.1 equiv of cyclooctane per Ir evolved after approximately one hour as confirmed by gas-liquid-chromatography (GLC), see Figure 7]. Although the uptake of 5.0 equiv of H_2 was nominally expected (Scheme 3), 6.8 ± 0.2 equiv of H_2 are consumed in the catalyst formation reaction. The additional 1.8 equiv of H_2 is very probably due to the well-known phenomenon of H_2 spillover onto the support,[61] especially since the

corresponding $Ir(0)_n$ nanoparticle formation reaction in solution[44] does not take up any "extra" H_2 (so that $Ir(0)_n(H)_2$ hydride species, for example, are *not* seen, at least in the analogous $Ir(0)_n$ nanoparticle formation reaction in solution[44,62]). This is a good example of the value of studying a system in which the products, kinetics and mechanism of the analogous $Ir(0)_n$ nanoparticle formation reaction in solution are available for comparison.[18,19,45,46,47] Interestingly (and in response to a reviewer's query), we note that the observed spillover (~1.8 H_2/Ir) is within 2-fold of that seen for the polyoxoanion "support" (~1 H_2/Ir), but far below spillover ratios of as high as, for example, 350 H_2/Pt seen in the literature.[61]

The dark gray $Ir(0)_n/\gamma\text{-}Al_2O_3$ products were examined by transmission electron microscopy (TEM) and high-resolution (HR) TEM (Figure 3, which also shows the associated particle size distribution), revealing well dispersed Ir nanoparticles on the $\gamma\text{-}Al_2O_3$ support. The resultant nanoparticles are 2.9 ± 0.4 nm in diameter (i.e., ±14%, so-called near monodisperse nanoparticles[63]), corresponding *on average* to an $Ir(0)_{\sim 900}/\gamma\text{-}Al_2O_3$ product.[64] HRTEM images confirm that the $Ir(0)_{\sim 900}$ nanoparticles present on the $\gamma\text{-}Al_2O_3$ are crystalline (at least under the TEM beam, crystallization artifacts under the TEM beam being well known[65]), with lattice a spacing of 2.21 Å as expected for (111) Ir(0) (additional TEM images and particle size histograms are provided in the Supporting Information). Interestingly, the observed, on average $Ir(0)_{\sim 900}/\gamma\text{-}Al_2O_3$ nanoparticle products are very close to the sixth full closed-shell "magic-number sized" clusters containing 923 atoms in the limit of those precise, magic-number sized clusters.[66] Relevant here again is a piece of information from the $Ir(0)_n$ solution nanoparticle formation system and precedent:[66,44b] a tendency to form closed-shell ("magic-number") nanoparticles is seen in solution nanoparticle formation occurring by the two-step mechanism[66] shown back in Scheme 1. The reason magic-number-sized nanoparticles tend to form is because the autocatalytic surface-growth step[18,66] of the two-step

mechanism produces full-shell nanoparticles “where each surface atom contains the maximum number of metal–metal bonds”.[66] Hence, once magic-number clusters are formed, they are more stable and then, as a result, grow further only relatively slowly, the end result being a tendency for the more stable, magic-number sized clusters to accumulate.[66]

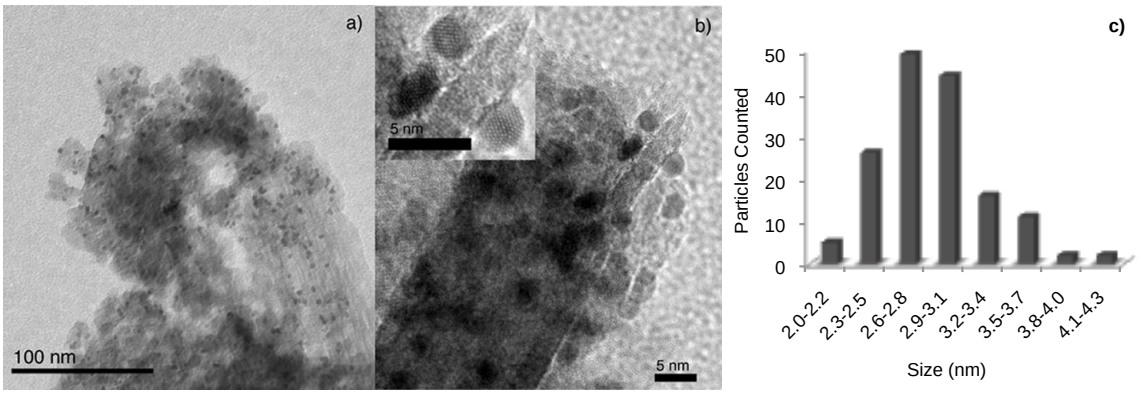

Figure 3. TEM imaging along with the associated particle size histogram of the $Ir(0)_{\sim 900}/\gamma\text{-}Al_2O_3$ catalyst. (a) A large-area view (scale bar 100 nm) showing that the nanoparticles are well dispersed on the support. (b) A close-up view (scale bar 5 nm), with the inset reveals the Ir nanoparticles are crystalline. (c) The associated particle size histogram for the resultant $Ir(0)_{\sim 900}/\gamma\text{-}Al_2O_3$ catalyst.

The $Ir(0)_{\sim 900}/\gamma\text{-}Al_2O_3$ product was further characterized using XAFS to evaluate the electronic structure and atomic interactions of the local environment. The Ir L_3-XANES spectrum obtained for $Ir(0)_{\sim 900}/\gamma\text{-}Al_2O_3$ shows a XANES white-line comparable to that of an Ir(0) black standard in both position and amplitude, suggesting a similar electronic structure (Figure 4a). In contrast, the near-edge spectrum of the $Ir(1,5\text{-COD})Cl/\gamma\text{-}Al_2O_3$ precatalyst features an increased white-line intensity, as well as a pronounced shift to higher energy relative to Ir black, consistent with a higher, formally Ir(I) oxidation state in comparison to the resultant $Ir(0)_{\sim 900}/\gamma\text{-}Al_2O_3$ sample. Figure 4b,c presents the background-subtracted and edge-step normalized EXAFS data in *k*- and *r*-spaces for $Ir(0)_{\sim 900}/\gamma\text{-}Al_2O_3$ in comparison to the $Ir(1,5\text{-COD})Cl/\gamma\text{-}Al_2O_3$ precatalyst and Ir black. The

in-phase EXAFS spectra of $Ir(0)_{\sim 900}/\gamma\text{-}Al_2O_3$ and Ir black point to the metallic nature of the $\gamma\text{-}Al_2O_3$ supported $Ir(0)_{\sim 900}$ nanoparticles. The independent theoretical modeling (shown in the Supporting Information) for $Ir(0)_{\sim 900}/\gamma\text{-}Al_2O_3$ reveals a 1NN value (coordination number) of 9.2 ± 2.8 (Table 1), corresponding to an average diameter of ~ 2.7 nm using the appropriate parameters for Ir,[67] fully consistent with the TEM results (2.9 ± 0.4 nm).

In summary, the supported-nanoparticle formation reaction stoichiometry of $Ir(0)_{\sim 900}$ nanoparticles on $\gamma\text{-}Al_2O_3$ shown in Scheme 3 was confirmed via cyclooctane evolution, H_2 uptake, TEM, EXAFS and XANES. Overall, the balanced stoichiometry from a well-defined precatalyst to a well-defined supported catalyst satisfies criteria i-iii for a prototype system as defined earlier. Pleasingly, an unusually active, as well as long-lived, "weakly ligated/labile-ligand" catalyst also results, since only acetone, cyclohexene, H_2 and the support are present as possible ligands, as detailed next.

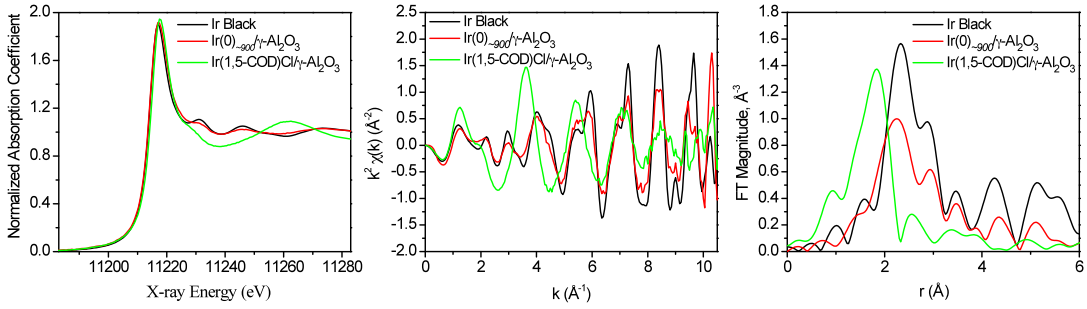

Figure 4. XAFS data for Ir black, the $Ir(0)_{\sim 900}/\gamma\text{-}Al_2O_3$ supported-nanoparticle, and Ir(1,5-COD)Cl/$\gamma\text{-}Al_2O_3$ precatalyst samples: (a) XANES spectra; (b) k^2-weighted, background-subtracted EXAFS signal, $\chi(k)$; and (c) Fourier transform magnitudes of $k^2\ \chi(k)$ (k = 2 – 10 $Å^{-1}$).

$Ir(0)_{\sim 900}/\gamma\text{-}Al_2O_3$: A Highly Coordinatively Unsaturated, and thus Highly Active and Long-Lived, Catalyst in Comparison to Literature Ir/Al_2O_3 Heterogeneous Catalysts. An important criterion (number iv, vide supra) of a prototype system is that the resultant catalyst be highly active and long-lived, in no small part to ensure that

subsequent detailed kinetic and mechanistic studies are worth the effort. Hence, we examined the catalytic ability of the $Ir(0)_{\sim 900}/\gamma\text{-}Al_2O_3$ product in the test reaction of cyclohexene hydrogenation. Specifically, we examined the turnover frequency (TOF, hr^{-1}) and observable total turnovers (TTOs) in comparison to those of two literature $Ir(0)_n/Al_2O_3$ catalysts previously rested in our laboratories.[44b] The results are shown in Table 2. The present $Ir(0)_{\sim 900}/\gamma\text{-}Al_2O_3$ catalyst affords 8200 (± 1700) turnovers per hour and 220 000 TTOs after correcting, as one should, for the number of surface Ir atoms (calculated from the TEM data and as described in the Experimental Section). This activity exceeds by ≥ 2.2- to 4.8-fold that of the literature $Ir(0)_n/Al_2O_3$ catalysts under the same conditions in our laboratories.[44b]

Table 2. Activity comparison of several $Ir(0)_n/Al_2O_3$ heterogeneous catalysts for the reduction of cyclohexene to cyclohexane.[a]

Catalyst	TOF (turnovers/hr)	TTOs (demonstrated)	Reference
Exxon's 80% dispersed $Ir/\eta\text{-}Al_2O_3$	1740±250[b,c]	20 000	44b
commercial 7.9% dispersed $Ir/\gamma\text{-}Al_2O_3$	3950±1000[b,c]	410 000	44b
$Ir(0)_{\sim 900}/\gamma\text{-}Al_2O_3$ (~ 38% dispersed)	≥ 8200±1700[d]	≥220 000[d]	this work

[a] Each reaction was carried out at 40 psig of H_2, 22 °C and in acetone, with stirring at 600 rpms. [b] These data are taken from D. Edlund's Ph.D. thesis from our labs[68] and were run in acetone, under 40 psig H_2 and 22 ºC, *conditions identical to those employed in herein*, with the exception that the acetone in these prior studies was dried over 3 Å molecular sieves.[44b] [c] These data are corrected for the number of available Ir atoms by H_2 chemisorption measurements. [d] The TOF as well as TTOs are corrected for the number of Ir surface atoms, which are based on calculations from the TEM data (as detailed in the Experimental section herein).

The high activity of the low-temperature, solution-prepared, coordinatively unsaturated $Ir(0)_{\sim 900}/\gamma\text{-}Al_2O_3$ catalyst is actually as expected, our plan being that a highly active catalyst would result since only *weakly coordinating solvent and the desired reactants* are present in the *"weakly ligated/labile-ligand"* nanoparticles[41,42] [i.e., where acetone solvent, H_2, cyclohexane, and the $\gamma\text{-}Al_2O_3$ support were the only possible

nanoparticle ligands available other than the (non-ligand) H^+Cl^-]. We have been working on "weakly ligated/labile-ligand" nanoparticles for some time[41a] and will detail additional results in a forthcoming publication.[42b] Overall, criterion number (iv) listed previously of a prototype system is satisfied considering that $Ir(0)_{\sim 900}/\gamma\text{-}Al_2O_3$ exhibits both high activity, > 8,200 turnovers/hr and a long lifetime, ≥ 220,000 total turnovers.

$Ir(0)_{\sim 900}/\gamma\text{-}Al_2O_3$ Catalyst Formation Kinetics in Contact with Solution: Rapid and Real Time Monitoring of the Supported-Nanoparticle Formation via the Cyclohexene Reporter Reaction Method. Using the cyclohexene reporter reaction[18-22] shown in Scheme 1, we have been able to obtain, easily and quickly, very precise kinetic data for the formation of $Ir(0)_{\sim 900}/\gamma\text{-}Al_2O_3$ and starting from the $Ir(1,5\text{-COD})Cl/\gamma\text{-}Al_2O_3$ precatalyst (10 kinetic runs, each with up to 60 data points at ± 0.025% psig precision out of 40 psig). Also performed and shown in the Supporting Information are (a) the necessary controls for the (lack of a) stirring-rate-dependence (Figures S3), ensuring that no H_2 gas-to-solution mass-transfer limitation effects are present, and (b) a control demonstrating a $[cyclohexene]^0$ dependence (Figure S4). These controls help ensure that the rapid, precise, and extremely useful—but indirect—cyclohexene reporter reaction is actually monitoring the desired $Ir(0)_{\sim 900}/\gamma\text{-}Al_2O_3$ formation kinetics detailed in Scheme 1 (i.e., that the cyclohexene reduction reporter reaction is indeed fast relative to the slower k_1 and k_2 nanoparticle formation steps, Scheme 1, vide supra, and therefore performing properly).

The observed sigmoidal kinetics for the formation of $Ir(0)_{\sim 900}/\gamma\text{-}Al_2O_3$ are shown in Figure 5. The data are nicely fit (R^2 = 0.998(1)) by the two-step mechanism for nanoparticle formation, A → B and A + B → 2B, where A is the $Ir(1,5\text{-COD})Cl/\gamma\text{-}Al_2O_3$ precursor complex and B is the growing $Ir(0)_n$ nanoparticle surface shown in Scheme 1.

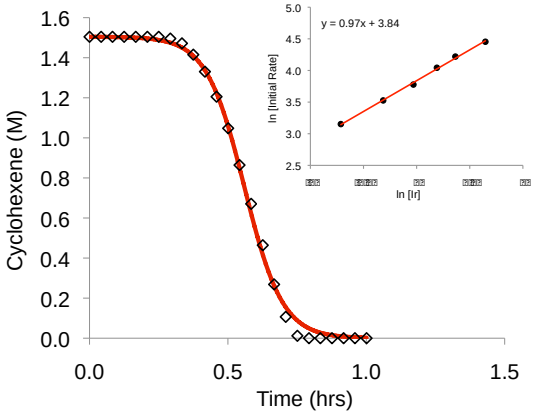

Figure 5. The observed kinetics for the formation of $Ir(0)_{\sim 900}/\gamma\text{-}Al_2O_3$ starting from the Ir(1,5-COD)Cl/γ-Al_2O_3 precatalyst. The diamonds are the experimental data (whose error bars are smaller than the symbols), and the red line is the fit to the two-step mechanism. The inset is a ln/ln plot of the slope after the induction period (which correlates with k_2)[18] and as a function of the supported [Ir], a plot done solely as a check to confirm the first-order kinetics in the amount of Ir(1,5-COD)Cl in the Ir(1,5-COD)Cl/γ-Al_2O_3 precatalyst in the k_2, growth step of the two-step mechanism.

The fit shown is obtained from a nonlinear least-squares fit to the analytic integrated rate equation derived from the two-step mechanism;[18] the rate equation and the associated integrated rate equation from the two-step mechanism are provided in the Supporting Information. The resultant fit yields the average rate constants and associated error[69] for nucleation (k_1 = 1.5(1.1) x 10^{-3} h^{-1}) and autocatalytic surface growth (k_{2corr} = 1.6(2) x 10^4 h^{-1} M^{-1}), where the error bars shown are the experimental error bars (i.e., and not just the less useful curve-fit errors) derived from 10 independent kinetic runs (including runs from three separately synthesized precatalyst batches and two bottles of commercially available acetone, the later since nanoparticle formation kinetics have been shown to be sensitive to the water and trace impurities in solvents such as acetone).[44b] The reproducibility of the kinetics is generally excellent in comparison to that of the well-studied $Ir(0)_n$ nanoparticle formation system in acetone solution[18,24,69]—once again exhibiting the value of being able to compare the supported system to the solution nanoparticle system. The reported k_{2corr} values have been corrected (as mathematically

required) for the ~1700 stoichiometry factor[18] introduced by the cyclohexene reporter reaction, Scheme 3 (the interested reader is referred to the Supporting Information for details regarding this required correction factor). The essential point here is that the resultant $k_{2corr} = k_2$ as defined in Scheme 3.

Further confirmation of the two-step mechanism was obtained by checking the initial rate dependence of the induction period (which correlates primarily with k_1)[18] and the slope after the induction period (which correlates with k_2)[18] of the supported-nanoparticle formation reaction as a function of the Ir(1,5-COD)Cl loading in the Ir(1,5-COD)Cl/γ-Al_2O_3 precatalyst. The Ir wt % loading was varied from 1.0 to 3.85 wt %, corresponding to 0.5–1.9 mM Ir in contact with solution. Consistent with the first-order A → B nucleation step of the two-step mechanism, a ln/ln plot of the nucleation rate (i.e., extracted when ≥ 0.05 psig of H_2 had been consumed)[18] vs the initial Ir(1,5-COD)Cl/γ-Al_2O_3 precatalyst concentration is linear with a slope of 1.0, within experimental error (Figure S8, Supporting Information). Also, a ln/ln plot of the initial nanoparticle growth rate vs the initial Ir(1,5-COD)Cl/γ-Al_2O_3 precatalyst concentration, shown in the inset of Figure 5, is linear and reveals a slope of 1.0, within experimental error. This further confirms the autocatalytic growth step (A + B → 2B) of the reaction is first-order in the Ir(1,5-COD)Cl/γ-Al_2O_3 precatalyst (i.e., $[A]^1$) over the concentration range studied.

Overall, the observed kinetics are fully consistent with and strongly supportive of the two-step mechanism of slow continuous nucleation A → B (rate constant, k_1), followed by fast autocatalytic surface growth A + B → 2B (rate constant, k_2) as the *minimum, Ockham's razor mechanism* able to account for the observed kinetic data. Also significant here is that the $Ir(0)_{\sim 900}$/γ-Al_2O_3 supported-nanoparticle formation kinetics (i) are quite reproducible and (ii) result in the formation of a supported, near-monodisperse (i.e., ± ≤ 15%[63]) 2.9 ± 0.4 nm (i.e., ± 14%) nanoparticle catalyst. These results mirror the

similar good reproducibility and near-monodisperse nanoparticle formation kinetics observed for the kinetically and mechanistically well-studied,[18,19,45,46,47] solution-based $Ir(0)_{\sim 300}$ and $Ir(0)_{\sim 900}$ nanoparticle formation systems[69]—the desired, but not previously demonstrated, reproducibility. Therefore, criterion v (real-time monitoring of the nanoparticle formation kinetics) and vi (observed reproducibility of those kinetics and the resultant products) of a prototype system as defined herein are also satisfied, especially with the additional controls checking and verifying the kinetic results obtained via the cyclohexene reporter reaction as described next.

Control of Directly Monitoring the $Ir(0)_{\sim 900}/\gamma\text{-}Al_2O_3$ Catalyst Formation Kinetics via Its Cyclooctane Evolution. The choice of $Ir(1,5\text{-COD})Cl/\gamma\text{-}Al_2O_3$ as a prototype precatalyst in the present work allows for an additional, valuable kinetic monitoring method. Specifically, using GLC, we have directly monitored the cyclooctane evolution kinetics for the conversion of $Ir(1,5\text{-COD})Cl/\gamma\text{-}Al_2O_3$ to $Ir(0)_{\sim 900}/\gamma\text{-}Al_2O_3$ (Figure S7, Supporting Information). The data were fit to the mathematically correct form of the two-step analytic equation derived in the Supporting Information (in which the math shows that the ~1700 stoichiometry factor, required for the cyclohexene reporter reaction, is not required for the GLC kinetics).[70] A good fit is obtained (R^2 = 0.988) considering the relatively few and imprecise data points obtainable by the GLC sampling method. The resultant rate constants were obtained, $k_{1GLC} = 1.2(2) \times 10^{-3}\ h^{-1}$ and $k_{2GLC} = 1.2(2) \times 10^{4}\ h^{-1}\ M^{-1}$.[71] Quantitatively, the nucleation (k_1) and autocatalytic growth (k_2) rate constants from the GLC cyclooctane evolution kinetics are in good agreement, within experimental error, vs those obtained from the cyclohexene reporter reaction method ($k_1 = 1.5(1.1) \times 10^{-3}\ h^{-1}$ and $k_{2corr} = 1.6(2) \times 10^{4}\ h^{-1}\ M^{-1}$), results which provide independent verification of the kinetics of supported-nanoparticle formation. The relatively few, less precise, and much more laboriously obtained GLC kinetic data make apparent the ease, precision,

and power of the reporter reaction method developed earlier[18-22] for solution nanoparticle formation, but now applied to heterogeneous catalyst formation in contact with solution. These data further satisfy criterion vi of a prototype system. They also show the value of starting from the well-defined Ir(1,5-COD)Cl/γ-Al_2O_3 precatalyst, a system modeled after the kinetically and mechanistically well-studied solution-based nanoparticle formation system starting from the polyoxoanion-supported organometallic complex, [Ir(1,5-COD)•$P_2W_{15}Nb_3O_{62}$]$^{8-}$.

[Ir(1,5-COD)Cl]$_2$ Kinetics Without γ-Al_2O_3 Present: Revealing the Role of the γ-Al_2O_3 Support. The reduction of [Ir(1,5-COD)Cl]$_2$ in acetone and under 40 psig of H_2 (i.e., identical to the "standard conditions"), *but without γ-Al_2O_3 present, yields bulk Ir(0)$_n$ metal* (Figure 6). Although not unexpected, the results demonstrate that the γ-Al_2O_3 support is crucial for limiting nanoparticle aggregation, and thereby stopping bulk Ir(0)$_n$ formation. Hence, another nice feature of the Ir(1,5-COD)Cl/γ-Al_2O_3 system is its ability to reveal the expected, but virtually undemonstrated,[4] role of the γ-Al_2O_3 support in the nanoparticle formation reactions in contact with solution

Note also that the [Ir(1,5-COD)Cl]$_2$ reduction kinetics for the formation of bulk Ir(0)$_n$

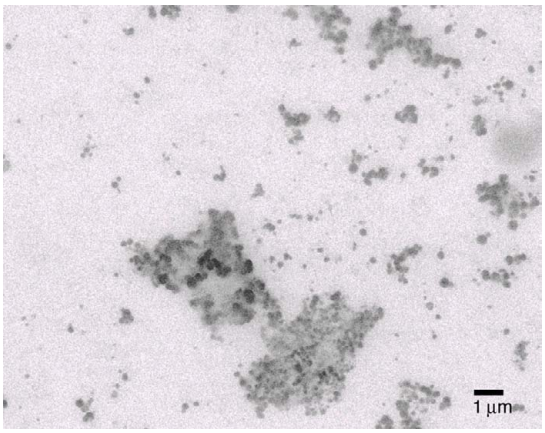

Figure 6. SEM imaging of the observed bulk metal products from the reduction of [Ir(1,5-COD)Cl]$_2$ in acetone, at 40 psig of H_2 and with stirring at 600 rpms, but *with no γ-Al_2O_3 present*. Note the much larger, now 1 µm (1000 nm) scale bars in comparison to the 5–100 nm scales in the earlier microscopy figures herein.

shown in Figure 7 are significantly different than the $Ir(0)_{\sim 900}/\gamma\text{-}Al_2O_3$ supported-nanoparticle formation kinetics (Figure 5, vide supra). Without the $\gamma\text{-}Al_2O_3$, support a short induction period is observed, followed by a fast uptake of H_2. Subsequently, an additional, large uptake of H_2 is observed (~1–5 hrs), corresponding to the hydrogenation of acetone to 2-propanol,[41a] a feature *not* seen in the $\gamma\text{-}Al_2O_3$ supported $Ir(0)_{\sim 900}/\gamma\text{-}Al_2O_3$ catalyst results (vide supra). Since HCl is crucial for the acid-assisted hydrogenation of acetone (added Proton Sponge totally stopping that catalysis, for example),[41a] the suppression of acetone hydrogenation in the $\gamma\text{-}Al_2O_3$ supported $Ir(0)_{\sim 900}/\gamma\text{-}Al_2O_3$ catalyst case is probably the result of alumina buffering[72] the effective pH, thereby inhibiting the otherwise extant HCl-assisted acetone hydrogenation.[41a]

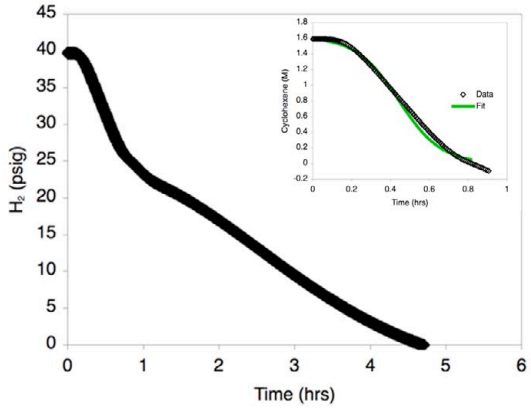

Figure 7. Reduction kinetics from $[Ir(1,5\text{-}COD)Cl]_2$ in acetone, at 40 psig of H_2 and stirring at 600 rpm (the error bars on the data are smaller than the point shown). The inset is an attempted fit of the early portion of the data to the two-step mechanism of nanoparticle formation, which reveals that the two-step mechanism only partially accounts for most, but not all, of the observed early kinetic data.

When the initial portion of the kinetic data for the reduction of $[Ir(1,5\text{-}COD)Cl]_2$ was fit to the two-step mechanism (inset in Figure 7), a statistically worse fit results (R^2 = 0.992) and the resultant rate constants are k_1 = 1.4(2) x 10^{-1} h^{-1} and k_{2corr} = 9.6(5) x 10^3 h^{-1} M^{-1} (averages from three separate kinetic runs). Comparing the above rate constants to

those obtained from the $Ir(0)_{\sim 900}/\gamma\text{-}Al_2O_3$ supported-nanoparticle formation reaction (k_1 = 1.5(1.1) x 10^{-3} h^{-1} and k_{2corr} = 1.6(2) x 10^4 h^{-1} M^{-1}) *reveals that the presence of the γ-Al_2O_3 affects primarily the nucleation step and rate constant (k_1)*. Preliminary evidence suggests that the underlying mechanism of this interesting and important effect of the γ-Al_2O_3 support is actually primarily due to the γ-Al_2O_3 operating indirectly by binding relatively tightly, but not completely, the Ir(1,5-COD)Cl—that is, by indirectly controlling the amount of Ir(1,5-COD)Cl *released into solution* where, our current evidence strongly suggests,[74] the actual nanoparticle formation reaction is primarily taking place. While a separate detailed paper has been required to flush out the details of where and how the catalyst formation occurs (i.e., in solution, on the solid support, or both?),[74] both the presence of the solid support, and the little investigated method of nanoparticle catalyst formation *in contact with solution*, are important aspects of the present system.

Summary

In conclusion, the following are the primary components and findings of this work:

(i) We presented, and then pursued, the hypothesis that the synthesis, and parallel study of the kinetics and mechanism, of supported-nanoparticle catalysts formed from speciation-controlled, supported organometallics *in contact with solution* is an important way to both (a) prepare a next generation of supported-nanoparticle catalysts with composition, size and shape control and to (b) helping bring what has been developed in the modern "nanoparticle revolution" to supported heterogeneous catalysts and their catalysis.

(ii) We defined eight criteria (vide supra and vide infra) for a so-called prototype system to focus the needed studies.

(iii) We then prepared and characterized the starting material and the product, established the balanced nanoparticle formation reaction stoichiometry, and studied the

kinetics of formation of Ir(1,5-COD)Cl/γ-Al_2O_3 to $Ir(0)_{\sim 900}$/γ-Al_2O_3, offered as a prototype system for the formation of supported-nanoparticles in contact with solution.

(iv) We showed that the kinetics of the nanoparticle formation reaction could be successfully monitored in real time by the cyclohexene reporter reaction method, by GLC as a control, and performed controls demonstrating $[cyclohexene]^0$ and stirring-rate-independencies to provide added confidence in the kinetic method(s) and resultant data.

(v) We found that the kinetic data were both reproducible and were well-fit by the two-step mechanism of slow, continuous nucleation (A → B; rate constant k_1 = 1.5(1.1) x 10^{-3} h^{-1}) and fast, autocatalytic surface growth (A +B → 2B; rate constant k_2 = 1.6(2) x 10^4 h^{-1} M^{-1}).[18] This is in turn significant in that it means that the nine synthetic and mechanistic insights from the two-step mechanism[73] should, at least in principle, be applicable to the synthesis of supported-nanoparticle heterogeneous catalysts in contact with solution. Moreover, since independent evidence from other groups via XAFS,[23c,d] SAXS,[23e] HRTEM,[23a] and other methods is now appearing for the two-step mechanism [and its four-step extension that includes two agglomeration steps, bimolecular agglomeration B + B → C (rate constant k_3), and novel autocatalytic agglomeration B + C → 1.5C (rate constant k_4)], this adds further confidence in and support for the broader applicability of the two (and four)-step mechanism(s) of particle formation and agglomeration.

(vi) Overall, we were able to demonstrate that seven of the eight criteria of a "prototype system" defined herein are met by the Ir(1,5-COD)Cl/γ-Al_2O_3 to $Ir(0)_{\sim 900}$/γ-Al_2O_3 system. Specifically, the offered system met the criteria of a prototype system: (i) where a compositionally and structurally well-defined supported precatalyst was developed and employed; (ii) where the system is in contact with solution and a lower temperature reaction (at least to start) is employed with the goal of minimizing further speciation of the precatalyst;[6,36] (iii) where one both could and did establish the balanced

stoichiometry of the supported-nanoparticle formation reaction en route to also well-defined supported-nanoparticle products; (iv) where an active and long-lived catalyst resulted (in the present case TOF 2.2–4.8 higher than literature $Ir(0)_n/Al_2O_3$ catalysts and ≥220 000 total turnovers, both for the test reaction of cyclohexene hydrogenation); (v) where a rapid, quantitative, real-time kinetic monitoring method can be and was applied to the forming supported-nanoparticle heterogeneous catalyst; and (vi) where reproducible kinetic data were obtained so that reliable, quantitative conclusions can be drawn [k_1 = 1.5(1.1) x 10^{-3} h^{-1}; k_2 = 1.6(2) x 10^4 $M^{-1}h^{-1}$].

Developing systems such as the Ir(1,5-COD)Cl/γ-Al_2O_3 to $Ir(0)_{\sim 900}$/γ-Al_2O_3 supported-nanoparticle system herein open up the pursuit of criterion viii, namely a systematic variation of key synthetic variables en route to ideally superior supported-nanoparticle catalysts with especially improved composition control, but also in principle rational size and shape control. Important here is demonstration that the nanoparticle formation appears to happen primarily in solution, off the support—research that has required its own, separate study, the results of will be reported in due course.[74]

Experimental

Materials. All solvents and compounds used were stored in the drybox prior to use. Acetone (water content <0.5%) was purchased from Burdick & Jackson and packed under nitrogen. Anhydrous ethyl acetate (Aldrich, 99.8%), anhydrous cyclohexane (Aldrich, 99.5%) decane (Aldrich, ≥99%), propylene carbonate (Aldrich, 99.7%) $[Ir(1,5\text{-}COD)Cl]_2$ (STREM, 99%), $[Ir(1,5\text{-}COD)\mu\text{-}OCH_3]_2$ (STREM, 98%) and $Ir(CO)_2(acac)$ (STREM, 98%) were all used as received. Cyclohexene (Aldrich, 99%) was freshly distilled over Na metal, under argon, and then stored in the drybox. Acidic activated γ-Al_2O_3 (Aldrich), with a surface area of 155 m^2/g was dried at 160 °C in air for 24 h. Nanopure 18 MΩ-cm H_2O was used from an in house purification system. H_2 gas

purchased from General Air (> 99.5% purity) was passed through O_2- and H_2O-scavenging traps (Trigon Technologies) before use.

Analytical Instrumentation and Procedures. Unless otherwise reported, all reaction solutions were prepared under O_2- and moisture-free conditions in a Vacuum Atmospheres N_2-filled drybox. The O_2 level (always ≤5 ppm; typically ≤1 ppm) was continuously monitored by a Vacuum Atmospheres O_2 sensor. IR spectroscopy was run on a Nicolet 380 FT-IR instrument in transmission mode, and the data were analyzed using OMNIC software; 256 scans were collected for each spectrum at a resolution of 4 cm^{-1}. XAFS experiments were performed at beam line X-19A at the National Synchrotron Light Source (NSLS, Brookhaven National Laboratory, Upton, NY). The storage ring energy was 2.5 GeV, and the ring current was in the range of 110–300 mA. A double-crystal Si(111) monochromator was used to scan the X-ray energy from 150 to 1400 eV relative to the Ir L_3-edge (11 215 eV). Gas—liquid chromatography (GLC) was performed using a Hewlett-Packard 5890 Series II chromatograph, along with a flame-ionization detector and equipped with a Supelco SPB-1 (Aldrich, 30m x 0.25mm x 0.25µm) fused silica column. The GLC parameters were as follows: initial oven temperature, 50 ºC; initial time, 3.0 minutes; rate, 10 ºC/min; final temperature, 160 ºC; injector temperature, 180 ºC; detector temperature, 200 ºC; and injection volume, 2 µL. TEM analysis was conducted at Clemson University with the expert assistance of JoAn Hudson and her staff. ICP-OES analysis for the detection of Ir on the Ir(1,5-COD)Cl/γ-Al_2O_3 precatalyst was done at Galbraith Laboratories.

Pre-Catalyst Preparation: Ir(1,5-COD)Cl/γ-Al_2O_3. All of the precatalysts were prepared in a drybox using preselected $[Ir(1,5\text{-}COD)Cl]_2$ to γ-Al_2O_3 weight-to-weight ratios. For example, a 2.0% weight-to-weight Ir(1,5-COD)Cl/γ-Al_2O_3 sample was prepared by the following procedure by adding 1.0 g acidic γ-Al_2O_3 to 20 mg $[Ir(1,5\text{-}COD)Cl]_2$ (in 15 mL of ethyl acetate), corresponding to a 2.0 wt % sample (i.e., wt % =

wt[Ir(1,5-COD)Cl]$_2$/(wt[Ir(1,5-COD)Cl]$_2$ + wt γ-Al_2O_3) x 100, as this is what we measure experimentally and hence know). Specifically, the appropriate amount of [Ir(1,5-COD)Cl]$_2$ was weighed in a 20 mL scintillation vial. A new 5/8 in. × 5/16 in. Teflon-coated octagon-shaped stir bar was added to the vial, and the solid was dissolved in 15 mL of ethyl acetate. The appropriate amount of solid oxide (e.g., 1.0 g of acidic γ-Al_2O_3 for the 2.0-wt% Ir catalyst) was added by pouring the metal-oxide into the vial (i.e., this order of addition is deliberate, and the indicated equilibration time is important, vide infra) and the solution was stirred for 24 h to equilibrate the [Ir(1,5-COD)Cl]$_2$ with the solid oxide and the solution. After 24 h, the reaction was taken to dryness in a drybox by placing the sample under vacuum for 8 h at room temperature. A control reaction using the opposite order of addition (i.e., in which the γ-Al_2O_3 was stirred in the ethyl acetate solution and the [Ir(1,5-COD)Cl]$_2$ was added to that stirring solid), yielded a darker grayish-yellow solid. The resultant catalyst formation kinetics were still sigmoidal; however, a ~0.2 hr induction period was observed (vs. 0.5(1) h for the reverse order of addition), yet the quantitative k_1 and k_{2corr} rate constants were within experimental error of the "standard conditions" preparation. The resulting supported precatalysts were stored in the drybox.

Carbon Monoxide IR Spectroscopy Experiments. To start, 300 mg of the 2.0 wt % Ir(1,5-COD)Cl/γ-Al_2O_3 precatalyst was placed in 5 mL of cyclohexane in a drybox. The solution was transferred into a culture tube (containing a 5/8 in. × 5/16 in. Teflon-coated stir bar), sealed inside the FP bottle, and attached to a gas line containing CO. The CO was admitted into the FP bottle at 20 psig, and the reaction vessel was purged every 30 s until 2:30 min had passed (i.e., for a total of 5 purges), all while stirring the solution at 300 rpm. After 10 min, the FP was vented, resealed, and transferred back into the drybox. The solution was dried under vacuum for 4 h, yielding a beige solid. A KBr pellet was pressed (in a drybox) out of a physical mixture of KBr and the beige solid and

transferred under N_2 outside the drybox to the IR instrument (i.e., in a jar sealed under N_2), and its IR spectrum was recorded.

The authentic $Ir^{I}(CO)_2/\gamma\text{-}Al_2O_3$ sample was prepared by slurrying 20 mg of $Ir(CO)_2(acac)$ in ethyl acetate with 1.0 g of $\gamma\text{-}Al_2O_3$ in a identical manner to the Ir(1,5-COD)Cl/$\gamma\text{-}Al_2O_3$ precatalyst synthesis as described above.

XAFS Sample Preparation and Measurements. XAFS experiments were performed at beamline X-19A at the NSLS. The samples were prepared in a glovebox under N_2 by brushing a fine powder uniformly onto an adhesive tape, which was then folded several times to achieve a suitable total thickness for the measurement. Measurements were carried out in a sealed cell purged with high-purity He. Specifically, Ir L_3-edge (edge energy = 11 215 eV) EXAFS spectra (taken from 150 below to 1400 eV above the Ir L_3-edge energy) were obtained for the Ir(1,5-COD)Cl/$\gamma\text{-}Al_2O_3$ precatalyst, the reference compounds $[Ir(1,5\text{-}COD)Cl]_2$ and $[Ir(1,5\text{-}COD)\mu\text{-}OCH_3]_2$, and the supported-nanoparticle product $Ir(0)_{\sim 900}/\gamma\text{-}Al_2O_3$. Ir(0) black was measured in reference mode simultaneously for the X-ray energy calibration and data alignment. Ion chambers with suitable gas mixtures were employed to record the intensity of the incident, transmitted, and reference beams in transmission mode. The $\gamma\text{-}Al_2O_3$ supported samples are low (~2%) in Ir content; therefore, fluorescence data collection was utilized. The fluorescence signal was measured using a Lytle detector filled with Ar gas. Zn filter and Soller slits were used to minimize scattering.

XAFS Data Analysis. Data processing and analysis were performed using the IFEFFIT package. EXAFS analysis was done by fitting the theoretical functions calculated with FEFF6 to the experimental data in *r*-space. All the fitted data were limited to the first nearest neighbor (1NN) contributions. The passive electron factors, S_o^2, were found to be 0.80 by fits to the Ir(0) black standard and then fixed for further analysis of the $Ir(0)_n/\gamma\text{-}Al_2O_3$ supported nanoparticles. The parameters describing the

electronic properties (e.g., correction to the photoelectron energy origin) and local structure environment (coordination numbers *N*, bond lengths *R,* and their mean squared disorder parameters σ^2) around the absorbing atoms were allowed to vary during fitting. The Ir(1,5-COD)Cl/γ-Al_2O_3 precatalyst and the reference compound $[Ir(1,5\text{-}COD)Cl]_2$, due to their molecular, nonmetallic nature, have significant differences in electronic structure compared to metallic Ir. Therefore, we separately obtained $S_o^2 = 1$ from the fit to the reference compound $[Ir(1,5\text{-}COD)\mu\text{-}OCH_3]_2$ while constraining $N_{Ir-C} = 4$ and $N_{Ir-O} = 2$ based on its known structure, and then fixed $S_o^2 = 1$ in the fits of the precatalyst as well as the $[Ir(1,5\text{-}COD)Cl]_2$ model compound. The photoelectron path between Ir and its carbon nearest neighbors (Ir–C) was used to simulate both the Ir–C and Ir–O contributions, as C and O are not readily distinguishable by EXAFS analysis. Additionally, a physically reasonable constraint, setting the CN(Ir–C) + CN(Ir–Cl) = 6, was applied in the EXAFS data fits for the precatalyst as well as $[Ir(1,5\text{-}COD)Cl]_2$. The XANES Ir(1,5-COD)Cl/γ-Al_2O_3 precatalyst spectrum was analyzed by fitting via a linear combination of spectra from the reference compounds $[Ir(1,5\text{-}COD)Cl]_2$ and $[Ir(1,5\text{-}COD)m\text{-}OCH_3]_2$ to approximate the substitution of chloride by oxo ligands from the γ-Al_2O_3 support, which could not be clearly demonstrated from the EXAFS analysis. Specifically, the XANES spectra for the Ir(1,5-COD)Cl/γ-Al_2O_3 precatalyst compound as well as both references were properly aligned and normalized. Subsequently the spectra in the energy range of -5 to 18 eV relative to the Ir L_3 absorption edge were subjected to linear combination fitting, where by the sum of weighting factors of the two reference spectra was constrained to be equal to 1.

Hydrogenation Apparatus and Data Handling. Hydrogenation experiments for monitoring the H_2 reduction of Ir(1,5-COD)Cl/γ-Al_2O_3 to $Ir(0)_n$/γ-Al_2O_3 were carried out in a previously described apparatus[18-22,44,46,48,49] to continuously monitor H_2 pressure loss. Briefly, the apparatus consisted of a FP bottle modified with Swagelock TFE-sealed

Quick-Connects to both a H_2 line and an Omega PX621 pressure transducer. The pressure transducer is interfaced to a PC through an Omega D1131 5V A/D converter with a RS-232 connection. Reactions were run at a constant temperature by immersing the FP bottle in a 500 mL jacketed reaction flask containing dimethyl silicon fluid (Thomas Scientific), which was regulated by a thermostatted recirculating water bath (VWR). Pressure uptake data were collected using LabView 7.1. The hydrogen uptake curves were converted to cyclohexene (M) curves using the previously established 1:1 H_2/cyclohexene stoichiometry.[18,44] The data were also corrected for the acetone solvent vapor pressure using the previously established protocol.[49] Specifically one can either measure the acetone vapor pressure independently and subtract that curve (point-by-point) from the raw H_2 uptake data during the cyclohexene reporter reaction, or one can simply back-extrapolate the experimental vapor pressure rise (seen in the induction period of the reaction).[49] Both methods yield the same k_1 and k_2 rate constants within ±15%. The cyclooctane formation and cyclohexene kinetic curves were fit to the analytic equations (equations S4 and S5, respectively, in the Supporting Information) for nucleation and autocatalytic surface growth of nanoparticle formation, A → B, rate constant k_1, plus A + B → 2B, rate constant k_2 (see Scheme 2),[70] using non-linear least-squares fitting in Origin 7.0.[49]

Formation of the Active Catalyst: Standard Conditions Reaction. In a drybox, 0.05 g of the Ir(1,5-COD)Cl/γ-Al_2O_3 catalyst precursor was weighed out into a 2 dram vial and transferred to a culture tube. To ensure a quantitative transfer, 2.5 mL of acetone and 0.5 mL of cyclohexene were added to the 2 dram vial. The solution was then transferred via a disposable polyethylene pipette into a new borosilicate culture tube (22 × 175 mm) with a new 5/8 in. × 5/16 in. Teflon-coated octagon-shaped stir bar. The culture tube was sealed in the FP bottle, removed from the drybox, and attached to the H_2 line. The sealed, H_2-line-attached FP bottle was placed into a temperature-

regulated water bath set at 22.0 ± 0.1 °C. A standard conditions purge cycle[18,44] was used to initiate the reaction, a series of H_2-flushing cycles in which the FP bottle is purged with H_2 every 15 s until 3 min and 30 sec have passed (a total of 14 purges). The stir plate was started and set at 600 rpm to allow the H_2 gas-to-solution equilibrium, and the H_2 pressure was then set to 40 psig, with the data recording started 4 min after the purge cycle began (i.e., by definition t = 0 for the kinetics).

Confirmation of the Molecularity ([A]^1) for Autocatalytic Surface Growth, A + B → 2B A series of precatalysts from 1.0-3.85-wt% were made following as described above ("Pre-Catalyst Preparation: Ir(1,5-COD)Cl/γ-Al_2O_3"). In each case, the maximum rate after the induction period was obtained through a linear least-squares fit in Excel.

GLC Cyclooctane Evolution Kinetics and Determination of the Ir(1,5-COD)Cl/γ-Al_2O_3 Reaction Stoichiometry. The procedure employed is very similar to that previously published.[48] In a drybox 0.05 g of the Ir(1,5-COD)Cl/γ-Al_2O_3 catalyst precursor was weighed out into a 2 dram vial. The Ir(1,5-COD)Cl/γ-Al_2O_3 precatalyst was transferred into a new borosilicate culture tube (22 × 175 mm) with a new 5/8 in. × 5/16 in. Teflon-coated octagon-shaped stir bar. To ensure a quantitative transfer 1.5 mL of acetone, 1.0 mL of a 0.29 mM decane/acetone solution (used as an internal standard) and 0.5 mL of cyclohexene were added to the 2 dram vial. The solution was then transferred via a disposable polyethylene pipette into the borosilicate culture tube containing the Ir(1,5-COD)Cl/γ-Al_2O_3 precatalyst. A "standard conditions" hydrogenation was started (vide supra). At pre-determined times, the stirring was stopped, the H_2 pressure was released from the FP bottle (but keeping a positive H_2 pressure of ≥ 15 psig) and aliquots (≤0.1 mL) of the reaction solution were drawn with a 9 in. needle attached to a gastight syringe. After the aliquot was drawn, the FP bottle was resealed, stirring was then restarted at 600 rpm, and the FP was purged 5 times (once every 5 s)

and then allowed to fill to 40 psig (30 s). Before each aliquot was drawn, the needle was rinsed with acetone 10 times, and then thoroughly dried with compressed air.

H_2 Uptake Experiments. 1.0 g of the 2.0 wt % Ir(1,5-COD)Cl/γ-Al_2O_3 precatalyst was placed in 7.5 mL of propylene carbonate in a culture tube in a drybox. The reaction was run following the "standard conditions" protocol, except the solution was stirred at 1000 rpm.

[Ir(1,5-COD)Cl]$_2$ Reduction Kinetics Without γ-Al_2O_3 Present. A 0.98 mg (0.974 mM) sample of [Ir(1,5-COD)Cl]$_2$ was weighed out into a 2 dram vial. Next, 2.5 mL of acetone and 0.5 mL of cyclohexene were added to the 2 dram vial via gas tight syringe. The resultant yellow solution was mixed with a polyethylene pipette and transferred into a new borosilicate culture tube (22 x 175 mm) with a new 5/8 in. x 5/16 in. Teflon-coated octagon-shaped stir bar. The reaction was continued following the same procedure as in the "Standard Conditions Reaction" section.

Cyclohexene Turnover Frequency Experiments: Calculations and Assumptions. The TOF was determined using a preformed Ir(0)$_{\sim 900}$/γ-Al_2O_3 catalyst, generated as described in the "Formation of the Active Catalyst: Standard Conditions Reaction" section above. After 1.5 h (i.e., after 1 equiv of cyclooctane per Ir is known to be evolved), the FP bottle was brought back into the drybox. The FP bottle was opened and an additional 3.0 mL of cyclohexene was added to the reaction solution. The FP was sealed and brought back out of the drybox and placed on the hydrogenation line, where another "standard conditions" purge cycle was performed, and stirring resumed at 600 rpms. Over the course of 4 h, the reaction took up on average 69.36 psig of H_2, an average between two independent experiments. The TOF was calculated from a calculated dispersion (D = surface atoms/total atoms), assuming that all the Ir(0)$_{\sim 900}$/γ-Al_2O_3 surface atoms were active.[75] The total (average) number of Ir atoms was estimated from the TEM data by the formula $N = \pi D_f^3 \rho N_A/6MW$.[44] Applying this formula,

one obtains on average $Ir(0)_{\sim 900}$ nanoparticles. Using the magic-number approximation[66] there are on average 362 Ir atoms present at the surface of each $Ir(0)_{\sim 900}$ nanoparticle, yielding a dispersion of 39%. This calculation assumes that the $Ir(0)_{\sim 900}$ nanoparticles observed by TEM are spherical, a reasonable approximation to their true shape.[76]

Total Turnover Demonstration. The $Ir(0)_{\sim 900}/\gamma\text{-}Al_2O_3$ catalyst was prepared as described in the "Standard Conditions" section. After 1.5 h (i.e., when 1 equiv of cyclooctane per Ir has evolved), the FP bottle was brought back into the drybox. The solution was transferred into a 20 mL scintillation vial and dried overnight. Next, 0.01 g of the catalyst material was weighed out into a 20 mL scintillation vial; then 5.0 mL of cyclohexene was added (corresponding to a maximum of 85 000 TTOs per total Ir and 220 000 TTOs per surface Ir atom) and the solution was transferred via a polyethylene pipet into a new borosilicate culture tube (22 × 175 mm) with a new 5/8 in. × 5/16 in. Teflon-coated octagon-shaped stir bar. The standard conditions purge cycle was used, stirring was set at 600 rpms at time = 3.5 min, and the solution was left open to 40 psig of H_2. After 86 h, GLC confirmed 100% conversion of cyclohexene to cyclohexane with no observable undesirable side products. We note here that the use of the $Ir(0)_{\sim 900}/\gamma\text{-}Al_2O_3$ catalyst under these specific conditions (i.e., with only cyclohexene and cyclohexane present as solvent) led to the catalyst sticking to the borosilicate culture tube thereby considerably slowing the reaction.

Preparation of TEM Grids. Following a "standard conditions" supported-nanoparticle formation reaction, and 0.5 hrs after the complete hydrogenation (i.e., after 1.0 equiv of cyclooctane per Ir had evolved), the FP bottle was transferred into the drybox. A 300 mesh Formvar-coated SiO_2 TEM grid was dipped in the sample for approximately 5 s and then allowed to dry. The grid was placed in a 2 dram vial, wax sealed and placed in a 20 mL scintillation vial and sent for TEM analysis.

Acknowledgement. R.G.F. and J.E.M. gratefully acknowledge support from the Chemical Sciences, Geosciences and Biosciences Division, Office of Basic Energy Sciences, Office of Science, U. S. Department of Energy, grant SE-FG02-03ER15453. The authors would like to thank Dr. JoAn Hudson for her expert assistance with the TEM imaging. A.I.F. and Q.W. acknowledge support from the U. S. Department of Energy, grant DE-FG02-03ER15476. Use of NSLS was supported by the U.S. Department of Energy, Office of Science, Office of Basic Energy Sciences, under Contract No. DE-AC02-98CH10886. Beamline X19A at the NSLS is supported in part by the Synchrotron Catalysis Consortium, U. S. Department of Energy Grant No DE-FG02-05ER15688.

Supporting Information Available. EXAFS 1NN fitting results for the Ir(1,5-COD)Cl/γ-Al_2O_3, $Ir(0)_{\sim 900}$/γ-Al_2O_3 catalyst, as well as the $[Ir(1,5\text{-}COD)Cl]_2$ and $[Ir(1,5\text{-}COD)\mu\text{-}OCH_3]_2$ model compounds; additional TEM images along with particle size histograms for the $Ir(0)_{\sim 900}$/γ-Al_2O_3 catalyst, as well as controls for mass-transfer limitations and plots demonstrating a zero-order cyclohexene dependence; the two-step rate law and integrated rate equation as well as the k_2 correction factor for the ~1700 cyclohexene stoichiometry factor; cyclooctane evolution kinetics from the 2.0 wt % Ir(1,5-COD)Cl/γ-Al_2O_3 catalyst; TEM imaging and cyclooctane evolution kinetics when cyclohexene is absent from the synthesis. This material is free of charge via the Internet at Web at http://pubs.acs.org.

References

[1] (a) Gates, B. C., *Catalytic Chemistry*. John Wiley & Sons: New York, 1992. (b) Bartholomew, C. H.; Farrauto, R. J., *Fundamentals of Industrial Catalytic Processes*. 2 ed.; John Wiley & Sons: Hoboken, 2006.

[2] Schlögl, R.; Abd Hamid., S. B. *Angew. Chem. Int. Ed.* **2004,** *43*, 1628.

[3] Altman, M. S. *Science* **2010,** *327*, 789.

[4] Mondloch, J. E.; Bayram, E.; Finke, R. G. *A Review of the Kinetics and Mechanisms of Formation of Supported-Nanoparticle Heterogeneous Catalysts,* Manuscript in Preparation.

[5] Chupas, P. J.; Chapman, K. W.; Jennings, G.; Lee, P. L.; Grey, C. P. *J. Am. Chem. Soc.* **2007,** *129*, 13822.

[6] Uzun, A.; Gates, B. C. *Angew. Chem. Int. Ed.* **2008,** *47*, 9245.

[7] Mondloch, J. E.; Yan, X.; Finke, R. G. *J. Am. Chem. Soc*. **2009,** *131*, 6389.

[8] (a) Catalysis for Energy: Fundamental Science and Long Term Impacts of the U.S. Department of Energy Basic Energy Sciences Catalysis Science Programs; National Research Council, The National Academies Press: Washington DC, 2009, accessible online at http://www.nap.edu/catalog/12532.html. (b) Basic Research Needs: Catalysis for Energy; PNNL-17214; Office of Basic Energy Sciences, U. S. Department of Energy, 2007, accessible online at http://www.sc.doe.gov/bes/reports/list.html. (c) Basic Energy Sciences Advisory Committee Subpanel Workshop Report, "Opportunities for Catalysis in the 21st Century", Workshop Chair, Prof. J. M. White; A report from the Basic Energy Sciences Advisory Committee, 2002, accessible online at http://www.er.doe.gov/production/bes/reports/archives.html.

[9] Bell, A. T. *Science* **2003,** *299*, 1688.

[10] (a) Lee, I.; Delbecq, F.; Morales, R.; Albiter, M. A.; Zaera, F. *Nature Materials* **2009,** *8*, 132. (b) Somorjai, G. A.; Park, J. Y. *Angew. Chem. Int. Ed.* **2008,** *47*, 9212.

[11] Joo, S. H.; Park, J. Y.; Tsung, C.-K.; Yamada, Y.; Yang, P.; Somorjai, G. A. *Nature Materials* **2009,** *8*, 126.

[12] (a) Thomas, J. M.; Johnson, B. F. G.; Raja, R.; Sankar, G.; Midgley, P. A. *Acc. Chem. Res.* **2003,** *36*, 20. (b) Alayoglu, S.; Nilekar, A. U.; Mavrikakis, M.; Eichhorn, B. *Nat. Mater.* **2008,** *7*, 333. (c) Stowell, C. A.; Korgel, B. A. *Nano Lett.* **2005,** *5*, 1203.

[13] Che, M.; Bennett, C. O. *Adv. Catal.* **1989,** *36*, 55.

[14] Some of the more recent reviews detailing syntheses of transition metal nanoparticles include the following: (a) Aiken III, J. D.; Finke, R. G. *J. Mol. Catal. A: Chemical* **1999**, *145*, 1. (b) Crooks, R. M.; Zhao, M.; Sun, L.; Chechik, V.; Yeung, L. K. *Acc. Chem. Res.* **2001**, *34*, 181. (c) Bönnemann, H.; Richards, R. M. *Eur. J. Inorg. Chem.* **2001**, 2455. (d) Roucoux, A.; Schulz, J.; Patin, H. *Chem. Rev.* **2002,** *102*, 3757. (e) Cushing, B. L.; Kolesnichenko, V. L.; O'Connor, C. J. *Chem. Rev.* **2004,** *104*, 3893. (f) Astruc, D.; Lu, F.; Aranzaes, J. R. *Angew. Chem. Int. Ed.* **2005,** *44*, 7852. (g) Wilcoxon, J. P.; Abrams, B. L. *Chem. Soc. Rev.* **2006,** *35*, 1162. (h) Ott, L. S.; Finke, R. G. *Coord. Chem. Rev.* **2007,** *251*, 1075. (i) Semagina, N.; Kiwi-Minsker, L. *Catal. Rev.* **2009,** *51*, 147.

[15] (a) Mednikov, E. G.; Jewell, M. C.; Dahl, L. F., *J. Am. Chem. Soc.* **2007,** *129*, 11619. Also see the extensive references therein for similar nanosized clusters. (b) Jadzinsky, P. D.; Calero, G.; Ackerson, C. J.; Bushnell, D. A.; Kornberg, R. D. *Science* **2007,** *318*,

430. (c) Zhu, M.; Aikens, C. M.; Hollander, F. J.; Schatz, G. C.; Jin, R. *J. Am. Chem. Soc.* **2008,** *130*, 5883. Other non-atomically precise, but compositionally well-understood nanoparticles are known and have been reviewed.[14a]

[16] Corain, B.; Schmid, G.; Toshima, N., Eds. Metal Nanoparticles in Catalysis and Materials Science: The Issue of Size Control; Elsevier: Amsterdam, 2008.

[17] (a) Ahmadi, T. S.; Wang, Z. L.; Green, T. C.; Henglein, A.; El-Sayed, M. A. *Science* **1996,** *272*, 1924. (b) Burda, C.; Chen, X.; Narayanan, R.; El-Sayed, M. A. *Chem. Rev.* **2005,** *105*, 1025. (c) Tao, A. R.; Habas, S.; Yang, P. *Small* **2008,** *4*, 310. (d) Xia, Y.; Xiong, Y.; Lim, B.; Skrabalak, S. E. *Angew. Chem. Int. Ed.* **2009,** *48*, 60.

[18] Watzky, M. A.; Finke, R. G. *J. Am. Chem. Soc.* **1997,** *119*, 10382.

[19] Hornstein, B. J.; Finke, R. G. *Chem. Mater.* **2004,** *16*, 139 (see also: Chem. Mater. 2004, 16, 3972).

[20] Besson, C.; Finney, E. E.; Finke, R. G. *J. Am. Chem. Soc.* **2005,** *127*, 8179.

[21] Besson, C.; Finney, E. E.; Finke, R. G. *Chem. Mater.* **2005,** *17*, 4925.

[22] Finney, E. E.; Finke, R. G. *Chem. Mater.* **2008,** *20*, 1956.

[23] For a few, selected additional recent references to the growing mechanistic insights into the synthesis of nanoparticles from the modern revolution in nanoparticle science include: (a) Zheng, H.; Smith, R. K.; Jun, Y.-W.; Kisielowski, C.; Dahmen, U.; Alivisatos, A. P. *Science* **2009,** *324*, 1309. (b) Murray, C. B. *Science* **2009,** *324*, 1276. (c) Harada, M.; Inada, Y. *Langmuir* **2009,** *25*, 6049. (d) Polte, J.; Ahner, T. T.; Delissen, F.; Sokolov, S.; Emmerling, F.; Thünemann, A. F.; Kraehnert, R. *J. Am. Chem. Soc.* **2010,** *132*, 1296. (e) Polte, J.; Erler, R.; Thünemann, A. F.; Sokolov, S.; Ahner, T. T.; Rademann, K.; Emmerling, F.; Kraehnert, R. *ACS Nano* **2010,** *4*, 1076.

[24] Finney, E. E.; Finke, R. G. *Journal of Colloid and Interface Science* **2008**, *317*, 351.

[25] The model UHV literature related to heterogeneous catalyst formation is extensive. For key reviews of that literature, see: (a) Venables, J. A. *Philosophical Magazine* **1973,** *27*, 697. (b) Venables, J. A.; Spiller, G. D. T.; Hanbücken, M. *Rep. Prog. Phys.* **1984,** *47*, 399. (c) Poppa, H. *Catal. Rev.-Sci. Eng.* **1993,** *35*, 359. (d) Campbell, C. T. *Surf. Sci. Rep.* **1997,** *27*, 1. (e) Henry, C. R. *Vacuum* **1998,** *50*, 157. (f) Henry, C. R. *Surf. Sci. Rep.* **1998,** *31*, 231. (g) Bäumer, M.; Freund, H.-J. *Prog. surf. Sci.* **1999,** *61*, 127. (h) Henry, C. R. *Chemical Physics of Solid Surfaces* **2003,** *11*, 247.

[26] (a) Goodman, D. W. *J. Phys. Chem.* **1996,** *100*, 13090. (b) Gunter, P. L. J.; Niemantsverdriet, J. W.; Ribeiro, F. H.; Somorjai, G. A. *Catal. Rev.-Sci. Eng.* **1997,** *39*, 77. (c) Ertl, G.; Freund, H.-J. *Physics Today* **1999,** *52*, 32. (d) Freund, H.-J.; Kuhlenbeck, H.; Libuda, J.; Rupprechter, G.; Bäumer, M.; Hamann, H. *Topics in Catalysis* **2001,** *15*, 201. (e) van Santen, R. A.; Neurock, M. *Molecular Heterogeneous Catalysis*; Wiley-VCH: Weinheim, 2006. (f) Imbihl, R.; Behm, R. J.; Schlögl, R. *Phys. Chem. Chem. Phys.* **2007,** *9*, 3459.

[27] Thomas, J. M. *J. Chem. Phys.* **2008,** *128*, 182502.

[28] Dalla Betta, R. A.; Boudart, M. In *International Congress on Catalysis (5th)*; North-Holland: Palm Beach, Fla, 1972; Vol. 5th Annual, p 1329.

[29] (a) Tzou, M. S.; Sachtler, W. M. H. *Catalysis* **1987,** *38*, 233. (b) Homeyer, S. T.; Sachtler, W. M. H. *J. Catal.* **1989,** *118*, 266.

[30] Oudenhuijzen, M. K.; Kooyman, P. J.; Tappel, B.; van Bokhoven, J. A.; Koningsberger, D. C. *J. Catal.* **2002,** *205*, 135.

[31] (a) Okumura, K.; Honma, T.; Hirayama, S.; Sanada, T.; Niwa, M. *J. Phys. Chem. C* **2008,** *112*, 16740. (b) Okumura, K.; Matsui, H.; Sanada, T.; Arao, M.; Honma, T.; Hirayama, S.; Niwa, M. *J. Catal.* **2009,** *265*, 89.

[32] Wang, Y.; Xu, X.; Tian, Z.; Zong, Y.; Cheng, H.; Lin, C. *Chem. Eur. J.* **2006,** *12*, 2542.

[33] When a $Ir(C_2H_4)_2$•zeolite precatalyst is placed under H_2, Gates and co-workers detected the formation of Ir_4 tetrahedral clusters containing both ethylidyne and di-σ-bonded ethylene by modeling the XAFS.[6] These Ir_4 clusters were shown to undergo reversible fragmentation back to the monomer Ir species upon exposure to C_2H_4 (but then back to Ir_4 under a H_2 rich atmosphere).[6] Kinetic studies of the evolution of the $Ir(C_2H_4)_2$•zeolite to Ir_4•zeolite catalyst under H_2, by the kinetic reporter reaction methods utilized herein, have proven successful in a collaborative investigation with the Gates laboratory and will be reported separately in due course.

[34] Liang, A. J.; Gates, B. C. *J. Phys. Chem. C* **2008,** *112*, 18039.

[35] Fierro-Gonzalez, J. C.; Gates, B. C. *J. Phys. Chem. B* **2005,** *109*, 7275.

[36] For lead references on the subject of H_2PtCl_6 speciation both in H_2O as well as the presence of γ-Al_2O_3, see: (a) Spieker, W. A.; Liu, J.; Miller, J. T.; Kropf, A. J.; Regalbuto, J. R. *Appl. Catal. A: General* **2002,** *232*, 219. (b) Spieker, W. A.; Liu, J.; Miller, J. T.; Kropf, A. J.; Regalbuto, J. R. *Appl. Catal. A: General* **2003,** *243*, 53. (c) Shelimov, B. N.; Lambert, J.-F.; Che, M.; Didillon, B. *J. Mol. Catal. A: Chemical* **2000,** *158*, 91. (d) Mang, T.; Breitscheidel, B.; Polanek, P.; Knozinger, H. *Appl. Catal. A: General* **1993,** *106*, 239. (e) Brunelle, J. P. *Pure & Appl. Chem.* **1978,** *50*, 1211. Also see footnote 29 in reference[7] for further discussion of this subject.

[37] Schwarz, J. A.; Contescu, C.; Contescu, A. *Chem. Rev.* **1995,** *95*, 477.

[38] Our recent, comprehensive review of the relevant literature[4] reveals that studies of the formation kinetics and mechanisms of practical,[25,26,27] non-ultra-high-vacuum (UHV)[26a] supported-nanoparticle heterogeneous catalysts date back to the early 1970's. Specifically, (i) Boudart and co-workers systematically studied how catalyst pretreatment affected the formation of a $Pt(0)_n$/zeolite catalyst from a $Pt(NH_3)_4Cl_2$/zeolite precursor;[28] and (ii) Sachtler,[28] Koninsberger[30] and Okumura[31] each studied the classic system $M^{II}(NH_3)_4(anion)_2$ (where M = Pt and Pd, and anion = NO_3^- and Cl^-). Other well-studied systems include: (iii) H_2PtCl_6 supported on γ-Al_2O_3,[7] carbon nanotubes[32] and TiO_2,[5] and (iv) Gates and co-workers' well-characterized $Ir(C_2H_4)_2$,[6,33] $Rh(C_2H_4)_2$[34] and $Au(CH_3)_2$[35]

supported organometallic-based precursors. Synthetically significant kinetic and mechanistic insights able to guide supported-nanoparticle heterogeneous catalyst preparation are, however, relatively rare despite such classic studies.[4] This broader lack of mechanistically guided synthetic knowledge can be attributed in large part to a lack of compositionally and structurally fully defined precatalysts (other than some notable exceptions such as Gates's systems[6,33,34,35]), for example, in the H_2PtCl_6 system, where multiple Pt precatalyst species exist in both the impregnation solution and on the support.[36] Furthermore, the supported-nanoparticle heterogeneous catalyst formation stoichiometry is not often established,[4] and "controlling the high-temperature treatment of nanostructures is often problematic",[2] since multiple precatalyst preparation steps such as calcination and activation are often used, but the catalyst's evolution and resultant form is rarely followed directly, further contributing to the presence of multiple precatalyst species[37] en route to the final supported-nanoparticle heterogeneous catalyst.

[39] For example, Somorjai and co-workers have made extensive efforts to remove stabilizing ligand overlayers from both $Pt(0)_n$ and $Rh(0)_n$ nanoparticles with varying—but not complete—degrees of success: (a) Rioux, R. M.; Song, H.; Hoefelmeyer, J. D.; Yang, P.; Somorjai, G. A. *J. Phys. Chem. B* **2005,** *109,* 2192. (b) Song, H.; Rioux, R. M.; Hoefelmeyer, J. D.; Komor, R.; Niesz, K.; Grass, M.; Yang, P.; Somorjai, G. A. *J. Am. Chem. Soc.* **2006,** *128,* 3027. (c) Rioux, R. M.; Hsu, B. B.; Grass, M. E.; Song, H.; Somorjai, G. A. *Catal. Lett.* **2008,** *126,* 10. (d) Borodko, Y.; Jones, L.; Lee, H.; Frei, H.; Somorjai, G. A. *Langmuir* **2009,** *25,* 6665. (e) Park, J. Y.; Aliaga, C.; Russell Renzas, J.; Lee, H.; Somorjai, G. A. *Catal. Lett.* **2009,** *129,* 1. (f) Aliaga, C.; Park, J. Y.; Yamada, Y.; Sook Lee, H.; Tsung, C.-H.; Yang, P.; Somorjai, G. A. *J. Phys. Chem. C* **2009,** *113,* 6150. (g) Grass, M. E.; Joo, S. H.; Zhang, Y.; Somorjai, G. A. *J. Phys. Chem. C* **2009,** *113,* 8616. (h) Borodko, Y. G.; Lee, H. Y.; Joo, S. H.; Zhang, Y.; Somorjai, G. A. *J. Phys. Chem. C* **2010,** *114*, 1117. (i) Kuhn, J. N.; Tsung, C.–H.; Huang, W.; Somorjai, G. A. *J. Catal.* **2009,** 209.

[40] Lee, I.; Morales, R.; Albiter, M. A.; Zaera, F. *Proc. Natl. Acad. Sci. U.S.A.* **2008,** *105*, 15241.

[41] More specifically the "weakly ligated/labile-ligand" problem is simply the need for the efficient syntheses of nanoparticles with easily 100% removable or replaceable ligands by only the desired reactants (or solvent) for the reaction of choice. Others have worked on related concepts such as "naked nanoparticles": (a) Schmid, G.; Meyer-Zaika, W.; Pungin, R.; Sawitowski, T.; Majoral, J.-P.; Caminade, A.-M.; Turrin, C.-O. *Chem. Eur. J.* **2000**, *6*, 1693. (b) Evanoff, D. D.; Chumanov, G. *J. Phys. Chem. B* **2004**, *108*, 13948. For studies of putatively "solvent-only" stabilized nanoparticles, see: (c) Ott, L. S.; Finke, R. G. *Inorg. Chem.* **2006**, *45*, 8382 and references therein. See also our recent review on nanoparticle stabilizers;[14h] that review further details the use of anion free metal precursors that in principle can generate "weakly ligated/labile-ligand" or "solvent-only" stabilized nanoparticles, for example important work by Chaudret and co-workers using the precursor Ru(COD)(COT) (d) Vidoni, O.; Philippot, K.; Amiens, C.; Chaudret, B.; Balmes, O.; Malam, J.-O.; Bovin, J.-O.; Senocq, F.; Casanove, M.-J. *Angew. Chem. Int. Ed.* **1999**, *38*, 3736. (e) Pelzer, K.; Vidoni, O.; Philippot, K.; Chaudret, B.; Colliere, V. *Adv. Func. Mater.* **2003**, *13*, 118. For studies using $Pd_2(dba)_3$ see: (f) Dhas, N. A.; Cohen, H.; Gedanken, A. *J. Phys. Chem. B* **1997**, *101*, 6384.

[42] For our efforts to date on the "weakly ligated/labile-ligand" nanoparticle catalysts concept, see: (a) Özkar, S.; Finke, R. G. *J. Am. Chem. Soc.* **2005,** *127*, 4800 (where an active and selective neat-acetone reduction catalyst and only HCl plus cyclooctane are formed from $[Ir(1,5\text{-}COD)Cl]_2$ under H_2); (b) Bayram, E.; Zahmakiran, M.; Özkar, S.; Finke, R. G. *In-Situ Formed "Weakly Ligated/Labile Ligand" Ir(0) Nanoparticles and Aggregates as Catalysts for the Complete Hydrogenation of Neat Benzene at Room Temperature and Mild Pressures, Langmuir, **2010,** 26,* 12455. (c) A lead reference to putative "solvent-only stabilized" nanoparticles: Ott, L. S.; Finke, R. G. *Inorg. Chem.* **2006,** *45,* 8382.; (d) See also pages 1093-1094 on putative "solvent only stabilized nanoparticles" in our review on nanoparticle stabilization.[14h]

[43] The term "operando" is from the Latin for "working" or "operating": (a) J. M. Thomas, G. A. Somorjai *Top. Catal.* **1999,** 8 preface. (b) B. M. Weckhuysen *Chem. Commun.* **2002,** 97. (c) M. O. Guerrero-Pérez, M. A. Bañares *Chem. Commun.* **2002,** 1292. (d) F. Meunier, M. Daturi *Catal. Today* **2006,** *113,* 1.

[44] (a) Lin, Y.; Finke, R. G. *J. Am. Chem. Soc.* **1994,** *116*, 8335. (b) Lin, Y.; Finke, R. G. *Inorg. Chem.* **1994,** *33*, 4891.

[45] Ott, L. S.; Hornstein, B. J.; Finke, R. G. *Langmuir* **2006**, *22*, 9357.

[46] Aiken III, J. D.; Finke, R. G. *J. Am. Chem. Soc.* **1998,** *120*, 9545.

[47] (a) Özkar, S.; Finke, R. G. *J. Am. Chem. Soc.* **2002,** *124*, 5796. (b) Ott, L. S.; Finke, R. G. *J. Nanosci. Nanotechnol.* **2008,** *8*, 1551. (c) Ott, L. S.; Finke, R. G. *Chem. Mater.* **2008,** *20*, 2592.

[48] Aiken III, J. D.; Finke, R. G. *Chem. Mater.* **1999,** *11*, 1035.

[49] Widegren, J. A.; Aiken III, J. D.; Özkar, S.; Finke, R. G. *Chem. Mater.* **2001,** *13*, 312.

[50] Traditional heterogeneous catalyst synthesis is most often carried out via a gas–solid system and interface. In the present work, the supported-nanoparticle synthesis occurs in a solid-liquid system, a less common but not unprecedented synthetic method. For, leading reference to prior examples are: (a) De Jong, K. P.; Geus, J. W. *Appl. Catal. A: General* **1982,** *4*, 41. (b) Bond, G. C.; Rawle, A. F. *J. Mol. Catal. A: Chemical* **1996,** *109*, 261. (c) Sales, E. A.; Benhamida, B.; Caizergues, V.; Lagier, J.-P.; Fiévet, F.; Bozon-Verduraz, F. *Appl. Catal. A: General* **1998,** *172*, 273. (d) Bonet, F.; Grugeon, S.; Urbina, R. H.; Tekaia-Elhsissen, K.; Tarascon, J.-M. *Solid State Sciences* **2002,** *4*, 665. (e) Hulea, V.; Brunel, D.; Galarneau, A.; Philippot, K.; Chaudret, B.; Kooyman, P. J.; Fajula, F. *Microporous Mseoporous Mater.* **2005**, *79*, 185. (f) Zawadzki, M.; Okal, J. *Mater. Res. Bull.* **2008,** *43*, 3111. (g) Boutros, M.; Denicourt-Nowicki, A.; Roucoux, A.; Gengembre, L.; Beaunier, P.; Gédéon, A.; Launay, F. *Chem. Commun.* **2008,** 2920. (h) Xie, Y.; Ding, K.; Liu, Z.; Tao, R.; Sun, Z.; Zhang, H.; An, G. *J. Am. Chem. Soc.* **2009**, *131*, 6648. (i) Polisski, S.; Goller, B.; Wilson, K.; Kovalev, D.; Zaikowskii, V.; Lapkin, A. *J. Catal.* **2010**, *271*, 59.

[51] (a) Esteban, P.; Real, J.; Bayon, J. C.; Dexpert, H.; Bazin, D.; Maire, G. *J. Organo. Chem.* **1988,** *356*, 113. (b) Esteban, P.; Real, J.; Bayon, J. C.; Dexpert, H.; Bazin, D.; Garin, F.; Girard, P.; Maire, G. *J. de Chim. Phys.* **1989,** *86*, 1778. (c) Vierkötter, S. A.;

Barnes, C. E.; Hatmaker, T. L.; Penner-Hahn, J. E.; Stinson, C. M.; Huggins, B. A.; Benesi, A.; Ellis, P. D. *Organometallics* **1991,** *10*, 3803. (d) Barnes, C. E.; Ralle, M.; Vierkötter, S. A.; Penner-Hahn, J. E. *J. Am. Chem. Soc.* **1995,** *117*, 5861.

[52] (a) Esteban et al. have studied a similar $[Ir(1,5\text{-}COD)Cl]_2$ plus $\gamma\text{-}Al_2O_3$ supported-metal complex,[51] but did not emphasize the supported-nanoparticle heterogeneous catalyst formation steps or kinetics and mechanism. (b) Of interest and potential broader significance is that the precatalyst structure determined herein is *different* than that reported by Esteban et al.[51a,b] Those authors synthesized 2.5-wt% $[Ir(1,5\text{-}COD)Cl]_2$ on $\gamma\text{-}Al_2O_3$ via deposition from CH_2Cl_2 (e.g., vs the deposition from ethyl acetate employed herein), and then used subsequent CO trapping / IR plus EXAFS spectroscopy en route to proposing a "$[Ir(1,5\text{-}COD)\mu\text{–}O_{Support}]_2$" dimeric structure. Two possible interpretations of the different finding of our and their ostensibly closely analogous studies are that: (i) seemingly minor modifications in the precatalyst synthesis protocol (e.g., just the deposition solvent) or differences in the $\gamma\text{-}Al_2O_3$ support (e.g., perhaps its H_2O content; they dried theirs at 200 ^oC and 10^{-3} torr while we dried ours at 160 ^oC and 1 atm) can yield significant differences in the resultant precatalyst composition and structure; or possibly that (ii) one (or both) of the structural studies contains some at present undetected error in the analysis.

[53] (a) Rice, C. A.; Worley, S. D.; Curtis, C. W.; Guin, J. A.; Tarrer, A. R. *J. Chem. Phys.* **1981,** *74*, 6487. (b) van't Blik, H. F. J.; van Zon, J. B. A. D.; Huizinga, T.; Koningsberger, D. C.; Prins, R. *J. Am. Chem. Soc.* **1985,** *107*, 3139. (c) Frank, M.; Bäumer, M.; Kühnemuth, R.; Freund, H.-J. *J. Phys. Chem. B* **2001,** *105*, 8569.

[54] (a) Kawi, S.; Chang, J.-R.; Gates, B. C. *J. Phys. Chem.* **1993,** *97*, 5375. (b) Zhao, A.; Gates, B. C. *Langmuir* **1997,** *13*, 4024.

[55] (a) Roberto, D.; Cariati, E.; Psaro, R.; Ugo, R. *Organometallics* **1994,** *13*, 4227. (b) Bullitt, J. G.; Cotton, F. A. *Inorg. Chim. Acta* **1971,** *5*, 637. (c) Lawson, D. N.; Wilkinson, G. *J. Chem. Soc.* **1965,** 1900.

[56] (a) Crabtree, R. H.; Morris, G. E. *J. Organo. Chem.* **1977,** *135*, 395. (b) Cotton, F. A.; Lahuerta, P.; Sanau, M.; Schwotzer, W. *Inorg. Chim. Acta* **1986,** *120*, 153.

[57] (a) Uson, R.; Oro, L. A.; Cabeza, J. A. *Inorg. Syn.* **1985,** *23*, 126. (b) Green, M.; Kuc, T. A.; Taylor, S. H. *J. Chem. Soc. (A) Inorg. Phys.* **1971,** 2334.

[58] Rehr, J. J.; Albers, R. C. *Rev. Mod. Phys.* **2000**, *72*, 621.

[59] Zabinsky, S. I.; Rehr, J. J.; Ankudinov, A.; Albers, R. C.; Eller, M. J. *J. Phys. Rev. B* **1995,** *52,* 2995.

[60] A similar structure has been proposed on the basis of CO trapping/IR experiments for a different, but related, Ir^I complex supported on SiO_2,[55a] namely $[Ir(cyclooctane)_2(HOSi\equiv)Cl]$ (where $HOSi\equiv$ is the weak interaction of the Ir with a silanol group from the silica).

[61] Conner Jr., W. C.; Falconer, J. L. *Chem. Rev.* **1995,** *95*, 759.

[62] (a) Aiken, J. D.; Lin, Y.; Finke, R. G. *J. Mol. Catal. A: Chemical* **1996,** *114*, 29. (b) That paper provides evidence against Ir(0) nanoparticle hydrides, $Ir(0)_n(H)_2$, as at least the catalyst resting form in solution and when placing the well-defined Ir(0) nanoparticle precursor $(Bu_4N)_5Na_3[(1,5\text{-COD})Ir\bullet P_2W_{15}Nb_3O_{62}]$ under H_2. The resultant Ir(0) nanopraticle formation reaction consumes 3.5(0.3) equiv of H_2, with 2.0 equiv of the observed H_2 uptake being used for the reduction of 1,5-COD to cyclooctane, and 0.5 equiv H_2 for the reduction of Ir(I) to Ir(0). The additional 1.0 equivalent of H_2 forms the 2 electron reduced $P_2W_{13}{}^{VI}W_2{}^{V}Nb_3O_{62}{}^{11-}$ (plus two H^+) "heteropolyblue" which further condenses to $P_4W_{26}{}^{VI}W_4{}^{V}Nb_6O_{123}{}^{20-}$ + H_2O, a novel example of net H• "spillover" onto the soluble polyoxoanion "support". Overall, the H_2 reduction stoichiometry under 40 psig H_2 demonstrates that, at least in acetone solution, just Ir(0) and no $H_xIr(0)$ hydrides within experimental error.

[63] *Near monodisperse* nanoparticles are defined as ≤15% size distributions; see: Aiken III, J. D.; Lin, Y.; Finke, R. G. *J. Mol. Catal. A: Chemical* **1996,** *114*, 29.

[64] Note that the use of $Ir(0)_{\sim 900}$ is simply a convenient nomenclature that refers to the *average* number of metal atoms in the, *on average*, 2.9 nm $Ir(0)_n$ nanoparticles. This nomenclature is not meant to imply that the nanoparticles are truly monodisperse; indeed the 2.9 ± 0.4 nm size distribution implies that clusters ranging from $Ir_{\sim 600}$-$Ir_{\sim 1300}$.

[65] (a) Akita, T.; Okumura, M.; Tanaka, K.; Kohyama, M.; Haruta, M. *Catal. Today* **2006,** *117*, 62. (b) Hackett, S. F. J.; Brydson, R. M.; Gass, M. H.; Harvey, I.; Newman, A. D.; Wilson, K.; Lee, A. F. *Angew. Chem. Int. Ed.* **2007,** *46*, 8593. (c) Pyrz, W. D.; Buttrey, D. J. *Langmuir* **2008,** *24*, 11350. (d) Uzun, A.; Ortalan, V.; Hao, Y.; Browning, N. D.; Gates, B. C. *ACS Nano* **2009,** *3*, 3691.

[66] Watzky, M. A.; Finke, R. G. *Chem. Mater.* **1997,** *9*, 3083.

[67] Frenkel, A. I.; Hills, C. W.; Nuzzo, R. G. *J. Phys. Chem. B* **2001,** *105*, 12689.

[68] Edlund, D. J. Ph.D. Dissertation, University of Oregon, September 1987.

[69] For details on the observed error limits in k_1 of $\pm 10^{1.2}$ h^{-1} and in k_2 of ±3 fold (M^{-1} h^{-1}) derived over a >7 year period from data obtained from multiple investigator's hands, all for the best studied $P_2W_{15}Nb_3O_{62}{}^{9-}$ polyoxoanion-stabilized $Ir(0)_{\sim 300}$ nanoparticle system: Widegren, J. A.; Bennett, M. A.; Finke, R. G. *J. Am. Chem. Soc.* **2003,** *125*, 10301 (specifically p 10304).

[70] Morris, A. M.; Watzky, M. A.; Agar, J. N.; Finke, R. G. *Biochemistry* **2008,** *47*, 2413.

[71] The reported k_{1GLC} and $k_{2GLCcorr}$ error bars for the GLC data are derived from the non-linear-least-squares fit to the two-step mechanism (i.e., are *fit* errors); that is, they do not correspond to the *experimental error* inherent to the nucleation and autocatalytic surface growth kinetics obtained from multiple kinetic runs (i.e., and as was obtained for the reported reporter reaction kinetics, k_1 = 1.5(1.1) x 10^{-3} h^{-1} (i.e., ~ $\pm 10^1$) and k_{2corr} = 1.6(2) x 10^4 h^{-1} M^{-1}).

[72] Buffering effects of γ-Al_2O_3 are known, see for example: Park, J.; Regalbuto, J. R. *J. Colloid Interface Sci.* **1995,** 175, 239.

[73] Finney, E. E.; Finke, R. G. *Chem. Mater.* **2009**, *21*, 4692. The cited work lists nine insights from the two-step mechanism—insights that are also expected to apply at least in general to the present $Ir(0)_{\sim 900}$/γ-Al_2O_3 supported catalyst system formed in contact with solution (and given (a) the excellent fits of the sigmoidal kinetics to the two-step mechanism, and (b) since the first three insights from the two-step mechanism have been verified by the results presented herein): (i) that near monodisperse (≤±15%) size distributions typically result from the syntheses where the observed kinetics are sigmoidal;[66] (ii) on average "magic-number sized" nanoparticles tend to be formed, and (iii) avoiding H_2 gas-to-solution MTL ensures the formation of those near monodisperse products (±~14% in the present case).[48] Along with these already observed insights for the present $Ir(0)_{\sim 900}$/γ-Al_2O_3 supported catalyst system, six additional mechanistic insights are therefore expected to apply: (iv) rational size control should be possible via a recent nanoparticle size vs time equation in terms of k_1, k_2 and $[A]_0$;[73] (v) additional size control should be possible via added ligands that can control k_1 and k_2 (some initial results are briefly presented in the Supporting Information herein); (vi) the use of seeded growth methods should allow the rational, mechanistically guided synthesis of all possible geometric isomers of multimetallic "nano-onions";[66] (vii) rational catalyst shape control should be possible via ligands capable of attaching to the otherwise autocataytically growing nanoparticle facets, effectively preventing autocatalytic surface growth at that facet;[73] (viii) nanoparticle surface ligands should be able to provide additional nanoparticle stability if desired[73]—an important area of future investigation; and finally (ix) nanoparticle size-dependent bond energies (i.e., surface metal-to-ligand bond energies) as previously found are expected,[20,21,22] which can change the nanoparticles fractional surface coverage and change whether smaller or larger nanoparticles are the superior catalysts in a given reaction.[20,21,22]

[74] Mondloch, J. E.; Finke, R. G. "*Supported-Nanoparticle Heterogeneous Catalyst Formation in Contact with Solution: Kinetics and Proposed Mechanism for the Conversion of Ir(1,5-COD)Cl/*γ-Al_2O_3 *to* $Ir(0)_{\sim 900}$/γ-Al_2O_3 *" J. Am. Chem. Soc.* **2011,** *133,* 7744-7756.

[75] More rigorously, "the number of exposed metal atoms determined by chemisorption experiments in the solid state is not necessarily equivalent to the number of catalytically active surface sites in solution", see p. 1626 and footnote #10 of (a) Hornstein, B. J.; Aiken III, J. D.; Finke, R. G. *Inorg. Chem.* **2002,** *41*, 1625. and other references of relevance (b) Gonzalez-Tejuca, L.; Namba, A. S.; Turkevich, J. *J. Phys. Chem.* **1977,** *81*, 1399. (c) Kivrak, H.; Mastalir, A.; Kiraly, Z.; Uner, D. *Catal. Comm.* **2009,** *10*, 1002.

[76] Supported nanoparticles can take on many different morphologies, for a few examples see: (a) Henry, C. R. *Prog. Surf. Sci.* **2005,** *80*, 92. (b) Pakarinen, O. H.; Barth, C.; Foster, A. S.; Henry, C. R. *J. Appl. Phys.* **2008,** *103*, 054313. (c) Haruta, M. *CATTECH* **2002,** *6*, 102.

Supporting Information for:

DEVELOPMENT PLUS KINETIC AND MECHANISTIC STUDIES OF A PROTOTYPE SUPPORTED-NANOPARTICLE HETEROGENEOUS CATALYST FORMATION SYSTEM IN CONTACT WITH SOLUTION: Ir(1,5-COD)Cl/γ-Al_2O_3 AND ITS REDUCTION BY H_2 TO Ir(0)$_n$/γ-Al_2O_3

Joseph E. Mondloch, Qi Wang, Anatoly I. Frenkel and Richard G. Finke

Additional Results and Discussion

EXAFS 1NN Fitting for the Ir(1,5-COD)Cl/γ-Al_2O_3 Precatalyst, $[Ir(1,5\text{-}COD)Cl]_2$ and $[Ir(1,5\text{-}COD)\mu\text{-}OCH_3]_2$ Reference Compounds as Well as the $Ir(0)_{\sim 900}$/γ-Al_2O_3 Catalyst. Data processing and analysis were performed using the IFEFFIT package. The EXAFS analysis was done by fitting the theoretical FEFF6 signals to the experimental data in *r*-space. All the fitted data was limited to the first nearest neighbor (1NN) contributions. The passive electron factors, S_0^2, were found to be 0.80 by fits to standard Iridium black, and thus fixed for further analysis of the $Ir(0)_n$ nanoparticles. The parameters describing the electronic properties (e.g., correction to the photoelectron energy origin) and local structure environment (coordination numbers *N*, bond lengths *R* and their mean squared disorder parameters σ^2) around the absorbing atoms were varied during the fitting. The molecular nature of the Ir(1,5-COD)Cl/γ-Al_2O_3 precatalyst , as well as the reference compounds $[Ir(1,5\text{-}COD)Cl]_2$ and $[Ir(1,5\text{-}COD)\mu\text{-}OCH_3]_2$ have significant differences in electronic structure compared to Ir(0) black. We obtained S_0^2 = 1 from the fit to the reference compound $[Ir(1,5\text{-}COD)\mu\text{-}OCH_3]_2$ while constraining $N_{Ir\text{-}C}$ and $N_{Ir\text{-}O}$ = 2 based on its known structure, and then fixed S_0^2 = 1 in the fits of the precatalyst as well as the $[Ir(1,5\text{-}COD)Cl]_2$ reference compound. The photoelectron path between Ir and its carbon nearest neighbors (Ir–C) was used to simulate both the Ir–C and Ir–O contributions, as C and O are not readily distinguishable by the EXAFS analysis. Additionally, a physically reasonable constraint holding the CN(Ir–C) and CN(Ir–Cl) equal to 6 was applied in the EXAFS fits for the precatalyst as well as $[Ir(1,5\text{-}COD)Cl]_2$. Furthermore, fits to the Ir(1,5-COD)Cl/γ-Al_2O_3 precatalyst were based on the fixed σ^2 for both Ir–C and Ir–Cl, found from fitting the $[Ir(1,5\text{-}COD)Cl]_2$ structure. The coordination numbers *N*, bond lengths *R* and their mean squared disorder parameters σ^2 obtained from the EXAFS fits (shown in Figure S1) are given in Table 1 of the main text.

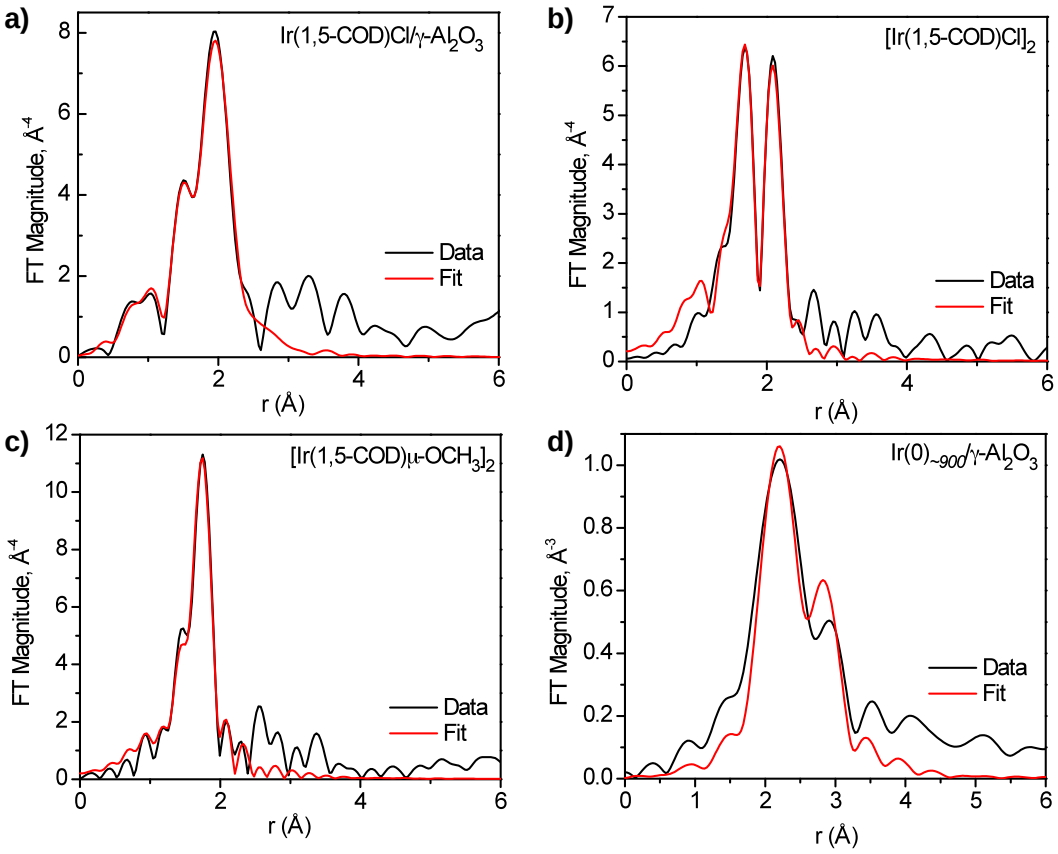

Figure S1. Fourier transform magnitudes of the Ir L_3-edge data (black) and their associated fits (red) for: (a) the Ir(1,5-COD)Cl/γ-Al_2O_3 precatalyst (k^3-weighting, k range from 2–11.5 Å^{-1}); (b) $[Ir(1,5\text{-COD})Cl]_2$ (k^3-weighting, k range from 2.5–14.5 Å^{-1}); (c) $[Ir(1,5\text{-COD})\mu\text{-}OCH_3]_2$ (k^3-weighting, k-range from 2.5–16 Å^{-1}) and (d) $Ir(0)_{\sim 900}$/γ-Al_2O_3 (k^2-weighting = 2, k range from 2.5–9.3 Å^{-1}).

Additional TEM Imaging and Particle Size Histograms for the $Ir(0)_{\sim 900}$/γ-Al_2O_3 Heterogeneous Nanoparticle Catalyst. Shown in Figure S2 are additional TEM images for the $Ir(0)_{\sim 900}$/γ-Al_2O_3 prototype catalyst and that correspond to Figure 4 of the main text. The additional images help further reveal the catalyst morphology.

Control Testing for H_2 Gas-to-Solution Mass Transfer Limitations (MTL). H_2 gas-to-solution MTL have been observed to cause undesired effects such as bulk $Rh(0)_n$ in the formation of Rh polyoxoanion stabilized nanoparticles.[1] This is due to the competing effects between diffusive aggregation and autocatalytic surface growth.[1] To test whether

H_2 gas-to-solution MTL is affecting the observed kinetics provided in the main text, stirring speed dependent plots were performed, a classic test for the presence of MTL.[1] If H_2 going into solution (i.e., MTL) is part of the overall rate-determining step, then the rate will be dependent on the stirring speed of the reaction.

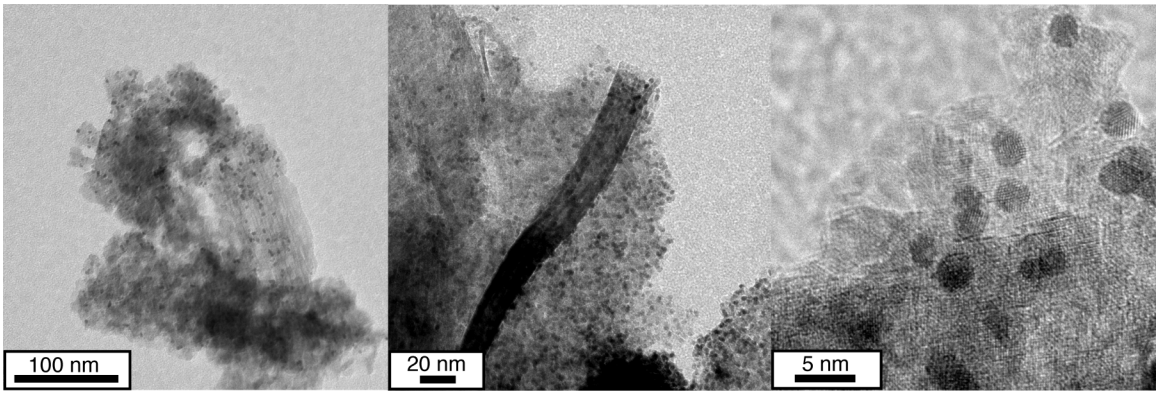

Figure S2. Additional TEM imaging for the $Ir(0)_{\sim 900}/\gamma\text{-}Al_2O_3$ heterogeneous catalyst. These images further reveal the catalyst morphology then is seen in Figure 4 of the main text.

Each of four "standard condition" reactions was prepared as described in the experimental section of the main text with the following exception. Stirring was carried out at the appropriate speeds (200-1000 rpm). Note that the "0,0" point in Figure S4 is not an experimentally observed data point, but one that should be true physically. The data in Figure S3 show that at 600 rpm stirring speed, where our experiments were performed, the reaction rate is largely independent of the stirring rate. For example, when the stirring speed is increased from 600 to 1000 rpm, the reaction rate increases only 3.5 parts in 47 corresponding to only a 7.5% increase in the rate of the reaction. This introduces an error of ≤15% into the resultant rate constants, an error less than that we typically see in the $Ir(0)_{\sim 900}/\gamma\text{-}Al_2O_3$ heterogeneous nanoparticle catalyst formation kinetics (Table 2) and thus negligible. In short, the stirring rate MTL controls in Figure S3 demonstrate that MTL are negligible in the present case and under our experimental

conditions in our specific experimental apparatus detailed in the Experimental section of the main text.

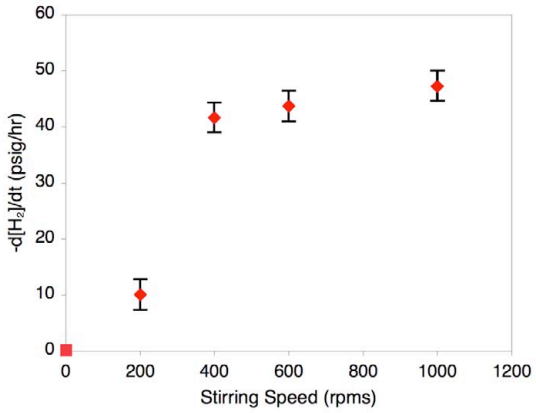

Figure S3. Stirring speed dependence for the $Ir(0)_{\sim 900}/\gamma\text{-}Al_2O_3$ heterogeneous nanoparticle formation reaction.

Testing the Cyclohexene Reporter Reaction for the Desired Zero-Order [Cyclohexene] Dependence. Six **"**standard condition" reactions were independently prepared as described in the Experimental section of the main text. In each separate experiment the cyclohexene concentration was varied, and the acetone concentration was adjusted to compensate for the amount of cyclohexene present so that the final solution volume was always 3.0 mL. For example, if 0.2 mL of cylohexene was used 2.8 mL of acetone would be used bringing the total volume to 3.0 mL.

The cyclohexene reporter reaction must be fast (see Scheme 2 of the main text), in comparison to the $Ir(0)_{\sim 900}/\gamma\text{-}Al_2O_3$ heterogeneous nanoparticle catalyst formation steps k_1 and k_2, if the reporter reaction is working properly. This requirement is experimentally testable by looking at the [cyclohexene] dependence of the reaction, the results of which are shown in Figure S4. Saturation kinetics are observed by the time 1.65 M cyclohexene is reached, the amount used in the present studies. Hence, the rate of

cyclohexene hydrogenation is indeed fast relative to k_1 and k_2, the desired nanoparticle formation steps whose kinetics are, therefore, actually being measured.

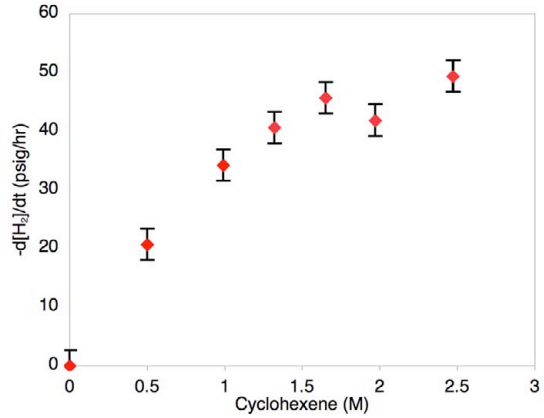

Figure S4. Cyclohexene dependent plots for the $Ir(0)_{\sim 900}/\gamma\text{-}Al_2O_3$ heterogeneous nanoparticle catalyst formation reaction. The Figure shows that the rate of the $Ir(0)_{\sim 900}/\gamma\text{-}Al_2O_3$ heterogeneous nanoparticle formation reaction is independent of the cyclohexene concentration at 1.65 M, the amount of cyclohexene experimentally used herein.

The Cyclohexene Reporter Reaction: Correcting the k_2 Observed Rate Constant for the Reporter Reaction Stoichiometry Factor. To get quantitative agreement between the observed rate constant $k_{2(curvefit)}$ obtained by the cyclohexene reporter reaction and the cyclooctane GLC kinetic monitoring methods, a mathematically required correction factor is needed. The appropriate equation and correction factor derived before[2,3] is reproduced below. Scheme 3 in the main text (bottom reaction) dictates that rate equation for the cyclohexene reporter reaction is that expressed in equation S1. Starting with the rate-determining steps, k_1 and k_2, and substituting the mass balance equation. $[B] = ([A]_0 - [A])$ we obtain the right hand side of equation S1.

$$-\frac{d[A]}{dt} = \frac{d[B]}{dt} = k_1[A] + k_2[A][B] = k_1[A] + k_2[A]([A]_0 - [A]) \qquad \text{(S1)}$$

Turning this into what is actually followed by the cyclohexene reporter reaction (that is we add ~1700 equivalents of cyclohexene per Ir) and with the known 1:1 cyclohexene-to-H_2 stoichiometry, one obtains the previously demonstrated equation S2.[4]

$$-\frac{d[A]}{dt} = \frac{d[B]}{dt} = -\frac{1}{\sim 1700}\frac{d[cyclohexene]}{dt} = -\frac{1}{\sim 1700}\frac{d[H_2]}{dt} \qquad \text{(S2)}$$

Through several lines of algebra equation S3 is obtained.[2]

$$-\frac{d[cyclohexene]}{dt} = k_1[cyclohexene]_t + \frac{k_2}{\sim 1700}[hexene]_t([cyclohexene]_0 - [cyclohexene]_t) \qquad \text{(S3)}$$

Integrating Equation S1 and expressing it in exponential form yields the integrated rate equation used to fit the kinetic data to the F–W 2-step mechanism.

$$[A]_t = \frac{\frac{k_1}{k_2} + [A]_0}{1 + \frac{k_1}{k_2[A]_0} * \exp(k_1 + k_2[A]_0)t} \qquad \text{(S4)}$$

When the kinetic data are fit by equation S4, $k_{2(\text{curvefit})}$ is obtained, which needs to be corrected for the 1700:1 cyclohexene to Ir stoichiometry factor. This is done by taking $k_{2curvefit} = k_2/\sim 1700$ that is $\sim 1700 * k_{2(curvefit)} = k_{2corr}$. Hence, when using the cyclohexene reporter reaction the obtained $k_{2(curvefit)}$ rate constant needs to be corrected for the experimentally determined stoichiometry factor of 1700:1 (cyclohexene:Ir) as shown above.

Fitting the Cyclooctane Evolution Kinetics via the 2-step Mechanism. To fit the observed cyclooctane evolution kinetics a modified form of the integrated rate equation (S4) must be used. By substituting the mass balance equation $[A]_t = [A]_0 - [B]_t$ into equation S4, and for a clean stoichiometric A → B reaction, equation S5 results.

$$[B]_t = [A]_0 - \frac{\frac{k_1}{k_2} + [A]_0}{1 + \frac{k_1}{k_2[A]_0}\exp(k_1 + k_2[A]_0)t} \qquad \text{(S5)}$$

In this case the obtained rate constant k_2 need not be corrected, as detailed below. Here we simplify the kinetic derivation by using the stoichiometry below, equation S6.

$$\frac{1}{2}[Ir(1,5-COD)Cl]_2 + \frac{5}{2}H_2 \rightarrow Ir(0) + \text{Cyclooctane} + HCl \qquad \text{(S6)}$$

Again starting from the rate-determining step and setting [A] = ½ $[Ir(1,5\text{-COD})Cl]_2$ and $[B]_t = [Ir(0)]_t = [\text{cyclooctane}]_t$.

$$\frac{d[B]}{dt} = \frac{d[Ir(0)]}{dt} = \frac{d[\text{cyclooctane}]}{dt} = k_1[A]_t + k_2[A]_t[B]_t \qquad \text{(S7)}$$

The following mass balance equations apply: (i) $[A]_0 = [\text{cyclooctane}]_\infty$, and (ii) $[A]_0 = [A]_t + [Ir(0)]_t = [A]_t + [\text{cyclooctane}]_t$. Thus (iii) $[A]_t = [\text{cyclooctane}]_\infty - [\text{cyclooctane}]_t$. Substituting (iii) and (ii) into S7 yields equation S8:

$$\frac{d[\text{cyclooctane}]}{dt} = k_1([\text{cyclooctane}]_\infty - [\text{cyclooctane}]_t) + k_2([\text{cyclooctane}]_\infty - [\text{cyclooctane}]_t)[\text{cyclooctane}]_t \quad \text{(S8)}$$

Thus a plot of cyclooctane vs time, yields k_1 and k_2 rate constants *without any correction factors*.

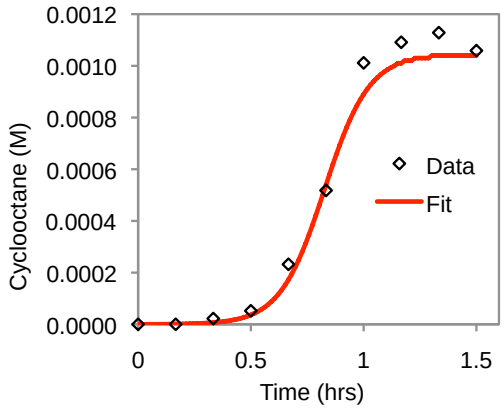

Figure S5. Cyclooctane evolution kinetics for the formation of $Ir(0)_{\sim 900}/\gamma\text{-}Al_2O_3$. The black diamonds are the experimental data and the blue line is the fit to the 2-step mechanism.

Cyclooctane Evolution Kinetics for 1.96-wt% Ir(1,5-COD)Cl/γ-Al_2O_3. The choice of Ir(1,5-COD)Cl/γ-Al_2O_3 as a prototype precatalyst in the present work allows for an additional, very valuable kinetic monitoring method, one which functions as a direct control to check the results of the cyclohexene reporter reaction method. Specifically, using GLC we have directly monitored the cyclooctane evolution kinetics, of the Ir(1,5-COD)Cl/γ-Al_2O_3 supported-nanoparticle heterogeneous catalyst formation reaction, Figure S5. The data were fit to equation S8, and the resultant rate constants are, k_{1GLC} = 1.2(2) x 10^{-3} and k_{2GLC} = 1.2(2) x 10^{4} h^{-1} M^{-1}. The quantitative agreement (within experimental error) between the rate constants obtained by the two methods, and post the mathematically required correction factor for the reporter-reaction method, offers

compelling evidence that both methods are correctly monitoring the same process in real time, namely the $Ir(0)_{\sim 900}/\gamma\text{-}Al_2O_3$ supported-nanoparticle heterogeneous catalyst formation reaction.

TEM Imaging, Corresponding Particle Size Histogram and Cyclooctane Evolution Kinetics for the $Ir(0)_n/\gamma\text{-}Al_2O_3$ Supported-Nanoparticle Heterogeneous Catalyst Formation when Cyclohexene is not Present. In the synthesis of polyoxoanion $Ir(0)_n$ stabilized nanoclusters in acetone, $Ir(0)_{\sim 300}$ nanoclusters form when cyclohexene is present, but larger $Ir(0)_{\sim 900}$ nanoclusters are formed in the absence of cyclohexene but still under H_2 as the reducing agent.[4,5] Hence it was of interest to see if cyclohexene has similar effects or not in the present supported-nanoparticle system.

An $Ir(0)_n/\gamma\text{-}Al_2O_3$ catalyst was therefore synthesized under the identical standard reaction conditions described above, except without cyclohexene present. A TEM of the resultant products is shown in Figure S6; on average 3.1 ± 0.5 nm nanoclusters are observed, and with the corresponding histogram shown in Figure S6. The corresponding particle size histogram for $Ir(0)_{\sim 1100}/\gamma\text{-}Al_2O_3$. Their size is within error of the 2.9 ± 0.4 nm ($Ir(0)_{\sim 900}/\gamma\text{-}Al_2O_3$) products when cyclohexene is present; hence cyclohexene plays little to no role in the observed $Ir(0)_n/\gamma\text{-}Al_2O_3$ supported-nanoparticle heterogeneous catalyst product.

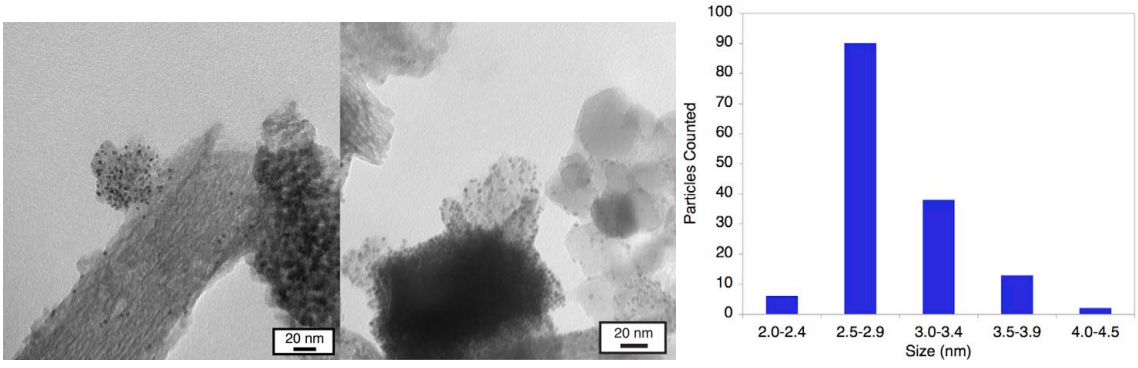

Figure S6. TEM imaging of the $Ir(0)_{\sim 1100}/\gamma\text{-}Al_2O_3$ supported-nanoparticle catalyst formed when cyclohexene is absent during the synthesis and the corresponding particle size histogram revealing 3.1 ± 0.5 nm nanoparticles.

To confirm this result, the cyclooctane evolution kinetics were monitored, and are shown in Figure S7 along with a fit to the 2-step mechanism. The resultant rate constants without the cyclohexene present, k_{1GLC} = 3.5(2) x 10^{-2} h^{-1} M^{-1} and k_{2GLC} = 3.9(2) x 10^{4} h^{-1} M^{-1}, are within error of those when cyclohexene is present (k_{1GLC} = 1.2(2) x 10^{-3} h^{-1} and k_{2GLC} = 1.2(2) x 10^{4} h^{-1} M^{-1}).[6]

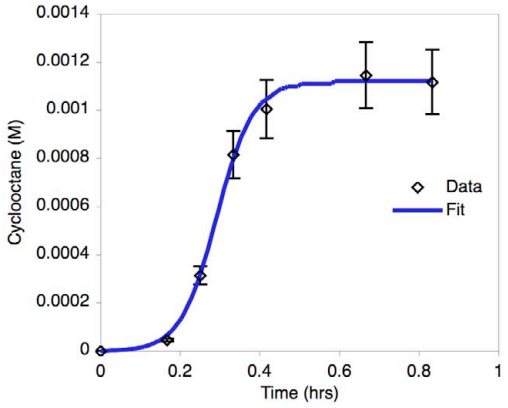

Figure S7. Cyclooctane evolution kinetics starting from the Ir(1,5-COD)Cl/γ-Al_2O_3 precatalyst with the olefin cyclohexene not present. The black diamonds are the experimental data and the blue line is the fit to the 2-step mechanism.

Confirming the Molecularity ($[A]^1$) of Nucleation, A → B, Starting with Ir(1,5-COD)Cl/γ-Al_2O_3. A series of precatalysts from 1.0–3.85-wt% were made following as described in the experimental section of the main text (Pre-Catalyst Preparation: Ir(1,5-COD)Cl/γ-Al_2O_3. In each case the nucleation rate (-d[A]/dt) was taken once the H_2 uptake was ≥ 0.05 psig (albeit arbitrarily, but consistently and as precedented[2]).

The ln/ln plot of the nucleation rate (-d[A]/dt vs. Ir-wt%) shown in Figure S8 is linear and reveals a slope of 1.01, that is 1.0 within experimental error and further verifying the $[A]^1$ molecularity of the A → B nucleation step of the 2-step mechanism.

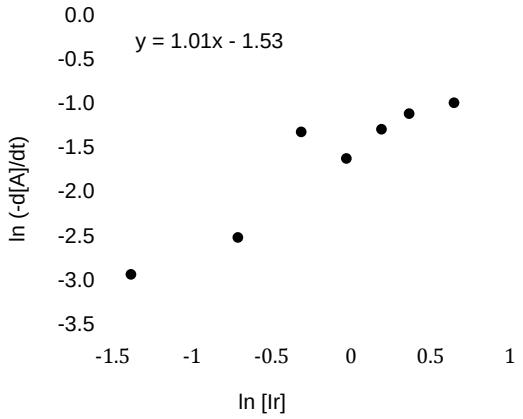

Figure S8. The ln/ln plot revealing first order kinetics for the nucleation step A → B, starting with Ir(1,5-COD)Cl/γ-Al_2O_3.

References

[1] Aiken III, J. D.; Finke, R. G. *J. Am. Chem. Soc.* **1998**, *120*, 9545.

[2] Watzky, M. A.; Finke, R. G. *J. Am. Chem. Soc.* **1997**, *119*, 10382.

[3] Widegren, J. A.; Aiken III, J. D.; Özkar, S.; Finke, R. G. *Chem. Mater.* **2001**, *13*, 312.

[4] Lin, Y.; Finke, R. G. *J. Am. Chem. Soc.* **1994**, *116*, 8335.

[5] Lin, Y.; R.G. Finke, *Inorg. Chem.* **1994,** *33,* 4891.

[6] The reporter k_{1GLC} and k_{2GLC} error bars are only derived from the non-linear least squares fit to the F–W 2-step mechanism, and do not correspond to the true experimental error inherent to the nucleation and growth kinetics. The true error bars for the supported-nanoparticle heterogeneous catalyst formation reaction are more accurately reflected in the reported k_1 value of ~ $10^{-3.4(5)}$ and k_{2corr} = 1.6(2) x 10^4 h^{-1} M^{-1} obtained from multiple runs via the cyclohexene reporter reaction kinetics (for references and more discussion, see the main text).

CHAPTER V

SUPPORTED-NANOPARTICLE HETEROGENEOUS CATALYST FORMATION IN CONTACT WITH SOLUTION: KINETICS AND PROPOSED MECHANISM FOR THE CONVERSION OF Ir(1,5-COD)Cl/γ-Al_2O_3TO $Ir(0)_{\sim 900}$/γ-Al_2O_3

This dissertation chapter contains the manuscript of a paper published in the *Journal of American Chemical Society* **2011,** 133, 7744–7756 and is available online at http://dx.doi.org/10.1021/ja110550h. This chapter probes the critical question of whether the Ir(1,5-COD)Cl/γ-Al_2O_3 to $Ir(0)_{\sim 900}$/γ-Al_2O_3 supported-nanoparticle heterogeneous catalyst formation reaction occurs on the support, in solution or possibly on both for one or more of the catalyst formation steps (i.e., the A → B nucleation and A + B → 2B autocatalytic growth steps).

The experiments in this chapter were designed by Joseph E. Mondloch and Professor Richard G. Finke. All of the experiments were performed by Joseph E. Mondloch. Data analysis was performed by Joseph E. Mondloch with help from Professor Richard G. Finke. The manuscript was written by Joseph E. Mondloch and edited by Professor Richard G. Finke.

SUPPORTED-NANOPARTICLE HETEROGENEOUS CATALYST FORMATION IN CONTACT WITH SOLUTION: KINETICS AND PROPOSED MECHANISM FOR THE CONVERSION OF Ir(1,5-COD)Cl/γ-Al_2O_3TO Ir(0)$_{\sim 900}$/γ-Al_2O_3

Joseph E. Mondloch and Richard G. Finke

Overview

A current goal in heterogeneous catalysis is to transfer the synthetic, as well as developing mechanistic, insights from the modern revolution in nanoparticle science to the synthesis of supported-nanoparticle heterogeneous catalysts. In a recent study (Mondloch, J. E.; Wang, Q.; Frenkel, A. I,; Finke, R. G. *J. Am. Chem. Soc.* **2010,** *132,* 9701–9714), we initialized tests of the global hypothesis that quantitative kinetic and mechanistic studies, of supported-nanoparticle heterogeneous catalyst formation *in contact with solution*, can provide synthetic and mechanistic insights that can eventually drive improved syntheses of composition-, size-, and possibly shape-controlled catalysts. That study relied on the development of a well-characterized Ir(1,5-COD)Cl/γ-Al_2O_3 precatalyst which, when in contact with solution and H_2, turns into a non-aggregated Ir(0)$_{\sim 900}$/γ-Al_2O_3 supported-nanoparticle heterogeneous catalyst. The kinetics of the Ir(1,5-COD)Cl/γ-Al_2O_3 to Ir(0)$_{\sim 900}$/γ-Al_2O_3 conversion were followed and fit by a two-step mechanism consisting of nucleation (A → B, rate constant k_1) followed by autocatalytic surface growth (A + B → 2B, rate constant k_2). *However, a crucial, but*

previously unanswered question is whether the nucleation and growth steps occur primarily in solution, on the support, or possibly in both phases for one or more of the catalyst-formation steps. The present work investigates this central question for the prototype Ir(1,5-COD)Cl/γ-Al_2O_3 to $Ir(0)_{\sim 900}$/γ-Al_2O_3 system. Solvent variation-, γ-Al_2O_3-and acetone-dependent kinetic data, along with UV–vis spectroscopic and gas–liquid chromatography (GLC) data, are consistent with and strongly supportive of a supported-nanoparticle formation mechanism consisting of Ir(1,5-COD)Cl(solvent) dissociation from the γ-Al_2O_3 support (i.e., from Ir(1,5-COD)Cl/γ-Al_2O_3), solution-based nucleation from that dissociated Ir(1,5-COD)Cl(solvent) species, fast $Ir(0)_n$ nanoparticle capture by γ-Al_2O_3 and then subsequent solid-oxide-based nanoparticle growth from $Ir(0)_n$/γ-Al_2O_3 and with Ir(1,5-COD)Cl(solvent), the first kinetically documented mechanism of this type. Those data disprove a solid-oxide-based nucleation and growth pathway involving only Ir(1,5-COD)Cl/γ-Al_2O_3 and also disprove a solution-based nanoparticle growth pathway involving Ir(1,5-COD)Cl(solvent) and $Ir(0)_n$ in solution. The present mechanistic studies allow comparisons of the Ir(1,5-COD)Cl/γ-Al_2O_3 to $Ir(0)_{\sim 900}$/γ-Al_2O_3 supported-nanoparticle formation system to the kinetically and mechanistically well-studied, Ir(1,5-COD)•$P_2W_{15}Nb_3O_{62}^{8-}$ to $Ir(0)_{\sim 300}$•$(P_2W_{15}Nb_3O_{62}^{8-})_n^{-8n}$ solution-based, polyoxoanion-stabilized nanoparticle formation and stabilization system. That comparison reveals closely analogous, solution $Ir(1,5\text{-}COD)^+$ or Ir(1,5-COD)Cl mediated, mechanisms of nanoparticle formation. Overall, the hypothesis supported by this work is that these and analogous studies hold promise of providing a way to transfer the synthetic and mechanistic insights, from the modern revolution in nanoparticle synthesis and characterization in solution, to the rational, mechanism-directed syntheses of solid oxide-supported nanoparticle heterogeneous catalysts, also in contact with solution.

Introduction

Small metal nanoparticles supported on metal-oxide supports constitute a large, important subset of heterogeneous catalysts.[1] Despite their importance, the synthesis of these industrially significant catalysts is still largely empirical.[2] Hence, a current goal in catalyst preparation is to transfer the synthetic,[3] as well as developing mechanistic,,[4,5,6,7,8,9,10] insights from the modern revolution in nanoparticle science—including control over nanoparticle composition,[11] size[12] and shape[13]—to the synthesis of supported-nanoparticle heterogeneous catalysts.[14] However, despite the now considerable insights into the synthesis, characterization and mechanisms of formation of nanoparticles in solution, transferring that synthetic and mechanistic knowledge to the preparation of supported heterogeneous catalysts remains largely unaccomplished, if not elusive.

At present, a common approach to preparing supported-nanoparticle catalysts is to first make the nanoparticles in solution (often with polymer or other ligands as stabilizers to prevent aggregation[15,16]), isolate the nanoparticles, and then deposit those ligand-stabilized nanoparticles onto a support.[15,16] Unfortunately, the polymer or other stabilizers are thereby unavoidably co-deposited. Complete removal of the stabilizing polymer or other ligands has proven difficult to impossible[15,16] (such ligand removal being required for the most facile, coordinatively unsaturated catalysts). The resultant, partially ligand- or polymer-poisoned, supported-nanoparticles are then, and in turn, also compositionally ill-defined. That poorly defined composition as well as their size and shape are often then further altered by harsh thermal, oxidative, reductive or other treatments aimed at removing the poisoning ligands or polymers.[16]

A more attractive, alternative synthetic approach, one that dates in part back to at least 1982[18a] and which is now attracting increasing attention,[14,17,18] is to start from supported molecular precursors and then synthesize the supported-nanoparticles in situ

(i.e., in contact with solution) and *with only the desired catalytic reaction substrates or other ligands present*. At least in principle, this in-situ method can provide additional control over the supported-nanoparticle composition, size and shape, because one can readily add desired solvents, ligands or other additives at will during the synthesis. Having only the desired reactants or other weakly bound ligands present can lead to what we have termed "weakly ligated/labile ligand" nanoparticles.[19,20]

Another potential advantage of the in situ, solution-based method is the ability to follow directly the supported-nanoparticle heterogeneous catalyst formation kinetics.[14,17] Kinetic and mechanistic studies are expected to be significant because key catalytic properties,[21] including selectivity,[22] activity,[21] lifetime and stability,[23] depend on the nanoparticle catalyst surface composition,[24] size[25] and structure. These properties are in turn dependent on the kinetics and mechanism(s) of nanoparticle formation (i.e., minimally nanoparticle nucleation and growth),[22] plus the specific solvent and ligands present.

Only six prior studies have addressed the mechanisms of supported-nanoparticle heterogeneous catalyst formation in contact with solution.[14,17,26,27,28,29] Of those six studies, only two[14,17] have provided kinetic data consistent with their proposed mechanisms, a point confirmed by our recent review[30] of the surprisingly limited number of prior studies examining the kinetics and mechanisms of practical heterogeneous catalyst formation under any conditions. Furthermore, no prior study begins from a fully characterized, speciation-controlled organometallic precatalyst[14,31] where the supported-nanoparticle stoichiometry is established[14] and where the kinetics of the supported-nanoparticle formation are also followed.[14] Nor has any of the solvent variation-, γ-Al_2O_3- or acetone-dependent kinetic data given herein been previously reported for any prior system.

The Prototype Ir(1,5-COD)Cl/γ-Al_2O_3 to $Ir(0)_{\sim 900}$/γ-Al_2O_3 System. Recently, we reported the development of the Ir(1,5-COD)Cl/γ-Al_2O_3 to $Ir(0)_{\sim 900}$/γ-Al_2O_3 supported-nanoparticle heterogeneous catalyst formation system in contact with just acetone solvent plus the catalytic reactants cyclohexene and H_2, Scheme 1.[14] Crucial to the

Scheme 1. The Recently Developed[14] Ir(1,5-COD)Cl/γ-Al_2O_3 (left) to $Ir(0)_{\sim 900}$/γ-Al_2O_3 (Right, TEM Imaging) Supported-Nanoparticle Heterogeneous Catalyst Formation System in Contact with Solution

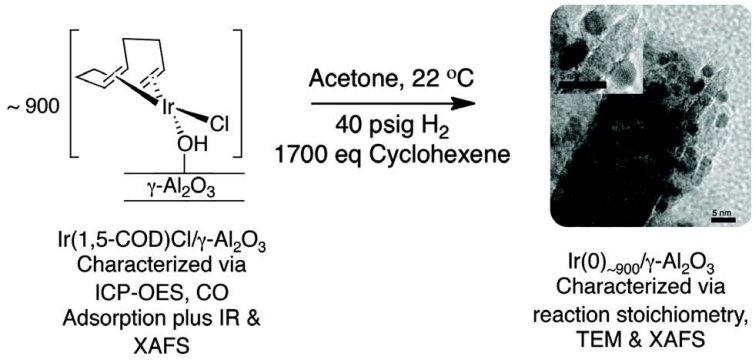

kinetic and mechanistic studies presented herein, the speciation controlled Ir(1,5-COD)Cl/γ-Al_2O_3 precatalyst (Scheme 1, left; a single supported species) was fully characterized via inductively coupled optical emission spectroscopy, CO/IR trapping experiments as well as X-ray absorbance fine structure spectroscopy (XAFS).[14] A balanced stoichiometry for the conversion of the Ir(1,5-COD)Cl/γ-Al_2O_3 precatalyst into the supported-nanoparticle product (Scheme 1, right) was also obtained along with characterization of the resultant $Ir(0)_{\sim 900}$/γ-Al_2O_3 catalyst by transmission electron microscopy (TEM) and XAFS. The results reveal non-aggregated, near-monodisperse (i.e., ≤±15%) 2.9 ± 0.4 nm nanoparticles supported on γ-Al_2O_3 (i.e., $Ir(0)_{\sim 900}$/γ-Al_2O_3).[14] Such a well-characterized, speciation controlled Ir(1,5-COD)Cl/γ-Al_2O_3 precatalyst and resultant near-monodisperse $Ir(0)_{\sim 900}$/γ-Al_2O_3 catalyst are important prior results[14] that underpin the present studies. The eight criteria previously developed as the working

definition of a prototype supported-nanoparticle heterogeneous catalyst formation system *in contact with solution* are detailed in a footnote for the interested reader.[32]

Initial kinetic studies, followed by the precedented[4-8,14,17] cyclohexene reporter reaction method (Scheme 2, left), were also performed as part of our prior work[14] and revealed that the supported-nanoparticle heterogeneous catalyst formation kinetics (Figure 1) are well fit to a two-step mechanism of nucleation (A → B, rate constant k_{1obs}) followed by autocatalytic surface growth (A + B → 2B, rate constant k_{2obs}), Scheme 2 (right). However, a crucial but until now unanswered question is whether nucleation and growth take place (i) homogeneously in solution, (ii) heterogeneously on the support, or conceivably (iii) in both phases for one or more of the catalyst formation steps. It is the answer to these questions that is the focal point of the present study.

Scheme 2. The Cyclohexene Reporter Reaction Method Used To Follow the Supported-Nanoparticle Heterogeneous Catalyst Formation Kinetics (Left), Along with the Two-Step Mechanism That Has Been Shown to[14] Fit the Overall Ir(1,5-COD)Cl/γ-Al_2O_3 to Ir(0)$_{\sim 900}$/γ-Al_2O_3 Supported-Nanoparticle Formation Kinetics (Right)

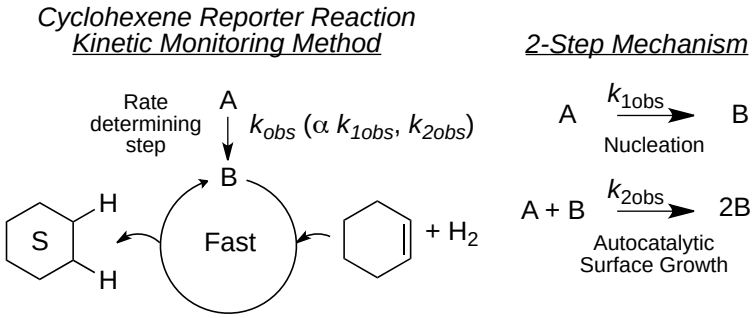

Herein we present kinetic and mechanistic studies probing precisely in which phase (or phases; solution, solid-state, or both) the nucleation and growth catalyst formation steps occur for the Ir(1,5-COD)Cl/γ-Al_2O_3 to Ir(0)$_{\sim 900}$/γ-Al_2O_3 system while in contact with acetone or acetone/cyclohexane solution. Solvent variation-, γ-Al_2O_3- and acetone-dependent kinetic data (as well as UV–vis spectroscopic and GLC data) offer evidence

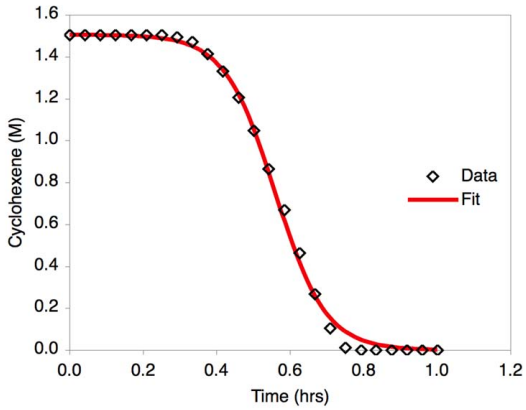

Figure 1. Sigmoidal kinetics previously observed[14] for Ir(1,5-COD)Cl/γ-Al_2O_3 to $Ir(0)_{\sim 900}$/γ-Al_2O_3 supported-nanoparticle heterogeneous catalyst formation (black diamonds) using the cyclohexene reporter reaction method (Scheme 2), plus the subsequent curve-fit to the two-step, A → B (rate constant, k_1) A + B → 2B (rate constant, k_2) mechanism for nanoparticle formation (red line).[14] The experimental error bars for the k_1 and k_2 values, are reported in Table 1, vide infra.

consistent with and strongly supportive of Ir(1,5-COD)Cl(solvent) solution-based nucleation, fast $Ir(0)_n$ nanoparticle capture by γ-Al_2O_3 and solid-oxide-based supported-nanoparticle growth from that $Ir(0)_n$/γ-Al_2O_3 with Ir(1,5-COD)Cl(solvent). This proposed mechanism is also consistent with our prior product studies,[14] namely the observation of non-aggregated 2.9 ± 0.4 nm supported $Ir(0)_n$ nanoparticles on γ-Al_2O_3. Importantly, the data also disprove a Ir(1,5-COD)Cl/γ-Al_2O_3 solid-oxide-based nucleation and growth mechanism as well as a solution-based nanoparticle growth pathway. We have also been able to make the first comparisons between the present Ir(1,5-COD)Cl/γ-Al_2O_3 to $Ir(0)_{\sim 900}$/γ-Al_2O_3 nanoparticle formation system and the previously well-studied, polyoxoanion-supported/stabilized Ir(1,5-COD)•$P_2W_{15}Nb_3O_{62}^{8-}$ to $Ir(0)_{\sim 300}$•$(P_2W_{15}Nb_3O_{62}^{8-})_n^{-8n}$ nanoparticle formation and stabilization system. Intriguingly, that first-of-its kind comparison reveals that both systems exhibit a $Ir(1,5\text{-COD})^+$ dissociative, solution-based mechanism of nanoparticle catalyst formation. Overall, the results presented herein support the global hypothesis underlying the present work, namely that quantitative kinetic and mechanistic studies, of the formation of well-defined supported-nanoparticle

heterogeneous catalysts from supported-organometallic precatalysts such as Ir(1,5-COD)Cl/γ-Al_2O_3 while in contact with solution, will yield insights into this potentially important, but to-date relatively little[14,17,26-29] investigated, alternative method of heterogeneous catalyst synthesis.

Results and Discussion

Demonstration of Highly Solvent-Dependent Nucleation and Growth Kinetics Starting from Ir(1,5-COD)Cl/γ-Al_2O_3. To start, four solvents were surveyed including our standard solvent for nanoparticle formation, acetone,[14] to see how such solvent changes would affect the observed supported-nanoparticle heterogeneous catalyst formation kinetics. Solution-based, "homogeneous" nanoparticle nucleation and growth pathways are expected to be especially sensitive to solvent coordination/ligation ability.

Table 1. Kinetic Data for the Formation of $Ir(0)_n$/γ-Al_2O_3 from Ir(1,5-COD)Cl/γ-Al_2O_3 in the Four Solvents Surveyed

Solvent	k_{1obs} (h^{-1}) [a]	k_{2obs} (h^{-1} M^{-1}) [a,b]
acetone	$1.5(1.1) \times 10^{-3}$	$1.6(2) \times 10^{4}$
propylene carbonate	$2.2(8) \times 10^{-4}$	$2.1(2) \times 10^{3}$
CH_2Cl_2	$5(4) \times 10^{-7}$	$2.4(2) \times 10^{3}$
cyclohexane	$8(6) \times 10^{-5}$	$2.2(5) \times 10^{2}$

[a] Each entry is the average (and standard deviation) of at least three separate supported-nanoparticle heterogeneous catalyst formation reactions under otherwise identical conditions. Specifically, 0.05 g of the 2.0 wt% Ir(1,5-COD)Cl/γ-Al_2O_3 precatalyst was suspended in 2.5 mL solvent, 0.5 mL cyclohexene and reduced under 40 psig of H_2 while being stirred at 600 rpm. [b] The k_{2obs} values were corrected by the mathematically required stoichiometry factor of ~1700 as detailed elsewhere.[30] That stoichiometry factor simply reflects the 1700:1 (Ir(1,5-COD)Cl/γ-Al_2O_3:cyclohexene) ratio employed in the reporter reaction, Scheme 2.[14]

The solvents chosen were based primarily on our prior $Ir(0)_n$ nanoparticle formation and stabilization studies,[33,34b] as well as their anticipated ability to coordinate (or not) to the supported Ir(1,5-COD)Cl moiety to yield dissociated Ir(1,5-COD)Cl(solvent). Table 1 summarizes the results of the kinetic experiments in the four solvents (the kinetic curves,

plus their fits to the two-step mechanism, are provided in the Supporting Information). The data demonstrate rather clearly that the more coordinating solvent acetone exhibits facile nucleation and growth kinetics, while more weakly coordinating solvents such as propylene carbonate, CH_2Cl_2 and cyclohexane have much slower nucleation (k_{1obs}) and autocatalytic surface-growth (k_{2obs}) kinetics. Quantitatively, k_{1obs} varies by ~3000-fold and k_{2obs} by ~70-fold over the range of the four solvents examined. In short, the solvent is exhibiting a large effect on especially the observed nucleation kinetics, data suggestive of a kinetically important, if not dominant, solution-based component in the underlying mechanism.

For what follows, we have found it best for the typical reader if we present first the proposed mechanism, the evidence for that mechanism, and finally the alternative mechanisms that have been ruled out en route to the proposed mechanism. The mechanistic work itself of course proceeded in the opposite order historically, with the alternative mechanisms being disproved over more than a year period before we arrived at the proposed mechanism that follows.

The Proposed Mechanism: Ir(1,5-COD)Cl(solvent) Solution-Based Nucleation, Fast Nanoparticle Capture by $[\gamma\text{-}Al_2O_3]_{sus}$ and Subsequent Solid-Oxide-Based Supported-Nanoparticle Growth via Ir(1,5-COD)Cl(solvent) Plus $Ir(0)_n/\gamma\text{-}Al_2O_3$. The proposed mechanism in Scheme 3 (bold) begins with a dissociative equilibrium (K_{Diss}) between Ir(1,5-COD)Cl/γ-Al_2O_3 and Ir(1,5-COD)Cl(solvent) (abbreviated $[Ir^{I}/Al_2O_3]_{sus}$ and $[Ir^{I}{*}solvent]$ in eqs 1–4, respectively). Nucleation in Scheme 3 is proposed to occur from the dissociated "homogeneous" Ir(1,5-COD)Cl(solvent) complex in solution (k_1'), followed by fast nanoparticle capture by $[\gamma\text{-}Al_2O_3]_{sus}$ (consistent with the observation of the unaggregated, 2.9 ± 0.4 nm supported $Ir(0)_n$ nanoparticles). Subsequently, "heterogeneous", solid-oxide-based $Ir(0)_n/\gamma\text{-}Al_2O_3$ nanoparticle growth is then proposed to occur between $Ir(0)_n/\gamma\text{-}Al_2O_3$ and the dissociated Ir(1,5-COD)Cl(solvent) complex.

In the associated kinetic expressions provided next (the full derivations for which are provided in the Supporting Information), the Ir(1,5-COD)Cl/γ-Al_2O_3 precatalyst and γ-Al_2O_3 (abbreviated $[Al_2O_3]_{sus}$) have necessarily been approximated as being "homogeneously suspended in solution", as indicated by the "sus" subscripts (for suspended) in Scheme 3. That is, the hypothetical "concentration" of active "Ir(1,5-COD)Cl" binding sites of the suspended $[\gamma\text{-}Al_2O_3]_{sus}$ are treated as if they increase linearly when in contact with solution (or, really, with the amount of solvent-exposed [γ-Al_2O_3] surface area). As we will see, this necessary assumption is justified ex post facto by the results obtained.

Scheme 3. The Proposed Supported-Nanoparticle Heterogeneous Catalyst Formation Mechanism (Bold) Involving Ir(1,5-COD)Cl(solvent) Solution-Based Nucleation, Fast $Ir(0)_n$ Nanoparticle Capture by $[\gamma\text{-}Al_2O_3]_{sus}$ and Subsequent Solid-Oxide-Based Nanoparticle Growth Between $Ir(0)_n/\gamma\text{-}Al_2O_3$ and Ir(1,5-COD)Cl(solvent). [a]

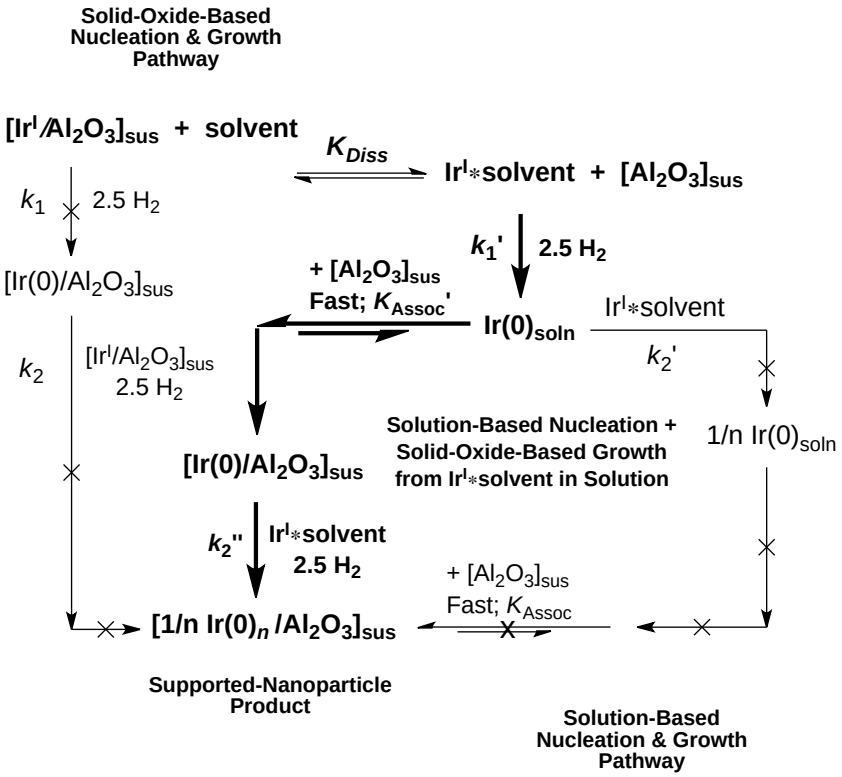

[a] Also Shown are Two Alternative Supported-Nanoparticle Heterogeneous Catalyst Formation Mechanisms that Were Disproved (Vide Infra; the Pathways Crossed Out).

In terms of evidence supporting the proposed mechanism, to start the Ir(1,5-COD)Cl/γ-Al_2O_3 to $Ir(0)_n$/γ-Al_2O_3 supported-nanoparticle heterogeneous catalyst formation kinetics are quantitatively accounted for (fit) by the two-step mechanism shown in Scheme 2 (e.g., from Figure 1), that is, by A → B and A + B → 2B (k_{obs}, Scheme 2).[14] Therefore, we can begin the needed kinetic derivations associated with Scheme 3 by writing the rate equation for the two-step mechanism, but now with solution-based nucleation from Ir(1,5-COD)Cl(solvent), fast $Ir(0)_n$ nanoparticle capture by $[\gamma\text{-}Al_2O_3]_{sus}$, and then solid-oxide-based nanoparticle growth (i.e., k_1' and k_2''), eq 1 and all as shown in Scheme 3.

$$-\frac{d[Ir^I/Al_2O_3]_{sus}}{dt} = k_1'[Ir^I * solvent]_t + k_2''[Ir^I * solvent]_t[Ir(0)_n/Al_2O_3]_{sus,t} \quad (1)$$

In eq 1 and the equations that follow, the subscript "i" represents initial concentrations, while the subscript "*t*" denotes each species as a function of time. Next, we express eq 1 in terms of the $[Ir^I/Al_2O_3]_{sus,i}$ that we experimentally begin with (i.e., what we measure out). Solving eq 2 for $[Ir^I*solvent]_t$, followed by subsequent substitution into the mass balance equation, eq 3, are straight-forward, but key, steps in the complete derivation provided in the Supporting Information.

$$K_{Diss} = \frac{[Ir^I * solvent]_t[Al_2O_3]_{sus,t}}{[Ir^I/Al_2O_3]_{sus,t}[solvent]_t} \quad (2)$$

$$[Ir^I/Al_2O_3]_{sus,i} = [Ir^I/Al_2O_3]_{sus,t} + [Ir^I * solvent]_t \quad (3)$$

Substitution of the resultant $[Ir^{I}/Al_2O_3]_{sus,t}$ equation back into eq 1 yields the relevant rate equation for Scheme 3, eq 4, where the resultant k_{1obs} and k_{2obs} rate constants are given by eqs 5 and 6, respectively.

$$-\frac{d[A/Al_2O_3]_{sus}}{dt} = k_{1obs}[Ir^{I}/Al_2O_3]_{sus,i} + k_{2obs}[Ir^{I}/Al_2O_3]_{sus,i}[Ir(0)_n/Al_2O_3]_{sus,t} \quad (4)$$

$$k_{1obs} = \frac{k_1' K_{Diss}[solvent]_t}{[Al_2O_3]_{sus,t} + K_{Diss}[solvent]_t} \quad (5)$$

$$k_{2obs} = \frac{k_2'' K_{Diss}[solvent]_t}{[Al_2O_3]_{sus,t} + K_{Diss}[solvent]_t} \quad (6)$$

The mechanism in Scheme 3 (bold), along with eqs 5 and 6, predicts that both [γ-$Al_2O_3]_{sus}$ and [solvent] will directly influence k_{1obs} and k_{2obs}, as makes sense conceptually based on the K_{Diss} equilibrium and its [γ-$Al_2O_3]_{sus}$ and [solvent] terms shown in Scheme 3.

Effects of [γ-$Al_2O_3]_{sus}$ on k_{2obs} and k_{1obs} Starting from Ir(1,5-COD)Cl/γ-Al_2O_3: Evidence Consistent with and Strongly Supportive of the Proposed Mechanism in Scheme 3. To test the predictions of the mechanism in Scheme 3, we started by varying the amount of well-stirred, suspended γ-Al_2O_3 in acetone, [γ-$Al_2O_3]_{sus}$, from 0.25 M to 0.98 M.[35] In each case the observed kinetics were sigmoidal and well-fit to the two-step mechanism, data further consistent with and supportive of the two-step nucleation and growth mechanism employed in the underlying derivation of eqs 5 and 6.

We looked first at the k_{2obs} (nanoparticle growth) vs [γ-$Al_2O_3]_{sus}$ dependence data as our prior experience as well as a a multitude of literature[36] shows that the inherent error in nucleation rate constants (i.e., k_{1obs}) are large (up to $10^{\pm 1.2}$ in even the best behaved

systems, for example[36]). Restated, our expectation was that the typical nucleation rate constant error bars would likely prohibit quantification of the k_{1obs} vs $[\gamma\text{-}Al_2O_3]_{sus}$ data, so we focused, instead, on the k_{2obs} vs $[\gamma\text{-}Al_2O_3]_{sus}$ data to start.

The extracted k_{2obs} values are plotted vs the $[\gamma\text{-}Al_2O_3]_{sus}$, Figure 2, black circles.[37] Qualitatively, k_{2obs} decreases with increasing $[\gamma\text{-}Al_2O_3]_{sus}$ as predicted by the mechanism in Scheme 3 and its associated equations, eq 6. This expected trend is due to the increased $[\gamma\text{-}Al_2O_3]_{sus}$ shifting the K_{Diss} equilibrium in Scheme 3 to the left, resulting in less Ir(1,5-COD)Cl(solvent) in solution, with a subsequent concomitant decrease in k_{2obs}. Significantly, we were also able to confirm, via UV–vis spectroscopy, that there is in fact less Ir(1,5-COD)Cl(solvent) in solution with increasing $[\gamma\text{-}Al_2O_3]_{sus}$, data which is nicely accounted for by the K_{Diss} equilibrium in Scheme 3 (see the Supporting Information, Figure S2). In short, the combined kinetic and spectroscopic results are consistent with Ir(1,5-COD)Cl(solvent) being a kinetically dominant intermediate en route to $Ir(0)_n/\gamma\text{-}Al_2O_3$.

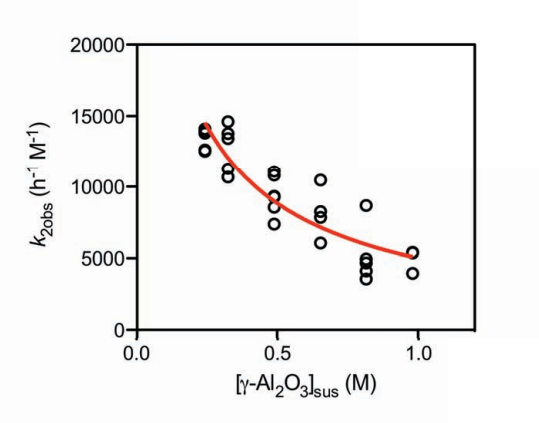

Figure 2. Dependence of the k_{2obs} rate constant on $[\gamma\text{-}Al_2O_3]_{sus}$, black circles. The red line is the weighted nonlinear least-squares fit to equation 6 derived for the proposed mechanism (the bold pathway) in Scheme 3. The resultant K_{Diss} and k_2' values are 1.3(6) $\times 10^{-2}$ and 4(1) $\times 10^4$ h^{-1} M^{-1}, respectively.

Quantitatively, using weighted nonlinear least-squares analysis (as detailed in the Experimental Section), eq 6 was found to provide a good fit to the $[\gamma\text{-}Al_2O_3]_{sus}$ dependent k_{2obs} data, Figure 2 (red line), yielding values of $k_2'' = 4(1) \times 10^4$ h^{-1} M^{-1} and $K_{Diss} = 1.3(6) \times 10^{-2}$. In addition, independent verification of the K_{Diss} equilibrium was obtained in a control experiment using GLC. This was done by filtering off the solution from the (equilibrated) Ir(1,5-COD)Cl/γ-Al_2O_3 plus acetone solution, then hydrogenating the Ir(1,5-COD)Cl(solvent) complex and quantifying the amount of cyclooctane released in solution (i.e., as a marker for the amount of Ir(1,5-COD)Cl(solvent) that was present in solution). Pleasingly, the independently determined K_{Diss}, equilibrium value (via GLC) was found to be $K_{Diss} = 1.1 \times 10^{-2}$, the same within experimental error as the k_{2obs} vs $[\gamma\text{-}Al_2O_3]_{sus}$ fit-determined K_{Diss} value, $K_{Diss} = 1.3(6) \times 10^{-2}$. The quantitative agreement between the kinetic- vs GLC-obtained K_{Diss} values provides very strong if not compelling support for (i) the mechanism in Scheme 3, (ii) the assumptions necessary in the derivation of the associated kinetic equations (e.g., that the γ-Al_2O_3 behaves as if it where "homogeneously suspended" with a "concentration", $[\gamma\text{-}Al_2O_3]_{sus}$, of Ir(1,5-COD)Cl binding sites), and (iii) also for the kinetic and GLC experiments, analyses and resultant data. The results yield the first experimental determination of such a K_{Diss}[30] equilibrium for supported-nanoparticle heterogeneous catalyst formation in contact with solution.

Returning to the observed nucleation rate constant data, we were encouraged to see if the extracted k_{1obs} values might not at least show the expected trend vs the $[\gamma\text{-}Al_2O_3]_{sus}$, and despite the always observed large errors in such nucleation rate constants.[36] The resultant k_{1obs} vs the $[\gamma\text{-}Al_2O_3]_{sus}$ plot is shown in Figure 3, black circles.[37] Again pleasingly and fully consistent with eq 5 derived from Scheme 3, k_{1obs} does indeed show an $[\gamma\text{-}Al_2O_3]_{sus}$ dependency in the "correct direction". That is, *qualitatively*, k_{1obs} decreases with increasing $[\gamma\text{-}Al_2O_3]_{sus}$ as expected if nucleation is occurring from the

dissociated, Ir(1,5-COD)Cl(solvent) complex in solution, Scheme 3 and its K_{Diss} equilibrium. There is the expected large scatter[36] in k_{1obs} for the 28 experimental data points plotted in Figure 3; not unexpectedly, weighted nonlinear least-squares curve-fitting using eq 5 did not converge on k_1' and K_{Diss} values. *However*, constraining the K_{Diss} to its known value of 1.3×10^{-2}, eq 5 was able to at least qualitatively account for the rough shape of the k_{1obs} vs $[\gamma\text{-}Al_2O_3]_{sus}$ data, Figure 3 (red line), resulting in a value of $k_1' = 2.6(4) \times 10^{-2}$ h^{-1}. While the k_{1obs} vs $[\gamma\text{-}Al_2O_3]_{sus}$ data are noisy as expected,[36] the results are still consistent with the proposed mechanism in Scheme 3.

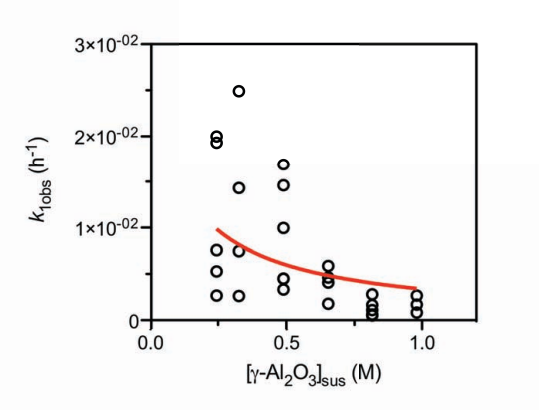

Figure 3. Dependence of the k_{1obs} rate constant on $[\gamma\text{-}Al_2O_3]_{sus}$, black circles. The red line is the weighted nonlinear least-squares fit to equation 5 obtained by constraining the K_{Diss} equilibrium to 1.3×10^{-2}, yielding a value for $k_1' = 2.6(4) \times 10^{-2}$ h^{-1}.

Overall, the k_{2obs} and k_{1obs} vs $[\gamma\text{-}Al_2O_3]_{sus}$ kinetic data, the independent verification of the K_{Diss} equilibrium via GLC, and the decrease in Ir(1,5-COD)Cl(solvent) with increasing $[\gamma\text{-}Al_2O_3]_{sus}$ (monitored via UV–vis spectroscopy) are all highly consistent with and strongly supportive of the mechanism in Scheme 3: Ir(1,5-COD)Cl(solvent) dissociation followed by solution-based nucleation, fast $Ir(0)_n$ nanoparticle capture by $[\gamma\text{-}Al_2O_3]_{sus}$ and then subsequent nanoparticle growth from the solid-oxide-supported $Ir(0)_n/\gamma\text{-}Al_2O_3$ plus the dissociated Ir(1,5-COD)Cl(solvent) complex.

Effects of [Acetone] on k_{2obs} and k_{1obs} Starting from Ir(1,5-COD)Cl/γ-Al_2O_3: Further Evidence Consistent with the Proposed Mechanism in Scheme 3. Equations 5 and 6 derived from the mechanism in Scheme 3 predict that both k_{2obs} and k_{1obs} should also depend on the "solvent" concentration. Experimentally, under our "standard conditions" acetone is the (neat) solvent making it impossible to change the concentration of acetone to probe its exact role in the observed nucleation and growth kinetics (i.e., and so long as one is in neat acetone). This led us to explore a cyclohexane-plus-acetone mixed solvent system, one that turned out to have nearly ideal experimental properties.[38,39] Specifically, we varied the acetone concentration from 0.5 to 2.7 M, while keeping the total volume of cyclohexane-plus-acetone constant at 2.5 mL. In each case, the supported-nanoparticle heterogeneous catalyst formation kinetics are sigmoidal and were again well-fit by the two-step mechanism. The extracted k_{2obs} and then also k_{1obs} vs [acetone] values are plotted in Figures 4 and 5, black circles.

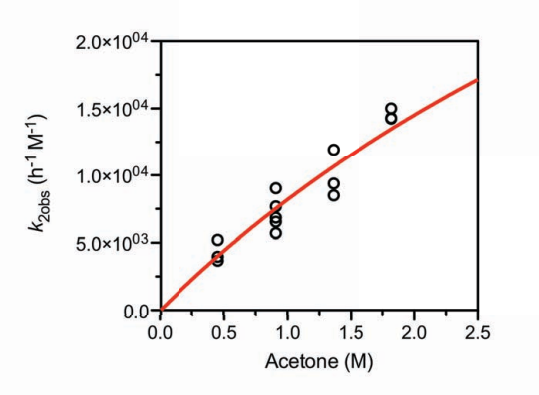

Figure 4. Dependence of the k_{2obs} rate constant on [acetone], black circles. The red line is a weighted nonlinear least-squares fit to the slightly modified forms of eqs 6 (a form of eq 6 which accounts for the formation of ½ $[Ir(1,5\text{-}COD)Cl]_2$ under the mixed-solvent conditions). The resultant K_{Diss}' and k_2''' values are 3(2) × 10^{-2} and 6(5) × 10^4 h^{-1} M^{-1}, respectively.

Qualitatively, both k_{2obs} and k_{1obs} show the predicted [acetone] dependence of eqs 6 and 5, respectively, over the range studied.[40] Conceptually, increasing the acetone

concentration shifts the K_{Diss} equilibrium to the right, resulting in more, what turns out to be detectable $[Ir(1,5\text{-}COD)Cl]_2$, in solution (rather than Ir(1,5-COD)Cl(solvent)) under the mixed solvent conditions (see Figure S3) along with a concomitant increase in k_{2obs} and k_{1obs}. Significantly, we were able to confirm by UV–vis spectroscopy that the concentration of $[Ir(1,5\text{-}COD)Cl]_2$ in solution increases with increasing [acetone]. We were also able to obtain an independent verification of the K_{Diss} equilibrium in cyclohexane/acetone (vide infra), direct spectroscopic evidence consistent with $[Ir(1,5\text{-}COD)Cl]_2$ being a kinetically dominant intermediate en route to $Ir(0)_n/\gamma\text{-}Al_2O_3$ (as detailed further in the Supporting Information).

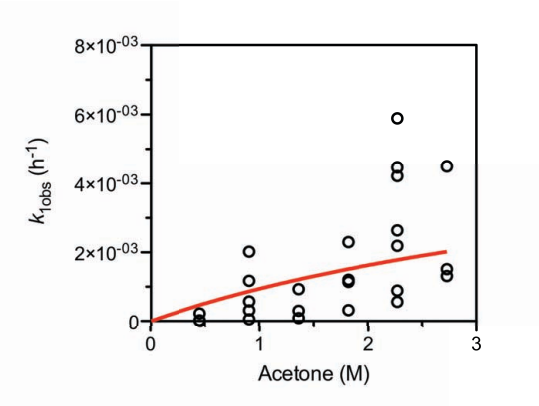

Figure 5. Dependence of the k_{1obs} rate constant on [acetone], black circles. The red line is a weighted nonlinear least-squares fit to the slightly modified form of eqs 5 (a form of eq 5 which accounts for the formation of ½ $[Ir(1,5\text{-}COD)Cl]_2$ under the mixed-solvent conditions). The value of K_{Diss}'' was held constant at 0.03 and k_1'' was found to be 6(1) × 10^{-3} h^{-1}.

Quantitatively, we again first considered the k_{2obs} vs $[\gamma\text{-}Al_2O_3]_{sus}$ data (Figure 4, black circles) due to the again anticipated large error in the k_{1obs} nucleation rate constants.[36] Since the $[Ir(1,5\text{-}COD)Cl]_2$ dimer forms in solution, slightly modified forms of eqs 5 and 6 needed to be, and were, derived (see eqs S36–S41 in the Supporting Information for the details of the kinetic treatment and resultant equations under the mixed, cyclohexane plus acetone solvent conditions). The relevant rate and equilibrium constants are now

designated k_1'', k_2''' and K_{Diss}', due to their slight differences from the rate constants in Scheme 3, because of the presence of $[Ir(1,5\text{-COD})Cl]_2$. Weighted nonlinear least-squares fitting of the k_{2obs} vs [acetone] data, using eq S41 (which has the same general form as eq 6), yielded values of k_2''' = 6(5) × 10^4 h^{-1} M^{-1} and K_{Diss}' = 3(2) × 10^{-2} (Figure 4, red line). We were again able to independently verify the K_{Diss}' equilibrium, this time by measuring the $[Ir(1,5\text{-COD})Cl]_2$ in solution via UV–vis spectroscopy (Figure S3 of the Supporting Information). The spectroscopically determined value of K_{Diss}' was found to be 2.8(6) × 10^{-2}, identical within experimental error to the fit-determined K_{Diss}' value of 3(2) × 10^{-2}. The independent confirmation of the K_{Diss}' equilibrium is once again consistent with and fully supportive of the mechanism shown in Scheme 3. It also provides very strong support for the both the kinetic and UV–vis experiments and resultant data as well as the equations and methods used in their quantitative analysis.

Returning back to the k_{1obs} vs [acetone] data (Figure 5, black circles), weighted non-linear least squares using eq S40 (which has the same general form as eq 5) again did not converge to unique k_1'' and K_{Diss}' values due to the expected and observed fluctuation in the k_{1obs} nucleation rate constants.[36] However, by constraining K_{Diss}' to its known value of 3 × 10^{-2}, eq 6 could be used to account for at least the general shape of the k_{1obs} vs [acetone] data, Figure 5 (red line). An estimate of k_1'' = 6(1) × 10^{-3} h^{-1} resulted.

In summary of the [acetone] dependence kinetic and spectroscopic data, the k_{2obs} and k_{1obs} vs [acetone] data, as well as the increase in $[Ir(1,5\text{-COD})Cl]_2$ in solution (monitored via UV–vis spectroscopy) with increasing acetone plus the independent confirmation of K_{Diss}', are all consistent with and supportive of the mechanism proposed in Scheme 3 (in bold).

Disproof of the "Heterogeneous" (i.e., All Solid-Oxide-Based) Nucleation (k_1) and Growth (k_2) and the "Homogeneous" (i.e., All Solution-based) Growth Pathway (k_2'). While all of the kinetic, nanoparticle product[14] and spectroscopic or GLC data are consistent with and strongly supportive of the mechanism shown back in Scheme 3, as noted earlier we actually arrived at the mechanism in Scheme 3 by first (i) disproving the all solid-oxide-based (k_1 and k_2) nucleation and growth pathway, and then (ii) disproving the all solution-based (k_2') growth pathway as detailed next.

The essence of those disproofs proceeded as follows. First we considered the all solid-oxide-based, "heterogeneous" nucleation and growth pathway with the indicated rate constants, k_1 and k_2. The relevant rate equation (the full derivation of which is given in the Supporting Information) is identical to eq 4 except k_{1obs} and k_{2obs} are now given by eqs 7 and 8 respectively.

$$k_{1obs} = \frac{k_1[Al_2O_3]_{sus,t}}{[Al_2O_3]_{sus,t} + K_{Diss}[solvent]_t} \quad (7)$$

$$k_{2obs} = \frac{k_2[Al_2O_3]_{sus,t}}{[Al_2O_3]_{sus,t} + K_{Diss}[solvent]_t} \quad (8)$$

Inspection of eqs 7 and 8 reveals that k_{1obs} and k_{2obs} should increase with increasing $[\gamma\text{-}Al_2O_3]_{sus}$ if the all solid-oxide based, "heterogeneous" mechanism were correct. Of course and in fact, k_{2obs} and k_{1obs} decrease with increasing $[\gamma\text{-}Al_2O_3]_{sus}$ (Figures 2 and 3 respectively), effectively disproving the "heterogeneous" pathway. In addition, eqs 7 and 8 for the "heterogeneous" pathway predict that k_{1obs} and k_{2obs} will decrease with increasing [acetone], while Figures 4 and 5 reveal the opposite dependence: k_{1obs} and k_{2obs} increase with increasing [acetone]. In short, the $[\gamma\text{-}Al_2O_3]_{sus}$- and [acetone]-

dependent kinetic data disprove the all solid-oxide-based, “heterogeneous” nucleation and growth mechanism.

Second, en route to the proposed mechanism in Scheme 3, we consider the case of an all solution-based, “homogeneous” nucleation and growth mechanism (k_1’ and k_2’). The kinetic and spectroscopic data (Supporting Information) presented so far are consistent with the solution-based nucleation pathway k_1’. However, the overall reaction stoichiometry (Ir(1,5-COD)Cl/γ-Al_2O_3 to $Ir(0)_n$/γ-Al_2O_3) is inconsistent with a solely, $Ir(0)_{n,soln}$ solution-based nanoparticle growth mechanism; the “weakly ligated/labile ligand” $Ir(0)_n$ nanoparticles are known to aggregate,[14,20] and therefore, typically give a broader size distribution then the ±14% that we experimentally observe.[14] It is thus necessary to introduce a fast, K_{Assoc} equilibrium, $[\gamma\text{-}Al_2O_3]_{sus}$ capture step in order to account for the observed, γ-Al_2O_3-suported $Ir(0)_{\sim 900}$ product. Such an assumption requires either (i) a size dependent $Ir(0)_n$ K_{Assoc} equilibrium with $[\gamma\text{-}Al_2O_3]_{sus}$, or (ii) k_2’K_{Assoc} to be fast relative to k_2’’K_{Assoc}’. The relevant rate equation is identical to that of eq 4 (the full derivation of which is given in the Supporting Information), k_{1obs} is equivalent to eq 5, and k_{2obs} is now given by eq 9 for the putative “all homogeneous” mechanism.

$$k_{2obs} = \frac{k_2' K_{Diss}[solvent]_t}{K_{Assoc}[Al_2O_3]^2_{sus,t} + K_{Diss}K_{Assoc}[Al_2O_3]_{sus,t}[solvent]_t} \qquad (9)$$

Inspection of eq 9 reveals that k_{2obs} is proportional to an inverse-squared term in $[\gamma\text{-}Al_2O_3]_{sus}$, that is, to $1/[\gamma\text{-}Al_2O_3]_{sus}^2$. Attempts to fit the k_{2obs} vs $[\gamma\text{-}Al_2O_3]_{sus}$ data using eq 9 and by constraining K_{Diss} to its experimentally established value of 1.3×10^{-2} (and thus fitting for only two parameters) did *not* converge, arguing against and effectively disproving the solution-based nanoparticle growth pathway. In addition, simulations

show that a $1/[\gamma\text{-}Al_2O_3]_{sus}^2$ dependence provides too-steep of a curve to fit the data, data that we know is tightly fit by eq 6 corresponding to the proposed mechanism, Figure 2.

In short, the $[\gamma\text{-}Al_2O_3]_{sus}$- and [acetone]-dependent k_{1obs} and k_{2obs} data (i) disprove the "heterogeneous" (i.e., all solid-oxide-based) nucleation and growth pathway (k_1 and k_2), while the k_{2obs} vs $[\gamma\text{-}Al_2O_3]_{sus}$ data (ii) disprove the "homogeneous" (i.e., all solution-based) $Ir(0)_n$ nanoparticle growth pathway (k_2').

Caveats: the Apparent Nature of the Rate and Equilibrium Constants, A Possible Role of Ir_nH_m Species, and Comment Regarding Diffusional Processes. An important part of the present work is that it provides the first (semi)-quantitative, *but apparent*, values for the parameters k_1', k_1'', k_2'', k_2''' (K_{Diss} and K_{Diss}' were independently verified). That is, we wish to emphasize that all these parameters should be regarded as apparent rate constants in a rigorous sense. Uncertainty arises in the precise, completely elementary/correct values for the rate constants determined herein as a result of primarily three sources: (i) the pseudo-order $[H_2]$ treatment[4] introduced from the cyclohexene reporter reaction kinetic monitoring method (see the Supporting Information for more details regarding the pseudo-order $[H_2]$ treatment); (ii) the treatment of $\gamma\text{-}Al_2O_3$ as a uniform, homogeneously suspended species with an effective "concentration"; and (iii) the inherent experimental[36] error in the nucleation and growth kinetic data. Hence, anyone using these first-of-their-kind rate "constants" needs to be aware of, and take into account, these uncertainties and the apparent nature of these parameters.

One additional caveat meriting mention is that where we write "$Ir(0)_n/\gamma\text{-}Al_2O_3$" (consistent with this being the demonstrated product[14]), it is possible that $Ir_nH_m/\gamma\text{-}Al_2O_3$ (i.e., hydride species) are what are actually the kinetically dominant form of Ir during the nucleation and early growth stages.[30,41] Noteworthy is that this same caveat, regarding the possible, but at present unsubstantiated, role of polymetallic hydrides in nanoparticle nucleation reactions, also exists in the extant mechanistic studies of nanoparticle

formation in solution (see p 359 elsewhere[9]). Smaller, polymetallic metal hydrides as one possible key intermediate in nanoparticle nucleation and growth is a topic meriting careful experimental study, in our opinion, a topic we are currently addressing.

The careful reader will also have noted that we have not addressed any issues associated with the more complex nature of the γ-Al_2O_3 support, including its ca. ~100 μm pellet and ca. 5.8 nm pore size (manufacturers specifications), in relation to diffusion. We can, however, rule out diffusion-limited processes since the kinetic data can be fit to the chemical-reaction-rate limited, two-step mechanism. Our kinetic data require that any diffusional processes be fast relative to the A → B and A + B → 2B chemical-reaction rate-determining steps that we measure. An additional point relevant to diffusion, pointed out by an insightful referee (that we thank), is that 2.9 nm $Ir(0)_{\sim 900}$ nanoparticles likely will not readily diffuse through the 5.8 nm γ-Al_2O_3 pores, yet the final $Ir(0)_{\sim 900}$ nanoparticles are well dispersed throughout the γ-Al_2O_3 (see the TEM images in Scheme 1). We agree, and note that these observations support the proposed mechanism in Scheme 3 in which smaller, $Ir(0)_n$ nanoparticles are captured by the γ-Al_2O_3.[42,43] Those particles then grow via the chemical-reaction limited autocatalytic surface growth step (i.e., A + B → 2B) from Ir(1,5-COD)Cl(solvent) in solution. In other words, all of our experimental evidence indicates that the overall supported-nanoparticle heterogeneous catalyst formation reaction (in contact with solution) is chemical-reaction-rate limited and not diffusion limited.

Desirable, future studies include, then: (i) a precise determination of the concentration of "Ir(1,5-COD)Cl" binding sites on the γ-Al_2O_3; (ii) direct observation and kinetic measurements of the Ir(1,5-COD)Cl/γ-Al_2O_3 to $Ir(0)_n$/γ-Al_2O_3 supported-nanoparticle heterogeneous catalyst formation under in situ, or better under operating (i.e., "operando"), conditions; (iii) direct evidence for or against possible "Ir_nH_m" intermediates, and (iv) independent direct measurement and verification or refinement of the key,

apparent parameters k_1', k_1'', k_2''and k_2'''. Despite these needed additional studies, the present study is still the first of its kind, and as such provides both the specific parameters to be verified or updated as well as the general mechanistic scheme, Scheme 3, around which one can now design additional measurements.

A Comparison of Solid-Oxide-Supported Ir(1,5-COD)Cl/γ-Al_2O_3 to Ir(0)$_{\sim 900}$/γ-Al_2O_3 Nanoparticle Formation to Polyoxoanion-Supported and Stabilized Ir(1,5-COD)•$P_2W_{15}Nb_3O_{62}^{8-}$ to Ir(0)$_{\sim 300}$•$(P_2W_{15}Nb_3O_{62}^{8-})_n^{-8n}$ Nanoparticle Formation in Solution. The Ir(1,5-COD)Cl/γ-Al_2O_3 to Ir(0)$_{\sim 900}$/γ-Al_2O_3 nanoparticle formation system allows an interesting, first-of-its-kind, comparison to the kinetically and mechanistically well studied [Ir(1,5-COD)•$P_2W_{15}Nb_3O_{62}]^{8-}$ to Ir(0)$_{\sim 300}$•$(P_2W_{15}Nb_3O_{62}^{8-})_n^{-8n}$ nanoparticle formation system in solution,[4,45,34] Scheme 4, top.

Scheme 4. The Kinetically and Mechanistically Well Studied Ir(1,5-COD)•$P_2W_{15}Nb_3O_{62}]^{8-}$ to Ir(0)$_{\sim 300}$•$(P_2W_{15}Nb_3O_{62}^{8-})_n^{-8n}$, Soluble, Nanoparticle Formation System (Top) and its Ir(1,5-COD)$^+$ Based, Dissociative Equilibrium En Route to Ir(0)$_{\sim 300}$•$(P_2W_{15}Nb_3O_{62}^{8-})_n^{-8n}$ Nanoparticle Formation.

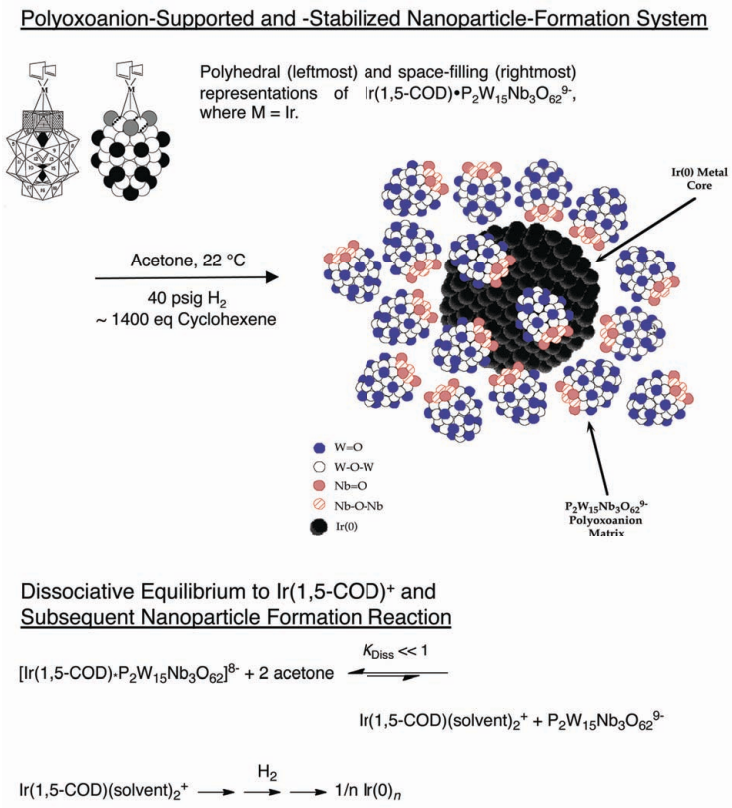

Comparison of the Ir(1,5-COD)Cl/γ-Al_2O_3 to $Ir(0)_{\sim 900}$/γ-Al_2O_3 system herein, Scheme 1, to the polyoxoanion supported and stabilized system in Scheme 4, reveals two striking similarities between the supported- and solution-based systems, specifically the involvement in both systems of: (i) a dissociated, solution-based $Ir(1,5\text{-}COD)^+$ moiety, and (ii) a solution-based nucleation mechanism under H_2 to $Ir(0)_n$. In the case of the polyoxoanion-supported system, evidence for a dissociative equilibrium to $Ir(1,5\text{-}COD)(solvent)_2^+$ was first obtained in 1994 starting from the $[Ir(1,5\text{-}COD)\bullet P_2W_{15}Nb_3O_{62}]^{8-}$ precatalyst and en route to soluble, polyoxoanion stabilized ("supported") $Ir(0)_{\sim 300}\bullet(P_2W_{15}Nb_3O_{62}^{8-})_n^{-8n}$, Scheme 4, bottom.[34b] Key evidence at the time for a $[Ir(1,5\text{-}COD)\bullet P_2W_{15}Nb_3O_{62}]^{8-}$ to $Ir(1,5\text{-}COD)(solvent)_2^+$ dissociative equilibrium included: (i) a solvent dependency,[33,34b] similar to that in Table 1 (i.e., facile kinetics were observed in the coordinating solvent acetone, but were much slower in the less coordinating solvent CH_2Cl_2), (ii) demonstration that small amounts of added $P_2W_{15}Nb_3O_{62}^{9-}$ dramatically inhibit the nanoparticle formation kinetics[4,44] and the (iii) demonstration that trace amounts of $Ir(1,5\text{-}COD)(solvent)_2^+$ significantly accelerated the nanoparticle formation kinetics (especially reducing the nucleation time),[4,44] direct kinetic evidence for the involvement of $Ir(1,5\text{-}COD)(solvent)_2^+$ in the nucleation and growth processes. Overall, the solvent, $P_2W_{15}Nb_3O_{62}^{9-}$ and $Ir(1,5\text{-}COD)(solvent)_2^+$ dependent kinetic data are strongly supportive of the K_{Diss} equilibrium shown in Scheme 4, a key step in the mechanism that parallels the kinetically dominant, Ir(1,5-COD)Cl(solvent) and K_{Diss} pathway back in Scheme 3.

In summary, this first comparison between a solid- vs polyoxoanion-soluble oxide-supported nanoparticle formation systems: (i) reveals striking similarities in their mechanisms, specifically that both involve (a) dissociated, *solution-based* $Ir(1,5\text{-}COD)^+$ (or Ir(1,5-COD)Cl) moieties, and (b) *solution nucleation* under H_2 to $Ir(0)_n$; (ii) reveal the value of having the soluble $Ir(0)_{\sim 300}\bullet(P_2W_{15}Nb_3O_{62}^{8-})_n^{-8n}$ nanoparticle formation system

and its kinetics already in hand for such qualitative comparisons, and (iii) satisfies criterion number seven of our previous definition[14,32] of the key attributes of a prototype, solid-oxide supported nanoparticle formation system in contact with solution, namely that such a comparison be possible and made. The comparison of the soluble, polyoxoanion-based oxide and solid-oxide systems also (iv) provides the best test to date of the long-standing hypothesis that custom-made polyoxoanions can serve as "soluble metal-oxide analogues",[4,45,34] and (v) provides the strongest evidence to date in support of the "soluble metal-oxide analogues" hypothesis.

Conclusions

Herein, we have continued to pursue the global hypothesis that quantitative kinetic and mechanistic studies of supported-nanoparticle heterogeneous catalyst formation, in contact with solution, will allow exploration of an important, but to-date little investigated, subarea of heterogeneous catalyst synthesis—specifically, the transformation of solid-supported organometallics into supported-nanoparticle catalysts while in contact with solution. The solvent variation-, γ-Al_2O_3-, and acetone-dependent kinetic data (as well as GLC and UV–vis spectroscopic data) are all consistent with and strongly supportive of nucleation occurring from the dissociated Ir(1,5-COD)Cl(solvent) complex in solution, fast $Ir(0)_n$ nanoparticle capture by γ-Al_2O_3, and subsequent solid-oxide-supported nanoparticle growth between $Ir(0)_n$/γ-Al_2O_3 and Ir(1,5-COD)Cl(solvent). The kinetic data disprove the Ir(1,5-COD)Cl/γ-Al_2O_3 "heterogeneous" (i.e., all solid-oxide-based) nucleation and growth mechanism (i.e., the k_1 and k_2 pathways back in Scheme 3) as well any "homogeneous" (i.e., all solution-based) nanoparticle growth pathway involving Ir(1,5-COD)Cl(solvent) (i.e., such as k_2', Scheme 3).

We expect the finding of solution-based nucleation to prove more general for (i) other coordinatively saturated (e.g., d^8 square planar) supported-organometallic species, that

is, supported complexes that don't have facile reduction mechanisms to $M(0)_n$ under H_2 (i.e., and while still on the support), and for (ii) other high-valent supported organometallics and metal salts (e.g., Ir(III), Rh(III), Au(III), and so on) that may not also have facile H_2 activation[45] mechanisms to $M(0)_n$ when supported. The kinetic studies herein have also allowed the first experimental estimations of the associated k_1', k_1'', k_2'', k_2''' apparent rate constants and the K_{Diss} and K_{Diss}' equilibrium constants defined in Scheme 3. Comparative studies of the Ir(1,5-COD)Cl/γ-Al_2O_3 to $Ir(0)_{\sim 900}$/γ-Al_2O_3 nanoparticle formation system in contact with solution to the kinetically and mechanistically well-studied Ir(1,5-COD)•$P_2W_{15}Nb_3O_{62}^{8-}$ to $Ir(0)_{\sim 300}$•$(P_2W_{15}Nb_3O_{62}^{8-})_n^{-8n}$ solution nanoparticle formation system, revealed closely similar Ir(1,5-COD)$^+$ (and Ir(1,5-COD)Cl) dissociation, solution-based nucleation mechanisms.[4,34b] That comparison also provided the first compelling evidence that suitable, custom-made polyoxoanions can function as soluble models/analogues of solid-oxide-supported heterogeneous catalysts ("soluble heterogeneous catalyst analogues").[46]

Looking forward, it seems reasonable to expect that supported-nanoparticle heterogeneous catalyst formation in contact with solution may yield a more direct avenue for transferring both the synthetic and mechanistic insights, which have resulted from the modern revolution in nanoparticle science in solution to supported-nanoparticle heterogeneous catalysts and their subsequent catalysis. Our own, additional studies in this direction are continuing and will be reported in due course.

Experimental Section

Materials. All solvents and compounds used were stored in the drybox prior to use. Used as received were the following (all of which came sealed under N_2): acetone (Burdick & Jackson, water content <0.5%), anhydrous cyclohexane (Aldrich, 99.5%), anhydrous CH_2Cl_2 (Aldrich, ≥99.8%) anhydrous propylene carbonate (Aldrich, 99.7%)

and $[Ir(1,5\text{-}COD)Cl]_2$ (STREM, 99%). Cyclohexene (Aldrich, 99%) was freshly distilled over Na metal and under argon or purified via a MicroSolv solvent purification system (Innovative Technology) using an activated γ-Al_2O_3 column under N_2. Ethyl acetate (Aldrich, ≥ 99.8%, < 0.05% H_2O) was degassed prior to use in the drybox. Acidic activated γ-Al_2O_3 (Aldrich), with a surface area of 155 m^2/g was dried at 160 °C in air for 24 hours (the average relative humidity in Fort Collins, CO ranges from ~38% to ~72% over the course of the year[47,48,49]). H_2 gas purchased from Airgas (> 99.5% purity) was passed through O_2- and H_2O-scavenging traps (Trigon Technologies) before use.

Analytical Instrumentation and Procedures. Unless otherwise reported all reaction solutions were prepared under O_2- and moisture-free conditions in a Vacuum Atmospheres N_2-filled drybox. The O_2 level (always ≤5 ppm; typically ≤1 ppm) was continuously monitored by a Vacuum Atmospheres O_2 sensor. GLC was performed using a Hewlett-Packard 5890 Series II chromatograph, along with a flame-ionization detector and equipped with a Supelco SPB-1 (Aldrich, 30m x 0.25mm x 0.25µm) fused silica column. The GLC parameters were as follows: initial oven temperature, 50 ºC; initial time, 3.0 minutes; rate, 10 ºC/min; final temperature, 160 ºC; injector temperature, 180 ºC; detector temperature, 200 ºC; and injection volume, 2 µL. UV–vis spectroscopy experiments were run on a Hewlett Packard 8452A diode array spectrophotometer and the data were analyzed via Hewlett Packard's UV–vis ChemStation software.

Hydrogenation Apparatus and Data Handling. Hydrogenation experiments for monitoring the H_2 reduction of $Ir(1,5\text{-}COD)Cl/\gamma\text{-}Al_2O_3$ to $Ir(0)_n/\gamma\text{-}Al_2O_3$ were carried out in a previously described apparatus[4-8] which continuously monitors the H_2 pressure loss. Briefly, the apparatus consists of a Fisher-Porter (FP) bottle modified with Swagelok TFE-sealed Quick-Connects to both a H_2 line and an Omega PX621 pressure transducer. The pressure transducer is interfaced to a PC through an Omega D1131 5V

A/D converter with a RS-232 connection. Reactions were run at a constant temperature by immersing the FP bottle in a 500 mL jacketed reaction flask containing dimethyl silicon fluid (Thomas Scientific), the temperature of which was regulated by a thermostatted recirculating water bath (VWR). Pressure uptake data were collected using LabView 7.1. The hydrogen uptake curves were then converted to cyclohexene (M) curves using the previously established 1:1 H_2/cyclohexene stoichiometry.[4,34] The data were also corrected for the acetone solvent vapor pressure using the previously established protocol.[45] Specifically, one can either measure the acetone vapor pressure independently and subtract that curve (point-by-point) from the raw H_2 uptake data during the cyclohexene reporter reaction, or one can simply back extrapolate the experimental vapor pressure rise (seen in the induction period of the reaction). Both methods yield the same k_1 and k_2 rate constants within ±15%.[45] The resultant cyclohexene loss kinetic curves were fit to the two-step analytic equation[4] for nucleation and autocatalytic surface growth of nanoparticle formation, A → B, rate constant k_1, plus A + B → 2B, rate constant k_2 (see Scheme 2) using nonlinear least-squares fitting in Origin 7.0.

The k_{1obs} and k_{2obs} vs $[\gamma\text{-}Al_2O_3]_{sus}$ and [acetone] curves were fit using weighted nonlinear least-squares analysis in GraphPad Prism 5.0. Relative weighting (i.e., $1/Y^2$) was used as the average absolute distance, between the curve and the data points, is larger when Y is larger. Use of $1/Y^2$ weighted nonlinear least-squares analysis minimizes the sum-of-squares of eq 10.[50,51] For the $[\gamma\text{-}Al_2O_3]_{sus}$ dependent k_{1obs} and k_{2obs} curve-fitting, [acetone] was taken to be constant at a value of 11.37 M. For the [acetone] dependent fitting, $[\gamma\text{-}Al_2O_3]_{sus}$ was taken to be constant at a value of 0.163 M.

$$\sum \frac{1}{Y^2}(Y_{Data} - Y_{Curve})^2 \qquad (10)$$

Precatalyst Preparation. All of the precatalysts were prepared in a drybox using pre-selected $[Ir(1,5\text{-}COD)Cl]_2/\gamma\text{-}Al_2O_3$ weight-to-weight ratios. For example, a 2.0 % weight-to-weight $Ir(1,5\text{-}COD)Cl/\gamma\text{-}Al_2O_3$ sample was prepared by adding 1.0 g acidic $\gamma\text{-}Al_2O_3$ to 20 mg $[Ir(1,5\text{-}COD)Cl]_2$ corresponding to a 2.0 wt % sample (i.e., wt % = [wt $[Ir(1,5\text{-}COD)Cl]_2$/(wt $[Ir(1,5\text{-}COD)Cl]_2$ + wt $\gamma\text{-}Al_2O_3$)] x 100, as this is what we experimentally measure out and hence know), by the following procedure. The appropriate amount of $[Ir(1,5\text{-}COD)Cl]_2$ was weighed out in a 20 mL scintillation vial. A new 5/8 in. × 5/16 in. Teflon-coated octagon-shaped stir bar was added to the vial and the solid was dissolved in 15 mL of ethyl acetate. Subsequently, the appropriate amount of solid oxide (e.g., 1.0 g of acidic $\gamma\text{-}Al_2O_3$ for the 2.0 wt % Ir catalyst) was added by pouring the metal oxide into the vial (i.e., this order of addition is deliberate; see pg 9712 of our prior publication for why this is important[14]) and the solution was stirred for 24 h to equilibrate the $[Ir(1,5\text{-}COD)Cl]_2$ with the solid oxide and the solution. After a 24 h equilibration period, the slurry was taken to dryness in the drybox by placing the sample under vacuum for 8 h at room temperature. The resulting supported precatalysts were then stored in the drybox.

Solvent-Dependent Nucleation and Growth Kinetics: A Standard Conditions Reaction. In a drybox 0.05 g of the $Ir(1,5\text{-}COD)Cl/\gamma\text{-}Al_2O_3$ catalyst precursor was weighed out into a 2-dram vial and transferred to a culture tube (22 × 175 mm) with a new 5/8 in. × 5/16 in. Teflon-coated octagon-shaped stir bar. To ensure a quantitative transfer, 2.5 mL of acetone and 0.5 mL of cyclohexene were added to the 2-dram vial, and transferred via a disposable polyethylene pipette into the same borosilicate culture tube containing the $Ir(1,5\text{-}COD)Cl/\gamma\text{-}Al_2O_3$ precatalyst. The culture tube was then sealed in the FP bottle, removed from the drybox, and attached to the H_2 line. The sealed, H_2-line attached FP bottle was placed into a temperature regulated water bath set at 22.0 ±

0.1 °C. A standard conditions purge cycle was used to initiate the reaction where, a series of H_2-flushing cycles in which the FP bottle is purged with H_2 every 15 s until 3.5 min have passed (a total of 14 purges). The stir plate was started and set at 600 rpm to allow the H_2 gas-to-solution equilibrium, and the H_2 pressure was then set to 40 psig with the data recording started at four minutes after the purge cycle began (which defined *t* = 0 for the kinetics).

Variation of the $[\gamma\text{-}Al_2O_3]_{sus}$. As described in the Standard Conditions Reaction section, 0.05 g of the Ir(1,5-COD)Cl/γ-Al_2O_3 catalyst precursor was weighed out into a 2-dram vial and transferred to a culture tube. To ensure quantitative transfer 2.5 mL of the appropriate solvent was placed into the 2-dram vial and transferred via a polyethylene disposable pipette into the same culture tube. Next, the pre-selected amount of 160 °C dried γ-Al_2O_3 was weighed out into a separate 2-dram vial and transferred into the same culture tube. The reaction slurry (that is the 0.05 g precatalyst, the 2.5 mL of acetone and the additional γ-Al_2O_3) was sealed in the borosilicate culture tube and stirred in the drybox for 8 h. Control reactions demonstrated that equilibration periods > 8 h, for both the low (0.25 M) and high (0.98 M) $[\gamma\text{-}Al_2O_3]_{sus}$, did not affect the resultant nucleation and growth kinetics. After the 8 h stirring period, 0.5 mL of cyclohexene was added to the slurry. The borosilicate culture tube was then placed in a FP bottle and a Standard Conditions Reaction was initiated as described above.

Variation of the Acetone Concentration: Cyclohexane/Acetone Mixed Solvent Conditions. In a drybox 50 mg of the 2.0 wt % Ir(1,5-COD)Cl/γ-Al_2O_3 prototype precatalyst was weighed out into a 20 mL scintillation vial and a new 5/8 in. × 5/16 in. Teflon-coated octagon-shaped stir bar was added. Subsequently, 2.5 mL of the prechosen cyclohexane/acetone mixture (vide supra) was added and the slurry was stirred for 24 h in the drybox. After the 24 h stirring equilibration period, 0.5 mL cyclohexene was added to the slurry and was transferred via a disposable polyethylene

pipette into a new borosilicate culture tube (22 × 175 mm) with a new 5/8 in. × 5/16 in. Teflon-coated octagon-shaped stir bar then, a Standard Conditions Reaction was initiated as described above. At $[Ir(1,5\text{-}COD)Cl]_2$ concentrations above ~0.2 mM, stirring speeds of 1000 rpm were necessary to maximize H_2 gas-to-solution mass transfer.[40]

Independent Verification of the Loss of Ir(1,5-COD)Cl(solvent) via UV–vis Spectroscopy and K_{Diss} via GLC and the Formation of $[Ir(1,5\text{-}COD)Cl]_2$ and K_{Diss}' via UV–vis Spectroscopy. Control reactions done to probe if Ir(1,5-COD)Cl(solvent) decreases with increasing $[\gamma\text{-}Al_2O_3]_{sus}$ were all done under O_2-free conditions (i.e., in the drybox). To start 0.05 g of the 2.0 wt% Ir(1,5-COD)Cl/γ-Al_2O_3 precatalyst was placed in a 20 mL scintillation vial along with 2.5 mL acetone. Subsequently the appropriate amount of additional γ-Al_2O_3 (0.25 M to 0.65 M) was added and the slurry was stirred for 8 h. The slurry was then filtered through a 0.2 μm nylon filter (NALGENE) and into an O_2 free UV–vis cell, sealed and then brought out of the drybox; the visible spectrum was then recorded. K_{Diss} was independently verified in nearly an identical manner, except 0.5 mL of cyclohexene along with 2 μL of decane (as an internal standard) was added to the filtered solution of Ir(1,5-COD)Cl(solvent) and a standard conditions hydrogenation was run (employing the same purge cycle, etc. as described above). Upon completion of the hydrogenation of cyclohexene GLC was used to determine the quantity of cyclooctane in solution.

Control reactions, all done under O_2 free conditions, to determine if $[Ir(1,5\text{-}COD)Cl]_2$ increased with increasing [acetone] were run from 0.14 to 2.7 M [acetone]. To start 0.05 g of the 2.0 wt% Ir(1,5-COD)Cl/γ-Al_2O_3 precatalyst was placed in a 20 mL scintillation vial along with 2.5 mL of the total mixed solvent (i.e., cyclohexane + acetone = 2.5 mL). The slurry was then filtered through a 0.2 μm nylon filter into an O_2 free UV–vis cell.

Acknowledgement: We gratefully acknowledge support from the Chemical Sciences, Geosciences and Biosciences Division, Office of Basic Energy Sciences, Office of Science, U.S. Department of Energy, Grant SE-FG02-03ER15453.

Supporting Information Available: Solvent-dependent supported-nanoparticle heterogeneous catalyst formation kinetics and their fits to the two-step mechanism; kinetic derivation of the proposed mechanism (k_1' and k_2''), Scheme 3 (bold); kinetic derivation for the "heterogeneous" (i.e., all solid-oxide-based) nucleation (k_1) and growth (k_2) mechanism; kinetic derivation for the "homogeneous" (i.e., all solution-based) nucleation (k_1') and growth (k_2') mechanism; mechanistic and curve fitting treatment of k_{1obs} and k_{2obs} vs [acetone]; comparison of the loss of Ir(1,5-COD)Cl(solvent) and the decrease in k_{1obs} and k_{2obs} with increasing $[\gamma\text{-}Al_2O_3]_{sus}$; comparison of the increase in $[Ir(1,5\text{-}COD)Cl]_2$ and the increase in k_{1obs} and k_{2obs} with increasing [acetone]; further consideration and use of the direct GLC and spectroscopic data to independently calculate K_{Diss} and K_{Diss}'; discussion of direct spectroscopic monitoring of the Ir(1,5-COD)Cl/γ-Al_2O_3 to $Ir(0)_n/\gamma\text{-}Al_2O_3$ supported-nanoparticle formation reaction. This material is available free of charge via the Internet at http://pubs.acs.org.

References

[1] (a) Gates, B. C., *Catalytic Chemistry*. John Wiley & Sons: New York, 1992. (b) Bartholomew, C. H.; Farrauto, R. J., *Fundamentals of Industrial Catalytic Processes*. 2 ed.; John Wiley & Sons: Hoboken, 2006.

[2] Schlögl, R.; Abd, H., S. B. *Angew. Chem. Int. Ed.* **2004,** *43*, 1628.

[3] Some recent reviews on the synthesis of transition metal nanoparticles include (please see also the extensive references therein for additional, earlier reviews of nanoparticle chemistry): (a) Aiken III, J. D.; Finke, R. G. *J. Mol. Catal. A: Chemical* **1999**, *145*, 1. (b) Crooks, R. M.; Zhao, M.; Sun, L.; Chechik, V.; Yeung, L. K. *Acc. Chem. Res.* **2001**, *34*, 181. (c) Bönnemann, H.; Richards, R. M. *Eur. J. Inorg. Chem.* **2001**, 2455. (d) Roucoux,

A.; Schulz, J.; Patin, H. *Chem. Rev.* **2002**, *102*, 3757. (e) Cushing, B. L.; Kolesnichenko, V. L.; O'Connor, C. J. *Chem. Rev.* **2004**, *104*, 3893. (f) Astruc, D.; Lu, F.; Aranzaes, J. R. *Angew. Chem. Int. Ed.* **2005**, *44*, 7852. (g) Wilcoxon, J. P.; Abrams, B. L. *Chem. Soc. Rev.* **2006**, *35*, 1162. (h) Ott, L. S.; Finke, R. G. *Coord. Chem. Rev.* **2007**, *251*, 1075. (i) Semagina, N.; Kiwi-Minsker, L. *Catal. Rev.-Sci. Eng.* **2009**, *51*, 147.

[4] Watzky, M. A.; Finke, R. G. *J. Am. Chem. Soc.* **1997**, *119*, 10382. See also the Table in the Supporting Information therein of the 19 prior key papers, which constituted the nanoparticle formation mechanism literature prior to 1997.

[5] Hornstein, B. J.; Finke, R. G. *Chem. Mater.* **2004**, *16*, 139 (see also *Chem. Mater.* **2004**, *16,* 3972).

[6] Besson, C.; Finney, E. E.; Finke, R. G. *J. Am. Chem. Soc.* **2005**, *127*, 8179.

[7] Besson, C.; Finney, E. E.; Finke, R. G. *Chem. Mater.* **2005**, *17*, 4925.

[8] Finney, E. E.; Finke, R. G. *Chem. Mater.* **2008**, *20*, 1956.

[9] A recent review of the kinetic and mechanistic studies of transition-metal nanoparticle nucleation and growth, with an emphasis on the nucleation process, has appeared. Finney, E. E.; Finke, R. G. *J. Colloid Interface Sci.* **2008**, *317*, 351.

[10] Some additional recent references, to the growing mechanistic insights into the synthesis of transition-metal nanoparticles resulting from the modern revolution in nanoparticle science, include: (a) Zheng, H.; Smith, R. K.; Jun, Y.-W.; Kisielowski, C.; Dahmen, U.; Alivisatos, A. P. *Science* **2009**, *324*, 1309. (b) Murray, C. B. *Science* **2009**, *324*, 1276. (c) Harada, M.; Inada, Y. *Langmuir* **2009**, *25*, 6049. (d) Polte, J.; Ahner, T. T.; Delissen, F.; Sokolov, S.; Emmerling, F.; Thunemann, A. F.; Kraehnert, R. *J. Am. Chem. Soc.* **2010**, *132*, 1296. (e) Polte, J.; Erler, R.; Thunemann, A. F.; Sokolov, S.; Ahner, T. T.; Rademann, K.; Emmerling, F.; Kraehnert, R. *ACS Nano* **2010**, *4*, 1076. (f) Yao, T.; Sun, Z.; Li, Y.; Pan, Z.; Wei, H.; Xie, Y.; Nomura, M.; Niwa, Y.; Yan, W.; Wu, Z.; Jiang, Y.; Liu, Q.; Wei, S. *J. Am. Chem. Soc.* **2010**, *130*, 7696.

[11] Discrete, atomically precise nanoparticles (or nanoclusters) are known in the literature; for example see: (a) Mednikov, E. G.; Jewell, M. C.; Dahl, L. F. *J. Am. Chem. Soc.* **2007,** *129*, 11619. Also see the extensive references therein for similar nanosized clusters. (b) Jadzinsky, P. D.; Calero, G.; Ackerson, C. J.; Bushnell, D. A.; Kornberg, R. D. *Science* **2007,** *318*, 430. (c) Shichibu, Y.; Negishi, Y.; Watanabe, T.; Chaki, N. K.; Kawaguchi, H.; Tsukuda, T. *J. Phys. Chem. C* **2007**, *111*, 7845. (d) Zhu, M.; Aikens, C. M.; Hollander, F. J.; Schatz, G. C.; Jin, R. *J. Am. Chem. Soc.* **2008,** *130*, 5883. (e) Heaven, M. W.; Dass, A.; White, P. S.; Holt, K. M.; Murray, R. W. *J. Am. Chem. Soc.* **2008**, *130*, 3754.

[12] Corain, B; Schmid, G.; Toshima, N., Eds. Metal Nanoparticles in Catalysis and Materials Science: The Issue of Size Control; Elsevier: Amsterdam, 2008.

[13] (a) Ahmadi, T. S.; Wang, Z. L.; Green, T. C.; Henglein, A.; El-Sayed, M. A. *Science* **1996**, *272*, 1924. (b) Burda, C.; Chen, X.; Narayanan, R.; El-Sayed, M. A. *Chem. Rev.*

2005, *105*, 1025. (c) Tao, A. R.; Habas, S.; Yang, P. *Small* **2008**, *4*, 310. (d) Xia, Y.; Xiong, Y.; Lim, B.; Skrabalak, S. E. *Angew. Chem. Int. Ed.* **2009**, *48*, 60.

[14] Mondloch; J. E.; Wang, Q.; Frenkel, A. I.; Finke, R. G. *J. Am. Chem. Soc.* **2010,** *132,* 9701.

[15] Examples where preformed nanoparticles are deposited onto supports can be found in the following references: (a) Kónya, Z.; Puntes, V. F.; Kiricsi, I.; Zhu, J.; Ager III, J. W.; Ko, M. K.; Frei, H.; Alivisatos, P.; Somorjai, G. A. *Chem. Mater.* **2003**, *15*, 1242. (b) Zheng, N.; Stucky, G. D. *J. Am. Chem. Soc.* **2006**, *128*, 14278. (c) Lee, I.; Morales, R.; Albiter, M. A.; Zaera, F. *Proc. Natl. Acad. Sci. U.S.A.* **2008**, *105*, 15241. (d) Huang, X.; Guo, C.; Zuo, J.; Zheng, N.; Stucky, G. D. *Small* **2009**, *5*, 361. (e) Boualleg, M.; Basset, J.-M.; Candy, J.-P.; Delichere, P.; Pelzer, K.; Veyre, L.; Thieuleux, C. *Chem. Mater.* **2009**, *21*, 775. (f) Zhu, Y.; Qian, H.; Drake, B. A.; Jin, R. *Angew. Chem. Int. Ed.* **2010**, *49*, 1.

[16] Examples from Somorjai and co-workers are available where they have made extensive, expert efforts to remove stabilizing ligand over-layers from both $Pt(0)_n$ and $Rh(0)_n$ nanoparticles with varying—albeit never complete—degrees of success: (a) Rioux, R. M.; Song, H.; Hoefelmeyer, J. D.; Yang, P.; Somorjai, G. A. *J. Phys. Chem. B* **2005,** *109,* 2192. (b) Song, H.; Rioux, R. M.; Hoefelmeyer, J. D.; Komor, R.; Niesz, K.; Grass, M.; Yang, P.; Somorjai, G. A. *J. Am. Chem. Soc.* **2006,** *128,* 3027. (c) Rioux, R. M.; Hsu, B. B.; Grass, M. E.; Song, H.; Somorjai, G. A. *Catal. Lett.* **2008,** *126,* 10. (d) Borodko, Y.; Jones, L.; Lee, H.; Frei, H.; Somorjai, G. A. *Langmuir* **2009,** *25,* 6665. (e) Park, J. Y.; Aliaga, C.; Russell Renzas, J.; Lee, H.; Somorjai, G. A. *Catal. Lett.* **2009,** *129,* 1. (f) Aliaga, C.; Park, J. Y.; Yamada, Y.; Sook Lee, H.; Tsung, C.-H.; Yang, P.; Somorjai, G. A. *J. Phys. Chem. C* **2009,** *113,* 6150. (g) Grass, M. E.;; Joo, S. H.; Zhang, Y.; Somorjai, G. A. *J. Phys. Chem. C* **2009,** *113,* 8616. (h) Borodko, Y. G.; Lee, H. Y.; Joo, S. H.; Zhang, Y.; Somorjai, G. A. *J. Phys. Chem. C* **2010,** *114*, 1117. (i) Kuhn, J. N.; Tsung, C.–H.; Huang, W.; Somorjai, G. A. *J. Catal.* **2009,** 209. There are also extensive examples attempting to remove dendrimer stabilizers, from dendrimer-stabilzed and supported nanoparticles, see for example: (j) Lang, H.; May, A.; L., I. B.; Chandler, B. D. *J. Am. Chem. Soc.* **2003**, *125*, 14832. (k) Liu, D.; Gao, J.; Murphy, C. J.; Williams, C. T. *J. Phys. Chem. B* **2004**, *108*, 12911. (l) Singh, A.; Chandler, B. D. *Langmuir* **2005**, *21*, 10776. (m) Deutsch, D. S.; Siani, A.; Fanson, P. T.; Hirata, H.; Matsumoto, S.; Williams, C. T.; Amiridis, M. D. *J. Phys. Chem. C* **2007**, *111*, 4246. (n) Albiter, M. A.; Zaera, F. *Langmuir* **2010**, *26,* 16204.

[17] Mondloch, J. E.; Yan, X.; Finke, R. G. *J. Am. Chem. Soc.* **2009**, *131*, 6389.

[18] Additional examples of supported-nanoparticle heterogeneous catalyst preparation in contact with solution include: (a) De Jong, K. P.; Geus, J. W. *Appl. Catal. A: General* **1982**, *4*, 41. (b) Bond, G. C.; Rawle, A. F. *J. Mol. Catal. A: Chemical* **1996**, *109*, 261. (c) Sales, E. A.; Benhamida, B.; Caizergues, V.; Lagier, J.-P.; Fievet, F.; Bozon-Verduraz, F. *Appl. Catal. A: General* **1998**, *172*, 273. (d) Guari, Y.; Thieuleux, C.; Mehdi, A.; Reyé, C.; Corriu, R. J. P.; Gomez-Gallardo, S.; Philippot, K.; Chaudret, B.; Dutartre, R. *Chem. Comm.* **2001,** 1374. (e) Guari, Y.; Thieuleux, C.; Mehdi, A.; Reyé, C.; Corriu, R. J. P.; Gomez-Gallardo, S.; Philippot, K.; Chaudret, B. *Chem. Mater.* **2003,** *15*, 2017. (f) Marconi, G.; Pertici, P.; Evangelisti, C.; Caporusso, A. M.; Vitulli, G.; Capannelli, G.;

Hoang, M.; Turney, T. W. *J. Organometallic Chem.* **2004**, *689*, 639. (g) Hulea, V.; Brunel, D.; Galarneau, A.; Philippot, K.; Chaudret, B.; Kooyman, P. J.; Fajula, F. *Microporous Mesoporous Mater.* **2005**, *79*, 185. (h) Jiang, Y.; Gao, Q. *J. Am. Chem. Soc.* **2006**, *128*, 716. (i) Zhong, L.-S.; Hu, J.-S.; Cui, Z.-M.; Wan, L.-J.; Song, W.-G. *Chem. Mater.* **2007**, *19*, 4557. (j) Zawadzki, M.; Okal, J. *Mater. Res. Bull.* **2008**, *43*, 3111. (k) Boutros, M.; Denicourt-Nowicki, A.; Roucoux, A.; Gengembre, L.; Beaunier, P.; Gedeon, A.; Launay, F. *Chem. Commun.* **2008**, 2920. (l) Xing, R.; Liu, Y.; Wu, H.; Li, X.; He, M.; P., W. *Chem. Comm.* **2008**, 6297. (m) Elmoula, M. A.; Panaitescu, E.; Phan, M.; Yin, D.; Richter, C.; Lewis, L. H.; Menon, L. *J. Mater. Chem.* **2009**, *19*, 4483. (n) Xie, Y.; Ding, K.; Liu, Z.; Tao, R.; Sun, Z.; Zhang, H.; An, G. *J. Am. Chem. Soc.* **2009**, *131*, 6648. (o) Besson, E.; Mehdi, A.; Reye, C.; Corriu, R. J. P. *J. Mater. Chem.* **2009**, *19*, 4746. (p) Lin, Z.; Chu, H.; Shen, Y.; Wei, L.; Liu, H.; Li, Y. *Chem. Comm.* **2009**, 7167. (q) Zahmakiran, M.; Özkar, S. *Langmuir* **2009**, *25*, 2667. (r) Zahmakiran, M.; Özkar, S. *J. Am. Chem. Soc.* **2010**, *132*, 6541. In addition the catalysts elsewhere[26-29] were also prepared in contact with solution.

[19] "Weakly ligated/labile ligand" nanoparticles are simply nanoparticles with ideally 100% removable or replaceable ligands prepared using only the desired reactants (or solvent) for the catalytic reaction at hand. Related concepts, such as putatively "solvent-only" stabilized nanoparticles, are discussed in (a) Ott, L. S.; Finke, R. G. *Inorg. Chem.* **2006,** *45,* 8382. A recent review has also been published[3h] detailing nanoparticle stabilization and the use of anion free metal precursors that, in principle, can generate such "weakly ligated/labile ligand" or "solvent only" stabilized nanoparticles. See footnote 41 elsewhere[14] for related work on putatively "naked nanoparticles".

[20] Our own efforts to date on the "weakly ligated/labile ligand" nanoparticle concept are reported in (a) Özkar, S.; Finke, R. G. *J. Am. Chem. Soc.* **2005,** *127,* 4800 and (b) Bayram, E.; Zahmakiran, M.; Özkar, S.; Finke, R. G. *Langmuir,* **2010,** *26,* 12455.

[21] Bell, A. T. *Science* **2003**, *299*, 1688.

[22] Lee, I.; Delbecq, F.; Morales, R.; Albiter, M. A.; Zaera, F. *Nat. Mater.* **2009**, *8*, 132.

[23] Joo, S. H.; Park, J. Y.; Tsung, C.-H.; Yamada, Y.; Yang, P.; Somorjai, G. A. *Nat. Mater.* **2009**, *8*, 126.

[24] (a) Thomas, J. M.; Johnson, B. F. G.; Raja, R.; Sankar, G.; Midgley, P. A. *Acc. Chem. Res.* **2003**, *36*, 20. (b) Alayoglu, S.; Nilekar, A. U.; Mavrikakis, M.; Eichhorn, B. *Nat. Mater.* **2008**, *7*, 333.

[25] Che, M.; Bennett, C. O. *Adv. Catal.* **1989**, *36*, 55.

[26] Two hypothesized,[27-28] but not experimentally tested, mechanisms have been put forth in the supported-nanoparticle heterogeneous catalyst formation in contact with solution literature. Marre et al.[27] studied the formation of $Cu(0)_n/(SiO_2)_n$ (silica spheres) starting from $Cu(hfac)_2 \bullet H_2O$ (where hfac = hexafluoroacetylacetonate) in supercritical CO_2/alcohol/H_2 mixtures. They propose that the $Cu(0)_n/(SiO_2)_n$ products are formed via a mechanism consisting of an *initial homogeneous nucleation, followed by deposition, and subsequent coagulation and coalescence*. Unfortunately the physical model used to test

their hypothesis is not based on rigorous chemical reactions (as is required in chemical kinetics), so that the words used to describe those processes (e.g., homogeneous nucleation, coagulation and so on) do not have a sound, reliable mechanistic basis—an insidious nomenclature problem that leads to considerable mechanistic confusion as addressed elsewhere.[26a] Furthermore no alternative mechanisms were disproved for that specific $Cu(0)_n/(SiO_2)_n$ system, as discussed further in our review.[30] Despite these issues, it is noteworthy the data herein (albeit for a different, Ir system) is consistent with the general mechanism proposed by Marre et al for their vs Cu system.

Rossi and co-workers[29] have also briefly reported Pd^{2+}/SiO_2 to $Pd(0)_n/SiO_2$ supported-nanoparticle formation kinetics in contact with solution, using the cyclohexene reporter reaction method shown in Scheme 2. Unfortunately, the needed stirring rate and $[cyclohexene]^0$ dependent controls were not performed making it unclear whether the $Pd(0)_n$ supported-nanoparticle formation kinetics are being faithfully monitored;[4,14] furthermore, no mechanism was proposed for the observed kinetics. Additional evidence consistent with a solution-based mechanism comes from the groups of Chaudret[26b] and Corain[26c,d] who demonstrated that solvents were needed for supported-nanoparticle products to form in their system.

Wang et al.[28] studied the formation of a $Pt(0)_n$/Carbon nanotube (CNT) catalyst starting from H_2PtCl_6 in ethylene glycol and in the presence of sodium dodecylsulfate. In contrast with Marre et al., they concluded that the $Pt(0)_n$/CNT catalyst formation occurred via *heterogeneous nucleation on the CNT surface*, followed by autocatalytic surface growth[4] effectively depleting the Pt^{4+} monomers in solution. Other literature, by Muramatsu and coworkers,[26e,f] further asserts that nucleation must occur on the surface at solid-liquid interfaces, for example in the presence of catalyst support materials. Overall, this brief survey of the literature makes apparent that definitive work on the mechanisms of nanoparticle formation in contact with solution is not available from the prior literature. (a) Finney, E. E.; Finke, R. G. *Chem. Mater.* **2009,** *21,* 4692. (b) Hulea, V.; Brunel, D.; Galarneau, A.; Philippot, K.; Chaudret, B.; Kooyman, P. J.; Fajula, F. *Micropourous Mesoporous Mater.* **2005**, *79*, 185. (c) Artuso, F.; D'Archivio, A. A.; Lora, S.; Jerabek, K.; Kralik, M.; Corain, B. *Chem. Eur. J.* **2003**, *9,* 5292. (d) Corain, B.; Jerabek, K.; Centomo, P.; Canton, P. *Angew. Chem. Int. Ed.* **2004**, *43*, 959. (e) Takahashi, H.; Sunagawa, Y.; Myagmarja, S.; Muramatsu, A. *Catalysis Surveys from Asia* **2005**, *9*. (f) Sunagawa, Y.; Yamamoto, K.; Takahashi, H.; Muramatsu, A. *Catal. Today* **2008**, *132*, 81.

[27] (a) Marre, S.; Cansell, F.; Aymonier, C. *Nanotechnology* **2006**, *17*, 4594. (b) Marre, S.; Erriguible, A.; Perdomo, A.; Cansell, F.; Marias, F.; Aymonier, C. *J. Phys. Chem. C* **2009**, *113*, 5096.

[28] Wang, Y.; Xu, X.; Tian, Z.; Zong, Y.; Cheng, H.; Lin, C. *Chem. Eur. J.* **2006**, *12*, 2542.

[29] Rossi, L. M.; Nangoi, I. M.; Costa, N. J. S. *Inorg. Chem.* **2009**, *48*, 4640.

[30] Mondloch, J. E.; Bayram, E.; Finke, R. G. ("A Review of the Kinetics and Mechanisms of Formation of Supported-Nanoparticle Heterogeneous Catalysts, (tentative title)).

[31] Our prior work[14] is certainly *not* the first example of a well-characterized organometallic precatalyst. Extensive examples of well-characterized organometallic precatalysts can be found in (i) Zakharov, V. A.; Yermakov, Y. I. *Catal. Rev.—Sci. Eng.* **1979,** *19,* 67 and (ii) *Modern Surface Organometallic Chemistry*, Basset, J.–M., Psaro,

R. , Roberto, D., Ugo, R., Eds.; WILEY-VCH: Weinheim, 2009. *However*, ours is the first study that starts from a well-characterized speciation-controlled supported organometallic precatalyst, and focuses on supported-nanoparticle heterogeneous catalyst formation in contact with solution, and which contains the necessary kinetic data to rule out alternative mechanisms en route to a kinetically supported proposed mechanism.

[32] The eight prototype criteria previously developed[14] are (i) a compositionally and structurally well-defined supported precatalyst (accomplished previously via inductively coupled plasma optical emission spectroscopy, CO/IR trapping experiments as well as X-ray absorbance fine structure (XAFS) spectroscopy[14]); (ii) a system in contact with solution and formed under low temperature conditions; and (iii) a system where a balanced stoichiometry of the supported-nanoparticle formation reaction is established (e.g., Scheme 1, and as previously confirmed elsewhere[14]), leading to a well defined $Ir(0)_{\sim 900}/\gamma\text{-}Al_2O_3$ supported-nanoparticle heterogeneous catalyst (confirmed for the present system by transmission electron microscopy (TEM) and XAFS[14]). In addition, a prototype system should: (iv) yield an active and lonγ-lived catalyst, and hence (v) provide a system where the initial kinetic and mechanistic studies of the in situ catalyst formation are worth the effort. The prototype system should also yield (vi) reproducible and quantitative kinetic data so that quantitative conclusions and mechanistic insights can be drawn; and ideally (vii) comparison to a kinetically and mechanistically well-studied nanoparticle formation system in solution should also be possible for any insights that comparison might allow.[4,34,45] Lastly, once that prototype system is in hand, one would also like to (viii) systematically vary key synthetic variables such as the support, solvent and metal precursor to reveal their affects on supported-nanoparticle formation in contact with solution.

[33] Lyon, D. K. Ph.D. Dissertation, University of Oregon, September 1990.

[34] (a) Lin, Y.; Finke, R. G. *J. Am. Chem. Soc.* **1994**, *116*, 8335. (b) Lin, Y.; Finke, R. G. *Inorg. Chem.* **1994**, *33*, 4891.

[35] The mechanism in Scheme 3 predicts that k_{1obs} and k_{2obs} should be constant as a function of the $Ir(1,5\text{-}COD)Cl/\gamma\text{-}Al_2O_3$ wt%, a result which we confirmed. In order to probe the $[\gamma\text{-}Al_2O_3]_{sus}$ dependence on k_{1obs} and k_{2obs}, it is best to study this as a constant initial $Ir(1,5\text{-}COD)Cl/\gamma\text{-}Al_2O_3$ wt% as was done in the present studies.

[36] The details on the typically observed error limits in k_1 of $\pm 10^{1.2}$ h^{-1} derived over a > seven year period from data obtained from multiple investigations, all for the $P_2W_{15}Nb_3O_{62}^{9-}$ polyoxoanion-stabilized $Ir(0)_{\sim 300}$ nanoparticle system, have previously been described: Widegren, J. A.; Bennett, M. A.; Finke R. G. *J. Am. Chem. Soc.* **2003,** *125,* 10301 (specifically p 10304). Briefly, k_1 has been shown to be sensitive to water, acetone impurities, precursor purity and amount of any $Ir(1,5\text{-}COD)^+$ unbound to the $P_2W_{15}Nb_3O_{62}^{9-}$ polyoxoanion.[4,34,45] While significantly less data has been collected for the prototype $Ir(1,5\text{-}COD)Cl/\gamma\text{-}Al_2O_3$ to $Ir(0)_{\sim 900}/\gamma\text{-}Al_2O_3$ system, the observed error limits to data are $\sim\pm 10^1$ h^{-1} for k_1,[14] and are also expected to be sensitive to water, acetone and precursor purity, and the amount of any excess or otherwise unbound $Ir(1,5\text{-}COD)^+$. Another relevant point is that other k_1 nucleation rate constants, given elsewhere,[6,7,8] (e.g., for a four-step mechanism for nanoparticle nucleation, autocatalytic surface

growth, bimolecular agglomeration and autocatalytic agglomeration) have been shown to vary by ~ ±10[4].

[37] A datum point at 0.163 M γ-Al_2O_3 (i.e., without any additional γ-Al_2O_3) is available, with the following observed rate constants: k_{1obs} = 1.5(1.1) x 10^{-3} h^{-1} and k_{2obs} = 1.6(2) x 10^4 h^{-1} M^{-1}.[14] However, this point was not, and should not, be co-plotted with the data in Figures 2 and 3 since that system is not equilibrated with any additional [γ-Al_2O_3]$_{sus}$. Such equilibration steps, and the order(s) of addition of the reagents, have been shown to be experimentally important variables in the Ir(1,5-COD)Cl/γ-Al_2O_3 precatalyst preparation and subsequent supported-nanoparticle heterogeneous catalyst formation kinetics.[14] Hence, it follows that only samples prepared under the same synthetic conditions should be (and were) plotted in Figures 2 and 3.

[38] In neat cyclohexane, the UV-vis spectrum of the filtered solution (Figure S3 Supporting Information) reveals that no Ir(1,5-COD)Cl(solvent) is present in solution. However, in *acetone* two metal-to-ligand charge transfer bands are present from 340-540 nm (detailed in the Supporting Information), data consistent with the presence of a square planar Ir(I) complex in acetone.[39]

[39] Epstein, R. A.; Geoffroy, G. L.; Keeney, M. E.; Mason, W. R. *Inorg. Chem.* **1970,** *18,* 478.

[40] The acetone-dependent data above ~1.75 M acetone show saturation behavior, consistent with the solution-based mechanism. However, those data are convoluted due to competing H_2 gas-to-solution mass-transfer limitations (MTLs) due to the lower solubility of H_2 in the mixed cyclohexane/acetone solvent system vs in acetone. The MTLs were revealed by stirring the supported-nanoparticle heterogeneous catalyst formation reactions (i.e., those above ~1.75 M acetone) at 1000 rpm. That 40% increase in stirring rate yielded a 40% increase in the H_2 uptake rate, -d[H_2]/dt. The observed H_2 gas-to-solution MTL largely affect k_{2obs} as it correlates with the H_2 uptake during nanoparticle growth (i.e., post the induction period), but has a minimal affect on k_{1obs} (i.e., the nucleation step uses little H_2 and, therefore, is not MTL under these conditions).[4]

[41] Dalla Betta, R. A.; Boudart, M. In International Congress on Catalysis (5th); North Holland: Palm Beach, Fla, 1972; Vol. 5th Annaual, 1329.

[42] One relevant question is "approximately how large, on average, are the Ir(0)$_n$ nanoparticles when they are captured by the γ-Al_2O_3 support?". This can be estimated using our previously obtained[14] cyclooctane evolution kinetic data. Those data reveal that at the end of the induction period (approximately 20 to 30 min) only 2.1 or 4.9% of the Ir(1,5-COD)Cl/γ-Al_2O_3 precatalyst has evolved into Ir(0)$_n$. Since nucleation and growth are separated in time, we can estimate from the average Ir(0)$_{\sim 900}$ supported-nanoparticle product that, on average, Ir(0)$_{\sim 19}$ to Ir(0)$_{\sim 44}$ nanoparticles are captured by the γ-Al_2O_3. That is, approximately 0.8 to 1.1 nm nanoparticles are formed during the nucleation step, which are then captured by the γ-Al_2O_3 and then grow (via autocatalytic surface growth) to the observed, on average 2.9 nm Ir(0)$_{\sim 900}$ nanoparticles on the γ-Al_2O_3.

[43] Watzky, M. A.; Finney, E. E.; Finke, R. G. *J. Am. Chem. Soc.* **2008,** *130,* 11959.

[44] Ott, L. S.; Finke, R. G. *J. Nanosci. Nanotechnol.* **2008,** *8,* 1551.

[45] Widegren, J. A.; Aiken III, J. D.; Özkar, S.; Finke, R. G. *Chem. Mater.* **2001**, *13*, 312.

[46] Aiken III, J. D.; Lin, Y.; Finke, R. G. *J. Mol. Catal. A: Chemical* **1996,** *114,* 29.

[47] http://www.city-data.com/city/Fort-Collins-Colorado.html (accessed Nov 7, 2010)

[48] An important control experiment, using 500 °C partially dehydroxylated γ-Al_2O_3,[49] ensured that the γ-Al_2O_3 degree of hydroxylation/water content was controlled for the kinetic experiments herein. The average of two supported-nanoparticle heterogeneous catalyst formation kinetic experiments, using 500 °C partially dehydroxylated 2.0 wt% Ir(1,5-COD)Cl/γ-Al_2O_3, yielded a k_1 rate constant of 1.3(2) x 10^{-3} h^{-1} and a k_2 rate constant of 1.6(2) x 10^4 h^{-1} M^{-1} (vs the 160 °C thermally treated γ-Al_2O_3 k_1 and k_2 rate constants of 1.5(1.1) x 10^{-3} h^{-1} and 1.6(2) x 10^4 h^{-1} M^{-1}, respectively). Hence, there is no difference in the k_1 and k_2 rate constants for the 160 °C and 500 °C thermally treated γ-Al_2O_3 samples.

[49] Partially dehydroxylated γ-Al_2O_3 was made following the procedure of Lobo-Lapidus, R. J.; McCall, M. J.; Lanuza, M.; Tonnesen, S.; Bare, S. R.; Gates, B. C. *J. Phys. Chem. C* **2008,** *112,* 3383. Specifically, the γ-Al_2O_3 powder was calcinced for 4 h at 500 °C in flowing O_2 at 1 atm, followed by evacuation under vacuum for 24 h.

[50] Motulsky, H.; Chrsitopoulos, A. *Fitting Models to Biological Data Using Linear and Nonlinear Regression*; Oxford University Press: New York, 2004.

[51] We thank a reviewer for arguing for the need to use *weighted* nonlinear regression to accurately fit the k_{1obs} and k_{2obs} vs $[\gamma\text{-}Al_2O_3]_{sus}$ and [acetone] data.

Supporting Information for:

SUPPORTED-NANOPARTICLE HETEROGENEOUS CATALYST FORMATION IN CONTACT WITH SOLUTION: KINETICS AND PROPOSED MECHANISM FOR THE CONVERSION OF Ir(1,5-COD)Cl/γ-Al_2O_3TO $Ir(0)_{\sim 900}$/γ-Al_2O_3

Joseph E. Mondloch and Richard G. Finke

Additional Results and Discussion

Solvent-Dependent Nucleation and Growth Kinetics Starting From Ir(1,5-COD)Cl/γ-Al_2O_3. Four solvents were surveyed to see how they would affect the observed supported-nanoparticle heterogeneous catalyst formation kinetics when starting from Ir(1,5-COD)Cl/γ-Al_2O_3. The general prediction is that solution-based nanoparticle nucleation and growth pathways should be sensitive to such changes in the solvent (e.g., solvent coordinating ability) and if a solution-based pathway is present. The experimental details are described in the main text of the paper.

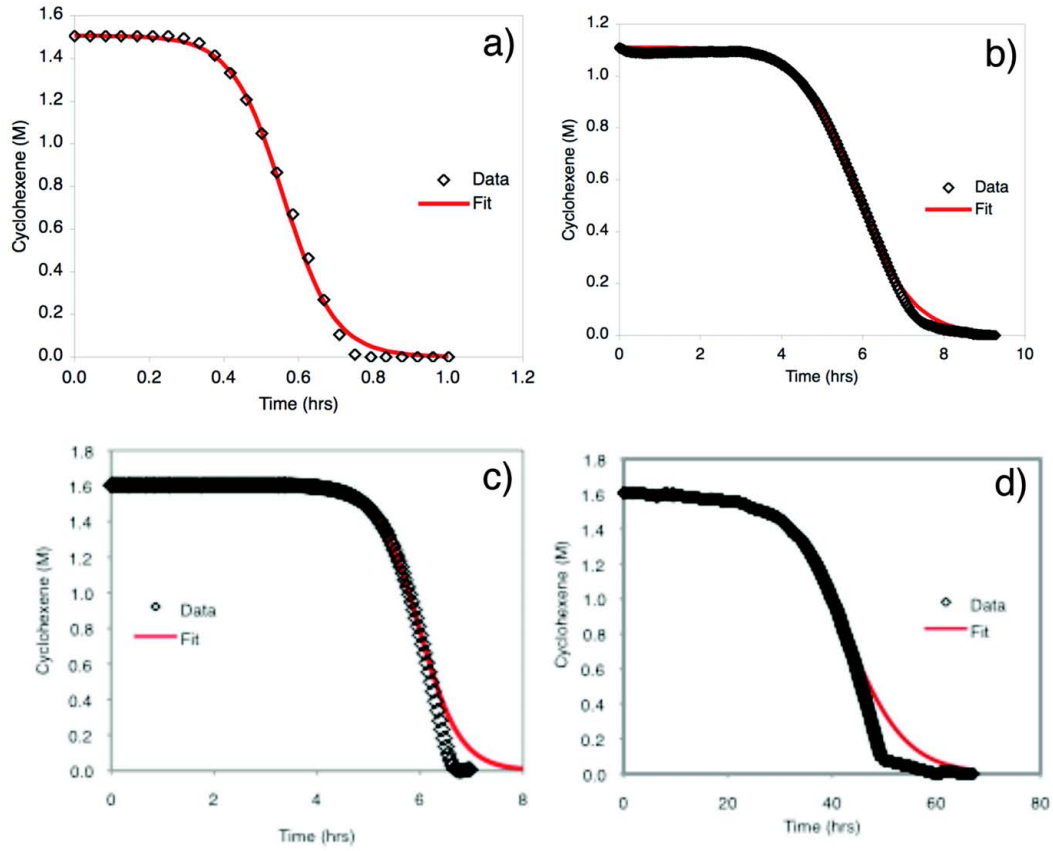

Figure S1. Solvent-dependent supported-nanoparticle heterogeneous catalyst formation kinetics in acetone (a), propylene carbonate (b), CH_2Cl_2 (c) and cyclohexane (d) and their fits to the two-step mechanism of nucleation (A → B, rate constant k_1) followed by autocatalytic surface growth (A + B → 2B, rate constant k_2). The results show that the supported-nanoparticle formation reaction is highly solvent dependent.

Representative kinetic curves, along with their fits to the two-step mechanism, are shown in Figure S1 (in acetone—the prototype solvent for nanoparticle formation from our prior, solution-based studies of nanoparticle nucleation and growth—and also in propylene carbonate, dichloromethane and cyclohexane). Consistent with the data in Table 1 of the main text, the supported-nanoparticle heterogeneous catalyst formation kinetics are highly solvent dependent over the four solvents surveyed (note the necessarily different time scales on the x-axes in Figure S1, a–d).

Scheme S1. The Proposed Supported-Nanoparticle Heterogeneous Catalyst Formation Mechanism (Bold) Involving Ir(1,5-COD)Cl(solvent) Solution-Based Nucleation, Fast $Ir(0)_n$ Nanoparticle Capture by $[\gamma\text{-}Al_2O_3]_{sus}$ and Subsequent Solid-Oxide Based Nanoparticle Growth Between $Ir(0)_n/\gamma\text{-}Al_2O_3$ and Ir(1,5-COD)Cl(solvent). Also Shown are Two Alternative Supported-Nanoparticle Heterogeneous Catalyst Formation Mechanisms that Were Disproved (Vide Infra; the Pathways Crossed Out).

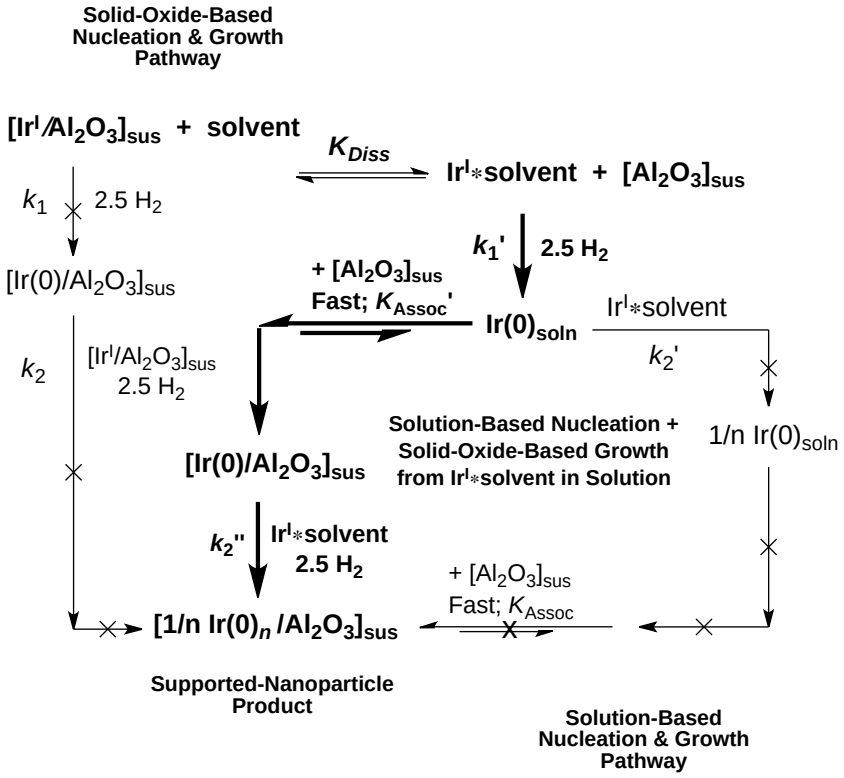

Derivation of The Currently Proposed Mechanism: Ir(1,5-COD)Cl(solvent) Solution-Based Nucleation, Fast Nanoparticle Capture by $[\gamma\text{-}Al_2O_3]_{sus}$ and

Subsequent Solid-Oxide-Based Nanoparticle Growth via Ir(1,5-COD)Cl(solvent) Plus $[Ir(0)_n/\gamma\text{-}Al_2O_3]_{sus}$. The proposed mechanism, Scheme S1, begins with a dissociative equilibrium (K_{Diss}) between Ir(1,5-COD)Cl/γ-Al_2O_3 and Ir(1,5-COD)Cl(solvent) (abbreviated $[Ir^I/Al_2O_3]_{sus}$ and $[Ir^I{*}solvent]$, respectively). Nucleation is proposed to occur from the dissociated Ir(1,5-COD)Cl(solvent) complex in solution (k_1'), followed by fast nanoparticle capture by $[\gamma\text{-}Al_2O_3]_{sus}$ (abbreviated $[Al_2O_3]_{sus}$). Subsequently, "heterogeneous", solid-oxide-based $Ir(0)_n/\gamma\text{-}Al_2O_3$ nanoparticle growth is then proposed to occur between $Ir(0)_n/\gamma\text{-}Al_2O_3$ and the dissociated Ir(1,5-COD)Cl(solvent) complex.

To start, we know that the Ir(1,5-COD)Cl/γ-Al_2O_3 to $Ir(0)_n/\gamma\text{-}Al_2O_3$ supported-nanoparticle heterogeneous catalyst formation kinetics are accounted for by the two-step mechanism, A → B (rate constant k_1) and A + B → 2B (rate constant k_2), shown in Scheme 2 of the main text.[1] Hence, we have formulated the bold pathway in Scheme S1 in terms of the two-step mechanism, eqs S1 to S6, where *A is the dissociated Ir(1,5-COD)Cl(solvent) complex in solution and B is the γ-Al_2O_3-supported, $Ir(0)_n$ surface, $Ir(0)_n/\gamma\text{-}Al_2O_3$*. It is also important to note that while the $Ir(0)_n$ nanoparticle is growing on the $[Al_2O_3]_{sus}$ surface, *the growth is still proposed to be occurring by reaction with the dissociated Ir^I*solvent species*. For convenience and simplicity, some of the products (i.e., cyclooctane and HCl) have been deliberately omitted from eqs S1 to S6 as well as from the rest of the equations throughout, vide infra. It should also be recognized that "$[Ir(0)/\gamma\text{-}Al_2O_3]_{sus}$" may really be "$[(Ir^I\text{–}H)_n/\gamma\text{-}Al_2O_3]_{sus}$", for example, a detail regarding nanoparticle nucleation that is not yet understood but under investigation, as also discussed in the main text.[2] Abbreviations in terms of the A → B and A + B → 2B two-step mechanism, that is generally found to fit the kinetic data, are also given in bold for clarity throughout.

$$Ir^{I}/Al_2O_3 + \text{solvent} \underset{}{\overset{K_{Diss}}{\rightleftharpoons}} Ir^{I}{*}\text{solvent} + Al_2O_3 \quad \text{(S1)}$$

$$\mathbf{[A/Al_2O_3]_{sus}} \qquad \mathbf{[A]}$$

$$Ir^{I}{*}\text{solvent} \xrightarrow[2.5\ H_2]{k_1'} Ir(0)_{soln} + \text{solvent} \quad \text{(S2)}$$

$$\mathbf{[A]} \qquad \mathbf{[B]}$$

$$Ir(0)_{soln} + Al_2O_3 \xrightarrow{\text{Fast}} Ir(0)/Al_2O_3 \quad \text{(S3)}$$

$$\mathbf{[B]} \qquad \mathbf{[B/Al_2O_3]_{sus}}$$

$$Ir^{I}/Al_2O_3 + \text{solvent} \underset{}{\overset{K_{Diss}}{\rightleftharpoons}} Ir^{I}{*}\text{solvent} + Al_2O_3 \quad \text{(S4)}$$

$$\mathbf{[A/Al_2O_3]_{sus}} \qquad \mathbf{[A]}$$

$$Ir^{I}{*}\text{solvent} + Ir(0)/Al_2O_3 \xrightarrow[2.5\ H_2]{k_2''} 2\,[Ir(0)/Al_2O_3] + \text{solvent} \quad \text{(S5)}$$

$$\mathbf{[A] + [B/Al_2O_3]_{sus}} \qquad \mathbf{2\,[B/Al_2O_3]_{sus}}$$

$$\text{SUM:} \quad [Ir^{I}/Al_2O_3]_{sus} \xrightarrow[2.5\ H_2]{k_{obs}''} [Ir(0)/Al_2O_3]_{sus} \quad \text{(S6)}$$

$$\mathbf{[A/Al_2O_3]_{sus}} \qquad \mathbf{[B/Al_2O_3]_{sus}}$$

By the mechanism proposed, Scheme S1 (bold) and eqs S1 to S6, we can write the differential equation, eq S7. In eq S7 and the equations that follow, the subscript "*t*" denotes each species as a function of time, while the subscript "i" will represent initial concentrations. We also employ the assumption, as before,[3] that the $[H_2]$ is effectively constant to a ± ~11% error[3] over the first, approximately half of a H_2 uptake curve emphasized by our kinetic measurements; that is, k_1' and k_2'' are, themselves, apparent, pseudo-order rate constants with a possible $[H_2]$ dependence, one reason we call these "apparent rate constants" in the main text.

$$-\frac{d[Ir^{I}/Al_2O_3]_{sus}}{dt} = k_1'[Ir^{I}{*}\text{solvent}]_t + k_2''[Ir^{I}{*}\text{solvent}]_t[Ir(0)_n/Al_2O_3]_{sus,t} \quad \text{(S7)}$$

Next, we need to express $[Ir^{I}*solvent]_t$ in terms of the $[Ir^{I}/Al_2O_3]_{sus,i}$ that we actually begin with. This is done by solving the dissociative equilibrium, eq S8, for $[Ir^{I}/Al_2O_3]_{sus,t}$, which yields eq S9.

$$K_{Diss} = \frac{[Ir^{I} * solvent]_t [Al_2O_3]_{sus,t}}{[Ir^{I}/Al_2O_3]_{sus,t}[solvent]_t} \tag{S8}$$

$$[Ir^{I}/Al_2O_3]_{sus,t} = \frac{[Ir^{I} * solvent]_t [Al_2O_3]_{sus,t}}{K_{Diss}[solvent]_t} \tag{S9}$$

Substitution of eq S9 into the mass balance equation, eq S10, yields eq S11.

$$[Ir^{I}/Al_2O_3]_{sus,i} = [Ir^{I}/Al_2O_3]_{sus,t} + [Ir^{I} * solvent]_t \tag{S10}$$

$$[Ir^{I} * solvent]_t = [Ir^{I}/Al_2O_3]_{sus,i}\left\{\frac{[solvent]_t K_{Diss}}{[Al_2O_3]_{sus,t} + [solvent]_t K_{Diss}}\right\} \tag{S11}$$

Equation S11 is then substituted into the differential equation, eq S7, which yields eq S12.

$$\begin{aligned} -\frac{d[Ir^{I}/Al_2O_3]_{sus}}{dt} &= k_1'[Ir^{I}/Al_2O_3]_{sus,i}\left\{\frac{[solvent]_t K_{Diss}}{[Al_2O_3]_{sus,t} + [solvent]_t K_{Diss}}\right\} \\ &+ k_2''[Ir^{I}/Al_2O_3]_{sus,i}\left\{\frac{[solvent]_t K_{Diss}}{[Al_2O_3]_{sus,t} + [solvent]_t K_{Diss}}\right\}[Ir(0)_n/Al_2O_3]_{sus,t} \end{aligned} \tag{S12}$$

Equation S12 is more conveniently expressed as eq S13, where k_{1obs} and k_{2obs} are given by eqs S14 and S15 respectively.

$$-\frac{d[Ir^{I}/Al_2O_3]_{sus}}{dt} = k_{1obs}[Ir^{I}/Al_2O_3]_{sus,i} + k_{2obs}[Ir^{I}/Al_2O_3]_{sus,i}[Ir(0)_n/Al_2O_3]_{sus,t} \quad \text{(S13)}$$

$$k_{1obs} = \frac{k_1' K_{Diss}[solvent]_t}{[Al_2O_3]_{sus,t} + K_{Diss}[solvent]_t} \quad \text{(S14)}$$

$$k_{2obs} = \frac{k_2'' K_{Diss}[solvent]_t}{[Al_2O_3]_{sus,t} + K_{Diss}[solvent]_t} \quad \text{(S15)}$$

Because we use a pseudoelementary step to follow the production of "$[B]_t$" (i.e., either $[Ir(0)_{n,soln}]_t$ or $[Ir(0)_n/Al_2O_3]_{sus,t}$), via its (magnified) catalytic hydrogenation of cyclohexene,[3,4,] we must express eq S15 in a differential form with respect to cyclohexene. This is done via the stoichiometry of the pseudoelementary step, eq S16, where for simplicity k_{1obs} and k_{2obs} can in principle be any combination of the k_1 and k_2 pathways (i.e., k_1, k_1', k_2, k_2' or k_2'' shown back in Scheme S1).

$$[Ir^{I}/Al_2O_3]_{sus} + \sim 1700\ H_2 \xrightarrow{k_{1obs};\ k_{2obs}} [Ir(0)_n/Al_2O_3]_{sus} + \sim 1700 \text{ (cyclohexene)} + \sim 1700 \text{ (cyclohexane)} \quad \text{(S16)}$$

$$-\frac{d[Ir^{I}/Al_2O_3]_{sus}}{dt} = \frac{d[Ir(0)_n/Al_2O_3]_{sus}}{dt} = -\frac{d[cyclohexene]}{\frac{dt}{1700}} = -\frac{d[H_2]}{\frac{dt}{1700}} \quad \text{(S17)}$$

The pseudoelementary step allows us to write equation S17, which couples the loss of cyclohexene to the loss of H_2 pressure (i.e., $-\mathrm{d[cyclohexene]/dt} = -\mathrm{d[H_2]/dt}$) and then to the slower supported-nanoparticle formation steps (i.e., k_{1obs} and k_{2obs}) shown in Scheme 2 of the main text. This is important because we actually follow H_2 loss via a sensitive (± 0.01 psig[3,4]) pressure transducer, and convert that into cyclohexene loss (via the known[35] 1:1 H_2 to cyclohexene stoichiometry), eq S18 and as shown in Figure 1 of the main text. The steps of the derivation between eqs S17 and S18 are identical to those given previously,[3] eqs A.2(a) to A.5 elsewhere,[3] and, hence, are not repeated here.

$$-\frac{\mathrm{d[cyclohexene]}}{\mathrm{dt}} = k_1[\mathrm{cyclohexene}]_t + \frac{k_2}{1700}[\mathrm{cyclohexene}]_t\{[\mathrm{cyclohexene}]_0 - [\mathrm{cyclohexene}]_t\} \quad \text{(S18)}$$

Derivation of the "Heterogeneous" (i.e., All Solid-Oxide-Based) Nucleation (k_1) and Growth (k_2) Pathway. The putative "heterogeneous" (i.e., all solid-oxide-based) nucleation and growth pathway (left most pathway, Scheme S1) occurs by definition exclusively on the γ-Al_2O_3 support. Analogous to the derivation above, the Ir(1,5-COD)Cl/γ-Al_2O_3 to $Ir(0)_n$/γ-Al_2O_3 supported-nanoparticle heterogeneous catalyst formation kinetics were formulated in terms of the two-step mechanism, eqs S19 to S21. For the "heterogeneous" (i.e., all solid-oxide-based) nucleation (k_1) and growth (k_2) supported-nanoparticle heterogeneous catalyst formation pathway, A is the supported precatalyst $[Ir^I/Al_2O_3]_{sus}$ and B is the supported catalyst $[Ir(0)_n/Al_2O_3]_{sus}$.

$$\underset{\textbf{[A/Al}_2\textbf{O}_3\textbf{]}_{\textbf{sus}}}{Ir^I/Al_2O_3} \xrightarrow[2.5\ H_2]{k_1} \underset{\textbf{[B/Al}_2\textbf{O}_3\textbf{]}_{\textbf{sus}}}{Ir(0)/Al_2O_3} \qquad \text{(S19)}$$

$$\underset{\textbf{[A/Al}_2\textbf{O}_3\textbf{]}_{\textbf{sus}}\textbf{ + [B/Al}_2\textbf{O}_3\textbf{]}_{\textbf{sus}}}{Ir^I/Al_2O_3 + Ir(0)/Al_2O_3} \xrightarrow[2.5\ H_2]{k_2} \underset{\textbf{2 [B/Al}_2\textbf{O}_3\textbf{]}_{\textbf{sus}}}{2\,[Ir(0)/Al_2O_3]} \qquad \text{(S20)}$$

$$\text{SUM:} \quad \underset{\textbf{[A/Al}_2\textbf{O}_3\textbf{]}_{\textbf{sus}}}{Ir^I/Al_2O_3} \xrightarrow[2.5\ H_2]{k_{obs}} \underset{\textbf{[B/Al}_2\textbf{O}_3\textbf{]}_{\textbf{sus}}}{Ir(0)/Al_2O_3} \qquad \text{(S21)}$$

The relevant rate equation for the solid-oxide based, "heterogeneous" nucleation and growth pathway (k_1 and k_2) is given by eq S22.

$$-\frac{d[Ir^I/Al_2O_3]_{sus}}{dt} = k_1[Ir^I/Al_2O_3]_{sus,t} + k_2[Ir^I/Al_2O_3]_{sus,t}[Ir(0)_n/Al_2O_3]_{sus,t} \qquad \text{(S22)}$$

Next we express the $[Ir^I/Al_2O_3]_{sus,t}$ in terms of what we actually start with $[Ir^I/Al_2O_3]_{sus,i}$. This is analogous to the derivation of eq S11 (above), except for we now solve the dissociative equilibrium for $[Ir^I{*}solvent]_t$, eq S23.

$$[\mathrm{Ir^I} * \mathrm{solvent}]_t = \frac{K_{\mathrm{Diss}}[\mathrm{Ir^I/Al_2O_3}]_{\mathrm{sus},t}[\mathrm{solvent}]_t}{[\mathrm{Al_2O_3}]_{\mathrm{sus},t}} \quad \text{(S23)}$$

Substitution of eq S23 into the mass balance equation (eq S10) followed by rearrangement yields eq S24.

$$[\mathrm{Ir^I/Al_2O_3}]_{\mathrm{sus},t} = [\mathrm{Ir^I/Al_2O_3}]_{\mathrm{sus,i}}\left\{\frac{[\mathrm{Al_2O_3}]_{\mathrm{sus},t}}{[\mathrm{Al_2O_3}]_{\mathrm{sus},t} + K_{\mathrm{Diss}}[\mathrm{solvent}]_t}\right\} \quad \text{(S24)}$$

Finally, substitution of eq S24 into eq S22 yields eq S25, where $k_{1\mathrm{obs}}$ and $k_{2\mathrm{obs}}$ are eqs S26 and S27 respectively.

$$-\frac{\mathrm{d}[\mathrm{Ir^I/Al_2O_3}]_{\mathrm{sus}}}{\mathrm{dt}} = k_{1\mathrm{obs}}[\mathrm{Ir^I/Al_2O_3}]_{\mathrm{sus,i}} + k_{2\mathrm{obs}}[\mathrm{Ir^I/Al_2O_3}]_{\mathrm{sus,i}}[\mathrm{Ir}(0)_n/\mathrm{Al_2O_3}]_{\mathrm{sus},t} \quad \text{(S25)}$$

$$k_{1\mathrm{obs}} = \frac{k_1[\mathrm{Al_2O_3}]_{\mathrm{sus},t}}{[\mathrm{Al_2O_3}]_{\mathrm{sus},t} + K_{\mathrm{Diss}}[\mathrm{solvent}]_t} \quad \text{(S26)}$$

$$k_{2\mathrm{obs}} = \frac{k_2[\mathrm{Al_2O_3}]_{\mathrm{sus},t}}{[\mathrm{Al_2O_3}]_{\mathrm{sus},t} + K_{\mathrm{Diss}}[\mathrm{solvent}]_t} \quad \text{(S27)}$$

Derivation of the "Homogeneous" (i.e., All Solution-Based) Nucleation (k_1') and Growth (k_2') Pathway. The putative "homogeneous" (i.e., all solution-based) nucleation and growth pathway (i.e., the k_1' and k_2' right most pathway, Scheme S1) also begins with a dissociative equilibrium (K_{Diss}) between $[\mathrm{Ir^I/Al_2O_3}]_{\mathrm{sus}}$ and $\mathrm{Ir^I}*\mathrm{solvent}$. Furthermore,

nucleation then also occurs from the dissociated Ir^{I}∗solvent complex in solution (k_1') and in this particular mechanism. However, instead of the fast γ-Al_2O_3 capture step occurring prior to the nanoparticle growth, that step occurs after the nanoparticle has finished growing, and, therefore the nanoparticle growth step occurs exclusively in solution from Ir^{I}∗solvent and $Ir(0)_{n,soln}$ in this mechanism. For the "homogeneous" (i.e., all solution-based) nucleation and growth pathway, A is the Ir^{I}∗solvent complex in solution and B is $Ir(0)_{n,soln}$.

The Ir(1,5-COD)Cl/γ-Al_2O_3 to $Ir(0)_n$/γ-Al_2O_3 supported-nanoparticle heterogeneous catalyst formation kinetics can again be formulated in terms of the two-step mechanism, eqs S28 to S32.

$$2\,[Ir^{I}/Al_2O_3 + \text{solvent} \overset{K_{Diss}}{\rightleftharpoons} Ir^{I}{*}\text{solvent} + Al_2O_3] \qquad \text{(S28)}$$

$$\mathbf{[A/Al_2O_3]_{sus}} \qquad\qquad \mathbf{[A]}$$

$$Ir^{I}{*}\text{solvent} \xrightarrow[2.5\ H_2]{k_1'} Ir(0)_{soln} + \text{solvent} \qquad \text{(S29)}$$

$$\mathbf{[A]} \qquad\qquad \mathbf{[B]}$$

$$Ir^{I}{*}\text{solvent} + Ir(0)_{soln} \xrightarrow[2.5\ H_2]{k_2'} 2\ Ir(0)_{soln} + \text{solvent} \qquad \text{(S30)}$$

$$\mathbf{[A]\ +\ [B]} \qquad\qquad \mathbf{2\ [B]}$$

$$2\,[Ir(0)_{soln} + Al_2O_3 \overset{\text{Fast; } K_{Assoc}}{\rightleftharpoons} Ir(0)/\gamma\text{-}Al_2O_3] \qquad \text{(S31)}$$

$$\mathbf{2\ [B]} \qquad\qquad \mathbf{2\ [B/Al_2O_3]_{sus}}$$

$$\text{SUM:} \quad [Ir^{I}/Al_2O_3]_{sus} \xrightarrow[2.5\ H_2]{k_{obs}'} [Ir(0)/Al_2O_3]_{sus} \qquad \text{(S32)}$$

$$\mathbf{[A/Al_2O_3]_{sus}} \qquad\qquad \mathbf{[B/Al_2O_3]_{sus}}$$

In the "homogeneous" (i.e., all solution-based) nucleation and growth pathway, the K_{Diss} and K_{Assoc} equilibria are both important, (eqs S8 and S33), even though K_{Assoc} occurs after the rate-determining nucleation and growth steps. Furthermore the associative equilibrium in eq S33 must be fast and large in order to account for the observed

product, $Ir(0)_n/\gamma\text{-}Al_2O_3$. The mechanistic treatment of a fast K_{Assoc} step, post the solution-based nanoparticle growth step, requires either (i) a size dependent $Ir(0)_n$ K_{Assoc} equilibrium with $[\gamma\text{-}Al_2O_3]_{sus}$ or (ii) $k_2'K_{Assoc}$ to be fast relative to $k_2''K_{Assoc}'$.

$$K_{Assoc} = \frac{[Ir(0)_n/Al_2O_3]_{sus,t}}{[Ir(0)_{n,soln}]_t[Al_2O_3]_{sus,t}} \quad \text{(S33)}$$

The relevant rate equation for the "homogeneous" (i.e., all solution-based) nucleation and growth pathway (k_1' and k_2') is given by eq S34.

$$-\frac{d[Ir^I/Al_2O_3]_{sus}}{dt} = k_1[Ir^I * solvent]_t + k_2[Ir^I * solvent]_t[Ir(0)_{n,soln}]_t \quad \text{(S34)}$$

The derivation of eq S35 is analogous to the derivation of eq S13.

$$-\frac{d[Ir^I/Al_2O_3]_{sus}}{dt} = k_{1obs}[Ir^I/Al_2O_3]_{sus,i} + k_{2obs}[Ir^I/Al_2O_3]_{sus,i}[Ir(0)_{n,soln}]_t \quad \text{(S35)}$$

Next, we need to express $[Ir(0)_{n,soln}]_t$ (eq S35) in terms of the observed product $[Ir(0)_n/Al_2O_3]_{sus,t}$. This is done by solving the associative equilibrium equation, eq S33, for $[Ir(0)_{n,soln}]_t$ followed by substitution into eq S35. The result is the rate equation, S36, in terms of $[Ir^I/Al_2O_3]_{sus,i}$ and the observed product $[Ir(0)_n/Al_2O_3]_{sus,t}$, which accounts for the solution-based nucleation and growth pathway as well as the supported, non-aggregated $Ir(0)_{\sim 900}/\gamma\text{-}Al_2O_3$ supported-nanoparticle product described in Scheme S1.

$$-\frac{d[Ir^I/Al_2O_3]_{sus}}{dt} = k_{1obs}[Ir^I/Al_2O_3]_{sus,i} + k_{2obs}[Ir^I/Al_2O_3]_{sus,i}[Ir(0)_n/Al_2O_3]_{sus,t} \quad \text{(S36)}$$

The k_{1obs} and k_{2obs} are now given by eqs S37 and S38 respectively.

$$k_{1obs} = \frac{k_1' K_{Diss}[solvent]_t}{[Al_2O_3]_{sus,t} + K_{Diss}[solvent]_t} \quad \text{(S37)}$$

$$k_{2obs} = \frac{k_2' K_{Diss}[solvent]_t}{[Al_2O_3]^2_{sus,t} + K_{Diss}K_{Assoc}[Al_2O_3]_{sus,t}[solvent]_t} \quad \text{(S38)}$$

Mechanistic and Curve-Fitting Treatment of the k_{1obs} and k_{2obs} vs [Acetone] Data for the Mixed Cyclohexane/Acetone Solvent System. In the cyclohexane/acetone system, $[Ir^I]_2$ dimer (an abbreviation for $[Ir(1,5\text{-COD})Cl]_2$), but little Ir^I∗solvent (i.e., Ir(1,5-COD)Cl(solvent)), is observable by UV–vis spectroscopy, Figure S2. The mechanism in Scheme S1 must, then, be updated for the mixed solvent system, Scheme S2. Note that

Scheme S2. Two Plausible Mechanistic Pathways for the Mixed, Cyclohexane Plus Acetone, Supported-Nanoparticle Heterogeneous Catalyst Formation System.

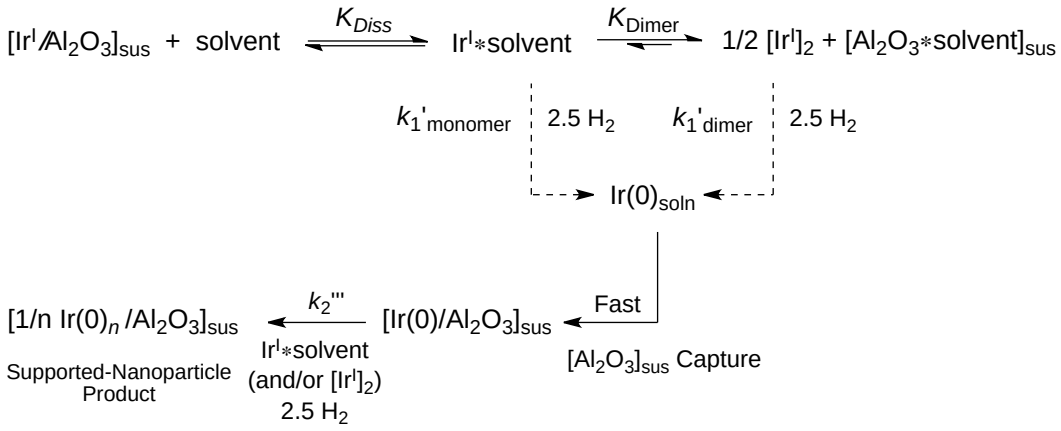

the disproved mechanistic pathways, k_1, k_2 and k_2', have now been omitted for clarity. There are three limiting mechanistic subcases from Scheme S2: (i) only $k_1'_{monomer}$

contributes (i.e., k_1'$_{monomer}$ >> k_1'$_{dimer}$), (ii) only k_1'$_{dimer}$ contributes (i.e., k_1'$_{dimer}$ >> k_1'$_{monomer}$), or (iii) both k_1'$_{monomer}$ and k_1'$_{dimer}$ contribute to the observed nucleation and subsequent nanoparticle growth kinetics. The k_{1obs} vs [acetone] data, Figure 5 of the main text, would seem to argue against a k_1'$_{dimer}$, $[Ir^I]_2$ only pathway since it should not have a ca. [acetone]^1 dependence (and unless there is a general polarity dependence with added acetone that mimics a [acetone]$^{\sim -1}$ dependence). We were able to directly monitor the $[Ir^I]_2$ concentration via UV–vis spectroscopy and $[Ir^I]_2$ indeed increases with increasing [acetone], Figure S3. In addition, a control experiment using 0.49 mM $[Ir(1,5\text{-}COD)Cl]_2$ (i.e., 0.97 mM total Ir) in 2.5 mL cyclohexane, plus the standard conditions of 0.5 mL cyclohexene and 40 psig of H_2, yields formation of bulk Ir(0) metal and a k_{1obs} value of 3.2×10^{-3} h^{-1}, suggesting that k_1'$_{dimer}$ can in principle be comparable in magnitude to the k_{1obs} values. Furthermore, empirical fitting of the k_{2obs} and k_{1obs} vs [acetone] data in Figures 4 and 5 of the main text revealed that equations of the general form of S14 and S15 can fit the [acetone] dependent data.

Scheme S3. The Minimalistic, Ockham's Razor Scheme to Account for the k_{2obs} and k_{aobs} vs [Acetone] Data Shown in Figures 4 and 5 of the Main Text, where by definition $Ir^I_{soln} = Ir^I$*solvent + 2 $[Ir^I]_2$.

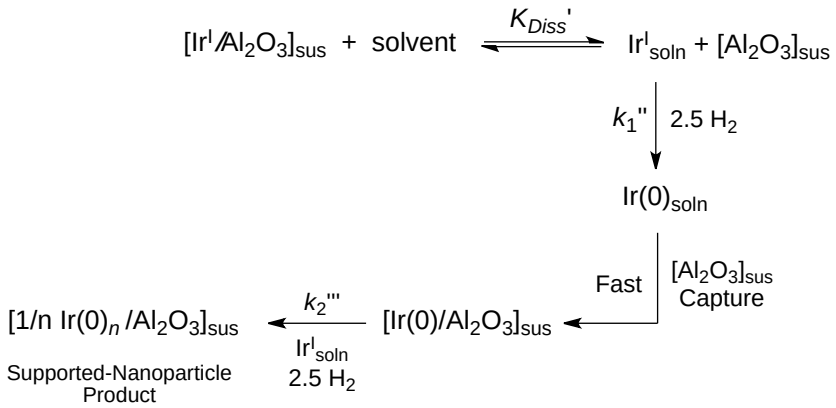

What this suggests mathematically, and looking from the prior derivation of eqs S14 and S15, is that the Ir^{I}*solvent and ½ $[Ir^{I}]_2$ in Scheme S2 are behaving effectively as a single Ir^{I} term (i.e., with $k_1'_{monomer} \approx k_1'_{dimer}$), so that equations of the form of S14 and S15 can result. In addition, multiple pages of derivations treating Ir^{I}*solvent, ½ $[Ir^{I}]_2$, $k_1'_{monomer}$ and $k_1'_{dimer}$ separately did not result in treatable/useful kinetic equations, at least in our hands. In short, we were lead by both the empirical curve-fitting and the mathematical equations to propose Scheme S3 as a minimalistic (Ockham's razor) scheme to account for the [acetone] dependent data shown in Figures 4 and 5 of the main text.

For this mechanism we can write the differential equation, eq S39, the dissociative equilibrium, K'_{Diss} (eq S40) and the mass balance equation, S41. Equations S39 to S41 are needed to derive the differential equation, eq S42, all as done in eqs S7 to S12 above.

$$-\frac{d[Ir^{I}/Al_2O_3]_{sus}}{dt} = k_1''[Ir^{I}_{soln}]_{2,t} + k_2'''[Ir^{I}_{soln}]_{2,t}[Ir(0)_n/Al_2O_3]_{sus,t} \quad \text{(S39)}$$

$$K_{Diss}' = \frac{[Ir^{I}_{soln}]_{2,t}[Al_2O_{3soln}]_t}{[Ir^{I}/Al_2O_3]_{sus,t}[solvent]_t} \quad \text{(S40)}$$

Where, by definition, $[Ir^{I}_{soln}]_t \equiv [Ir^{I}{*}solvent]_t + 2\,[Ir^{I}]_{2,t}$ and $[Al_2O_{3soln}]_{sus,t} \equiv [Al_2O_3]_{sus,t} + [Al_2O_3{*}solvent]_{sus,t}$

$$[Ir^{I}/Al_2O_3]_{sus,i} = [Ir^{I}/Al_2O_3]_{sus,t} + [Ir^{I}_{soln}]_{2,t} \quad \text{(S41)}$$

$$-\frac{d[Ir^{I}/Al_2O_3]_{sus}}{dt} = k_{1obs}[Ir^{I}/Al_2O_3]_{sus,i} + k_{2obs}[Ir^{I}/Al_2O_3]_{sus,i}[Ir(0)_n/Al_2O_3]_{sus,t} \quad \text{(S42)}$$

and where now k_{1obs} and k_{2obs} are eqs S43 and S44 respectively.

$$k_{1obs} = \frac{k_1'' K'_{Diss}[solvent]_t}{[Al_2O_{3soln}]_{sus,t} + K'_{Diss}[solvent]_t} \quad \text{(S43)}$$

$$k_{2obs} = \frac{k_2''' K'_{Diss}[solvent]_t}{[Al_2O_{3soln}]_{sus,t} + K'_{Diss}[solvent]_t} \quad \text{(S44)}$$

Equations S43 and S44 (having the same general form as eqs S14 and S15) were, then, the equations used to fit successfully *both* the k_{1obs} and k_{2obs} data, Figure 4 of the main text.

Comparison of the loss of Ir(1,5-COD)Cl(solvent) (Figure S2) and the Decrease in k_{1obs} and k_{2obs} with Increasing [γ-Al_2O_3]$_{sus}$: Evidence Consistent with Ir(1,5-COD)Cl(solvent) Being a Kinetically Dominant Intermediate. The Ir(1,5-COD)Cl(solvent) solution-based nucleation and solid-oxide-based growth mechanism, Scheme S1 (also Scheme 3 of the main text) predicts that k_{1obs} and k_{2obs} will *decrease with increasing* [γ-Al_2O_3]$_{sus}$. Plots of k_{1obs} and k_{2obs} do indeed show an inverse dependence on [γ-Al_2O_3]$_{sus}$ over the range studied (Figures 2 and 3, main text). Qualitatively this is easily rationalized by a shift to the left of the K_{Diss} equilibrium shown in Scheme S1, resulting in less Ir(1,5-COD)Cl(solvent) in solution, which in turn leads to slower nucleation and growth kinetics. UV–vis spectroscopy allowed us to probe the change in Ir^{I}∗solvent with increasing [γ-Al_2O_3]$_{sus}$, as detailed next.

Control reactions done to probe if Ir(1,5-COD)Cl(solvent) decreases with increasing [γ-Al_2O_3]$_{sus}$ were all done under O_2-free conditions (i.e., beginning in the drybox). To start 0.05 g of the 2.0 wt% Ir(1,5-COD)Cl/γ-Al_2O_3 precatalyst was placed in a 20 mL scintillation vial along with 2.5 mL acetone. Subsequently the appropriate amount of

additional γ-Al_2O_3 (0.25 M to 0.65 M) was added and the slurry was stirred for 8 h. The slurry was then filtered through a 0.2 µm nylon filter[6] (NALGENE) and into an O_2 free UV–vis cell, sealed and then brought out of the drybox; the UV–vis spectrum was then recorded.

A single UV–vis spectrum of the filtered yellow solution is shown in Figure S2 (left). Two metal-to-ligand charge transfer bands are present from 340-540 nm, data consistent with the presence of a square planar Ir^{I} complex, tentatively assigned at present to Ir(1,5-COD)Cl(solvent).[7] A plot of the absorbance at 396 nm vs $[\gamma\text{-}Al_2O_3]_{sus}$, Figure S2 (right), reveals that *the Ir(1,5-COD)Cl(solvent) in solution does decrease with increasing* $[\gamma\text{-}Al_2O_3]_{sus}$. In short, the decrease in the absorbance at 396 nm with added $[\gamma\text{-}Al_2O_3]_{sus}$ confirms the expected shift of the K_{Diss} equilibrium in Scheme S1 back to the left with increasing $[\gamma\text{-}Al_2O_3]_{sus}$.

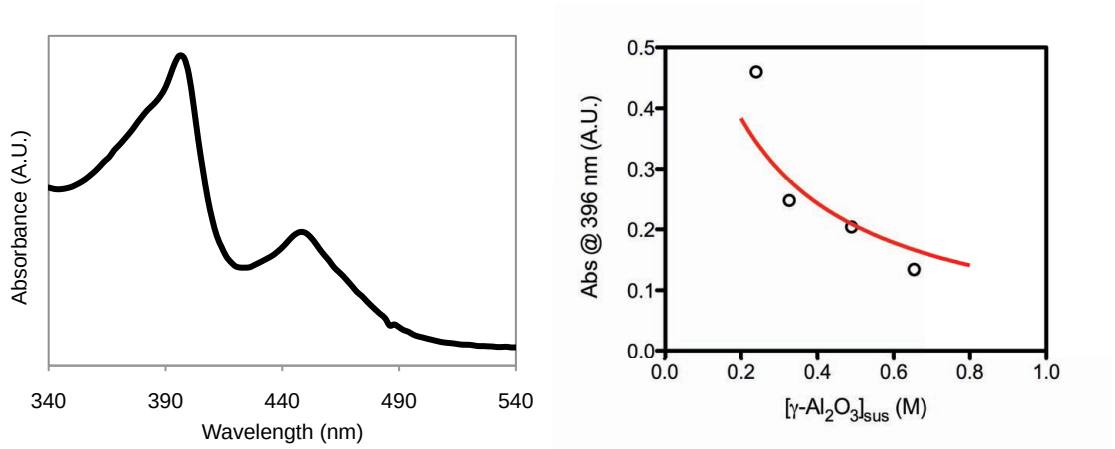

Figure S2. On the left is the UV–vis spectra of the filtered solution from Ir(1,5-COD)Cl/γ-Al_2O_3 in acetone. On the right is a plot of the absorbance @ 396 nm vs $[\gamma\text{-}Al_2O_3]_{sus}$ (taken from the filtered solution of Ir(1,5-COD)Cl(solvent) in acetone). The curve is a fit to eq S50 while constraining K_{Diss} to its known value of 1.3×10^{-2}. The resultant, curve-fit-determined, molar absorptivity was found to be $9(1) \times 10^2$ M^{-1} cm^{-1}.

If Ir(1,5-COD)Cl(solvent) (= Ir^{I}∗solvent) is indeed a kinetically competent intermediate in Scheme S1 (Scheme 3, main text), then the change in the absorbance data at 396 nm

(i.e., the decrease in Ir(1,5-COD)Cl(solvent) with increasing [γ-Al_2O_3]$_{sus}$) should have the same general shape as the k_{1obs} and k_{2obs} vs [γ-Al_2O_3]$_{sus}$ data, Figures 2 and 3 of the main text. Qualitatively, the absorbance data generally agrees quite nicely having the same general shape as the k_{1obs} and k_{2obs} vs [γ-Al_2O_3]$_{sus}$ data.

In order to seef if the K_{Diss} equilibrium, eq S8, can semiquantitatively account for the absorbance (at 396 nm) vs [γ-Al_2O_3]$_{sus}$ data (Figure S2, right) we coupled eq S8 to Beers' Law (eq S45) as described next.

$$A_{396} = \varepsilon_{396} b[\mathrm{Ir^I} * \mathrm{solvent}] \tag{S45}$$

Rearranging for [Ir^I∗solvent] (and with a path length of 1 cm) yields eq S46.

$$[\mathrm{Ir^I} * \mathrm{solvent}] = \frac{A_{396}}{\varepsilon_{396}} \tag{S46}$$

K_{Diss} (eq S8) can then be formulated in terms of a basic equilibrium calculation as in eq S47, with one notable exception. The concentration of [γ-Al_2O_3]$_{sus}$ is treated as a constant, C_0, plus the amount of "Ir(1,5-COD)Cl" sites that become available upon dissociation, x. This is simply a result of treating the γ-Al_2O_3 as being homogeneously suspended in solution (and, really, the assumption that the "Ir(1,5-COD)Cl" binding sites increase linearly with an increasing addition of γ-Al_2O_3).

$$\begin{array}{ccccccc} [Ir^I\!/\!Al_2O_3]_{sus} & + & \text{solvent} & \overset{K_{Diss}}{\rightleftharpoons} & Ir^I{*}\text{solvent} & + & [Al_2O_3]_{sus} \\ A_0 - x & & B_0 - x & & x & & C_0 + x \end{array} \tag{S47}$$

so that

$$K_{\mathrm{Diss}} = \frac{x[C_0 + x]}{[A_0 - x][B_0 - x]} \tag{S48}$$

and where x is given by eq S49.

$$\mathrm{x} = [\mathrm{Ir}^{\mathrm{I}} * \mathrm{solvent}] = \frac{A_{396}}{\varepsilon_{396}} \tag{S49}$$

To a first order approximation we assume that C_0 >> x and that B_0 >> x. Substituting eq S49 into the first order approximation of eq S48, followed by rearrangement for A_{396} yields eq S50.

$$A_{396} \approx \frac{K_{\mathrm{Diss}}\varepsilon_{396}A_0B_0}{C_0 + K_{\mathrm{Diss}}B_0} \tag{S50}$$

Equation S50 can semiquantitatively account for the absorbance vs $[Al_2O_3]_{sus}$ data (Figure S2, red line) via weighted nonlinear least-squares fitting when K_{Diss} is constrained to the known value of 1.3×10^{-2}. Interestingly, the fit (the red line shown in Figure S2, right most figure) yields an estimation of the molar absorptivity for Ir^{I}∗solvent of ε_{396} = 9(1) × 10^2 M^{-1} cm^{-1}. The first-order approximation, curve-fit-determined value of ε_{396} agrees generally with the molar absorptivities reported by Epstein et al. for the closely related solvate, Ir(1,5-COD)Cl(CH_3CN) (ε was found to be 1300 at 400 nm in CH_3CN).[7] In short, the results in Figure S2 are consistent with the currently proposed

mechanism shown in Scheme S1—in which Ir^{I}∗solvent acts as a kinetically competent intermediate for $Ir(0)_n/\gamma\text{-}Al_2O_3$ supported-nanoparticle heterogeneous catalyst formation.

Comparison of the Increase in $[Ir^{I}]_2$ (Figure S3) and the Increase in k_{1obs} and k_{2obs} with Increasing [Acetone]: Evidence Consistent with $[Ir^{I}]_2$ Being a Kinetically Dominant Intermediate. The mechanism shown in Scheme S1 also predicts that k_{1obs} and k_{2obs} will increase with increasing [acetone]. Plots of k_{1obs} and k_{2obs} do indeed increase with increasing [acetone] over the range studied (Figures 4 and 5, main text). Qualitatively, this is most easily rationalized if the K_{Diss} equilibrium shown in Scheme S3 shifts now *to the right* with increasing [acetone], resulting in more Ir(1,5-COD)Cl(solvent) in solution, which in turn leads to overall faster nucleation and growth kinetics. Again, UV–vis spectroscopy allowed us to probe the change in $[Ir^{I}]_2$ with increasing [acetone], as detailed next.

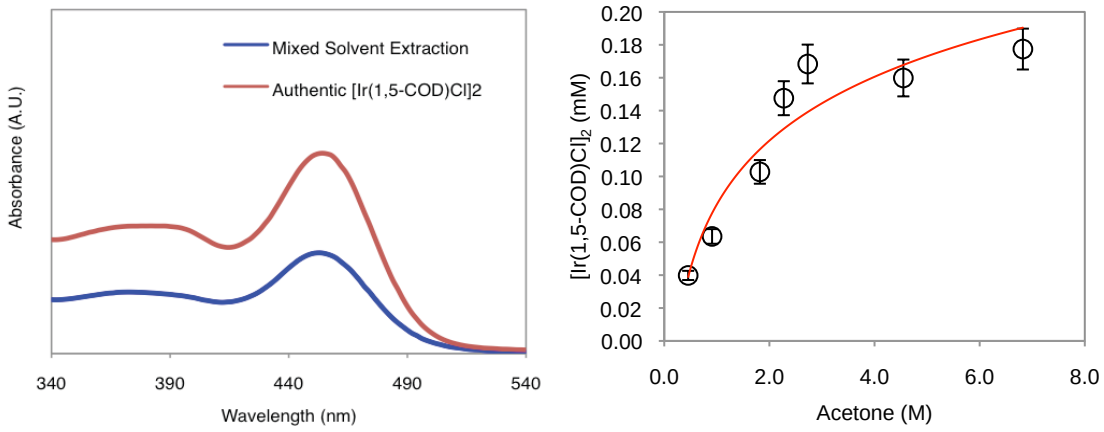

Figure S3. UV–vis spectra of the filtered solution of $Ir(1,5\text{-}COD)Cl/\gamma\text{-}Al_2O_3$ in acetone plus cyclohexane (left) in comparison to authentic $[Ir(1,5\text{-}COD)Cl]_2$ in acetone plus cyclohexane. On the right is a plot of the increasing $[Ir(1,5\text{-}COD)Cl]_2$ concentration in solution with increasing [acetone]. The curve is not from any fit; rather, it is a sketch to help guide the eye.

Control reactions, all done under O_2 free conditions, were run from 0.14 to 6.8 M [acetone]. To start 0.05 g of the 2.0 wt% $Ir(1,5\text{-}COD)Cl/\gamma\text{-}Al_2O_3$ precatalyst was placed

in a 20 mL scintillation vial along with 2.5 mL of the total mixed solvent (i.e., cyclohexane + acetone = 2.5 mL). The slurry was then filtered through a 0.2 μm nylon filter into an O_2 free UV–vis cell; the spectrum in Figure S3 was then recorded.

A single UV–vis spectrum of the filtered yellow solution is shown in Figure S3 (left). Two metal-to-ligand charge transfer bands are present from 340-540 nm (and which are different vs those in neat acetone). The UV–vis spectrum closely mimics that of authentic $[Ir(1,5\text{-}COD)Cl]_2$ in cyclohexane plus acetone, Figure S3.[7] Hence, under the mixed-solvent conditions the concentration of the Ir^I species present in solution (i.e., $[Ir(1,5\text{-}COD)Cl]_2$]) could be determined from a UV–vis calibration curve prepared using authentic $[Ir(1,5\text{-}COD)Cl]_2$. Plots of the resultant $[Ir(1,5\text{-}COD)Cl]_2$ (i.e., from the Ir(1,5-COD)Cl/γ-Al_2O_3) vs [acetone] are shown in Figure S3 (right), and provide direct spectroscopic evidence that *the $[Ir^I]_2$ in solution does increase with increasing [acetone]*, all as expected when the position of the K_{Diss}' equilibrium in Scheme S3 shifts to the right with increasing [acetone].

Again, the shape of the $[Ir^I]_2$ data agrees qualitatively with, (i.e., has the same general shape as) the k_{1obs} and k_{2obs} vs [acetone] data, Figures 4 and 5 of the main text. Semi-quantitatively, the observed increase in the $[Ir^I]_2$, in Figure S3, is 4.2 fold over the range of 0.46 to 2.73 M [acetone] (and while using 2 $[Ir^I]_2$ for the comparison to get the concentration data to a 1 Ir^I_{soln} equivalent). In comparison, k_{1obs} increased by 12.5 fold over the same range of [acetone]. Due to H_2 gas-to-solution mass transfer limitations (as described in footnote 39 of the main text), we can only use the k_{2obs} vs [acetone] data over the range of 0.46 to 1.82 M [acetone], and over that range $[Ir^I]_2$ increases by 2.6 fold. In comparison, k_{2obs} increased by 2.7 fold over the same range of [acetone]. In short, the changes seen in $[Ir^I]_2$ agree generally with the k_{1obs} and k_{2obs} vs [acetone] data. The results are qualitatively, if not semi-quantitatively, consistent with $[Ir^I]_2$ being a kinetically competent intermediate in Scheme S3.

Observation of and $[Ir^{I}]_2$ in Figures S2 and S3 to Independently Calculate K_{Diss} and K_{Diss}'. As described in the main text gas-liquid-chromatography (GLC) was used to independently verify the K_{Diss} equilibrium for the $[Al_2O_3]_{sus}$ dependent data. This was done by filtering off the solution from the (equilibrated) Ir^{I}/Al_2O_3 plus acetone solution and then hydrogenating the Ir(1,5-COD)Cl(solvent) complex. The amount of cyclooctane (the hydrogenated product of 1,5-cyclooctadiene from the Ir^{I}∗solvent complex in solution) was quantified via GLC. Since the mols of cyclooctane in solution are equivalent to the mols of Ir^{I} in solution, this was taken to be the value of x for the K_{Diss} equilibrium, eq S48. Equation S48 was then used to back calculate the K_{Diss} equilibrium, which was found to be $K_{Diss} = 1.1 \times 10^{-2}$.

The Ir^{I}∗solvent and $[Ir^{I}]_2$ UV–vis data (Figures S2 and S3 respectively) are direct spectroscopic observations of the Ir^{I} species in solution. When the extinction coefficient for the appropriate spectroscopically observed species are known, we can independently calculate the K_{Diss} and K_{Diss}' equilibrium constants and compare those values to the fit obtained K_{Diss} and K_{Diss}' values.

However, only for the cyclohexane/acetone mixed solvent system, where $[Ir^{I}_2]$ (i.e., $[Ir(1,5\text{-}COD)Cl]_2$) is seen, is the appropriate ε value known rigorously (i.e., so that Beers' Law, $A = \varepsilon bc$, can be used to determine K_{Diss}'). In that case, the use of Beers' Law, eq S51, then yields eq S52 (and where the path length $b = 1$).

$$A_{452} = \varepsilon_{452} b [Ir^{I}]_2 \tag{S51}$$

$$[Ir^{I}]_2 = \frac{A_{452}}{\varepsilon_{452}} \tag{S52}$$

K_{Diss}' (eq S53) can then be formulated in terms of a basic equilibrium calculation as in eq S53, with one notable exception. The concentration of $[Al_2O_3]_{sus}$ is treated as a constant, C_0, plus the amount of "Ir(1,5-COD)Cl" sites that become available upon dissociation, x. This is simply a result of treating the γ-Al_2O_3 as being homogeneously suspended in solution (and really, the assumption that the "Ir(1,5-COD)Cl" binding sites, or surface area, increase linearly with an increasing addition of γ-Al_2O_3).

$$\underset{A_0 - x}{[Ir^{I}/Al_2O_3]_{sus}} + \underset{B_0 - x}{\text{solvent}} \rightleftharpoons[K_{Diss}'] \underset{x}{Ir^{I}_{soln}} + \underset{C_0 + x}{Al_2O_{3(soln)}} \qquad \text{(S53)}$$

so that

$$K_{\text{Diss}}' = \frac{x[C_0 + x]}{[A_0 - x][B_0 - x]} \qquad \text{(S54)}$$

Rigorously, x = $[Ir^{I}_{soln}]$ = $[Ir^{I}$*solvent] + 2 $[Ir^{I}]_2$, but when 2 $[Ir^{I}]_2$ >> $[Ir^{I}$∗solvent], as the UV–vis in Figure S3 (left most figure) shows, we can write eq S55.

$$[\text{Ir}^{\text{I}}_{\text{soln}}] \approx 2[\text{Ir}^{\text{I}}]_2 = x \qquad \text{(S55)}$$

Substitution of eq S52 into S55 yields eq S56.

$$[\text{Ir}^{\text{I}}_{\text{soln}}] \approx 2\frac{A_{452}}{\varepsilon_{452}} = x \qquad \text{(S56)}$$

Subsequent substitution of eq S56 into S54 yields eq S57.

$$K_{\text{Diss}}' = \frac{\frac{A_{452}}{\varepsilon_{452}}[C_0 + \frac{A_{452}}{\varepsilon_{452}}]}{[A_0 - \frac{A_{452}}{\varepsilon_{452}}][B_0 - \frac{A_{452}}{\varepsilon_{452}}]} \quad \text{(S57)}$$

Analyzing the data in Figure S3 via eq S54 (where C_0 = 163 mM and A_0 = 0.974 mM) and at the seven non-zero data points yields an average K_{Diss}' value of 2.8(6) × 10^{-2}. This K_{Diss}' ~ 3 × 10^{-2}, determined via the UV–vis data, is the same within experimental error as the fit-determined K_{Diss} equilibrium value, K_{Diss} = 3(2) × 10^{-2}. In short, the [Ir(1,5-COD)Cl]$_2$ vs [acetone] UV–vis data provides an additional handle to independently calculate K_{Diss}', results which confirm the fit-determined K_{Diss}' equillibrium within experimental error.

A Brief Discussion of Possible Direct Spectroscopic Monitoring of the Kinetics of the Ir(1,5-COD)Cl/γ-Al_2O_3 to Ir(0)$_n$/γ-Al_2O_3 Supported-Nanoparticle Formation Reaction. In principle[8,9] these Ir^I spectroscopic handles could be used to follow directly the Ir(1,5-COD)Cl/γ-Al_2O_3 to Ir(0)$_n$/γ-Al_2O_3 supported-nanoparticle formation reaction. Such studies would require a solution-based-cell as well as stopped-flow mixing to fully follow the reaction—and stopped flow plus spectroscopic studies that could deal with the suspended γ-Al_2O_3, its light scattering, and so on. Alternatively, one could have slower mixing and monitor the equilibrium concentrations of [Ir^I∗solvent] and [Ir^I_2], as essentially is done for the points in Figures S2 and S3. We are aware of both of these possibilities, which are under consideration, but which are studies beyond the scope of this first mechanistic investigation.

References

[1] Mondloch, J. E.; Wang, Q.; Frenkel, A. I.; Finke, R. G. *J. Am. Chem. Soc.* **2010,** *132,* 9701.

[2] Laxson, W.; Mondloch, J. E.; Finke, R. G. unpublished results and experiments in progress.

[3] Watzky, M. A.; Finke, R. G. *J. Am. Chem. Soc.* **1997,** *119,* 10382.

[4] Mondloch, J. E.; Yan, X.; Finke, R. G. *J. Am. Chem. Soc.* **2009,** *131,* 6389.

[5] Lin, Y.; Finke, R. G. *Inorg. Chem.* **1994,** *33,* 4891.

[6] A subtle, but important experimental point is that, during the course of working on these experiments, NALGENE changed their 0.2 μm Nylon filter sterilization process from an ethylene oxide treatment to γ-irradiation treatment, treatments that are not chemically equivalent. The latter, γ-irradiation sterilization process leads to discolored syringe filters (a slight yellowing vs white filters by the ethylene oxide treatment), discolored filters that *we found are not able to filter the Ir(1,5-COD)Cl/γ-Al_2O_3 from the Ir(1,5-COD)Cl(solvent) solution*, and at least when employed as is necessary for this work in a drybox. Our current working hypothesis is that the filters have become brittle from the harsh γ-irradiation treatment, so that when pumped into the drybox (under vacuum) or perhaps in shipping or other handling, they simply micro-crack or break. Nalgene has kindly provided non-sterilized 0.2 μm Nylon filters (i.e., non γ-irradiated), that *are indeed able to filter* the Ir(1,5-COD)Cl/γ-Al_2O_3 from the Ir(1,5-COD)Cl(solvent) solution just as the ethylene oxide sterilized filters were able to. Hence, we suggest using the non-sterilized Nalgene filters for filtering the Ir(1,5-COD)Cl/γ-Al_2O_3 from Ir(1,5-COD)Cl(solvent).

[7] Epstein, R. A.; Geoffroy, G. L.; Keeney, M. E.; Mason, W. R. *Inorg. Chem.* **1970,** *18,* 478.

[8] To the best of our knowledge one example exists in the literature; time resolved diffuse reflectance UV–vis spectroscopy has been used to follow the formation of Ag clusters in zeolite H–MFI, but in a *gas-solid phase reaction*.[9]

[9] Shimizu, K.-I.; Sugino, K.; Kato, K.; Yokota, S.; Okumura, K.; Satsuma, A. *J. Phys. Chem. C* **2007,** *111,* 1683.

CHAPTER VI

SUMMARY

A comprehensive and critical review of the pertinent literature revealed that little is known about the mechanisms that govern supported-nanoparticle heterogeneous catalyst formation. This is largely due to: (i) the lack of routine kinetic monitoring methods capable of following such processes rapidly and in real time, and (ii) the lack of well-defined supported-nanoparticle formation systems that start from well-characterized supported-metal precatalysts, have demonstrated reaction stoichiometries and which also yield compositionally well-defined supported-nanoparticles. Hence, a simple, routine kinetic monitoring method (i.e., the cyclohexene reporter reaction) was developed for following the kinetics of H_2PtCl_6/Al_2O_3 to $Pt(0)_n/Al_2O_3$ supported-nanoparticle formation in contact with EtOH, cyclohexene and H_2. Subsequently, the well-characterized Ir(1,5-COD)Cl/γ-Al_2O_3 to $Ir(0)_{\sim 900}$/γ-Al_2O_3 supported-nanoparticle formation system in contact with acetone, cyclohexene and H_2 was developed for more rigorous kinetic and mechanistic studies.

The kinetics of both the $Pt(0)_n/Al_2O_3$ and $Ir(0)_{\sim 900}$/γ-Al_2O_3 supported-nanoparticle formation systems in contact with solution were fit to a mechanism previously detailed by Finke and Watzky consisting of nucleation (A → B, rate constant k_1) followed by autocatalytic surface growth (A + B → 2B, rate constant k_2). A more detailed analysis of the Ir(1,5-COD)Cl/γ-Al_2O_3 to $Ir(0)_{\sim 900}$/γ-Al_2O_3 supported-nanoparticle formation kinetics revealed that nucleation occurs in solution from Ir(1,5-COD)Cl(solvent), followed by fast

nanoparticle capture by the γ-Al_2O_3 and subsequent nanoparticle growth between the $Ir(0)_n$/γ-Al_2O_3 and Ir(1,5-COD)Cl(solvent). These studies suggest that a simple, more direct avenue, for transferring the mechanistic and synthetic insights from the modern revolution in nanoparticle science to the synthesis of supported-nanoparticle heterogeneous catalysts and their catalysis exist.

APPENDIX A

GENERAL STATEMENT ON "JOURNALS-FORMAT" THESES

(Written by Professor Richard G. Finke)

The Graduate School at Colorado State University allows, and the Finke Group in particular encourages, so-called journals-format theses. Journals-format theses, such as the present one, consist of a student written and lightly edited literature background section, chapters corresponding (in the limiting, ideal case) to final-form papers either accepted or at least submitted for publication, a summary or conclusions chapter, and short bridge or transition sections between the chapters as needed to make the thesis cohesive and understandable to the reader. The "bridge" sections and summary are crucial so that the thesis fulfills the requirement that the thesis be an entity (an official requirement of most Graduate Schools). All chapters (manuscripts) in a journals-format thesis must of course be written initially by the student, with subsequent (ideally light) editing by the Professor, the student's committee, and even the student's colleagues where appropriate and productive.

The advantages for doing a journals-format thesis are several-fold and compelling. Specifically, some of the major advantages are: the level of science (i.e., of refereed, accepted publications) is at the highest level; the student and Professor must interact closely and vigorously (i.e., to bring both the science and the writing to their highest level), hence the student is getting the best education possible and is being at least exposed to (if not held to) the highest standards; the needed clean-up or control

experiments that invariably come up have all been identified and completed before the student leaves; there are no further time demands once the student has left the University (since all publication are at least submitted; it is terribly inefficient to try to complete either writing or often specialized experiments once the student has left); and the American tax payers, who ultimately pay the bill for the research, are getting their money's worth since all the research is published and thus widely disseminated in the highest form, as refereed science. Professorial experience teaches that a student who has achieved a journals-format thesis has indeed received a better education and has learned critical thinking and clear writing skills that will serve them well for a lifetime.

Experience also teaches, however, that much more than light editing is often needed in at least some student theses; it follows, then, that considerable professorial writing and editing might be needed for at least the initial chapters of most journals-format thesis. Indeed, a journals-format thesis is not recommended (and may not even be possible) for less strong students. Hence, the issue arises of exactly how much of the science and the writing, in the final (or submittable) chapters, is due to the student vs. the Professor and whether or not this level of contribution constitutes that acceptable of a new Ph.D. and independent investigator.

To deal with this issue, several recommendations are made.

Recommendations

The recommendations are:

(i) That the present pages be enclosed in the thesis until such a time as it is no longer needed (i.e., when the policies and procedures for journals-format theses become routine);

(ii) That for each chapter it is detailed, and to the satisfaction of the committee and the advisor, who made what contributions, both of intellectual substance and writing. Substantial contributions of other students or Professors should of course be

acknowledged. In the case of disagreements, the various drafts (i.e., as their electronic files) can be examined by the committee (in light of a knowledge of who wrote which draft) to easily determine who contributed what. In possible borderline or controversial cases it may even be advisable to keep all (electronic) drafts of the papers as a record;

(iii) That it be specifically stated whether or not all the experimental work is the Ph.D. candidate's [as is usually the case, although the increasing (desirable) collaboration among scientists worldwide makes this a non-trivial point].

(iv) Furthermore, it is recommended that allowances be made for the expectation that a greater degree of involvement of the professorial advisor is likely in a journals-format thesis than in a traditional thesis. That this is reasonable follows from the fact that some Professors write 100% of all their papers; this, unfortunately, robs the student of the valuable experience of participating in the science and the end product as practiced at the highest levels. It also creates an unmanageable writing burden for Professors involved in all but the narrowest of research areas or for Professors involved in more than one competitive research area;

(v) Notwithstanding (iv), there needs to be ideally no more than ca. 40% Professorial writing contribution in a given *early* chapter in the thesis, and there should be a clear evolution in the thesis of a decreasing professorial involvement to, say, a 10-20% direct contribution in the last chapter or two.

(vi) As a further aid towards separating out the candidate's and the professorial (and other) contributions, it is recommended that the Introductory (usually literature background) chapter(s) and at least the final chapter be lightly edited only, so that authentic examples of the student's contributions are documented in an unambiguous form.